GRADUATE AERONAUTICAL LABORATORIES
CALIFORNIA INSTITUTE OF TECHNOLOGY

Chemical Reactions in Turbulent Mixing Flows

Paul E. Dimotakis*, James E. Broadwell** and Anthony Leonard†

Air Force Office of Scientific Research
Grant No. 90-0304
Annual Technical Report: Period ending 14 May 1991

14 September 1991

Firestone Flight Sciences Laboratory

Guggenheim Aeronautical Laboratory

Karman Laboratory of Fluid Mechanics and Jet Propulsion

Pasadena

GRADUATE AERONAUTICAL LABORATORIES
CALIFORNIA INSTITUTE of TECHNOLOGY
Pasadena, California 91125

Chemical Reactions in Turbulent Mixing Flows

Paul E. Dimotakis*, James E. Broadwell** and Anthony Leonard†

Air Force Office of Scientific Research
Grant No. 90-0304
Annual Technical Report: Period ending 14 May 1991

14 September 1991

* Professor, Aeronautics & Applied Physics.

** Senior Scientist, Aeronautics.

† Professor, Aeronautics.

REPORT DOCUMENTATION PAGE

Form Approved
OMB No. 0704-0188

1. AGENCY USE ONLY (Leave blank)	2. REPORT DATE	3. REPORT TYPE AND DATES COVERED
	14 Sept 1991	Annual 16 April 1990- 14 May 1991

4. TITLE AND SUBTITLE
Chemical Reactions in Turbulent Mixing Flows

5. FUNDING NUMBERS
PE - 61102F
PR - 2308
TA - A2
G - AFOSR-90-0304

6. AUTHOR(S)
Paul E. Dimotakis
James E. Broadwell
Anthony Leonard

7. PERFORMING ORGANIZATION NAME(S) AND ADDRESS(ES)
California Institute of Technology
Graduate Aeronautical Laboratories
Mail Stop 301-46
Pasadena, CA 91125

8. PERFORMING ORGANIZATION REPORT NUMBER

9. SPONSORING/MONITORING AGENCY NAME(S) AND ADDRESS(ES)
AFOSR/NA
Building 410
Bolling AFB DC 20332-6448

10. SPONSORING/MONITORING AGENCY REPORT NUMBER

11. SUPPLEMENTARY NOTES

12a. DISTRIBUTION/AVAILABILITY STATEMENT
Approved for public release; distribution is unlimited

12b. DISTRIBUTION CODE

13. ABSTRACT (Maximum 200 words)

The purpose of this research is to conduct fundamental investigations of turbulent mixing, chemical reaction and combustion processes in subsonic and supersonic flows. This program comprises experimental, analytical, computational, and modeling efforts, and a diagnostics development and data-acquisition effort, the latter as dictated by specific needs of the experiments. Our approach has been to carry out a series of detailed theoretical and experimental studies primarily in two, well-defined, fundamentally important flow fields: free shear layers and axisymmetric jets. To elucidate molecular transport effects, experiments and theory concern themselves with both liquids and gases, primarily in moderate to high Reynolds number flows. The computational studies are, at present, focused at fundamental issues pertaining to the computational simulation of both compressible and incompressible flows. Modeling has been focused on both shear layers and turbulent jets, with an effort to include the physics of the molecular transport processes, as well as formulations of models that permit the full chemical kinetics of the combustion process to be incorporated. Our primary diagnostic development efforts are currently developing data-acquisition electronics for very high-speed, high-volume data requirements, such as two-dimensional imaging or arrays of supersonic flow sensors.

14. SUBJECT TERMS
Turbulence, shear layers, jets, mixing, combustion, numerical simulation, fractals, light detection diagnostics turbulent mixing modeling

15. NUMBER OF PAGES
194

16. PRICE CODE

17. SECURITY CLASSIFICATION OF REPORT	18. SECURITY CLASSIFICATION OF THIS PAGE	19. SECURITY CLASSIFICATION OF ABSTRACT	20. LIMITATION OF ABSTRACT
Unclassified	Unclassified	Unclassified	UL

Abstract

The purpose of this research is to conduct fundamental investigations of turbulent mixing, chemical reaction and combustion processes in turbulent, subsonic and supersonic flows. This program is comprised of several efforts. In particular,

a. an experimental effort,

b. an analytical effort,

c. a computational effort.

d. a modeling effort,

and

e. a diagnostics development and data-acquisition effort,

the latter as dictated by specific needs of the experimental part of the overall program.

Our approach has been to carry out a series of detailed theoretical and experimental studies primarily in two, well-defined, fundamentally important flow fields:

- free shear layers

and

- axisymmetric jets.

To elucidate molecular transport effects, experiments and theory concern themselves with both liquids and gases, primarily in moderate to high Reynolds number flows. The computational studies are, at present, focused at fundamental issues pertaining to the computational simulation of both compressible and incompressible flows. Modeling has been focused on both shear layers and turbulent jets, with an effort to include the physics of the molecular transport processes, as well as formulations of models that permit the full chemical kinetics of the combustion process to be incorporated. Our primary diagnostic development efforts are currently developing data-acquisition electronics for very high-speed, high-volume data requirements, such as two-dimensional imaging or arrays of supersonic flow sensors.

1. Introduction

Progress under the sponsorship of this Grant, for the period ending 14 May 1991, has been realized in several areas. In particular,

a. in supersonic shear layers, namely:

1. completion of a thesis entitled *An Experimental Investigation of Structure, Mixing and Combustion in Compressible Turbulent Shear Layers* (Hall 1991), including investigations of

   i. non-reacting flows at low to moderately high compressibility,

   and

   ii. reacting flows at medium and moderately high compressibility.

   Two publications stemming from this work (Hall *et al.* 1991a, Hall *et al.* 1991b) have been presented in *AIAA* conferences thus far this year.

In addition,

2. laser Rayleigh-scattering imaging experiments of non-reacting flows were conducted.

b. in the investigations of turbulent jets,[‡] namely

1. completion of a thesis entitled *An Experimental Investigation of Chemically-Reacting, Gas-Phase Turbulent Jets* (Gilbrech 1991), that explored Reynolds number effects on turbulent flame length and the influence of buoyancy on turbulent jet flames;
2. completion of a thesis entitled *Mixing in High Schmidt Number Turbulent Jets* (Miller 1991), that examined Reynolds number effects, Schmidt number effects, and the influence of initial conditions on the turbulent jet's mixing behavior;
3. and the development of jet mixing models that permit the inclusion of full chemical kinetics calculations. Two papers (Broadwell & Mungal 1991, Lutz *et al.* 1991) from this part of the effort have appeared during this reporting period.

c. In our analytical effort, a thesis entitled *An Investigation of the Inviscid Spatial Instability of Compressible Mixing Layers* (Zhuang 1990) was completed, from which two publications have already appeared (Zhuang, Dimotakis, & Kubota 1990,[♯] and Zhuang, Kubota, & Dimotakis 1990*). Brief descriptions of the results of this part of the effort have appeared in previous annual reports.

---

‡ The investigations of turbulent mixing and combustion in turbulent jets are co-sponsored by the Gas Research Institute.

♯ Included as Appendix A in last year's annual report (Dimotakis, Broadwell & Leonard 1990).

* Included as Appendix A in this report.

d. In our computational effort, we are developing new, reliable methods for computing interactions of shock waves and other discontinuous waves that may arise in compressible flows. A first paper (Lappas *et al.* 1991) was presented at the recent *AIAA Aerospace Sciences Conference*.

e. In our diagnostics effort, we are proceeding with a new generation of data acquisition systems, as necessary to record the higher resolution and bandwidth signals generated by several experiments presently in progress.

These developments will be discussed briefly below. For further details, the interested reader is directed to the publications stemming from the research supported under this Grant, which have appeared in the literature during the reporting period, describing various aspects of these efforts. This material is designated by a bullet (•) in the list of references at the end of this report.

2. Mixing and combustion in supersonic, turbulent shear layers

Experimental investigations performed in the GALCIT Supersonic Shear Layer Facility during the last year included:

1. Non-reacting flows spanning the range from low to moderately high compressibility, *i.e.*, $0.09 \leq M_{c1}^{(i)} \leq 0.96$.
2. Reacting flows at medium and moderately high compressibility, *i.e.*, $M_{c1}^{(i)} = 0.51, 0.96$.
3. Laser Rayleigh-scattering imaging experiments of non-reacting flows spanning the range from low to moderately high compressibility, specifically, $0.14 < M_{c1}^{(i)} < 0.96$.

2.1 Non-reacting shear layers

These compressible shear layer experiments were designed to search for shear layer structures and shock waves, and to measure shear layer growth rates that could be compared to previous investigators (Papamoschou & Roshko 1988, Chinzei *et al.* 1986, Clemens & Mungal 1990). A first publication of this work was presented at the 29th *AIAA Aerospace Sciences Meeting* (Reno, NV), 7–10 January 1991 (Hall *et al.* 1991a, included as Appendix B in this report).

FIG. 1 Schlieren photograph of non-reacting He/Ar flow ($M_{c1}^{(i)} = 0.96$).

Figure 1 is a Schlieren photograph of a non-reacting, high-speed stream helium, over low-speed stream argon (He/Ar) shear layer. This shear layer represented the highest compressibility flow tested ($M_{c1}^{(i)} = 0.96$). The shear layer is seen to grow linearly and it appears to be devoid of any large-scale, two-dimensional structures of the kind found to exist in incompressible shear layers (*e.g.* Brown & Roshko 1974). This absence of two-dimensional structure, in our experiments, is generally found even in the low compressibility

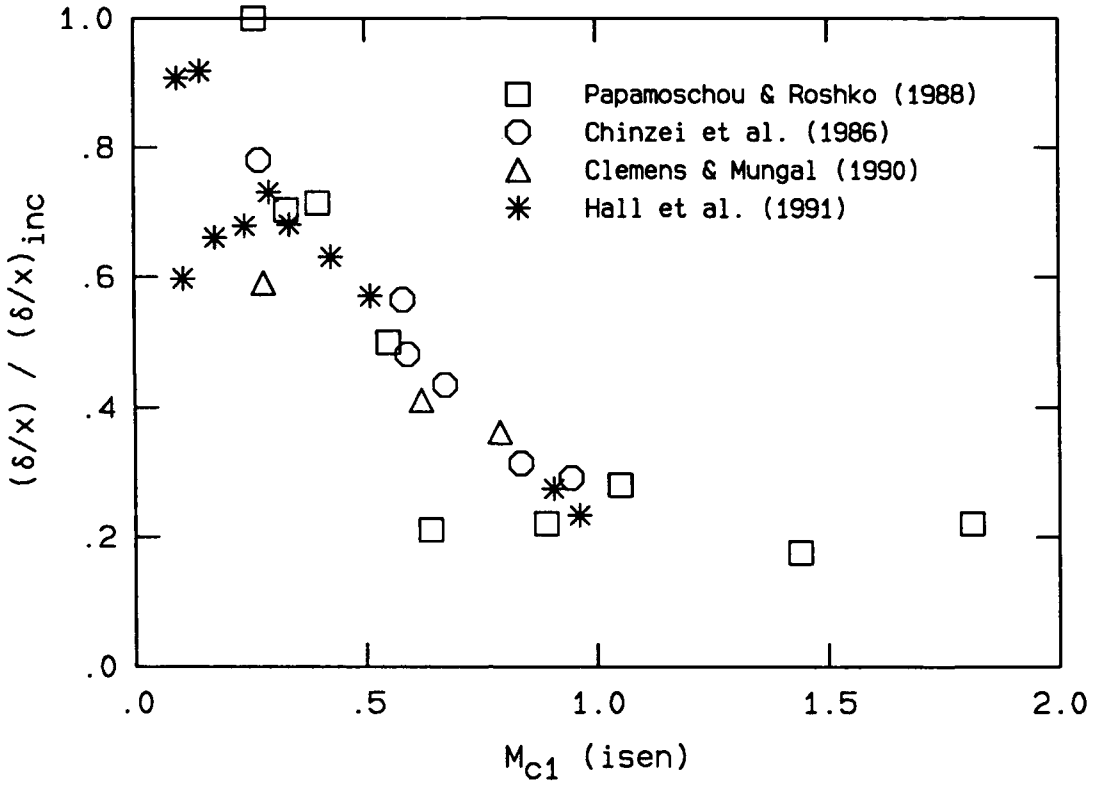

FIG. 2 Normalized growth rate data accumulated by various researchers.

flows, a result that is somewhat at variance with the results of Clemens & Mungal (1990). Also visible in Fig. 1 is a pattern of shock and expansion waves in the low-speed fluid, evidently created by unseen shear layer structures travelling at supersonic velocities with respect to the low-speed stream. The inferred convection velocity of these unseen structures is considerably higher than that predicted from the standard isentropic model, but it is in accord with the convection velocity measurements of Papamoschou (1989) and a new theoretical model by Dimotakis (1991, Appendix C).

Figure 2 is a plot of normalized growth rate data in which the current results are compared to those of previous investigators. The agreement is seen to be quite good except for a few cases at low compressibility. Our results suggest the existence of two branches at $M_{c1}^{(i)} \simeq 0.1$, depending on whether the high-speed freestream is supersonic or subsonic. The reasons for this difference are not understood at the present time, but they do suggest that the convective Mach number parameter $M_{c1}^{(i)}$ does not scale all of the compressibility effects in the planar shear layer.

2.2 Chemically reacting shear layers

These flows were based on $H_2/F_2/NO$ chemistry, patterned after the incompressible experiments of Mungal & Dimotakis (1984) and Hermanson & Dimotakis (1989). The experiments were designed to make direct measurements of the molecular mixing rate in supersonic shear layers. A first publication of this work was presented at the *AIAA* 22nd *Fluid Dynamics, Plasma Dynamics & Lasers Conference* (Honolulu, Hawaii), 24–26 June 1991 (Hall *et al.* 1991b, Appendix D).

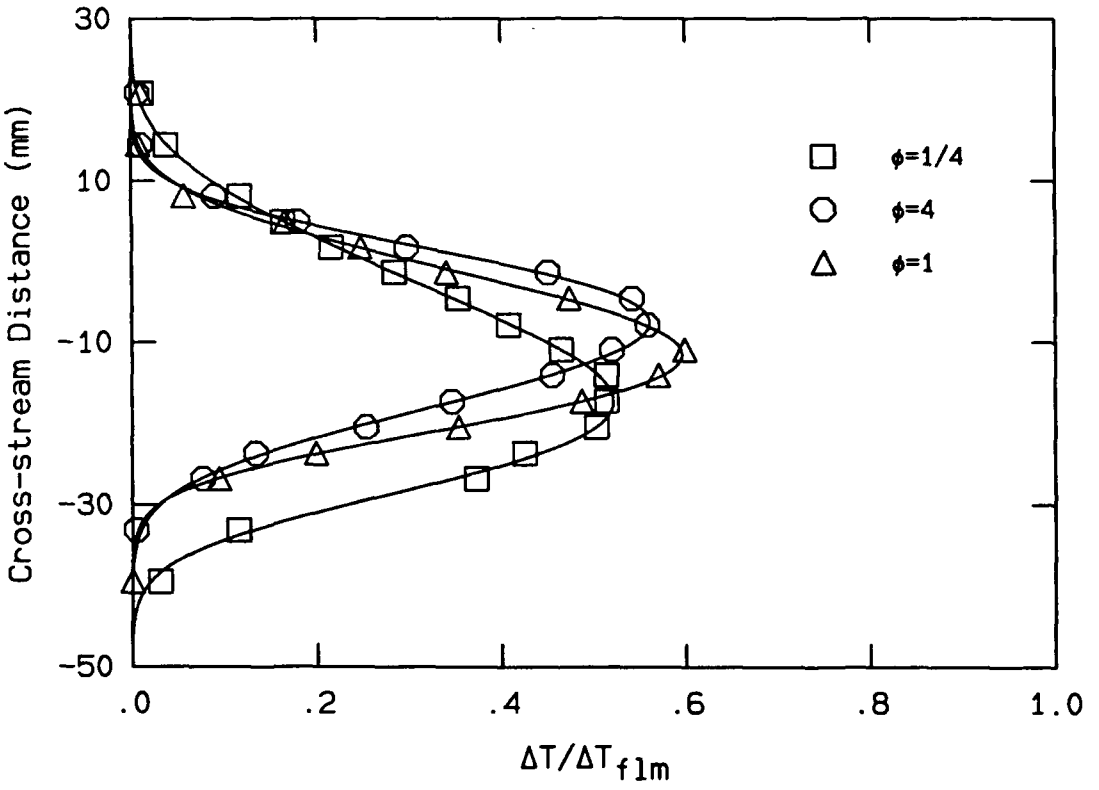

FIG. 3 Normalized temperature profiles for the Case 3 flip experiment.

In the reacting flow experiments, fast kinetics was achieved even in the highest compressibility flow ($M_{c1}^{(i)} = 0.96$) through the use of moderate concentrations (4%) of H_2 and F_2. The attainment of the fast chemistry regime enabled us to conduct 'flip' experiments (*cf.* Mungal & Dimotakis 1984, Koochesfahani & Dimotakis 1986) which yielded estimates for the amount of molecular mixing in the shear layer. Figure 3 shows a temperature profiles across the shear layer for the $M_{c1}^{(i)} = 0.51$ flip experiment. It can be seen that the profile shifts toward the lean reactant in a manner similar to the incompressible experiments performed by Mungal & Dimotakis (1984) *etc.* Analysis of these data yields the following estimates for δ_m/δ, the mole fraction of molecularly mixed fluid inside the shear layer:

$$\frac{\delta_m}{\delta} \simeq 0.40 \qquad \text{at} \quad M_{c1}^{(i)} = 0.51 \tag{1a}$$

and

$$\frac{\delta_m}{\delta} \simeq 0.31 \qquad \text{at} \qquad M_{c1}^{(i)} = 0.96\,. \tag{1b}$$

These can be compared with the estimate of $\delta_m/\delta \simeq 0.49$ for incompressible shear layers (Dimotakis 1989). While part of this difference may be attributable to the higher Reynolds numbers in these experiments, the inference to be drawn here is that compressibility *decreases* the molecular mixing in the shear layer.

2.3 Rayleigh-scattering data

Laser Rayleigh-scattering imaging experiments were performed at three convective Mach numbers, namely $M_{c1}^{(i)} = 0.16$, 0.51 and 0.92. They were designed to overcome the limitation of spanwise integration of the Schlieren imaging system which was used in the first two phases of the program to determine if the lack of obvious large scale flow structures in the schlieren data were the result of spanwise averaging.

The laser light-sheet was set up vertically, midspan in the streamwise direction using a Continuum YAG laser with a 7 ns pulse width and 300 mJ energy per pulse. The pictures were taken using a Photometrics camera system with a cryogenically cooled camera head containing a 1024 × 1024 pixel CCD focal plane array.

The usual problem of diffuse scattering from optical windows, which, being at the same wavelength, can often dwarf the low level, gas phase Rayleigh-scattering signal was circumvented using aerodynamic windows (slits in black-anodized aluminum) in the upper and lower flow guidewalls to pass the laser light sheet. In particular, since we were interested in imaging a free shear layer, which in this case is located away from walls, the narrow, high aspect-ratio slits that were used for this purpose did not result in any discernible disturbance to the flow region of interest. The signal-to-noise ratio was further improved through the of ethylene (C_2H_4) as the low-speed freestream gas, yielding a signal higher by a factor of six compared to nitrogen.

Image processing was performed on all of the raw data in order to make background corrections and to normalize the unavoidable light-sheet intensity nonuniformities. Sample images appear in Figs. 4, 5, and 6. Even though we feel that these do not represent the best that can be done with this technique, they nevertheless represent the highest signal-to-noise ratio images of supersonic flow to date to our knowledge.

Figure 4 shows the low compressibility case with $M_{c1}^{(i)} = 0.16$. Both streams are subsonic. A large vortex is clearly recognizable in the image. Note also that there is a hint of a *streamwise* vortex in the braid region. The vertical streak just upstream of the vortex core is a background feature. It seems likely that the large vortex seen in this Rayleigh-scattering image can be identified with the large-scale vortical structures seen in the many

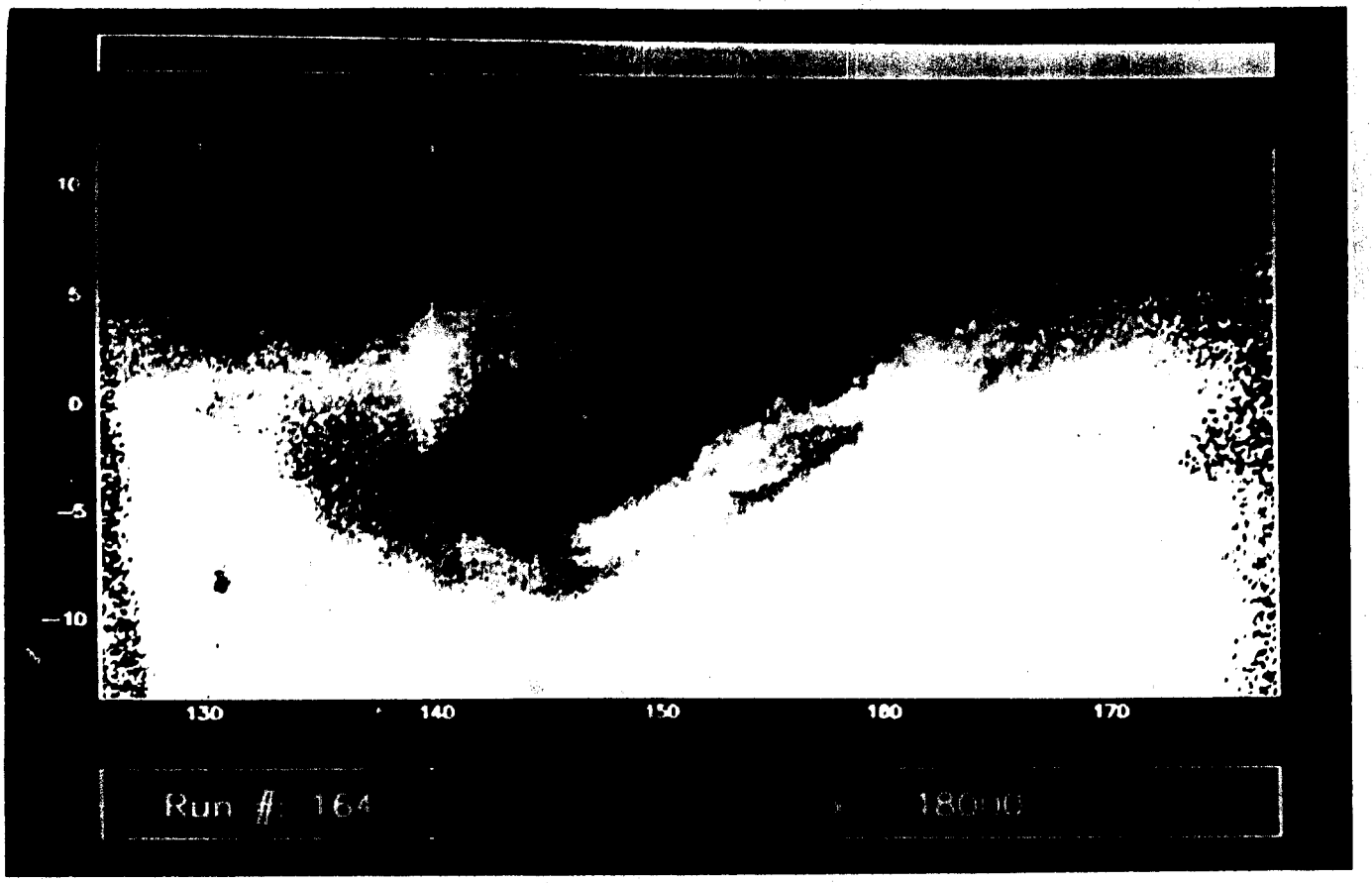

FIG. 4 Rayleigh image from a N_2/C_2H_4, $M_1 = 0.65$, $U_2 = 100\,\mathrm{m/s}$, $M_1^{(c)} = 0.16$ subsonic shear layer.

Schlieren photographs of incompressible turbulent shear layers over the past two decades (*cf.* Brown & Roshko 1974).

Once the high-speed stream becomes supersonic, however, well defined vortices can no longer be found in the Rayleigh-scattering images (Figs. 5 and 6). Note that the convective Mach numbers of these two flows are $M_1^{(c)} = 0.51$ and 0.92, respectively. The large feature in the right third of the picture in Fig. 5, and some smaller features in Fig. 6, might be the remnants of large scale vortices, but the structure of the flow seems to be much less organized. Nevertheless, there is *some* turbulent structure visible in the images, including deep incursions of unmixed fluid into the shear layer.

Recall that in the schlieren pictures for the supersonic flow cases (Hall *et al.* 1991a, Hall 1991) the shear layer appears as a wedge with sharp boundaries, but with no recognizable large scale structure inside. Since both the schlieren and the Rayleigh images are able to freeze the flow in time, the difference in appearance between the two imaging techniques can

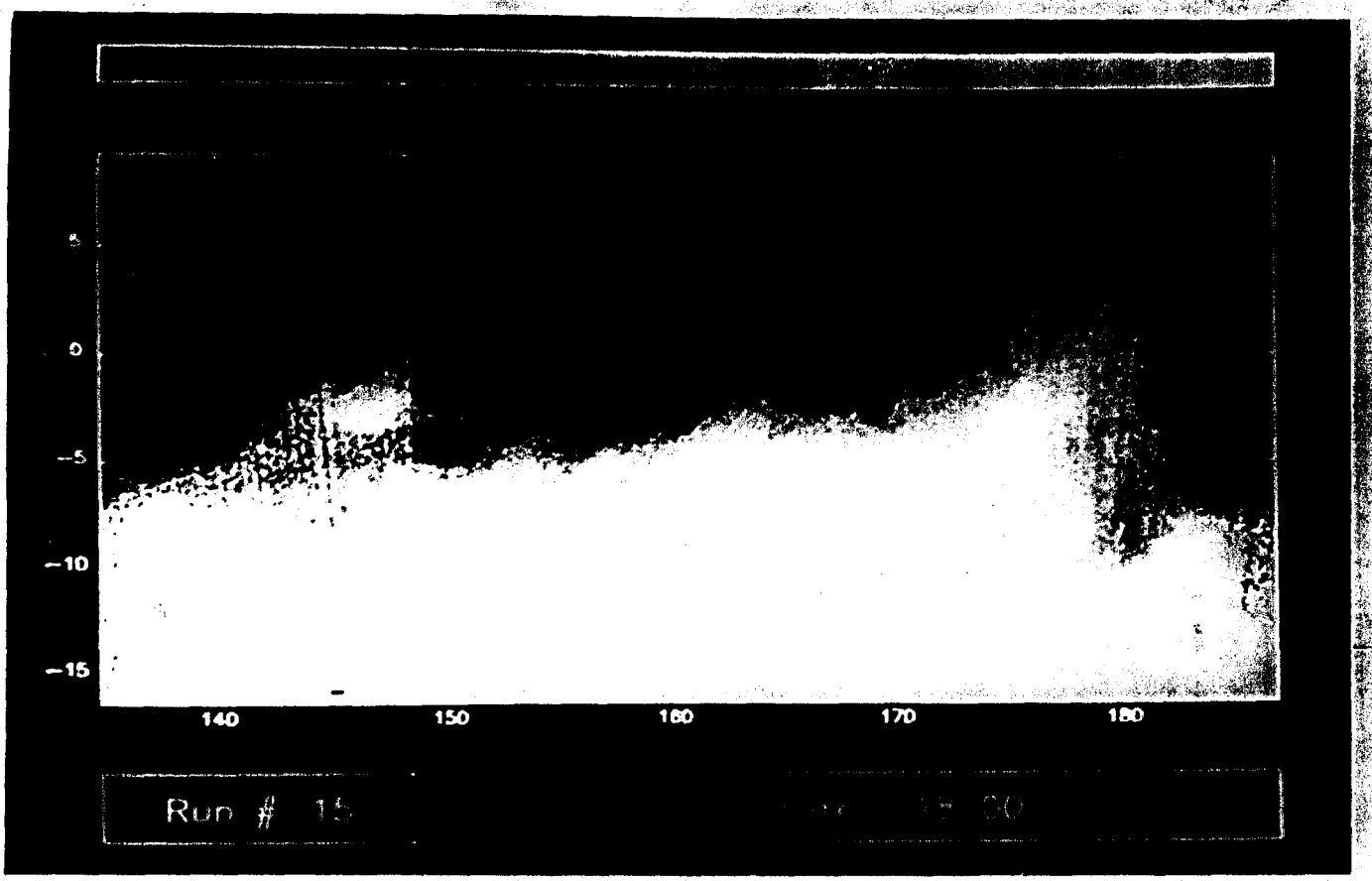

FIG. 5 Rayleigh image from a N_2/C_2H_4, $M_1 = 1.18$, $U_2 = 100\,\mathrm{m/s}$, $M_{c1}^{(i)} = 0.51$ supersonic shear layer.

be ascribed to the spanwise three-dimensionality of the flow. Specifically, schlieren imaging produces a spanwise-integrated view of the flow, one that obscures the underlying structure revealed by the non-integrating laser slice, Rayleigh-scattering image.

Finally, it is interesting to note that the travelling waves seen in the Schlieren photographs of the high compressibility flows of Hall *et al.* (1991) are not visible in Fig. 6. These waves are thought to be weak, however, and it is plausible that, despite the aerodynamic window employed, there is still too much stray light for them to be seen. Conversely, however, the noise should not be sufficient to obscure *strong* shock waves. One is lead to the conclusion that isolated strong shocks are not present in the flow.

The results summarized above have been part of the Ph.D. research of Dr. Jeffery Hall and the postdoctoral research of Dr. Henning Rosemann, in cooperation with Chris Bond, a Graduate Assistant, and Earl Dahl, a member of the GALCIT Technical Staff.

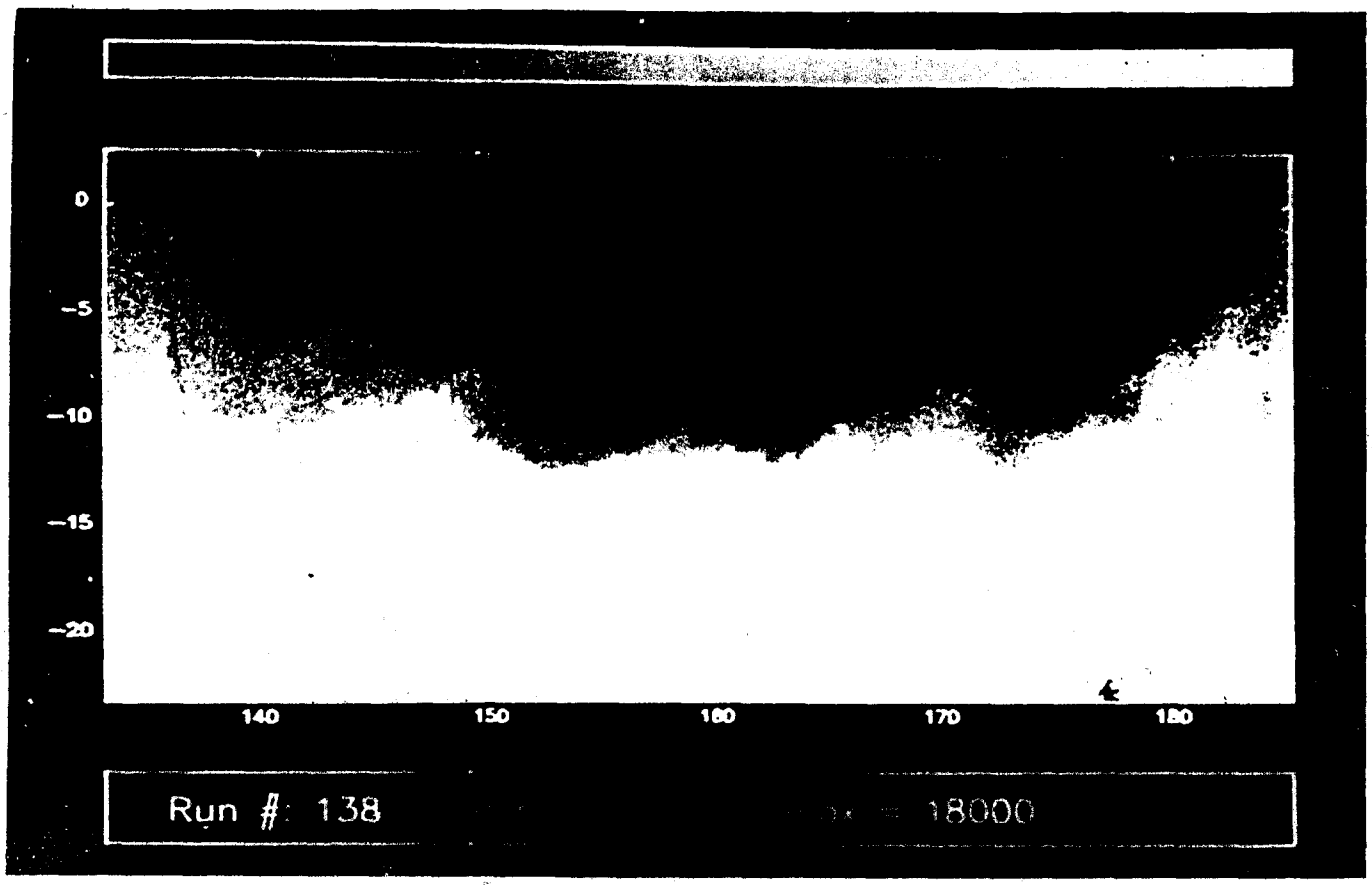

FIG. 6. Rayleigh image from a He/C_2H_4, $M_1 = 1.50$, $U_2 = 100$ m/s, $M_1^{CV} = 0.92$ supersonic shear layer.

3. Mixing and combustion in turbulent jets

The research effort on turbulent jet mixing, involving both the gas-phase, chemically reacting and liquid-phase, non-reacting jet investigations, is cosponsored by the Gas Research Institute, GRI Contract No. 5087–260–1467.

3.1 Gas phase chemically reacting jet investigations

During the current reporting period, the recirculation problem in the High Pressure Reactant Vessel was solved, a series of experiments to determine the dependence of flame length on Reynolds number was begun, and the issue of buoyancy was investigated.

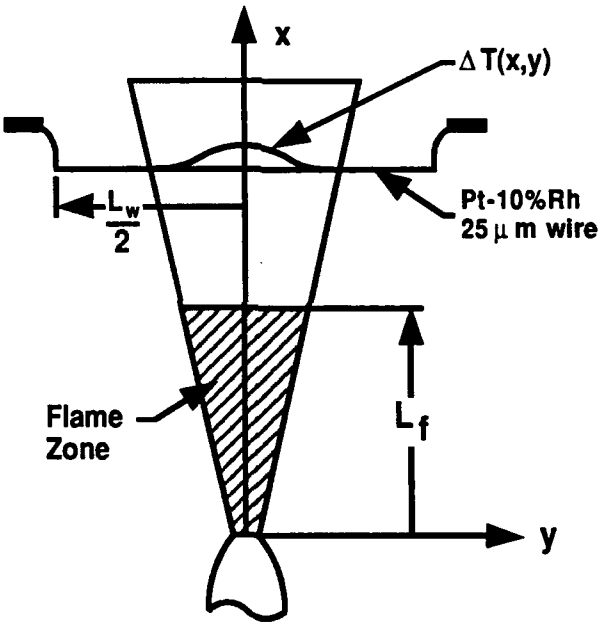

FIG. 7 Schematic of the jet reaction zone.

Once the new 2.5 mm exit diameter nozzle was installed, the recirculation problem that was limiting the uncontaminated run times of the experiments was solved. It was then possible to begin a Reynolds number study spanning a range of $1.0 \times 10^4 \leq Re \leq 1.5 \times 10^5$. The flame length at a given Reynolds number was determined from the time-averaged, line-integrated temperature measurements performed by the cold wires, as documented in our previous annual report (Dimotakis *et al.* 1990). Recall that the resistance of the cold wires, when stretched across the flame, yields an accurate estimate of the line-integrated heat release (temperature rise) resulting from the chemical reaction. Beyond the end of the

reaction zone, shown schematically in Fig. 7, the excess temperature is simply diluted by the subsequently entrained fluid.

The temperature rise ΔT becomes a conserved scalar obeying the similarity law

$$\frac{\Delta T(x,y)}{\Delta T_f} = \kappa \frac{d^*}{x - x_0} g(\eta) , \tag{2a}$$

where $\Delta T(x,y)$ is the temperature rise at (x,y), x is the streamwise (jet axis) coordinate, y is normal to it, ΔT_f is the adiabatic flame temperature, κ is an empirical constant (determined by experiment), d^* is the momentum diameter of the jet, g is the similarity mean profile function (determined by experiment), and

$$\eta \equiv \frac{y}{x - x_0} \tag{2b}$$

is the similarity variable with x_0 the virtual origin. The temperature measurement performed by each wire is the line integral at constant x given by

$$\langle \Delta T \rangle \equiv \frac{1}{L_w} \int_{-L_w/2}^{L_w/2} \Delta T(x,y)\, dy \tag{3}$$

where L_w is the length of the wire. This measurement is the same as the product thickness δ_P used for the shear layer by Dimotakis (1989). The product thickness (δ_P), normalized by L_w will be defined as

$$\frac{\delta_P}{L_w} \equiv \frac{1}{L_w} \int_{\infty}^{\infty} \frac{\Delta T(x,y)}{\Delta T_f} dy = \frac{\langle \Delta T \rangle}{\Delta T_f} . \tag{4}$$

It can be shown that Eq. 3 should asymptote to a constant value beyond the end of the flame tip at x_f.

The raw temperature data from the 16 cold wires spanning $x/d_0 = 30$ to 240 were averaged to produce Fig. 8 which plots the normalized product thickness δ_P/L_w versus $\log_{10}(x/d^*)$. The expected increase in the integrated temperature rise can be seen, as well as the asymptotic value at the end of the flame tip.

The semilogarithmic straight line region in the heat-release zone should be noted. It had been anticipated and was the reason for the logarithmic spacing of the wires in the experiment. Its confirmation represents a new and important result in turbulent jet mixing.

Also noteworthy is the high signal-to-noise ratio of these measurements. Considering the data in Fig. 8, recorded with an adiabatic flame temperature rise $\Delta T_f = 12.7$ K, as an example, the points at low x/d correspond to a time-averaged, line-integrated temperature rise of (*cf.* Eqs. 3 and 4)

$$\langle \Delta T \rangle = \frac{\delta_P}{L_w} \Delta T_f \approx 0.07 \times 12.7 \approx 0.89\,\mathrm{K} .$$

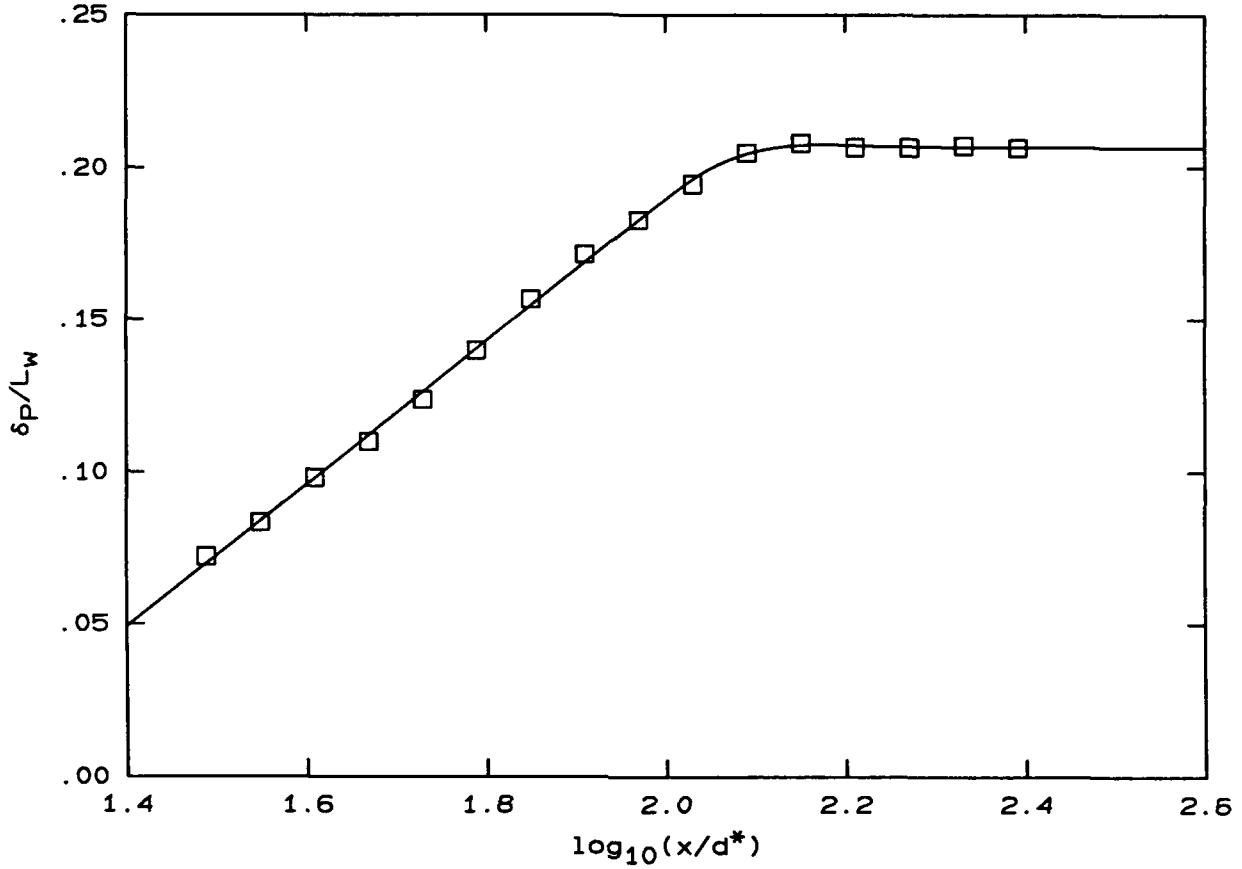

FIG. 8 Sample plot of normalized product thickness versus $\log_{10}(x/d^*)$, $Re = 1.0 \times 10^4$, $\phi_m = 18$, $\Delta T_f = 12.7\,\mathrm{K}$.

We estimate that, in these measurements, we could detect something like 30 mK with a signal-to-noise ratio of unity.

At each Reynolds number, runs at several mass equivalence ratios ϕ_m were performed to identify any Reynolds number effects on flame length. Figure 9 shows a sample plot of flame length L_f versus ϕ for $Re = 1.0 \times 10^4$. Experiments such as these, covering the above mentioned Reynolds range, have been completed. The results will be reported in the near future.

Buoyancy is an important issue that had to be addressed in these experiments. In particular, the similarity law of Eq. 2a is valid only for the momentum-dominated region of the jet. The temperature of a buoyant jet decays at a faster rate with increasing x/d than that of a momentum-dominated jet. Therefore, the line-integrated temperature will decay beyond the flame tip at some point when buoyancy forces become comparable to the jet source momentum flux. Becker and Yamazaki (1978) attempted to identify when the

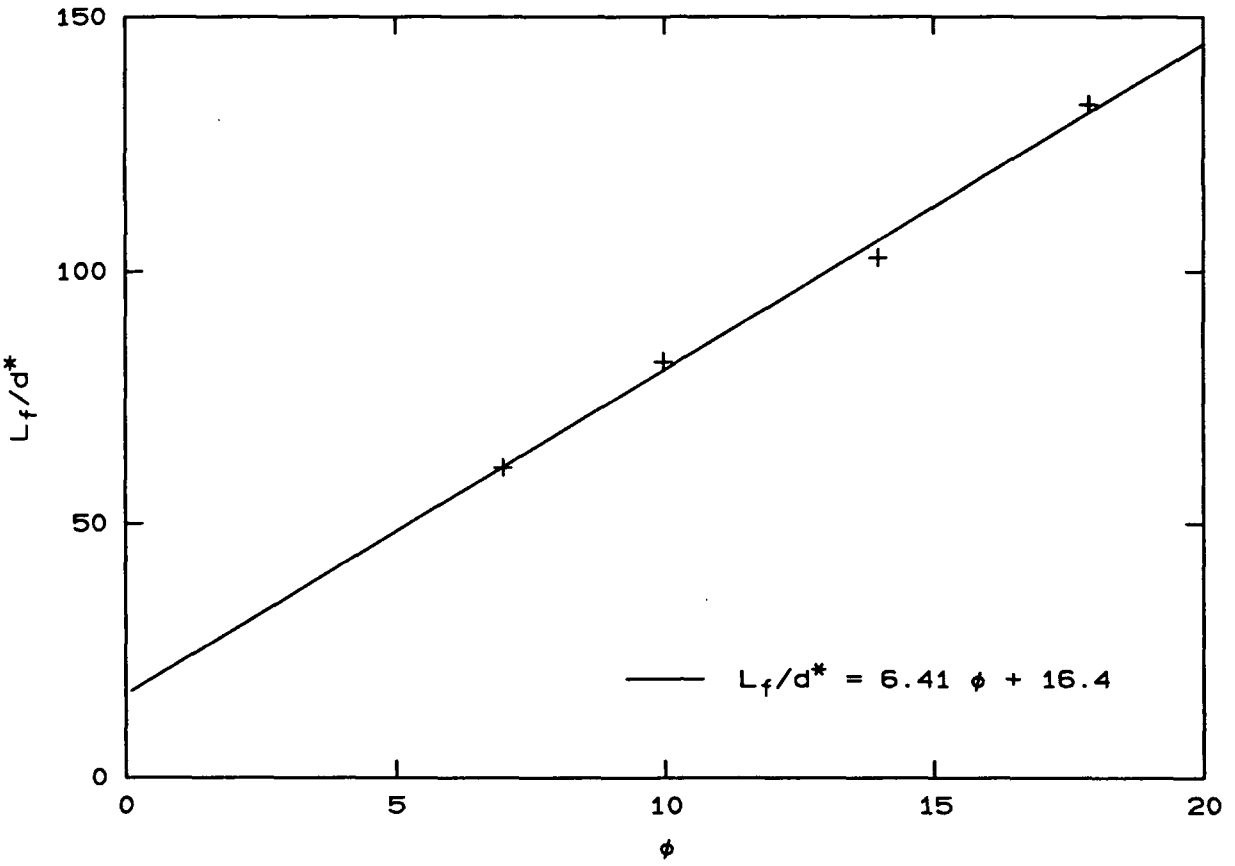

FIG. 9 Sample plot of flame length L_f versus ϕ for $Re = 1.0\times^4$, $\Delta T_f = 12.7\,\mathrm{K}$.

jet is momentum-dominated and where the transition to buoyancy occurs. They defined a non-dimensional downstream coordinate, ξ, as

$$\xi \equiv \left[\frac{\pi g \rho_\infty}{4 J_0}\right]^{1/3} x \tag{5}$$

where J_0 is the source impulse which, for a top-hat exit velocity profile, is given by

$$J_0 = \rho_0 U_0^2 \frac{\pi d_0^2}{4} .$$

Equation 5 assumes that $\rho_\infty - \overline{\rho} \approx \rho_\infty$, *i.e.*, that the average flame density, $\overline{\rho}$, is small compared to the ambient density, ρ_∞. For our experiments, $\rho_\infty - \overline{\rho} \ll \rho_\infty$ so $\overline{\rho}$ was used in the expression for ξ. Becker and Yamazaki claim that the jet is momentum-dominated for $\xi < 1$ and buoyancy-dominated for $\xi > 2.5$, based on their entrainment measurements. Fortunately, the far field similarity law provides an excellent means of estimating the transition point in the present experiments. Figure 8 demonstrates that the asymptotic level remains constant all the way to the last measuring station at $x/d_0 = 240$ and is therefore momentum-dominated up to that point.

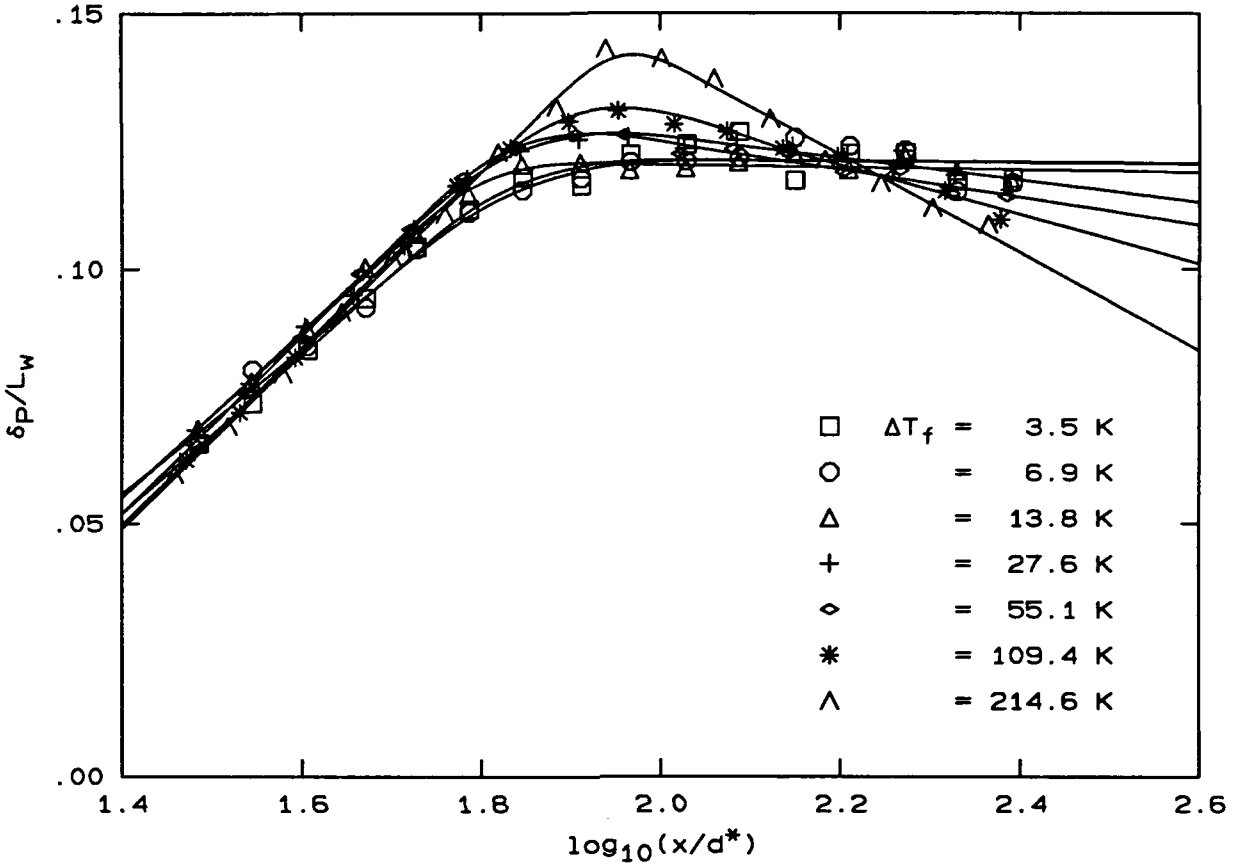

FIG. 10 Normalized product thickness versus $\log_{10}(x/d^*)$ for several adiabatic flame temperatures, $Re = 4.0 \times 10^4$, $\phi = 10$.

Knowing when buoyancy begins to affect the flow is important not only in these experiments but also in the joint modeling efforts underway with the Sandia National Laboratories, as will be discussed below. Experiments to test the buoyancy dependence on such parameters as exit velocity and flame temperature are in progress in an effort to better understand and predict when buoyancy effects begin influence the flow. Figure 10 shows a set of experiments spanning adiabatic flame temperatures ΔT_f from 3.5 K to 215 K. Note how the asymptotic level breaks down when the jet begins to feel the effects of buoyancy. All of these results will be soon be documented in the form of a thesis (Gilbrech 1991).

This work was co-sponsored by the Gas Research Institute, Contract No. 5087–260–1467, and is part of the Ph.D. research of Dr. Richard Gilbrech. A first publication of parts of this work has been accepted for the upcoming *AIAA Aerospace Sciences Meeting* (1992).

3.2 Liquid phase turbulent jet mixing

We are continuing our investigations of the fine scale turbulent structure in a high Schmidt number (liquid phase) axisymmetric jet. They have continued to produce a host of interesting and, at times, unexpected results. Some of these include details of the scalar interface geometry, Schmidt number, and Reynolds number effects on the structure of the jet and its mixing behavior, indications of Taylor-scale features, and the scalar power spectra at these high Schmidt numbers. In addition, the ideas concerning scalar boundedness and the implications for the Batchelor spectrum, described elsewhere in this report, where largely born out of reflections upon these data.

As mentioned in previous reports, we have direct experimental evidence that the geometry of scalar interfaces in the turbulent jet *is not* characterized by a constant fractal dimension. In addition, we now note that there are strong theoretical arguments against a constant fractal dimension occurring in the turbulent jet. A paper documenting these results has appeared recently in the literature (Miller & Dimotakis 1991a). A copy is included as Appendix E in this report.

We are examining the Reynolds number dependence of the behavior of scalar fluctuations and, by comparison with recently completed work in non-reacting, gas phase turbulent jet mixing (Dowling 1988, Dowling & Dimotakis 1990**), also Schmidt number effects. Again, in the context of the Air Force interests, the emphasis here is not so much on liquid phase mixing as on the behavior of the strain rate field at small scales. A first presentation of this work was made at a recent *IUTAM Symposium* and will appear in *Phys. Fluids A* in a special supplement to the May 1991 issue (Miller & Dimotakis 1991b).

In November, we presented a talk at the annual meeting of the Fluid Dynamics Division of the American Physical Society (Ithaca, NY). We described findings from our fractal investigations that suggest the presence of characteristic scales in the jet which are consistent with Taylor scaling. It appears that this is *direct* evidence of such scales in a turbulent flow. We believe this represents a useful application of fractal-type analysis. This work has not yet been submitted for publication.

In the course of these experiments in high Schmidt number jets, we reaffirmed that scalar fluctuation spectra on the centerline of turbulent jets do not exhibit the k^{-1} regime that had been predicted by Batchelor (1959) at high wavenumbers, *i.e.*, at small spatial scales. In addition to the experimental lack of support for this behavior of the spectral fluctuations, we also found theoretical reasons why the original Batchelor proposals may not be correct. In particular, we argued that such a spectrum power-law regime does not possess the correct asymptotic behavior in the limit of high Schmidt numbers (Dimotakis & Miller 1990, Appendix G). These experimental and theoretical findings have important

** Included in this report as Appendix F.

consequences in the context of turbulent mixing and combustion. They suggest that the classical models for the strain rate field, at high Reynolds numbers, at the smallest scales, where non-premixed combustion at fast kinetics is taking place, need to be reexamined. The strain rate field, in turn, is responsible for such behavior as local extinction phenomena and finite kinetic rate effects in general. It has to be mastered to the point where it can be correctly described if reliable models of mixing and combustion are to be formulated.

At this writing, a new phase of data acquisition is nearly completed, in which higher Reynolds numbers and a range of downstream locations in the jet are being investigated. It is clear that the high Schmidt number makes these jets different in important respects from their gas-phase counterparts. A thesis in preparation (Miller 1991) will discuss additional findings from these experiments.

This work was co-sponsored by the Gas Research Institute, Contract No. 5087–260–1467 and was part of the Ph.D. research of Dr. Paul Miller.

3.3 Joint Caltech–Sandia National Laboratories Modeling Effort

Significant progress has been made during the past year on further implementation of the Two-Scale Lagrangian model. Earlier applications of the model (Broadwell & Mungal 1991), with simplified chemistry, allowed an analytic treatment of the hydrogen-fluorene chemical reaction in a turbulent shear layer, with results that are in good agreement with experiment. In particular, the dependence of the amount of product on the Reynolds, Schmidt, and Damhkoler numbers was correctly predicted. A summary of these comparisons together with a description of the model is given in Appendix H of this report. In the current work, the objectives are to treat the full chemical reaction system for hydrocarbon fuels (two hundred or so reactions) and to replace the simplified treatment of the diffusion, or Taylor layer, element of the model with a detailed solution of the strained laminar layer. The first objective has been achieved for the simplified form of the model, as discussed below, and near the end of this reporting period, a scheme for the inclusion of the strained diffusion layer has been devised.

The model is applicable to both shear layers and jets and the work of the past year has focused on the latter. With joint support from the Gas Research Institute, and in collaboration with A. E. Lutz and R. J. Kee of the Sandia National Laboratory, and R. W. Dibble of the University of California, a study is being made of the nitric oxide generated in hydrogen and hydrocarbon fuel jets. While combustion generated pollution may not presently be of primary interest to the Air Force, the production and destruction of nitric oxide in the jet is so sensitive to the local composition and temperature that it serves as a rigorous test and diagnostic tool in the development of the model. Because atmospheric ozone is destroyed by nitric oxide, the results of the current study may also be of direct

interest.

In the model, mixing is taken to occur in two sequential steps:

1. as air enters the jet, diffusion layers form between the newly entrained air and the previously mixed nozzle fluid,

and

2. after the layers are stretched and lengthened by the large-scale motions, they merge to form a molecularly mixed blob.

Idealizations used include the assumptions that the strain causing the lengthening is proportional to the local mean velocity divided by the local diameter, and that when the layers begin to merge, they mix instantaneously to form a blob of uniform composition. In the model, this latter process and the subsequent reactions are described by a constant pressure, perfectly stirred reactor. The merging rate fixes the flow into the reactor and the rate of formation of the diffusion layers fixes the flow out. In previous studies of the model, and in the work up to the present, the reactions in the diffusion layers have also been treated as if they were taking place in a stirred reactor. In that form, therefore, the model consists of two coupled reactors as shown in Fig. 11 — the configuration which has been used so far to study the generation of nitric oxide in fuel jets.

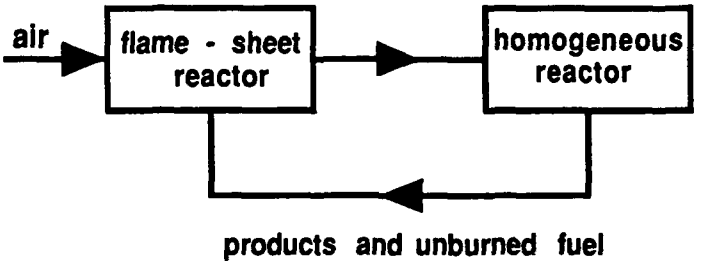

FIG. 11 Two-reactor model schematic.

The air addition rate to the diffusion reactor is an input in the model, and can, therefore, be that for a momentum driven jet or for one in which buoyancy is important. These

rates are taken from experiment and dimensional analysis. In this form, the model is computationally very efficient; a hydrogen-air jet runs in three minutes on a Vax and methane-air in twenty minutes. It is expected that this form of the model can be run on a personal computer.

Results for hydrogen and propane jets and comparisons with experiment are shown in Appendix I of this report. There the effects of residence time, buoyancy, and radiation on nitric oxide generation are shown for hydrogen and propane. The predicted trends are seen to be in general agreement with the experimental results. The absolute values, however, are approximately a factor of three too high. Continuing exercise of the model has shown the nitric level to be sensitive to the air entrainment rate, a parameter that is determined by the flame length. In the work just discussed, the rate was set to yield the *maximum* observed length; when the rate is more sensibly set to yield the *average* length, the nitric oxide concentration fails to become closer to the experimental value, at least in the momentum driven case. In the buoyancy regime, the behavior is more complex and requires further examination. Such study of the model is continuing.

As was noted above, the flow into the reactors is an input. Therefore, the model will be especially useful in complex practical configurations for which this quantity must be estimated from experiments or simply guessed at. With regard to supersonic shear layers, in those circumstances in which the relative Mach number is subsonic, the model is useful as it stands. In the more general case, again if the entrainment and molecular mixing rates are known, the model can be used.

It may be useful to discuss briefly the relationship between the Two-Stage Lagrangian model and conventional flamelet models. The first difference, and of lesser importance, arises from the necessity to distinguish between flame sheets and diffusion layers. When chemical reactions are fast, they take place in regions that are thin relative to those in which there are significant concentration gradients in the fuel and oxidizer. These thin regions are properly called flame sheets, but often the entire diffusion layer is approximated by a stirred reactor, it is important to recognize the distinction because only the flame sheet fraction of the layer is at stoichiometric conditions and hence at high temperature. Miller, *et al.*(1989) note this fact and modify the Lagrangian model accordingly for use in their study of reactions in a supersonic shear layer. When a solution to the diffusion layer is incorporated into the model, the matter is automatically dealt with. It may turn out that results from the full model will show how to choose this arbitrary parameter in the two stirred reactor version and thus allow the use of this more computationally efficient form.

The more significant difference between the Two-Stage Lagrangian model and earlier flamelet approaches is the homogeneous reactor. The fact that diffusion layers and flame sheets *must* merge was recognized, in Broadwell (1982), to be implicit in the dependence of jet flame lengths on their stoichiometric ration. The reasoning is outlined in Appendix I.

The theoretical arguments advanced in Broadwell (1982) apply to both shear layers and jets and hence, as stated, the model is applicable to both flows.

The next step in the implementation of the complete model is the incorporation of a numerical solution for the strained layer. In the jet, as opposed to the shear layer, one side of the layer, the nozzle fluid side, changes composition as the fluid moves down the jet axis. It is this complication that has made this step difficult to take. The experiments of Dahm & Dimotakis (1987), on the reactions in a turbulent water jet, provide information that has allowed the formulation of a straightforward procedure. These experiments show that the reaction takes place in steps of a size that scales with the local jet diameter. This result suggests that the atomic species on the nozzle fluid side of the layer be held constant in each of these steps. The molecular composition changes, of course, as further reactions take place. Thus our plan is to use the two reactor model to find the composition for, say, ten diameters, and then to proceed stepwise down the axis using the output of the homogeneous reactor to fix the composition at the beginning of each step. The numerical implementation of this idea is presently being formulated in the Sandia group.

4. Analytical and computational effort

4.1 Instability of compressible shear-layers

Near the beginning of the reporting period, a thesis entitled *An Investigation of the Inviscid Spatial Instability of Compressible Mixing Layers* (Zhuang 1990) was completed. A publication discussing some of this work (Zhuang *et al.*, 1990) is included as Appendix A in this report.

This effort was part of the Ph.D. research of Dr. Mei Zhuang.

4.2 Interactions of sharp fronts in compressible flows

The computational effort in compressible flows is currently focused on developing reliable methods for computing interactions of shock waves and other discontinuous waves that may arise in such flows. For the case of one-dimensional flows this is accomplished with the use of an adaptive Lagrangian grid, and was presented at the *AIAA Aerospace Sciences Meeting* (Lappas *et al.* 1991, included here as Appendix J). Work is under way to extend these ideas to multi-dimensional flows.

As a first step, a numerical scheme for computing two-dimensional gas flows with strong fronts is being developed. Most conservative shock-capturing schemes that have been successful in computing such flows tend to smear discontinuous waves over a finite number of grid cells. In some cases this loss of accuracy is not acceptable. The objective of this work is to develop a scheme with front-tracking capability, but which retains all the advantages of high-resolution conservative shock-capturing schemes. In many flows it is simply impossible to have the resolution required to resolve very steep fronts or in the case of inviscid gas flows, the discontinuous fronts that are present. There is a need for some degree of front-tracking in all such flows.

Most conventional front-tracking schemes use a fixed grid and additional computational elements to represent the fronts. The resolution of the fronts is usually time-dependent, since these computational elements deform with the fronts. Moreover, such schemes are usually nonconservative and the explicit calculation of the interaction of all fronts is required in order to obtain a solution. Because of this, they are not as robust as their conservative shock-capturing counterparts.

A new conservative front-tracking method is being developed, which allows fronts to be tracked with the resolution of the underlying grid. An important feature of the scheme

is that its conservative shock-capturing character is not diminished by the added front-tracking capability. The intersection points of a front with the fixed grid are used as the computational points carrying all the information about the front. By using these intersection points as the computational points for the front, all the cells of the grid are divided into a number of subcells by the fronts in a very natural way. This allows a straightforward implementation of a conservative shock-capturing algorithm to all cells and subcells. This scheme is currently being used to compute a number of simple test cases.

This effort is part of the Ph.D. research of Mr. Tasso Lappas.

5. Diagnostics, Instrumentation & Experimental Technology

Considerable development has taken place in this part of the effort, with several projects in progress. Some of these will be outlined below.

As described in Sec. 2.3, p. 7, an important first step was taken in developing high signal-to-noise, gas-phase, laser Rayleigh scattering images. This effort was begun as part of the post-doctoral research effort of Dr. Henning Rosemann, who has since returned to the DLR in Göttingen, is now continuing as part of the effort of Dr. Dominique Fourguette, who has recently joined us as a Post-doctoral Research Fellow in Aeronautics.

The design and fabrication of a new generation of computer-controlled data acquisition systems is underway. The first nodes of this potentially massively parallel data acquisition system should be operational this fall. It relies on networked, high-speed, high memory data acquisition channels,† any number of which can be hosted on a single 32-bit computer. This system will allow for a sufficiently significant extension of the resolution/bandwidth capabilities to permit a host of experiments to be performed that were previously out of reach. A first application, two such channels, is to digitize two of the three colors of a high spatial (700×800 pixel) and depth (~ 65 dB) resolution, color digital camera at video rates, for several seconds. Much higher bandwidth and/or bit resolution applications will be tackled with the completion of additional channels in the future. This work is part of the effort of Dr. Dan Lang, in collaboration with Paul Dimotakis.

A multiple-image CCD camera development, in collaboration with Prof. Mory Gharib, at UCSD, and the Imaging Systems Division of the Jet Propulsion Laboratory is also in progress.‡ In its first implementation, this device should allow two digital images to be recorded in quick succession (as closely as a few tens of microseconds apart). This capability should extend digital image correlation velocimetry from flow speeds of a few centimeters per second, as encountered in water tunnel applications, to supersonic, gas-phase flow applications. More details will be provided in next year's report.‼ This work is part of the effort of Dr. Phil Tokumaru, in collaboration with Paul Dimotakis, at Caltech, Prof. Mory Gharib at UCSD, and Jim Janesick and his co-workers at the Jet Propulsion Laboratory.

---

† For example, 12-bit A/D converter, feeding a 32-MegaByte buffer at 20 MegaSamples/sec (such data rates arise in digital image acquisition applications).

‡ Please note that as of 1 October 1991, we are expecting some supplementary support from DARPA for this project, with Caltech as a sub-contractor to UCSD.

‼ A patent has just been filed (P. Dimotakis), as of this writing, documenting and protecting this idea.

6. Personnel

In addition to the Principal Investigators:

P. E. Dimotakis: Professor, Aeronautics & Applied Physics;

J. E. Broadwell: Senior Scientist, Aeronautics;

A. Leonard: Professor, Aeronautics;

Other personnel who have participated directly in the effort during the current reporting period are listed below:

C. L. Bond: Graduate Research Assistant, Aeronautics;

E. Dahl: Member of the Technical Staff, Aeronautics;

R. J. Gilbrech: Graduate Research Assistant, Aeronautics; *;

J. L. Hall: Graduate Research Assistant, Aeronautics; **;

D. B. Lang: Staff Engineer, Aeronautics;

T. Lappas: Graduate Research Assistant, Aeronautics;

T. Kubota: Professor, Aeronautics;

P. L. Miller: Graduate Research Assistant, Applied Physics; †;

H. Rosemann: Post-doctoral Research Fellow, Aeronautics; ‡;

M. Zhuang: Graduate Research Assistant, Aeronautics; ‖.

---

* Ph.D., June 1991; presently working for NASA's Stennis Space Center, Mississippi

** Ph.D., June 1991; presently working for STD, Pasadena

† Ph.D., June 1991; presently Post-Doctoral Research Fellow at Caltech

‡ Appointment ended, June 1991; presently working for the DLR, Göttingen, Germany.

‖ Ph.D., June 1990; presently Post-Doctoral Research Fellow at the U. of Michigan.

7. References

Bibligraphical references denoted by a bullet (•) in this list below represent publications of work under the sponsorship of this Grant that have appeared during the present reporting period.

BATCHELOR, G. K. [1959] "Small-scale variation of convected quantities like temperature in turbulent fluid. Part 1. General discussion and the case of small conductivity," *J. Fluid Mech.* **5**, 113–133.

BECKER, H. A. AND YAMAZAKI, S. [1978] "Entrainment, Momentum and Temperature in Vertical Free Turbulent Difusion Flames," *Comb. and Flame* **33**, 123–149.

BROADWELL, J. E. [1982] "A Model of Turbulent Diffusion Flames and Nitric Oxide Generation. Part I," TRW Document No. 38515-6001-UT-00, EERC Final Report, PO No. 18889.

• BROADWELL, J. E. AND MUNGAL, M. G. [1991] "Large-scale structures and molecular mixing," *Phys. Fluids* A **3**(5), Pt. 2, 1193–1206 (Appendix H, this report).

BROWN, G. L. AND ROSHKO, A. [1974] "On Density Effects and Large Structure in Turbulent Mixing Layers," *J. Fluid Mech.* **64**(4), 775–816.

CHINZEI, N., MASUA, G., KOMURO, T. MURAKAMI, A. AND KUDOU, K. [1986] "Spreading of two-stream supersonic turbulent mixing layers," *Phys. Fluids* **29**(5), 1345-1347.

CLEMENS, N. T. AND MUNGAL, M. G. [1990] "Two- and Three-Dimensional Effects in the Supersonic Mixing Layer," Paper 90–1978.

DAHM, W. J. A. AND DIMOTAKIS, P. E. [1987] "Measurements of Entrainment and Mixing in Turbulent Jets," *AIAA J.* **25**(9), 1216–1223.

• DAHM, W. J. A. AND DIMOTAKIS, P. E. [1990] "Large Schmidt number mixing of a conserved scalar in the self-similar far field of turbulent jets," *J. Fluid Mech.* **217**, 299–330.

DIMOTAKIS, P. E. [1989] "Turbulent Free Shear Layer Mixing and Combustion," Proceedings, 9th *ISABE* (Athens, Greece), 3–9 September 1989, 58–79.

• DIMOTAKIS, P. E. [1991] "On the convection velocity of turbulent structures in supersonic shear layers," *AIAA* 22nd *Fluid Dynamics, Plasma Dynamics and Lasers Conference*, Paper 91–1724 (Appendix C, this report).

• DIMOTAKIS, P. E., BROADWELL, J. E. AND LEONARD, A. [1990] "Chemical Reactions in Turbulent Mixing Flows," California Institute of Technology, AFOSR–88–0155 Annual

Report for the period ending 15 April 1990, AFOSR-TR-91-0195.

- DIMOTAKIS, P. E. AND MILLER, P. L. [1990] "Some consequences of the boundedness of scalar fluctuations," *Phys. Fluids A* **2**(11), 1919–1920 (Appendix G, this report).

DOWLING, D. R. [1988] *Mixing in Gas Phase Turbulent Jets*, Ph.D. thesis, California Institute of Technology.

- DOWLING, D. R. AND DIMOTAKIS, P. E. [1990] "Similarity of the concentration field of gas-phase turbulent jets," *J. Fluid Mech.* **218**, 109 (Appendix F, this report).

GILBRECH, R. J. [1991] *An Experimental Investigation of Chemically-Reacting, Gas-Phase Turbulent Jets*, Ph.D. thesis, California Institute of Technology.

- HALL, J. L. [1991] *An Experimental Investigation of Structure, Mixing and Combustion in Compressible Turbulent Shear Layers*, Ph.D. thesis, California Institute of Technology.

- HALL, J. L., DIMOTAKIS, P. E. AND ROSEMANN, H. [1991a] "Experiments in non-reacting compressible shear layers," *AIAA* 29th *Aerospace Sciences Meeting*, Paper 91–0629 (Appendix B, this report).

- HALL, J. L., DIMOTAKIS, P. E. AND ROSEMANN, H. [1991b] "Some measurements of molecular mixing in compressible turbulent mixing layers," *AIAA* 22nd *Fluid Dynamics, Plasma Dynamics and Lasers Conference*, Paper 91–1719 (Appendix D, this report).

HERMANSON, J. C. AND DIMOTAKIS, P. E. [1989] "Effects of heat release in a turbulent reacting shear layer," *J. Fluid Mech.* **199**, 333–375.

KOOCHESFAHANI, M. M. AND DIMOTAKIS, P. E. [1986] "Mixing and chemical reactions in a turbulent liquid mixing layer," *J. Fluid Mech.* **170**, 83–112.

- LAPPAS, T., LEONARD, A. AND DIMOTAKIS, P. E. [1991] "An Adaptive Lagrangian Method for Computing 1-D Reacting and Non-Reacting Compressible Flows," *AIAA* 29th *Aerospace Sciences Meeting* (Appendix J, this report).

- LUTZ, A. E., KEE, R. J., DIBBLE, R. W. AND BROADWELL, J. E. [1991] "A Model for Detailed Chemical Kinetics in Turbulent Nonpremixed Jet Flames," *AIAA* 29th *Aerospace Sciences Meeting*, AIAA 91–0478 (Appendix I, this report).

MILLER, P. L. [1991] *Mixing in High Schmidt Number Turbulent Jets*, Ph.D. thesis, California Institute of Technology.

MILLER, M. F., BOWMAN, C. T., MILLER, J. A. AND KEE, R. J. [1989] "A Model for Chemical Reaction in a Compressible Mixing Layer," Paper 89-110, Western States

Section/The Combustion Institute Fall Meeting 1989 (Livermore, CA), 23-24 October.

- MILLER, P. L. AND DIMOTAKIS, P. E. [1991] "Stochastic geometric properties of scalar interfaces in turbulent jets," *Phys. Fluids A* **3**(1), 168–177 (Appendix E, this report).

MILLER, P. L. AND DIMOTAKIS, P. E. [1991] "Reynolds number dependence of scalar fluctuations in a high Schmidt number turbulent jet," *Phys. Fluids A* **3**(5), 1156–1163.

MUNGAL, M. G. AND DIMOTAKIS, P. E. [1984] "Mixing and combustion with low heat release in a turbulent mixing layer," *J. Fluid Mech.* **148**, 349–382.

PAPAMOSCHOU, D. [1989] "Structure of the compressible turbulent shear layer," *AIAA* 27th *Aerospace Sciences Meeting*, *AIAA J.* **29**(5), 680–681 (1991).

PAPAMOSCHOU, D. AND ROSHKO, A. [1988] "The Compressible Turbulent Shear Layer: An Experimental Study," *J. Fluid Mech.* **197**, 453–477.

- ZHUANG, M. [1990] *An Investigation of the Inviscid Spatial Instability of Compressible Mixing Layers*, Ph.D. thesis, California Institute of Technology.

ZHUANG, M., DIMOTAKIS, P. E. AND KUBOTA, T. [1990] "The Effect of Walls on a Spatially Growing Supersonic Shear Layer," *Phys. Fluids* A **2**(4), 599–604.

- ZHUANG, M., KUBOTA, T. AND DIMOTAKIS, P. E. [1990] "Instability of Inviscid, Compressible Free Shear Layers," *AIAA J.* **28**(10), 1728–1733 (Appendix A, this report).

Appendix A

ZHUANG, M., KUBOTA, T. AND DIMOTAKIS, P. E. [1990] "Instability of Inviscid, Compressible Free Shear Layers," *AIAA J.* **28**(10), 1728–1733.

Instability of Inviscid, Compressible Free Shear Layers

M. Zhuang, T. Kubota, P. E. Dimotakis

Reprinted from

AIAA Journal

Volume 28, Number 10, October 1990, Pages 1728-733

AMERICAN INSTITUTE OF AERONAUTICS AND ASTRONAUTICS, INC.
370 L'ENFANT PROMENADE, SW • WASHINGTON, DC 20024

Instability of Inviscid, Compressible Free Shear Layers

Mei Zhuang,* Toshi Kubota,† and Paul E. Dimotakis‡
California Institute of Technology, Pasadena, California 91125

The linear spatial instability of inviscid, compressible laminar mixing of two parallel streams, comprised of the same gas, has been investigated with respect to two-dimensional wave disturbances. The effects of the velocity ratio, temperature ratio, and the temperature profile across the shear layer have been examined. A nearly universal dependence of the normalized maximum amplification rate on the convective Mach number is found, with the normalized maximum amplification rate decreasing significantly with increasing convective Mach number in the subsonic region. These results are in accord with those of recent growth-rate experiments in compressible turbulent free shear layers and other similar recent calculations.

Introduction

THE instability of inviscid, laminar, two-dimensional shear layers in both incompressible and compressible flow has been studied in the past.

For incompressible parallel flow, the linear spatial instability of the hyperbolic tangent and Blasius mixing layers was investigated for different values of the ratio between the difference and sum of the velocities of the two coflowing streams by Monkewitz and Huerre.[1] They found that the maximum growth rate is approximately proportional to the velocity ratio.

For compressible flow, the instability of the free mixing layers with respect to two- and three-dimensional temporally growing disturbances was considered by Lessen et al.[2,3] for both subsonic and supersonic disturbances. Under the assumption that the flow was isoenergetic, they found that the flow is unstable with respect to supersonic disturbances, although the amplification rate is smaller than that for subsonic disturbances and that the increasing of the angle between the disturbance wave number vector and the principle flow direction tends to increase the instability. With spatially growing disturbances, Gropengiesser[4] studied this instability problem using the Crocco-Busemann relation as the mean temperature profile of the flows. He carried out the inviscid instability calculations at various freestream Mach numbers and temperature ratios. In order to simplify the stability problem, which was considered by Lessen et al., Blumen et al.[5] studied this problem by assuming that the thermodynamic state of a compressible inviscid free mixing layer is constant. They showed that there is instability of two-dimensional disturbances at all values of the Mach number and that there exists a second unstable supersonic mode. For compressible flow, however, the effects of shear layer Mach number, temperature ratio, velocity ratio, and temperature profile on the stability characteristics are very complicated. These authors offer no prediction about what the combined influences of these flow parameters will do. Recently, Ragab and Wu[6] studied the influence of the velocity ratio on the stability characteristics of the compressible shear layer, and they also investigated the effect of the convective Mach number, as proposed by Papamoschou and Roshko.[7] Their results indicate the convective Mach number is a parameter which correlates the compressibility effects on the spreading rate of mixing layers.

Papamoschou and Roshko performed experiments on compressible shear layers and suggested the convective Mach number M_c as the appropriate parameter scaling the effects of compressibility. This is defined for each stream as

$$M_{c1} = \frac{U_1 - U_c}{a_1}, \qquad M_{c2} = \frac{U_c - U_2}{a_2} \tag{1}$$

where U_1, U_2, and a_1, a_2 are the freestream velocities and speeds of sound, respectively. The quantity U_c is the convective velocity of the large scale structures and was estimated as $\tilde{U}_c$ by Papamoschou and Roshko assuming that the dynamic pressure match at stagnation points in the flow.[8,9] For compressible isentropic flow,[7] i.e.,

$$\left(1 + \frac{\gamma_1 - 1}{2}\tilde{M}_{c1}^2\right)^{\gamma_1/(\gamma_1 - 1)} = \left(1 + \frac{\gamma_2 - 1}{2}\tilde{M}_{c2}^2\right)^{\gamma_2/(\gamma_2 - 1)} \tag{2}$$

where γ_1, γ_2 are the ratios of the specific heats of the two streams, and

$$\tilde{M}_{c1} = \frac{U_1 - \tilde{U}_c}{a_1}, \qquad \tilde{M}_{c2} = \frac{U_c - \tilde{U}_2}{a_2} \tag{3}$$

For $\gamma_1 = \gamma_2$, $\tilde{U}_c$ can be obtained by

$$\tilde{U}_c = \frac{a_2 U_1 + a_1 U_2}{a_1 + a_2} \tag{4}$$

which, for equal static freestream pressures and specific heats, reduces to the incompressible expression.[9] They suggested that the growth rate of a compressible shear layer, normalized by the growth rate for an incompressible shear layer, might be expressible as a universal function of the convective Mach number $\tilde{M}_{c1}$, which is valid over a wide range of velocity and temperature ratios of a shear layer. They also found that the normalized growth rate decreases significantly with increasing $\tilde{M}_{c1}$.

Jackson and Grosch[10] presented their results of a study of the inviscid spatial stability of a parallel compressible mixing layer with one stream moving and the other stream stationary. It is shown that if the Mach number of the moving stream exceeds a critical value, there are always two groups of unstable waves. One of these groups is fast, with phase velocity greater than 1/2, and the other is slow with phase velocity less than 1/2.

The numerical calculations described here were performed under the assumptions of linear instability theory. The convective velocity is estimated as the phase velocity of the disturbances, i.e., $\tilde{U}_c = C_p$ (Mack[11] considered $\tilde{U}_c = C_r$ for

Received April 19, 1989; revision received Oct. 25, 1989.

*Graduate Student, Aeronautics, Graduate Aeronautical Laboratories.

†Professor, Aeronautics, Graduate Aeronautical Laboratories.

‡Professor, Aeronautics and Applied Physics, Graduate Aeronautical Laboratories. Member AIAA.

neutral disturbances). Therefore, a convective Mach number $\hat{M}_c$ for each stream can be written as

$$\hat{M}_{c1}^2 = \frac{U_1 - C_p}{a_1}, \qquad \hat{M}_{c2}^2 = \frac{C_p - U_2}{a_2} \tag{5}$$

where C_p is chosen to be the phase velocity of the most unstable eigenvalue. We think the definition given in Eq. (5) is more appropriate since the phase velocity of the disturbances is available from our computations.

The purpose of the present studies is to investigate the combined influence of the convective Mach number $\hat{M}_c$, which is different from the one used by Ragab and Wu ($\tilde{M}_c$), the velocity and temperature ratios, and the temperature profiles of the flow on the linear stability behavior of compressible shear layers. Studies are made of the case of inviscid flow under the assumptions that the gases in the two streams are the same, the main flow can be treated parallel, and that the disturbances in the flow are of small amplitude. The range of the unstable frequencies and wave numbers were numerically calculated for a two-dimensional, spatially growing disturbance.

Basic Disturbance Equations

We consider a two-dimensional flow of two parallel streams. With upper quantities as the reference and the local layer thickness δ as the length scale, the dimensionless quantities of the flow in Cartesian coordinates can be written as usual:

$$u_x = \bar{U} + u', \qquad u_y = v', \qquad T = \bar{T} + T'$$

$$\rho = \bar{\rho} + \rho', \qquad p = \bar{p} + p'$$

or, for the general field quantity,

$$Q(x,y,t) = \bar{Q}(y) + Q'(x,y,t)$$

where $\bar{Q}$ is a profile of the main flow, and Q' is the corresponding disturbance amplitude.

Consider now the disturbance to be a wave propagating in the x direction. The disturbance quantities in dimensionless form can be expressed as[2]

$$\{u',v',T',\rho',p'\} = \{f(y),\alpha\phi(y),\theta(y),r(y),\pi(y)\}\exp[i\alpha(x-ct)] \tag{6}$$

where α is a complex wave number, and c is a complex wave velocity. In the case of negligible viscous effects, the linearized disturbance equations for a two-dimensional compressible fluid with the same gas constants and specific heats are given by[2]

Continuity:

$$i(\bar{U}-c)r + \bar{\rho}(\phi' + if) + \bar{\rho}'\phi = 0 \tag{7a}$$

Momentum:

$$\gamma M_1^2\bar{\rho}[i(\bar{U}-c)f + \bar{U}'\phi] = -i\pi \tag{7b}$$

$$\gamma M_1^2\alpha^2\bar{\rho}[i(\bar{U}-c)\phi] = -\pi' \tag{7c}$$

Energy:

$$\bar{\rho}[i(\bar{U}-c)\theta + \bar{T}'\phi] = -(\gamma-1)(\phi' + if) \tag{7d}$$

State:

$$\frac{\pi}{\bar{p}} = \frac{r}{\bar{\rho}} + \frac{\theta}{\bar{T}} \tag{7e}$$

where M_1 is the upper stream Mach number and primes correspond to d/dy. These equations can be reduced to the second-order differential equation for the pressure disturbances,[2] i.e.,

$$\pi'' - \left(\frac{2\bar{U}'}{\bar{U}-c} - \frac{\bar{T}'}{\bar{T}}\right)\pi' - \alpha^2\left[1 - \frac{M_1^2}{\bar{T}}(\bar{U}-c)^2\right]\pi = 0 \tag{8}$$

Asymptotic Behavior of the Eigenfunctions

The asymptotic behavior of the eigenfunction $\pi(y)$ for $y \to \pm\infty$ is found from Eq. (8). With $y \to \pm\infty$, $\bar{U}$ and $\bar{T}$ are constants, and $\bar{U}', \bar{T}'$ are zeros. In that limit, Eq. (8) becomes

$$\pi'' - \lambda_k^2\pi = 0 \tag{9}$$

with

$$\lambda_k^2 = \alpha^2\left[1 - \frac{M_1^2}{\bar{T}_k}(\bar{U}_k - c)^2\right] = \Lambda_k = \Lambda_{kr} + i\Lambda_{ki} \tag{10}$$

and $k = 1,2$. Therefore, from Eq. (10), we get

$$\lambda_k = \lambda_{kr} + i\lambda_{ki} = \pm\Lambda_k^{1/2}$$

and the solution for large $|y|$ can be written as

$$\pi = A_k \exp(-\lambda_k|y|) \tag{11}$$

where A_k is a complex constant.

Since we have only considered the case of amplified disturbances ($\alpha_i < 0$), the boundary conditions for both supersonic and subsonic disturbances can be expressed by $\pi_r(y \to \pm\infty) \to 0$ and $\pi_i(y \to \pm\infty) \to 0$. In order to satisfy the boundary conditions, we set $\lambda_{kr} > 0$, and get

$$y = y_1 \to +\infty, \qquad \pi = A_1\exp(-\lambda_1 y) \tag{12a}$$

$$y = y_2 \to -\infty, \qquad \pi = A_2\exp(\lambda_2 y) \tag{12b}$$

where

$$\lambda_k = \lambda_{kr} + i\lambda_{ki} = \left[\frac{1}{2}(|\Lambda_k| + \Lambda_{kr})\right]^{1/2} + i\,\mathrm{sign}\{\Lambda_{ki}\}\left[\frac{1}{2}(|\Lambda_k| - \Lambda_{kr})\right]^{1/2}$$

Formulation of the Eigenvalue Problem

The eigenvalue problem is defined as follows. For a given real disturbance frequency β ($\beta = \alpha c$), the eigenvalues α_r and

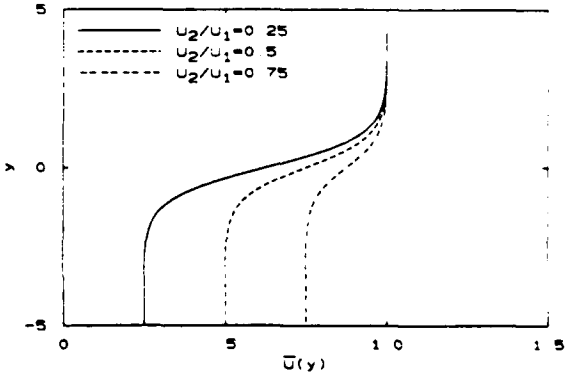

Fig. 1 Hyperbolic tangent mean velocity profiles for different values of the velocity ratio U_2/U_1.

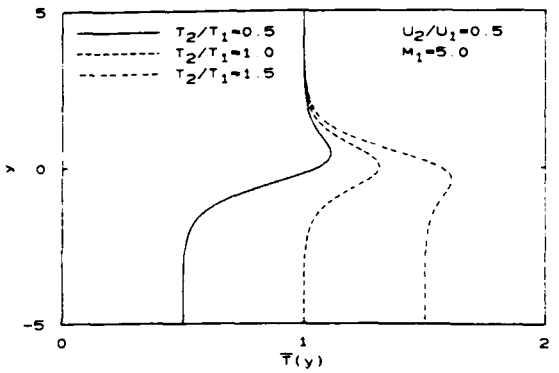

Fig. 2 Crocco-Busemann mean temperature profiles for different values of the temperature ratio T_2/T_1 for the case $U_2/U_1 = 0.5$ and $M_1 = 5.0$.

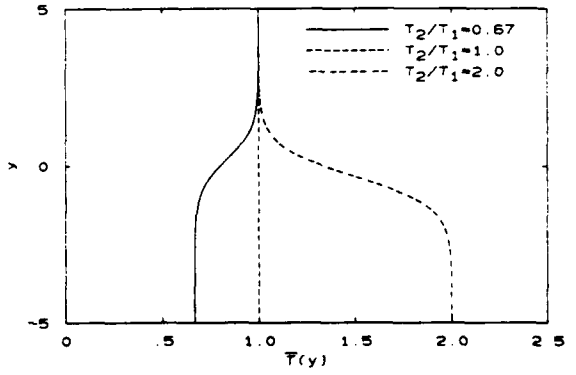

Fig. 3 Hyperbolic tangent $\bar{T}(y)$ mean temperature profiles for different values of the temperature ratio T_2/T_1.

α_i are to be determined in such a way that the eigenfunctions $\pi_r(y)$ and $\pi_i(y)$ satisfy the boundary conditions. Specifically, we used a Runge-Kutta method to solve the eigenvalue equation, with Eqs. (12a) and (12b) as boundary conditions. The equation was integrated from one side of the boundary ($y = y_1$) to the other side ($y = y_2$). The correct α was obtained for a given β by matching to the boundary conditions.

Velocity and Temperature Distributions

Lock's[12] numerical calculation of the velocity distribution for a compressible laminar boundary layer was approximated by Gropengiesser using a generalized hyperbolic tangent profile with three free constants. To simplify the problem, we assume that the dimensionless mean velocity profile is described by a hyperbolic tangent profile represented by the form

$$\bar{U}(y) = \eta(y) + U_R[1 - \eta(y)] \tag{13}$$

where $U_R = U_2/U_1$ is the velocity ratio across the shear layer, and $2\eta(y) - 1$ is approximated by a hyperbolic tangent [see mean velocity profiles $\bar{U}(y)$ in Fig. 1].

We note that the linearized flow equations do not prescribe the mean temperature profile. Accordingly, two different kinds of temperature profiles have been considered. One conforms to the Crocco-Busemann[13,14] relation, wherein the total temperature profile $T_t(y)$ for an equation ratio of the specific heats of the two freestreams is represented by

$$T_t(y) = T_{t1}\eta(y) + T_{t2}[1 - \eta(y)] \tag{14}$$

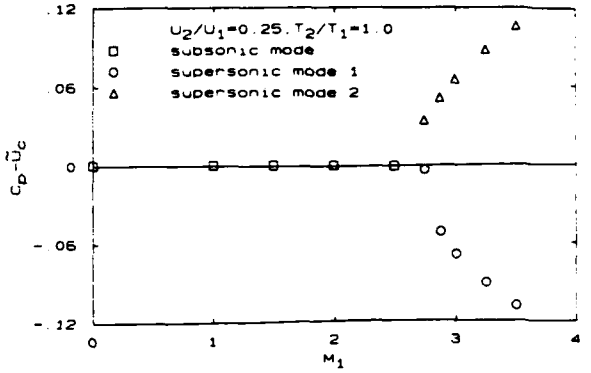

Fig. 4 The difference between C_p and $\bar{U}_c$ vs the freestream Mach number M_1.

where T_{t1}, T_{t2} are the freestream total temperatures. This yields the dimensionless mean static temperature profile,

$$\bar{T}(y) = c_1 + c_2\bar{U}(y) - \frac{(\gamma - 1)M_1^2}{2}\bar{U}^2(y) \tag{15}$$

where M_1 is the upper stream Mach number and c_1, c_2 are constants which satisfy the boundary conditions on the temperature profile. Such mean temperature profiles $\bar{T}(y)$ for $M_1 = 5$ are shown on Fig. 2. The other kind of dimensionless temperature profile is obtained by assuming that the dimensionless density distribution across the shear layer can also be approximated by a hyperbolic tangent profile, i.e.,

$$\tilde{\rho}(y) = \eta(y) + \rho_R[1 - \eta(y)] \tag{16}$$

where $\rho_R = \rho_2/\rho_1$ is the density ratio across the shear layer. Therefore, for a shear layer comprised of the same gas, the dimensionless temperature profile is $\bar{T}(y) = 1/\tilde{\rho}(y)$ (see Fig. 3).

Results

For a given combination of freestream Mach number M_1, temperature ratio $T_R(T_2/T_1)$, and velocity ratio U_R, the linear instability characteristics were calculated, yielding the most unstable eigenvalue ($\alpha_m = \alpha_{mr} + i\alpha_{mi}$) and its corresponding real frequency β_m. The phase velocity C_p of the disturbances was obtained as β_m/α_{mr}. This yields the convective Mach number $\bar{M}_{c1}$ and $\bar{M}_{c2}$ from Eq. (5).

For a free mixing layer with subsonic disturbances, there is only one unstable mode propagating with the phase velocity C_p approximately equal to $\bar{U}_c$, which is constant for given U_R and T_R. As the Mach number of the stream M_1 approaches or exceeds a critical value, there are always two unstable modes: one is with the phase velocity C_p less than $\bar{U}_c$ and the other is with the phase velocity greater than $\bar{U}_c$. These two unstable modes are called supersonic mode 1 and mode 2, respectively. If we increase the Mach number M_1, the phase velocities of the two modes will further increase or decrease (see Fig. 4).

Different combinations of velocity and temperature ratios using a velocity and temperature profile from Eqs. (13) and (15) were investigated for a convective Mach number $\bar{M}_{c1}$ from 0 to about 1.5. The velocity profiles for $U_R = 0.25$, 0.5, and 0.75 appear in Fig. 1 and the temperature profiles for $T_R = 0.5$, 1.0, and 1.5 appear in Fig. 2. In the region of supersonic convective Mach numbers, the modes with C_p less than $\bar{U}_c$ are more unstable than the modes with C_p greater than $\bar{U}_c$ in most cases of the velocity and temperature profiles given by Figs. 1 and 2. Therefore, we only considered the mode with C_p less than $\bar{U}_c$ for supersonic convective Mach

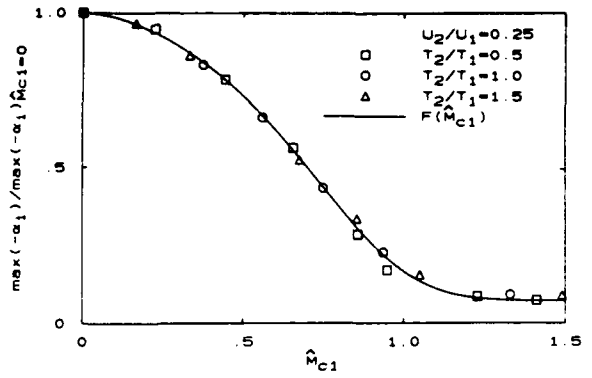

Fig. 5 Normalized maximum amplification rate vs $\hat{M}_{c1}$.

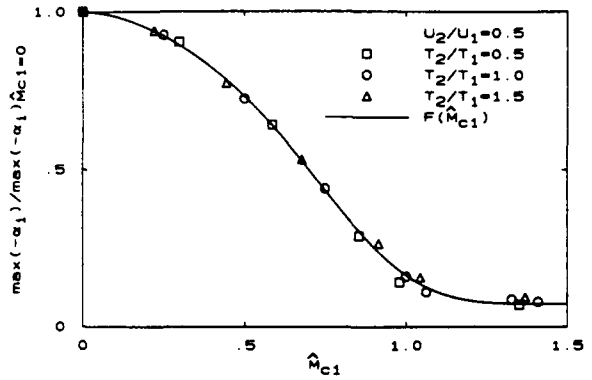

Fig. 6 Normalized maximum amplification rate vs $\hat{M}_{c1}$.

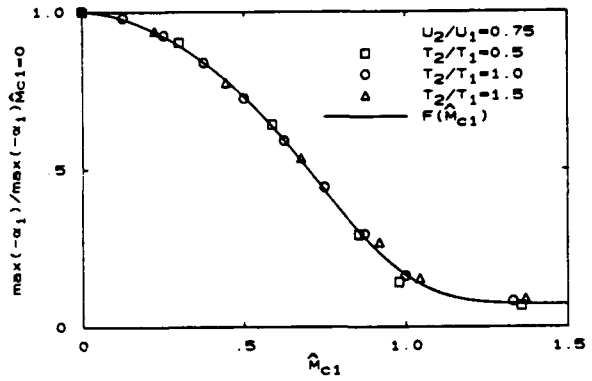

Fig. 7 Normalized maximum amplification rate vs $\hat{M}_{c1}$.

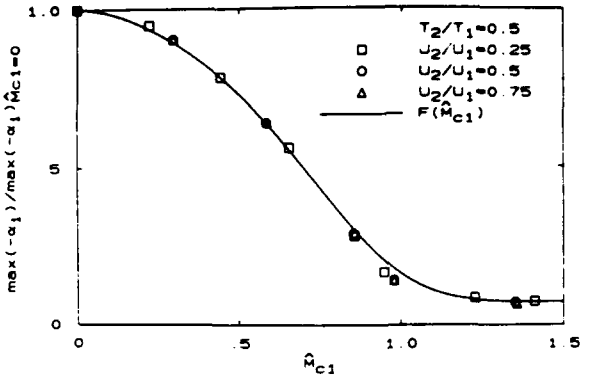

Fig. 8 Normalized maximum amplification rate vs $\hat{M}_{c1}$.

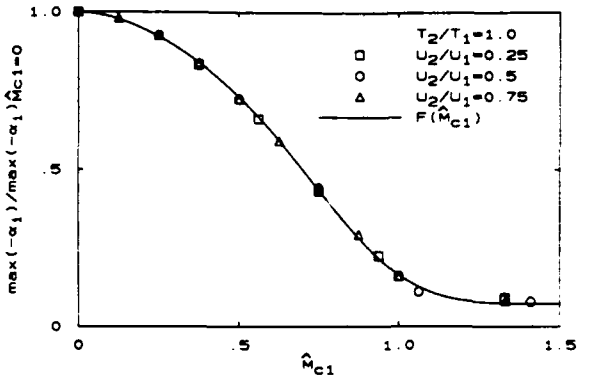

Fig. 9 Normalized maximum amplification rate vs $\hat{M}_{c1}$.

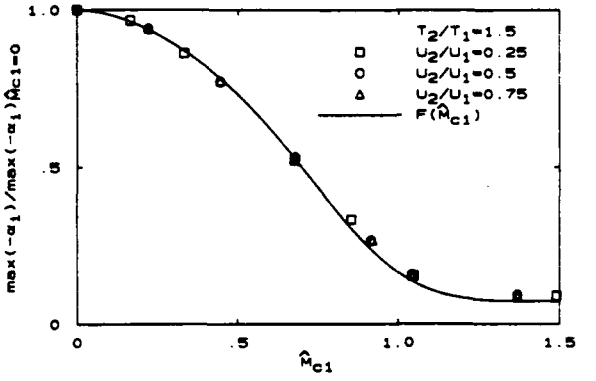

Fig. 10 Normalized maximum amplification rate vs $\hat{M}_{c1}$.

number. Results shown in Figs. 5–10, which were obtained from nine different combinations of T_R and U_R, indicate that if the most unstable eigenvalue for a compressible shear layer is normalized by its value corresponding to an incompressible shear layer (at the same velocity and temperature ratio), the ratio is well-approximated as a function of the convective Mach number only, i.e.,

$$\frac{\delta_x(\hat{M}_{c1})}{\delta_x(0)} \simeq \frac{\max\{-\alpha_i(U_2/U_1, T_2/T_1, \hat{M}_{c1})\}}{\max\{-\alpha_i(U_2/U_1, T_2/T_1, \hat{M}_{c1}=0)\}} \simeq F(\hat{M}_{c1}) \quad (17)$$

where $\delta_x = d\delta/dx$ for the shear layer of the particular freestream conditions and δ is the local layer thickness. The solid line estimate of $\delta_x(\hat{M}_{c1})/\delta_x(0)$ in Figs. 5–10 was computed by using all of the data of the nine different cases and least-squares fitting the normalized maximum amplification rate vs the convective Mach number $\hat{M}_{c1}$, for the range of $\hat{M}_{c1}$ from 0 to about 1.5 with a function of the form

$$\frac{\delta_x(\hat{M}_{c1})}{\delta_x(0)} \simeq 1 + p_0[e^{-(p_2\hat{M}_{c1}^2 + p_3\hat{M}_{c1}^3 + p_4\hat{M}_{c1}^4)} - 1] \quad (18)$$

where

$$p_0 = 0.928286, \qquad p_2 = 1.78285$$

$$p_3 = -2.16428, \qquad p_4 = 2.68579$$

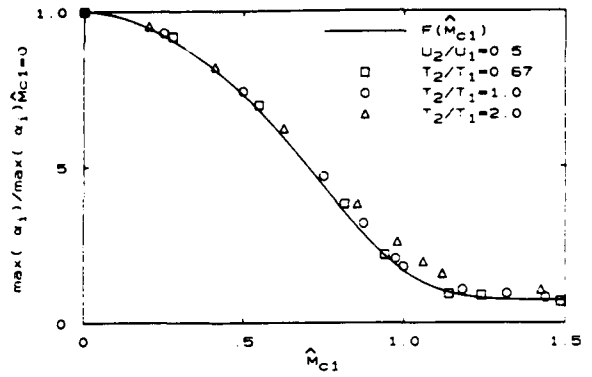

Fig. 11 Normalized maximum amplification rate vs $\hat{M}_{c1}$ for hyperbolic tangent mean temperature profiles comparison with $F(\hat{M}_{c1})$.

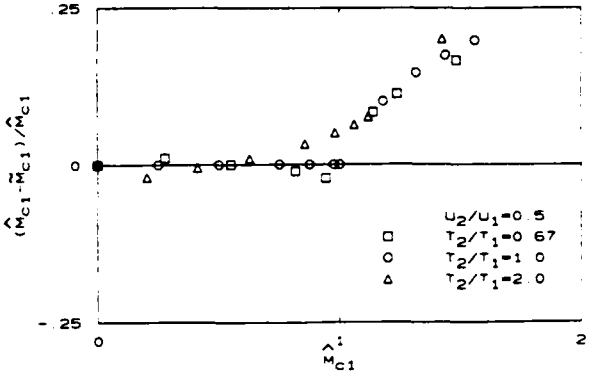

Fig. 13 Normalized difference between $\hat{M}_{c1}$ and $\tilde{M}_{c1}$ vs $\hat{M}_{c1}$ for hyperbolic tangent mean temperature profiles.

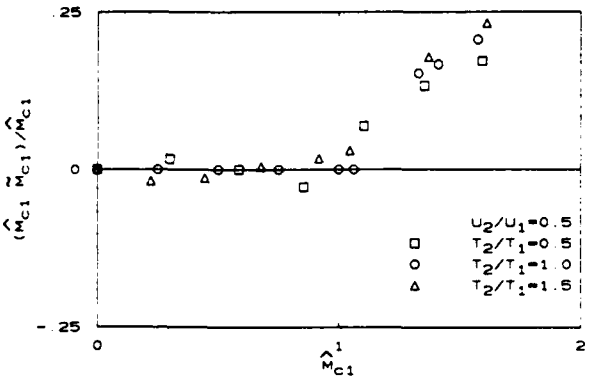

Fig. 12 Normalized difference between $\hat{M}_{c1}$ and $\tilde{M}_{c1}$ vs $\hat{M}_{c1}$.

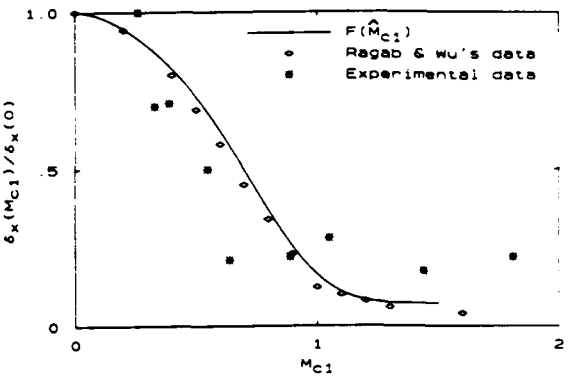

Fig. 14 Comparison of $F(\hat{M}_{c1})$ with Ragab and Wu's numerical data and with Papamoschou and Roshko's experimental data.

Note that $\delta_x(\hat{M}_{c1} \to \infty)/\delta_x(0) = 1 - p_0$, and that the coefficient p_2 is related to the second derivative at $\hat{M}_{c1} = 0$, etc. Note also that these results suggest that $F(\hat{M}_{c1} = 0) = 0$, as might have been argued a priori. The results, shown in Figs. 5–10, also suggest that the normalized maximum amplification rate decreases significantly with increasing $\hat{M}_{c1}$ for the subsonic convective Mach numbers. In the region $\hat{M}_{c1} > 1.5$, this normalized amplification rate decreases continuously to zero as the convective Mach number is increased.

In the second set of calculations, the mean temperature profile was specified via Eq. (16), i.e., $\bar{T}(y) = 1/\bar{\rho}(y)$. The resulting temperature profiles for $T_R = 0.67$, 1, and 2 are plotted in Fig. 3. The velocity ratio $U_R = 0.5$ with each of these three temperature ratios was studied for the convective Mach number $\hat{M}_{c1}$ from 0 to about 1.5. The results, shown in Fig. 11, substantiate the convective Mach number as the relevant compressibility parameter and also display good agreement with the plot $\delta_x(\hat{M}_{c1})/\delta_x(0)$ vs $\hat{M}_{c1}$ obtained from Eq. (18), even though these two mean temperature profiles are very different at supersonic convective Mach numbers (see Figs. 2 and 3).

With $\bar{U}_c$ calculated from Eq. (4) and C_p obtained from the numerical calculations under the linear theory, $\hat{M}_{c1}$ does not necessarily equal $\tilde{M}_{c1}$. In fact, the phase velocity C_p approximately equals $\bar{U}_c$ for subsonic convective Mach number; but because of the existence of second unstable modes for supersonic convective Mach numbers,[10] C_p is not unique and cannot be estimated by $\bar{U}_c$. Blumen et al.[5] have noted this behavior for a shear layer of an inviscid fluid with two-dimensional temporal disturbances. We can see that, for both temperature profiles [Eqs. (15) and (16) with $\bar{T}(y) = 1/\bar{\rho}(y)$], there are very small differences between $\hat{M}_{c1}$ and $\tilde{M}_{c1}$ from the plot of $(\hat{M}_{c1} - \tilde{M}_{c1})/\hat{M}_{c1}$ vs $\hat{M}_{c1}$ for $\hat{M}_{c1} \le 1$, but the differences only become substantial when $\hat{M}_{c1} > 1$ (see Figs. 12 and 13). We only studied the cases for $\hat{M}_{c1} < 1.5$, since shock waves can exist in a shear layer at high convective Mach numbers and, therefore, the validity of a linear description of these phenomena would be suspect.

A comparison of our estimate of $\delta_x(\hat{M}_{c1})/\delta_x(0)$ with Ragab and Wu's numerical data and with Papamoschou and Roshko's experimental data is made in Fig. 14. The data from our calculations are very close to Ragab and Wu's. The difference between $\hat{M}_{c1}$ and $\tilde{M}_{c1}$, although not small in the region $\hat{M}_{c1} > 1$, does not affect the results, since the normalized amplification rates are very small in this region. According to Papamoschou and Roshko's experimental data,[7] the growth rate of the shear layer tapers off as the convective Mach number becomes supersonic. As opposed to their findings, however, the growth rate of our calculations decreases to zero as $\hat{M}_{c1} \gg 1$. Preliminary calculations suggest that a large value for the growth rate at large M_{c1} is exhibited by more complex velocity and/or density profiles. Also, Sandham and Reynolds[15] showed that a large value of the growth rate can be obtained for three-dimensional wave disturbances at convective Mach numbers above 0.6.

Conclusion

The influences of the convective Mach number, the velocity and temperature ratios, and the temperature profiles of the flow on the linear spatial instability characteristics of a plane shear layer, formed by the same gas, were investigated. It was found that there is a nearly universal dependence of the

normalized maximum amplification rate on the convective Mach number, and this amplification rate decreases significantly with increasing $\hat{M}_{c,i}$ in the region of $\hat{M}_{c,i} < 1$.

Acknowledgments

This work was supported by the Air Force Office of Scientific Research Grants 83-0213 and 88-0155. We would like to thank Dimitri Papamoschou, Paul Miller, and Cliff Frieler for their helpful discussions and assistance.

References

[1]Monkewitz, P. A., and Huerre, P., "Influence of the Velocity Ratio on the Spatial Instability of Mixing Layers," *Physics of Fluids*, Vol. 25, No. 7, 1982, pp. 1137–1143.

[2]Lessen, M., Fox, J. A., and Zien, H. M., "On the Inviscid Stability of the Laminar Mixing of Two Parallel Streams of a Compressible Fluid," *Journal of Fluid Mechanics*, Vol. 23, 1965, pp. 335–367.

[3]Lessen, M., Fox, J. A., and Zien, H. M., "Stability of the Laminar Mixing of Two Parallel Streams with Respect to Supersonic Disturbances," *Journal of Fluid Mechanics*, Vol. 25, 1966, pp. 737–742.

[4]Gropengiesser, H., "Study of the Stability of the Boundary Layers in Compressible Fluids," NASA TT-F-12, 786, 1970.

[5]Blumen, W., Drazin, P. G., and Billings, D. F., "Shear-Layer Instability of an Inviscid Compressible Fluid," *Journal of Fluid Mechanics*, Vol. 71, 1975, pp. 305–316.

[6]Ragab, S. A., and Wu, J. L., "Instabilities in the Free Shear Layer Formed by Two Supersonic Streams," AIAA Paper 88-0038, Jan. 1988.

[7]Papamoschou, D., and Roshko, A., "Observations of Supersonic Free Shear Layers," AIAA Paper 86-0162, Jan. 1986.

[8]Coles, D., "Prospects for Useful Research on Coherent Structure in Turbulent Shear Flow," *Proceedings of the Indian Academy of Sciences*, Vol. 4, No. 2, 1981, pp. 111–127.

[9]Dimotakis, P. E., "Two-Dimensional Shear-Layer Entertainment," *AIAA Journal*, Vol. 24, No. 11, 1986, pp. 1791–1796.

[10]Jackson, T. L., and Grosch, C. E., "Spatial Stability of a Compressible Mixing Layer," ICASE Rept. 88-33, 1988.

[11]Mack, L. M., "Linear Stability and the Problem of Supersonic Boundary-Layer Transition," *AIAA Journal*, Vol. 13, 1975, pp. 278–289.

[12]Lock, R. C., "The Velocity Distribution in the Laminar Boundary Layer Between Parallel Streams," *Quarterly Journal Mech. Appl. Math.* Vol. 4, 1951, pp. 42–63.

[13]Crocco, L., "Sulla Transmissione del Calore da una Lamina Piana a un Fluido Scorrente ad Alta Velocita," *L'Aerotechnica*, Vol. 12, 1932, pp. 181–197.

[14]Busemann, A., "Gasstromung mit Laminarer Grenzschicht Entlang einer Platte," *ZAMM*, Vol. 15, 1935, pp. 23–25.

[15]Sandham, N., and Reynolds, W., "The Compressible Mixing Layer: Linear Theory and Direct Simulation," AIAA Paper 89-0371, Jan. 1989.

Appendix B

HALL, J. L., DIMOTAKIS, P. E. AND ROSEMANN, H. [1991] "Experiments in non-reacting compressible shear layers." *AIAA* 29th *Aerospace Sciences Meeting*, Paper 91-0629.

AIAA-91-0629

Experiments in Non-Reacting Compressible Shear Layers

J. L. Hall, P. E. Dimotakis and H. Rosemann
California Institute of Technology
Pasadena, CA

29th Aerospace Sciences Meeting
January 7–10, 1991/Reno, Nevada

EXPERIMENTS IN NON-REACTING COMPRESSIBLE SHEAR LAYERS*

J. L. Hall** , P. E. Dimotakis† and H. Rosemann‡

Graduate Aeronautical Laboratories
California Institute of Technology
Pasadena, CA 91125

Abstract

Two-dimensional, compressible turbulent shear layers are studied in a new wind tunnel facility. Helium, nitrogen and argon gases are used in various combinations to produce shear layers with isentropically computed convective Mach numbers that range from near zero to unity. Side-view Schlieren photographs of these compressible flows are generally devoid of the two-dimensional, large-scale structures seen in incompressible flows. Travelling shock and expansion waves are observed in the high compressibility flows, evidently created by turbulent structures convecting at supersonic velocities with respect to one of the free streams. Such waves are seen only in the low speed fluid, with apparent convection velocities much higher than those predicted by the usual isentropic pressure-matching arguments. The measured shear layer growth rates agree with previous results by other experimenters, except for a few unusual cases at low compressibility and low density ratio. Finally, it is observed that the shear layer growth rate is relatively insensitive to the effects of incident shock and expansion waves on the shear layer.

Introduction

Recent years have witnessed considerable experimental activity in the field of compressible turbulent shear layers, work that is largely motivated by the program to develop SCRAMJET engine technology for the National Aerospace Plane (Chinzei *et al.* 1986, Papamoschou & Roshko 1988, Papamoschou 1989, Clemens & Mungal 1990, Clark *et al.* 1990, Fourgette & Dibble 1990, Dutton *et al.* 1990). Such experiments are also motivated by the desire to understand compressible turbulent shear flows in the context of the coherent structure models that have been developed for incompressible shear layers over the past twenty years. In particular, the current work can be viewed as a logical extension of the shear layer research conducted at Caltech during that time (Brown & Roshko 1971, 1974, Konrad 1976, Dimotakis & Brown 1976, Breidenthal 1981, Broadwell & Breidenthal 1982, Mungal & Dimotakis 1984, Bernal & Roshko 1986, Koochesfahani & Dimotakis 1986, Frieler & Dimotakis 1988, Papamoschou & Roshko 1988, Papamoschou 1989, Hermanson & Dimotakis 1989).

** Graduate Student in Aeronautics, Student Member AIAA.

† Professor, Aeronautics & Applied Physics, Associate Fellow AIAA.

‡ Research Fellow in Aeronautics.

The existing evidence for large-scale structure in compressible shear layers is not definitive. Most of the available Schlieren photographic data do *not* clearly show the two-dimensional vortices seen in incompressible flows (Chinzei *et al.* 1986, Papamoschou & Roshko 1988). However, recent pictures by Clemens & Mungal (1990) do show such structures, but only at very low compressibility levels. Further evidence for coherent structures can be found in the axisymmetric jet experiments of Fourgette & Dibble (1990). Their planar Rayleigh scattered images clearly show distinct regions of fluid separated by regular intervals. Interestingly enough, this structure was detected at a compressibility level beyond that at which Clemens & Mungal (1990) were able to find such structures. The difference between a "slice" view (planar Rayleigh scattering) and a spanwise integrated view (Schlieren) is a possible explanation for this difference, one that points to a significant role played by three-dimensional effects in compressible turbulent shear layers.

The convective Mach number measurements of Papamoschou (1989) constitute another unresolved issue for compressible shear layers. Papamoschou used double-spark Schlieren photography to track turbulent features in the flow and thereby infer convection velocities, u_c. From these measurements, he was able to compute the convective Mach numbers for the flow; *i.e.* ,

$$M_{c1} = \frac{u_1 - u_c}{a_1} \qquad \text{and} \qquad M_{c2} = \frac{u_c - u_2}{a_2} \,, \tag{1}$$

where u_j and a_j are the free stream velocities and sound speeds respectively. His results are plotted in Fig. 1. It can be seen that the measured convection velocities tend to be very close to one free stream velocity or the other at compressible conditions, producing one low and one high convective Mach number. These results are not in accord with theoretical predictions based on isentropic pressure matching at the interstitial stagnation points in the convective frame of reference (Bogdanoff 1983, Dimotakis 1984, Coles 1985, Papamoschou & Roshko 1988, Dimotakis 1989). Specifically, an isentropic pressure balance requires

$$p_1 \left(1 + \frac{\gamma_1 - 1}{2} M_{c1}^2\right)^{\gamma_1/\gamma_1 - 1} = p_2 \left(1 + \frac{\gamma_2 - 1}{2} M_{c2}^2\right)^{\gamma_2/\gamma_2 - 1} \,, \tag{2}$$

where p_j is the static pressure and γ_j is the ratio of specific heats in free stream j. For $p_1 = p_2$ and $\gamma_1 = \gamma_2$, this yields $M_{c1} = M_{c2}$. Furthermore, it can be shown that M_{c1} and M_{c2} are still fairly close even when $\gamma_1 \neq \gamma_2$, provided that $p_1 \simeq p_2$, which is usually the case in experiments.

Therefore, the convection velocity measurements of Papamoschou (1989) indicate that grossly unequal pressure dissipation must occur on the two sides of the shear layer in order to satisfy the requirement of a pressure balance at the convective-frame stagnation points. This has led both Papamoschou (1989) and Dimotakis (1989) to speculate that shock waves exist on only one side of the shear layer in these flows, thereby providing a mechanism for unequal pressure losses. Unfortunately, such waves were not detected in any shear layer experiment prior to the current work, a curious omission considering that fairly strong waves are required to dissipate the amounts of pressure indicated by the observed convection velocities.

The current experiments were designed to address these issues, as well as provide growth rate data that could be compared to previous results from other experimenters (Chinzei *et al.* 1986, Papamoschou & Roshko 1988, Clemens & Mungal 1990). A new wind tunnel facility was employed for this purpose; it will be briefly described in the next section. Following that, the new experimental data will be presented and discussed.

Facility Decription

The current experiments were performed in the new GALCIT Supersonic Shear Layer Combustion Facility (Fig. 2). This is a two-stream blowdown wind tunnel with a nominal run time of 3 *sec*. It is capable of producing chemically reacting flows based on $H_2/F_2/NO$ chemistry; however, the work reported here is entirely based on non-reacting experiments. The facility is currently configured for a supersonic high-speed stream ($M_1 = 1.5$) and a subsonic low-speed stream ($M_2 < 0.5$). Different convective Mach numbers are generated primarily by using different gas combinations in the two streams. The static pressure of the shear layer is nominally 1 atm.

The operation of the facility is straightforward. The desired gases or gas mixtures are loaded into a pair of storage tanks. At run-time, parallel piping networks deliver these gases to the test section via shutoff and flow regulating valves. Inside the test section (Fig. 3) the gases flow through screens, honeycomb and appropriately contoured nozzles before coming into contact at the end of the splitter plate. The shear layer forms between two adjustable guidewalls on the top and bottom, and two windows on the sides. Upon exiting the test section, the shear layer gases enter a waste gas treatment system which is designed to neutralize the toxic and corrosive gases from $H_2/F_2/NO$ combustion experiments.

Test section flow diagnostics are comprised of the following elements:

1. Side-view Schlieren photography.
2. Guidewall static pressure transducers (6 per wall).
3. Cross-stream total pressure tubes (16 in all).
4. Cross-stream exposed junction thermocouples (16 in all).

With the exception of the Schlieren photography and a few of the guidewall pressure transducers, all of these diagnostics are fairly low frequency response sensors primarily used for time-averaged measurements. The Schlieren system spark source has a 20 $nsec$ pulse duration, which is sufficiently fast to freeze the flow. The few fast guidewall pressure transducers are 1 MHz piezoelectric devices which are also capable of temporally resolving the flow.

Further details on the facility design and operation can be found in Hall (1991).

Results and Discussion

Figure 4 shows the basic geometry and coordinate system for the shear layers to be discussed here. Stream 1 is defined to be the high-speed stream with velocity u_1, density ρ_1, pressure p_1, temperature T_1, Mach number M_1 and specific heat ratio γ_1. The same variables are used on the low-speed side with a subscript 2. The upper (high-speed) guidewall which bounds the flow is specified to be parallel to the x-axis. The lower guidewall is allowed to deflect to an angle β in order to control the streamwise pressure gradient dp/dx. The angles α_1 and α_2 describe the orientation of the shear layer within the channel. In this study, the shear layer growth rate, δ, is taken to be the visual thickness, as measured from Schlieren photographs.

A list of the experiments to be discussed can be found in Table 1. The test cases are listed in order from highest to lowest compressibility, as determined by the isentropic pressure-matching model value for M_{c1} (Eq. 2). The values for $(\delta/x)_{\text{inc}}$ are computed from Brown (1974); *i.e.* ,

$$\left(\frac{\delta}{x}\right)_{\text{inc}} = C_\delta \frac{(1-r)(1+s^{1/2})}{1+rs^{1/2}} , \tag{3}$$

where $r \equiv u_2/u_1$ is the velocity ratio, $s \equiv \rho_2/\rho_1$ is the density ratio and C_δ is a constant, here given the value of 0.17 as was done in Papamoschou & Roshko (1988). The Reynolds number is defined by

$$Re_x = \frac{\Delta U x}{\nu} , \tag{4}$$

where $\Delta U \equiv u_2 - u_1$ is the velocity difference across the layer, ν is the kinematic viscosity[‡] and x is the length of the shear layer from splitter tip to cross-stream instrument rake.*

A horizontal knife edge Schlieren photograph of the highest compressibility flow (Case 1) is presented in Fig. 5. Immediately obvious is a complex yet regular wave system in the low-speed flow. This is a *travelling* wave system created by shear layer structures that are convecting supersonically with respect to the low-speed stream. Note that they cannot be standing waves (as are seen in the high-speed flow near the nozzle exit) because $M_2 \ll 1$. Upon close inspection, the wave system is seen to be comprised of a set of waves originating at the shear layer and a set of reflected waves off the lower guidewall. Each set is composed of alternating compression and expansion waves, which must nearly balance each other to maintain a negligible streamwise pressure gradient. The incident wave system is reminiscent of those seen in the supersonic jet experiments of Lowson & Ollerhead (1968), Tam (1971) and Oertel (1979), and presumably shares the same origin.

It is not possible to discern from Fig. 5 the precise nature of the shear layer structures which created the travelling waves. In fact, the shear layer seems devoid of any kind of large-scale structure at all. Nevertheless, the spacing of the travelling waves is seen to be on the order of the local shear layer thickness, δ_{vis}, suggesting that some form of large-scale structure is present. Further attempts were made to image this large-scale structure by de-sensitizing the Schlieren system and by rotating the knife edge to the vertical position; however, none of the photographs from these experiments revealed any more large-scale structure than is seen in Fig. 5. There are at least two possible explanations for this result: Large-scale structure is highly distorted by spanwise three-dimensionality or large-scale structure is obscured by the signal from lots of small-scale, high-gradient turbulence superimposed on top of it. Unfortunately, it is not possible on the basis of the current data to choose between these possible explanations.

Despite the lack of observed structure, the travelling waves strongly suggest that there is a well-defined convection velocity for the fluid inside the shear layer. Specifically, the wave angles of these waves are tightly clustered in the range of $23° < \mu < 28°$, where μ is measured with respect to an imaginary line which roughly bisects the shear layer wedge.** These wave angles provide a direct measure of the convective Mach number for this flow, *i.e.*

$$M_{c2} \simeq \frac{1}{\sin\mu} . \tag{5}$$

---

‡ Averaged properties are used when different gases are present in the shear layer.

* In the current configuration, $x = 0.38\ m$.

** This direction is an estimate for the motion of the wave creating structures in the shear layer.

The range of wave angles quoted above yields $2.1 < M_{c2} < 2.6$ for this Case 1 flow. This Mach number range is also corroborated by static pressure measurements made on the low-speed guidewall. Specifically, two piezoelectric pressure transducers spaced 5 *cm* apart were used to measure the pressure "footprint" of the travelling waves. A crosscorrelation of the two pressure signals (Fig. 6) shows a peak centered at 59 μsec, which translates into a convective Mach number of $M_{c2} \simeq 2.54$.

This measured value is very different from the isentropic pressure-matching value of approximately unity (Table 1). Note that, given $M_{c2} \simeq 2.54$, Eq. 1 requires that $M_{c1} \simeq 0.31$. Here then is corroboration of the Papamoschou (1989) results which indicated very different convective Mach numbers for high-compressibility flows. The current results for Cases 1 and 2, which were the only flows to exhibit travelling waves, are plotted in Fig. 7 along with the Papamoschou (1989) data. Although the scatter in the data is large, it can at least be said that the new data do not contradict the old.

There remains a problem, however, in that the observed travelling waves are simply too weak to completely fulfil the pressure dissipation role required to reconcile the stagnation point pressure-matching model with the measured convection velocities. The agreement between the wave angle and pressure crosscorrelation measurements suggests that the observed waves are weak; furthermore, even a *normal* shock wave with a shock Mach number of $M_s = M_{c2} = 2.54$ cannot dissipate enough pressure to satisfy the requirement. A possible resolution of this dilemma can be found in the idea that shear layer vortices may be capable of locally accelerating the flow to Mach numbers much higher than M_{c2} (Papamoschou 1989). Such accelerated flow must eventually come to rest at the stagnation point in the convective reference frame (Fig. 8), a process which will require a very strong recompression shock *inside* the shear layer.

Although a very strong recompression shock can potentially satisfy the pressure dissipation requirements, no such shocks have been detected in any experiment to date. This includes the current experiments which tried a variety of knife edge configurations. It is possible that the same elements which possibly prevent detection of large-scale shear layer structures (three-dimensionality, superimposed small-scale turbulence) also hide embedded shock waves. Nevertheless, given the very strong shock waves required ($M_s \simeq 7$ for Case 1) it is surprising that they do not show up in the available Schlieren photographs.

The normalized growth rates for all eleven cases in the current study are plotted versus the isentropically computed convective Mach number, $M_{c1}^{(i)}$, in Fig. 9, along with data from other researchers. Note that the measured growth rate $(\delta/x)_{vis}$ has been normalized by the predicted incompressible growth rate, Eq. 3. For $M_{c1}^{(i)} > 0.3$, the collapse of the data is seen to be quite good. This collapse is somewhat surprising given the results already discussed for the high-compressibility cases which indicate that the measured convective Mach number is very different from $M_{c1}^{(i)}$. Perhaps this can be understood by considering $M_{c1}^{(i)}$ to be an *averaged* measure of compressibility in the flow, a parameter which, using the Case 1 flow as an example, combines the effects of a supersonic M_{c2} and a subsonic M_{c1}. The value of $M_{c1}^{(i)}$ is also close to the parameter $\Delta U/(a_1 + a_2)$ suggested by Papamoschou (1989) as a means of determining when compressibility effects become important in the flow. From this point of view, $M_{c1}^{(i)}$ is possibly still a valid measure of the overall compressibility of the shear layer, although the underlying physical ideas are somewhat different than originally thought.

For $M_{c1}^{(i)} < 0.3$, however, the data do not collapse at all. The results for the current experiments are particularly unusual, with Cases 7, 8 and 9 forming a trend of growth rate *reduction* at very low compressibility levels. This reduction is particularly surprising considering the all-subsonic flows of Cases 10 and 11 which almost recover the theoretical incompressible growth rate despite having the same value of $M_{c1}^{(i)}$ as Cases 8 and 9. It should be emphasized that the only real difference between these pairs of flows is the existence of $M_1 > 1$ in Cases 8 and 9, versus $M_1 < 1$ in Cases 10 and 11; the Reynolds number, Re, the velocity ratio, r, and the density ratio, s (Case 10 excluded), are all roughly the same in these flows.

Further clues to this unusual result can be gleaned from the Schlieren photographs of Cases 6, 7, 8 and 9 (Fig. 10). The Case 6 photograph (Fig. 10a) shows the flow before the growth rate reduction trend starts. Note the absence of large-scale coherent structures. In Cases 7 and 8, however, one can detect some structure, particularly in the downstream section of Case 8. Curiously enough, there are no structures in the Case 9 flow, although the growth rate reduction is quite pronounced. Taken together, this sequence of flows suggests that some kind of transition behaviour is taking place in Cases 7 and 8, one that is accompanied by shear layer thinning and the formation of some detectable structure. The absence of structure in Case 9 suggests, perhaps, that it lies beyond the transitional regime.

Very little is known about this transition phenomenon, except that it coincides with very low density ratios in the flow. The density ratios for Cases 7, 8 and 9 are in fact lower than any of the other compressible flows represented in Fig. 9. Such low density ratios were a necessary byproduct of the methodology of producing low $M_{c1}^{(i)}$ flows by increasing the helium content of the low-speed fluid and hence increasing its sound speed. Note that a low density ratio, by itself, does not result in abnormally low growth rates; witness the Case 11 flow result in this study and the previous low density, incompressible results of Brown & Roshko (1974) and Frieler & Dimotakis (1988). Only the coupling of a low density ratio and a supersonic free stream Mach number seems to produce usually low growth rates. One might reasonably suspect that the hyperbolic character of the $M_1 > 1$ free stream flow lies at the heart of the matter. Certainly, this will inhibit downstream to upstream feedback mechanisms in the flow (Dimotakis & Brown 1976). Of course, such inhibition is present whether the flow possesses a low density ratio or not. Therefore, this phenomenon must contain one or more additional elements that, for the present time, remain unknown.

One can speculate that a new growth rate mechanism has been encountered in these low density supersonic M_1 flows. This mechanism evidently becomes important in Cases 7 and 8, resulting in the transitional behaviour, and it dominates the Case 9 flow. Note that this new growth rate mechanism does not appear to be related to the so-called "wake effect" identified by Koochesfahani & Frieler (1987). They found that at *high* density ratios ($s \geq 6$) a second instability mode becomes important in addition to the usual Kelvin-Helmholtz instability, one that is related to the momentum deficit in the wake of the splitter tip.

The final results to be discussed here concern two off-design flows based on the medium compressibility Case 3 condition. The first flow (Fig. 11a) demonstrates the relative insensitivity of the overall growth rate to the impact of a strong planar wave. This wave is created at the splitter tip by a large pressure mismatch between the free stream static pressures at this point. The wave subsequently reflects off the upper guidewall and the shear layer and causes considerable bending of the

shear layer in the process. Nevertheless, the visual shear layer thickness at the downstream location is within 5% of the nominal Case 3 flow. Note also that some large-scale structure is apparent in this example.

Figure 11b shows another off-design Case 3 flow, although here the strength of the wave coming off the splitter tip is much weaker than in Fig. 11a; nevertheless, this shear layer possesses considerable large-scale, two-dimensional structure. It should be emphasized that these structures were not seen in the normal pressure-matched flows, suggesting that the planar wave from the splitter tip enhanced the formation of two-dimensional structure in the shear layer, perhaps by means of an unknown resonant forcing mechanism. It should be noted that relatively few of the off-design flows for which data exists demonstrated such enhanced two-dimensional structure, attesting perhaps to the difficulty in unintentionally achieving the required resonance conditions.

Conclusions

Non-reacting compressible turbulent shear layers were studied in a new wind tunnel facility. Side-view Schlieren photographs of the high compressibility flows ($M_{c1}^{(i)} = 0.90, 0.96$) revealed the presence of travelling shock and expansion waves in the low-speed fluid, waves created by unseen shear layer structures convecting at supersonic Mach numbers. The measured convection velocities of these structures is considerably higher than those predicted by models of isentropic pressure recovery at stagnation points in the convective frame. Large scale coherent structures were generally not seen in the compressible flows studied. For $M_{c1}^{(i)} > 0.3$, the measured shear layer growth rates agree with previous results by other experimenters. For $M_{c1}^{(i)} < 0.3$, a curious reduction in normalized growth rate was observed. It is suspected that this result is the product of an unknown growth rate mechanism for the compressible turbulent shear layer, one that results from the coupling of very low density ratios with a supersonic free stream Mach number. Finally, it was observed that the shear layer growth rate was not affected very much by the impact of strong planar waves created by a pressure mismatch at the splitter tip.

References

BERNAL, L. P. and ROSHKO, A. [1986] "Streamwise vortex structure in plane mixing layers", *J. Fluid Mech.* **170**, 499–525.

BOGDANOFF, D. W. [1983] "Compressibility Effects in Turbulent Shear Layers", (TN) *AIAA J.* **21**(6), 926–927.

BREIDENTHAL, R. E. [1981] "Structure in Turbulent Mixing Layers and Wakes Using a Chemical Reaction", *J. Fluid Mech.* **109**, 1–24.

BROADWELL, J. E. and BREIDENTHAL, R. E. [1982] "A Simple Model of Mixing and Chemical Reaction in a Turbulent Shear Layer", *J. Fluid Mech.* **125**, 397–410.

BROWN, G. L. [1974] "The Entrainment and Large Structure in Turbulent Mixing Layers", 5th *Australasian Conf. on Hydraulics and Fluid Mechanics*, 352–359.

BROWN, G. L. and ROSHKO, A. [1971] "The Effect of Density Difference on the Turbulent Mixing Layer", *Turbulent Shear Flows*, AGARD-CP-93, 23.1-12.

BROWN, G. L. and ROSHKO, A. [1974] "On Density Effects and Large Structure in Turbulent Mixing Layers", *J. Fluid Mech.* **64**(4), 775-816.

CHINZEI, N., MASUA, G., KOMURO, T. MURAKAMI, A. and KUDOU, K. [1986] "Spreading of two-stream supersonic turbulent mixing layers", *Phys. Fluids* **29**(5), 1345-1347.

CLARK, JR. R. L., NG, W. F., WALKER, D. A. and SCHETZ, J. A. [1990] "Large-Scale Structure in a Supersonic Slot-Injected Flow field", *AIAA J.* **28**(6), 1045-1051.

CLEMENS, N. T. and MUNGAL, M. G. [1990] "Two- and Three-Dimensional Effects in the Supersonic Mixing Layer", 26th *AIAA/SAE/ASME/ASEE Joint Propulsion Conference* (Orlando, FL), 10-12 July 1990, AIAA-90-1978.

COLES, D. [1985] "Dryden Lecture: The Uses of Coherent Structure", *AIAA* 23rd *Aerospace Sciences Meeting*, 14-17 January 1985 (Reno, Nevada), AIAA Paper 85-0506.

DIMOTAKIS, P. E. [1989] "Turbulent Free Shear Layer Mixing", *AIAA* 27th *Aerospace Sciences Meeting*, 9-12 January 1989 (Reno, Nevada), AIAA-89-0262.

DIMOTAKIS, P. E. and BROWN, G. L. [1976] "The Mixing Layer at High Reynolds Number: Large-Structure Dynamics and Entrainment", *J. Fluid Mech.* **78**(3), 535-560 + 2 plates.

DUTTON, J. C., BURR, R. F., GOEBEL, S. G. and MESSERSMITH, N. L. [1990] "Compressibility And Mixing In Turbulent Free Shear Layers", Twelfth Symposium on Turbulence (preprints), September 24-26, at the University of Missouri-Rolla.

FOURGUETTE, D. and DIBBLE, R. [1990] "Time Evolution of the Shear Layer of a Supersonic Jet at Matched Conditions", *AIAA* 28th *Aerospace Sciences Meeting*, 8-11 January 1990 (Reno, Nevada), AIAA-90-0508.

FRIELER, C. E. and DIMOTAKIS, P. E. [1988] "Mixing and Reaction at Low Heat Release in the Non-Homogeneous Shear Layer", *First National Fluid Dynamics Congress*, 24-28 July 1988 (Cincinatti, Ohio), AIAA Paper 88-3626.

HALL, J. L. [1991] *An Experimental Investigation of Structure, Mixing and Combustion in Compressible Turbulent Shear Layers*, Ph.D. thesis, California Institute of Technology.

HERMANSON, J. C. and DIMOTAKIS, P. E. [1989] "Effects of heat release in a turbulent reacting shear layer", *J. Fluid Mech.* **199**, 333-375.

KONRAD, J. H. [1976] *An Experimental Investigation of Mixing in Two-Dimensional Turbulent Shear Flows with Applications to Diffusion-Limited Chemical Reactions*, Ph.D. thesis, California Institute of Technology (also Project SQUID Technical Report CIT-8-PU, December 1976).

KOOCHESFAHANI, M. M. and DIMOTAKIS, P. E. [1986] "Mixing and chemical reactions in a

turbulent liquid mixing layer", *J. Fluid Mech.* **170**, 83–112.

KOOCHESFAHANI, M. M. and FRIELER, C. E. [1987] "Inviscid Instability Characteristics of Free Shear Layers with non-Uniform Density", *AIAA* 25th *Aerospace Sciences Meeting*, 12–15 January 1987 (Reno, Nevada), AIAA Paper 87-0047.

LOWSON, M. V. and OLLERHEAD, J. B. [1968] "Visualization Of Noise From Cold Supersonic Jets", *Journal of the Acoustical Society of America,* **44**, *No. 2.*

MUNGAL, M. G. and DIMOTAKIS, P. E. [1984] "Mixing and combustion with low heat release in a turbulent mixing layer", *J. Fluid Mech.* **148**, 349-382.

OERTEL, H. [1979] *Mach Wave Radiation Of Hot Supersonic Jets Investigated By Means Of The Shock Tube and New Optical Techniques* (Shock Tubes and Waves: Proceedings of the 12th International Symposium on Shock Tubes and Waves, Jerusalem, July 16-19, 1979).

PAPAMOSCHOU, D. [1989] "Structure of the compressible turbulent shear layer", *AIAA* 27th *Aerospace Sciences Meeting*, 9–12 January 1989 (Reno, Nevada), AIAA Paper 89–0126.

PAPAMOSCHOU, D. and ROSHKO, A. [1988] "The Compressible Turbulent Shear Layer: An Experimental Study", *J. Fluid Mech.* **197**, 453–477.

SHAU, Y. R. and DOLLING, D. S. [1990] "The Detection of Large Scale Structure in Undisturbed and Disturbed Compressible Shear Layers", *AIAA* 28th *Aerospace Sciences Meeting*, 8–11 January 1990 (Reno, Nevada), AIAA–90–0711.

TAM, C. K. W. [1971] "Directional acoustic radiation from a supersonic jet", *J. Fluid Mech.* **46**(4), 757–768.

Table 1: Summary Of Test Cases

Case	1	2	3	4	5	6
Side 1 Gases	100% He	100% He	100% N_2	100% N_2	100% N_2	100% N_2
Side 2 Gases	100% Ar	100% N_2	100% N_2	33% He 66% Ar	60% He 40% Ar	75% He 25% Ar
M_1	1.50	1.48	1.46	1.48	1.48	1.47
M_2	0.35	0.30	0.29	0.44	0.42	0.36
$r = u_2/u_1$	0.096	0.092	0.235	0.385	0.445	0.459
$s = \rho_2/\rho_1$	5.950	4.120	0.713	0.706	0.484	0.338
$M_{c1}^{(i)}$	0.962	0.906	0.511	0.426	0.336	0.292
$(\delta/x)_{inc}$	0.429	0.395	0.200	0.149	0.122	0.115
$(\delta/x)_{vis}$	0.100	0.108	0.114	0.092	0.083	0.084
$\delta_{vis}/\delta_{inc}$	0.233	0.274	0.570	0.630	0.680	0.730
Re_x	7.4×10^6	7.0×10^6	9.6×10^6	3.7×10^6	2.4×10^6	2.1×10^6
β	0°	1°	2°	0°	0.5°	0.5°

Table 1 (Continued)

Case	7	8	9	10	11
Side 1 Gases	100% N_2	100% N_2	100% Ar	100% N_2	100% N_2
Side 2 Gases	90% He 10% Ar	100% He	100% He	33% He 66% Ar	100% He
M_1	1.48	1.48	1.50	0.59	0.65
M_2	0.28	0.23	0.23	0.27	0.10
$r = u_2/u_1$	0.469	0.510	0.636	0.510	0.462
$s = \rho_2/\rho_1$	0.194	0.101	0.058	0.958	0.132
$M_{c1}^{(i)}$	0.240	0.175	0.106	0.143	0.093
$(\delta/x)_{inc}$	0.108	0.094	0.067	0.110	0.107
$(\delta/x)_{vis}$	0.073	0.062	0.040	0.101	0.097
$\delta_{vis}/\delta_{inc}$	0.678	0.660	0.597	0.918	0.907
Re_x	1.8×10^6	1.8×10^6	1.1×10^6	1.5×10^6	6.9×10^5
β	1°	2°	2°	0.5°	1.0°

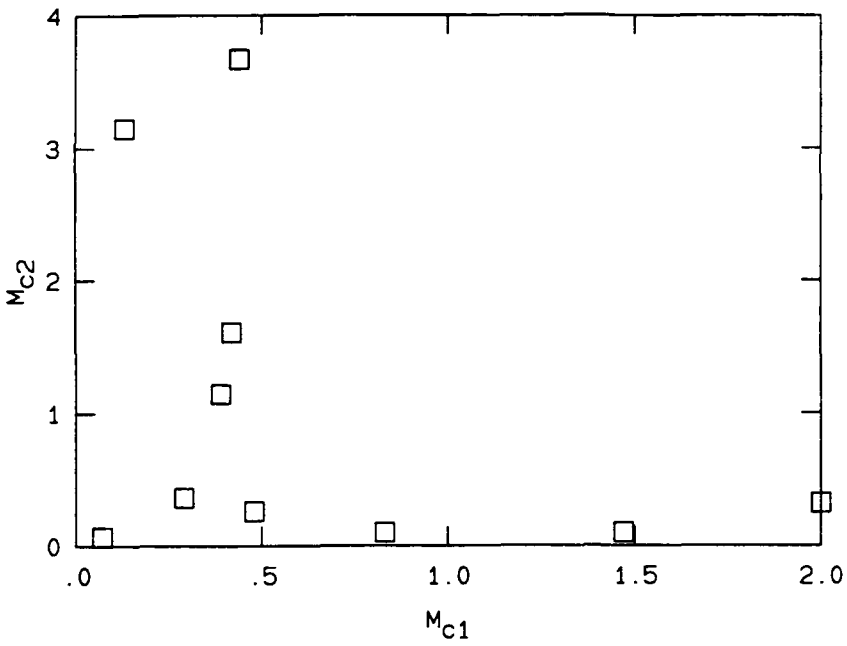

Fig. 1: Unequal Convective Mach Numbers Measured by Papamoschou (1989).

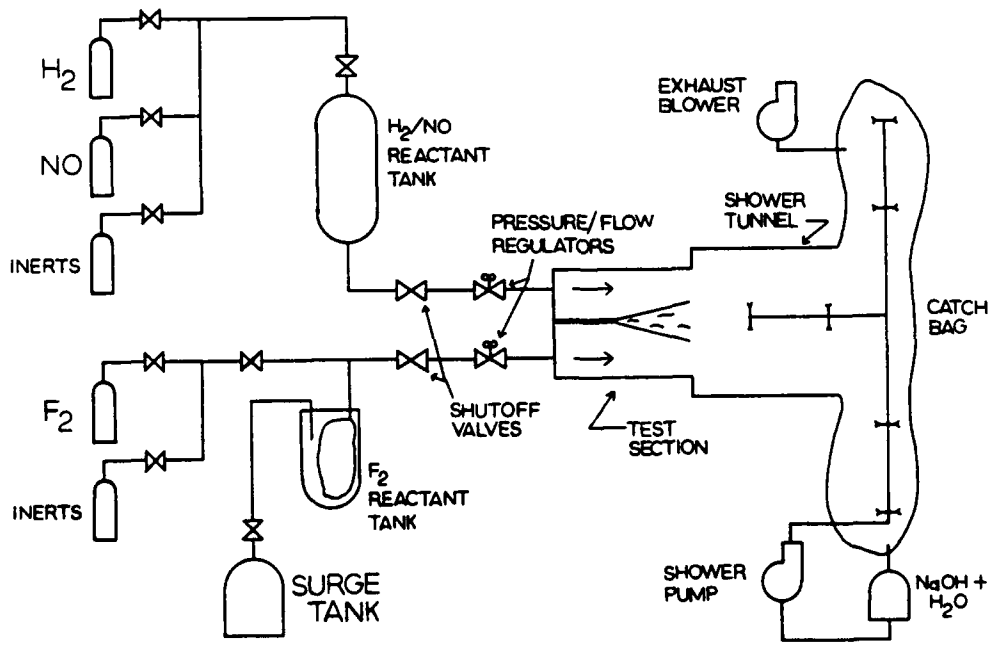

Fig. 2: Flow Schematic of the Supersonic Shear Layer Combustion Facility

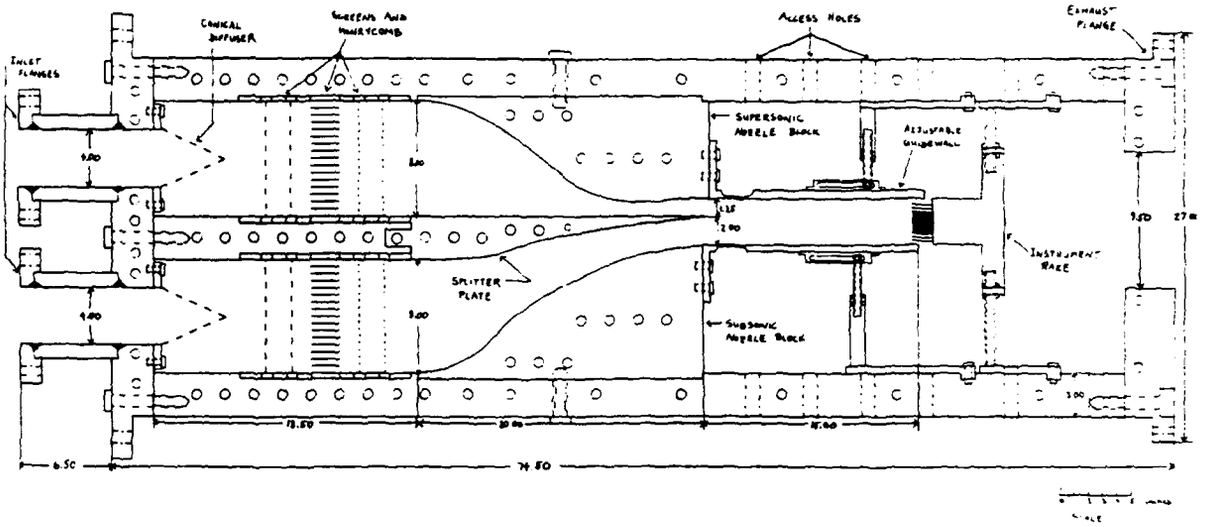

Fig. 3: Cross-sectional View of Test Section

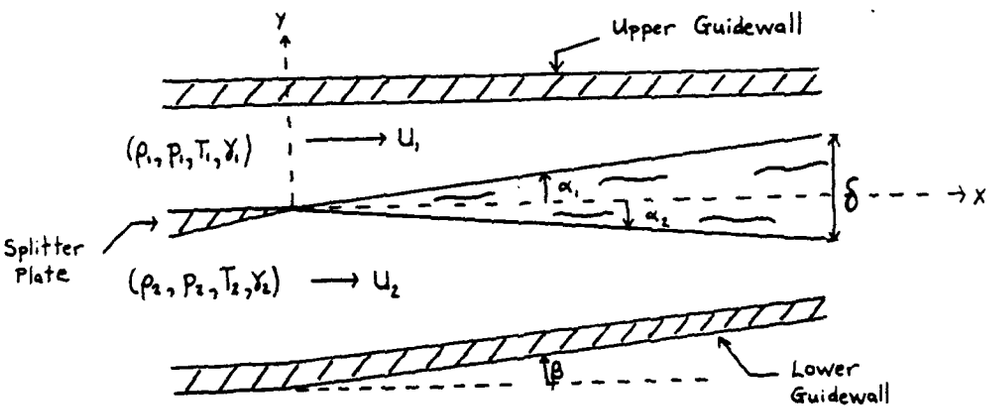

Fig. 4: Shear Layer Geometry

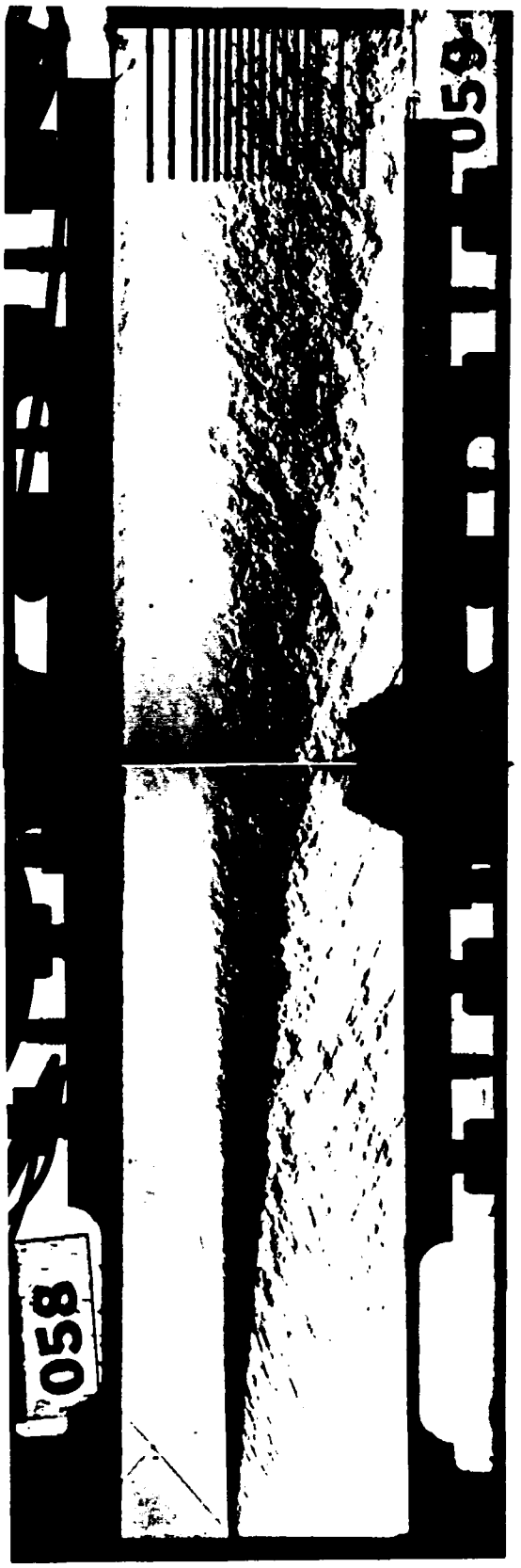

Fig. 5: Side-View Schlieren Photograph of Case 1 (He/Ar) Flow.

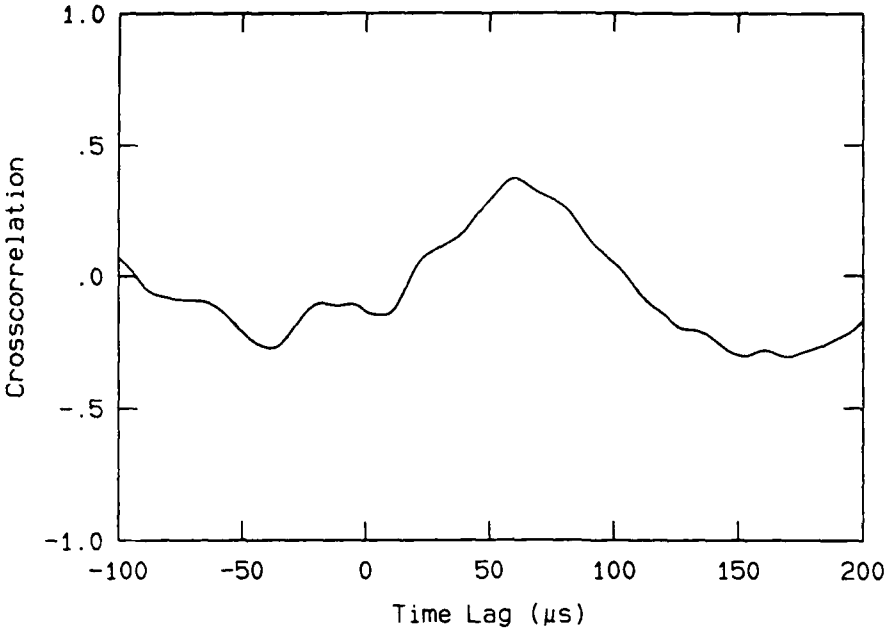

Fig. 6: Crosscorrelation Of Guidewall Pressure Transducers.

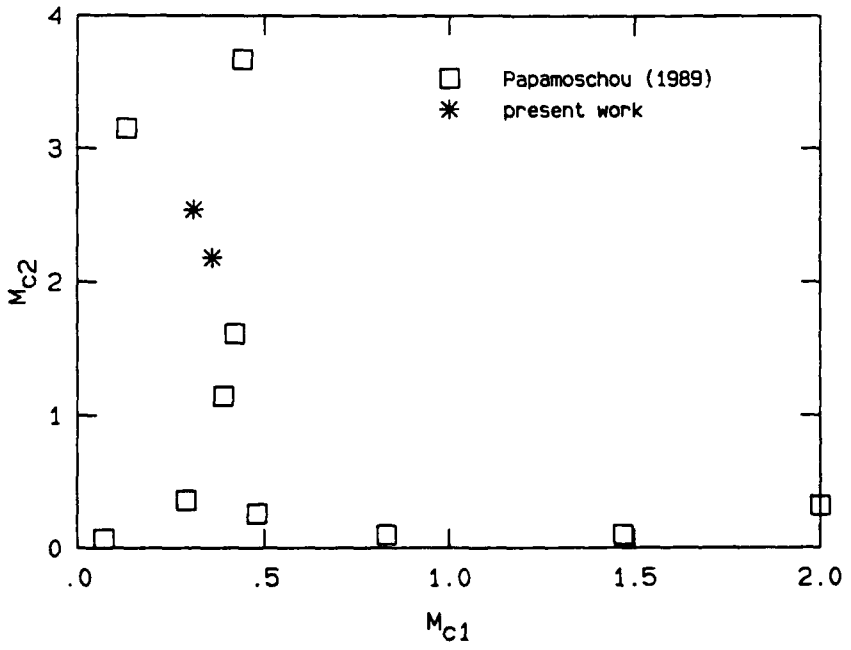

Fig. 7: Measured Convective Mach Numbers
Plotted With Papamoschou (1989) data.

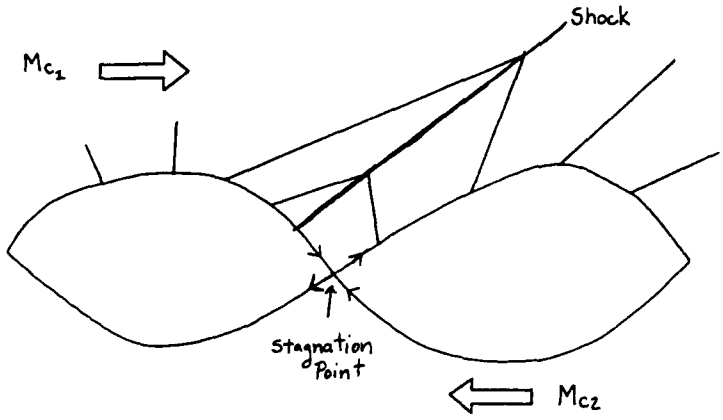

Fig. 8: Model For Shear Layer Recompression Shock (from Papamoschou 1989)

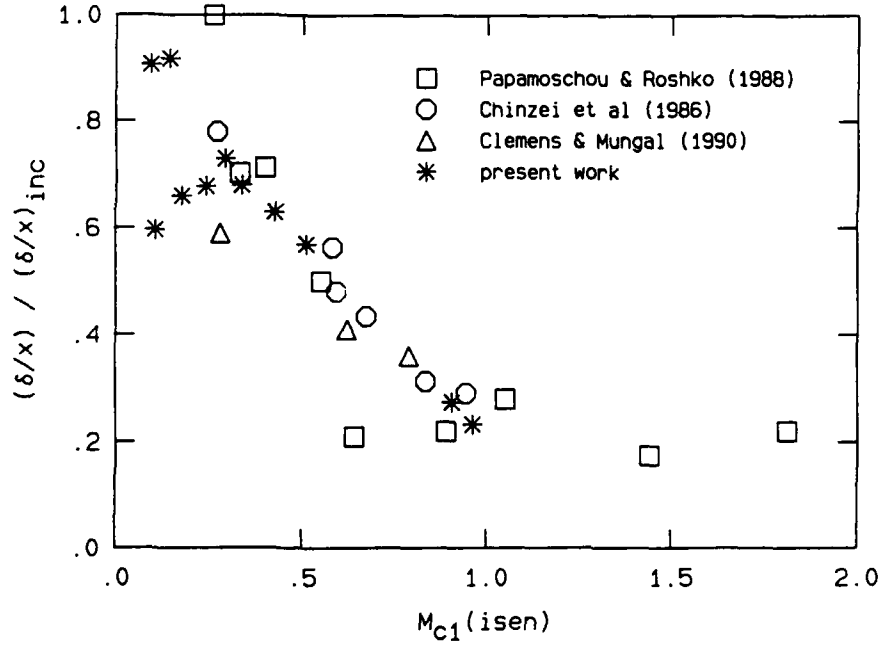

Fig. 9: Normalized Growth Rate Of All Cases Plotted With Other Available Data.

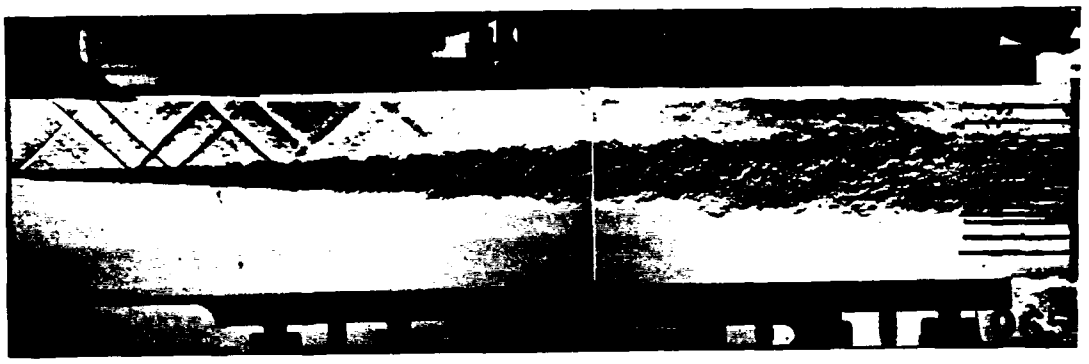

(a) Case 6

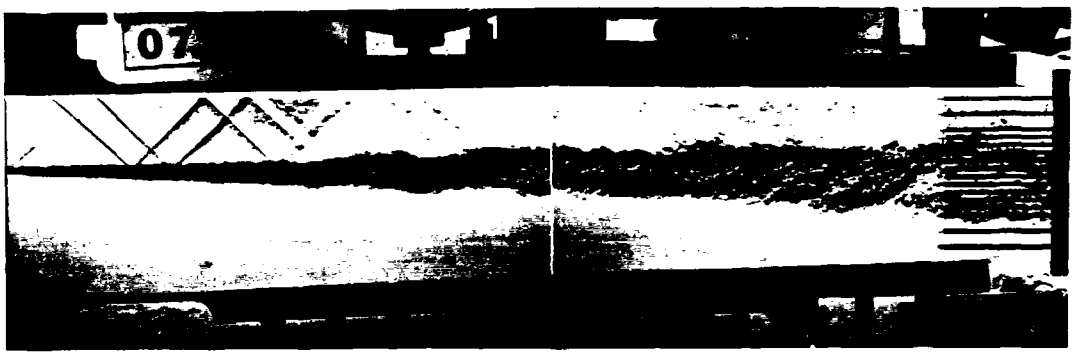

(b) Case 7

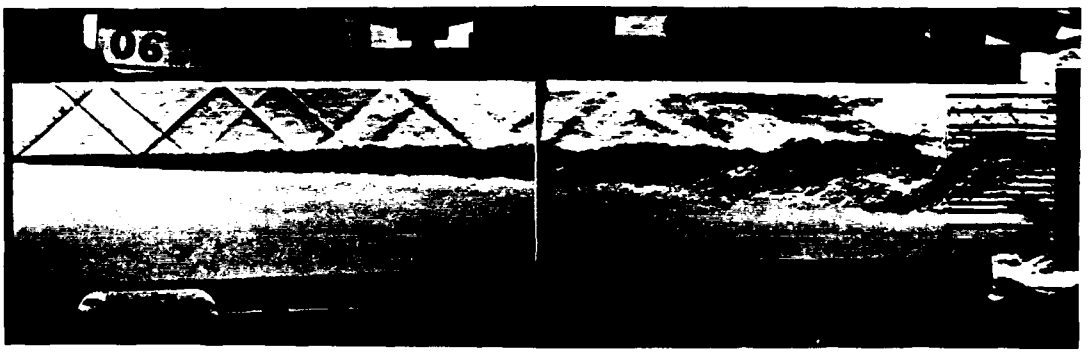

(c) Case 8

(d) Case 9

Fig. 10: Side-View Schlieren Photographs of Cases 6-9.

(a) Growth Rate Insensitivity

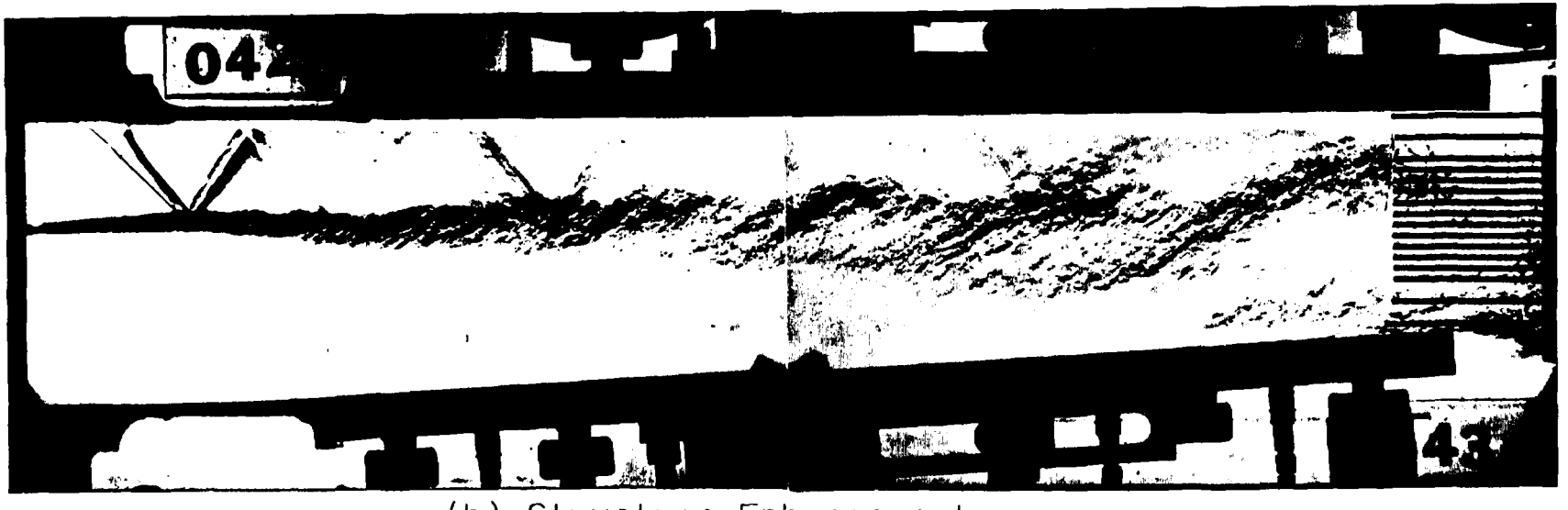

(b) Structure Enhancement

Fig. 11: Side-View Schlieren Photographs of Two Off-Design Case 3 Flows.

Appendix C

DIMOTAKIS, P. E. [1991] "On the convection velocity of turbulent structures in supersonic shear layers," *AIAA* 22nd *Fluid Dynamics, Plasma Dynamics and Lasers Conference*, Paper 91–1724.

AIAA 91–1724

On the Convection Velocity of Turbulent Structures in Supersonic Shear Layers

Paul E. Dimotakis

California Institute of Technology

Pasadena, CA

AIAA 22nd Fluid Dynamics, Plasma Dynamics & Lasers Conference

June 24-26, 1991 / Honolulu, Hawaii

On the Convection Velocity of Turbulent Structures in Supersonic Shear Layers*

by,

Paul E. Dimotakis**

Graduate Aeronautical Laboratories
California Institute of Technology
Pasadena, California 91125

Abstract

An ansatz is proposed, complemented by appropriate selection rules, to estimate the convection velocity U_c of turbulent vortical structures in low Mach number, supersonic shear layers. The proposed scheme assumes that, for low supersonic convective Mach numbers, shocks will form in one of the two shear layer free streams. The strength of the shocks is estimated by assuming that the flow configuration, in a frame moving at the convection velocity U_c, is stationary with respect to perturbations in the mean flow quantities caused by the turbulent fluctuations. Given the shock strength, the convection velocity U_c and the associated convective Mach numbers are calculated by matching the estimated total pressure at stagnation points in the convected frame. Presently available data indicate a convection velocity U_c that is close to U_1, or U_2, the high and low speed stream velocities, respectively, with an empirical stream selection rule that U_c is closer to U_1, when the low speed stream is subsonic, and closer to U_2 when both streams are supersonic. With the proviso that the predicted shock-bearing stream is as suggested by the empirical stream selection rule, the experimentally observed values for U_c appear to be well accounted for by the proposed scheme. These results have important implications for supersonic mixing and hypersonic propulsion applications.

** Professor, Aeronautics & Applied Physics, Associate Fellow AIAA.

Introduction

Recent experiments in compressible flow shear layers indicate that the convection velocity U_c of turbulent structures in two-dimensional, supersonic shear layers is much closer to the high or low speed free stream velocities, U_1 or U_2, respectively, than has been found to be the case in subsonic shear layers (Papamoschou 1989a, Fourguette *et al.* 1990, Hall *et al.* 1991). These data suggest that, at least for supersonic shear layers with Mach numbers that are not too high, the flow drives U_c to be close to U_1, when the low speed stream is subsonic, and closer to U_2 when the both streams are supersonic.

It is easy to appreciate that temporal shear layer growth models, or models that limit the description to one in a frame convected with the large scale flow structures, are not likely to capture such a stream selection rule. If borne out by further experimentation, such a rule can only stem from the fact that the flow, in the case of a subsonic low speed stream, *i.e.*, $M_1 > 1$ but $M_2 < 1$, contains an elliptical region connecting the downstream exit with the inflow low speed stream nozzle, whereas in the latter case ($M_1 > 1$, $M_2 > 1$) the flow is purely hyperbolic (Dimotakis 1989, Papamoschou 1989b).

An important attribute of the turbulent structure convection velocity is the proposed role it plays in the shear layer entrainment process. Specifically, it was proposed that E_v, the volumetric entrainment ratio in spatially growing mixing layers, *i.e.*, the entrained volume (flux) of high speed fluid fluid per unit volume flux of low speed fluid can be estimated as

$$E_v \approx \frac{U_1 - U_c}{U_c - U_2} \left(1 + \frac{\ell}{x}\right) , \tag{1a}$$

where ℓ/x is the local large scale structure streamwise extent-to-position ratio (Dimotakis 1984). Note that, given the volumetric entrainment ratio E_v, the mass flux entrainment ratio would be given by

$$E_m = \frac{\rho_1}{\rho_2} E_v , \tag{1b}$$

while the molar entrainment ratio would be given by (assuming the ideal gas law)

$$E_n = \frac{p_1 T_2}{p_2 T_1} E_v , \tag{1c}$$

where ρ_j, p_j and T_j denote the (static) density, pressure and temperature of the j^{th} free stream.

The large structure streamwise extent ℓ is expected to be of the order of the local transverse extent (visual thickness) of the layer δ, *i.e.*,

$$\frac{\ell}{x} \approx C_\ell \frac{\delta}{x} , \tag{2a}$$

with subsonic experiments yielding a value for the constant of proportionality of

$$C_\ell \approx 2 . \tag{2b}$$

It was recently suggested (Clemens & Mungal 1990) that the fact that compressible shear layers do not appear to be characterized by two-dimensional, spanwise coherent structures may render the validity of the use of the expression in Eq. 1, for example, questionable. To address this issue, a brief review of the arguments that lead to this expression may be useful.

The first factor in Eq. 1a derives from the induction velocity ratio and scales the relative shear sustained between the turbulent structures and the corresponding free stream. No relative velocity, no shear, no entrainment†. Under supersonic flow conditions and the possible presence of shocks on one side of the turbulent structures or the other (but not both), the symmetry expected under subsonic flow conditions, with respect to the high and low speed stream in the vortical structure convecting frame, would be lost. Nevertheless, the relative velocity ($\approx$ shear) ratio should come close to scaling the volumetric entrainment ratio (Dimotakis 1984).

The second factor in Eq. 1a is a consequence of the geometry of the spatially growing layer and of the large scale structures that dominate the entrainment process. It should be noted that the large scale flow structures are assumed to be basically vortical, not necessarily two-dimensional, for the second factor to represent a reasonable estimate of this effect. The second factor plays an important role in subsonic shear layers and, indeed, accounts for the observed asymmetries in E_v for the case of equal free stream density ($\rho_1 = \rho_2$) subsonic shear layers, for which $U_1 - U_c \approx U_c - U_2$. Nevertheless, it is not expected to contribute to asymmetries that are as significant, as the convective Mach numbers of the flow rise. This is a consequence of the likely dependence on the ratio of the flow structure size to the streamwise coordinate and the decrease in the growth rate δ/x with increasing convective Mach number, as documented by Papamoschou & Roshko (1988) and others (*cf.* Eq. 2). See also discussion in Dimotakis (1989).

---

† It should be recognized that this may not represent a consensus opinion. See, for example, discussion in Ferri *et al.* (1962) and Ferri (1973).

These arguments lead us to conclude that the considerable asymmetries in U_c, with respect to the free stream velocities that have been documented, should be expected to be responsible for corresponding asymmetries in the volumetric entrainment ratio E_v. This has important consequences for supersonic mixing and combustion applications, with the resulting stoichiometry of the mixed fluid potentially substantially different than what would be predicted on the basis of conventional models of turbulent entrainment and mixing.

For subsonic shear layers, experimental data and computations support the proposal that the convection velocity can be estimated by matching the total pressures realized, from each of the free streams, on interstitial stagnation points in between the large scale vortical structures in the convective frame (Coles 1981). The experimental data also support the notion that the respective stagnation pressures p_s can be estimated by applying the Bernoulli equation for each stream (Dimotakis 1984, Coles 1985), *i.e.*,

$$p_s = p_1 + \frac{1}{2}\left(U_1 - U_c^{(i)}\right)^2 = p_2 + \frac{1}{2}\left(U_c^{(i)} - U_2\right)^2 . \tag{3a}$$

At higher, but still subsonic, convective Mach numbers, the convection velocity can be estimated by using the corresponding compressible isentropic pressure recovery relations for the pressure p_s at the stagnation point (Bogdanoff 1983, Papamoschou & Roshko 1988, Papamoschou 1989a, Dimotakis 1989), *i.e.*,

$$p_s = p_1\left[1 + \frac{\gamma_1 - 1}{2}\left(\frac{U_1 - U_c^{(i)}}{a_1}\right)^2\right]^{\frac{\gamma_1}{\gamma_1 - 1}} = p_2\left[1 + \frac{\gamma_2 - 1}{2}\left(\frac{U_c^{(i)} - U_2}{a_2}\right)^2\right]^{\frac{\gamma_2}{\gamma_2 - 1}} . \tag{3b}$$

The quantity $U_c^{(i)}$ in these expressions denotes the turbulent structure convection velocity, as estimated assuming matched free stream static pressures, *i.e.*, $p_1 \approx p_2$, and an equal fraction of the isentropic total pressure recovered from each stream at the convected stagnation points, as above.

It may be interesting to ask for input on this issue from linear stability analyses of this flow, with the appreciation that finite amplitude wave effects, such as the loss in total pressure attendant on entropy production in shock waves, cannot properly be captured by linear stability analysis. Nevertheless, the very small entropy generation from weak oblique shocks, as would be expected under many flow conditions, might render linear stability analysis results useful for convective Mach numbers that are not too high.

Both temporal and spatial stability analyses have appeared recently, for both free (unbounded) flow (*e.g.*, Jackson & Grosch 1988, 1989, 1990; Ragab & Wu 1989a, 1989b; Sandham & Reynolds 1989a, 1989b, 1990; Zhuang *et al.* 1988) and bounded flow (*e.g.*, Tam

& Hu 1988; Tam & Hu 1989; Zhuang *et al.* 1989). Unfortunately, no consensus exists as to how the convection velocity of the flow structures is to be estimated using linear stability analysis results. Some investigators have suggested that the phase velocity of the most unstable mode can be used to provide an estimate (*e.g.*, Zhuang *et al.* 1988), while others have used the phase velocity at the neutral point of the solution branch of the most unstable mode (Sandham & Reynolds 1989b).‡ These analyses suggest that, under supersonic flow conditions, an unbounded shear layer can support more than one mode, *i.e.*, a "fast mode" with a convection velocity U_c higher than the isentropically estimated value $U_c^{(i)}$ (Eq. 3b), and a "slow mode" with $U_c < U_c^{(i)}$. Sandham & Reynolds (1989b, Fig. 2.25) have made a comparison of the convective Mach numbers estimated in this fashion (temporally growing, unbounded shear layers) with the data of Papamoschou (1989a).

The agreement at low convective Mach numbers is quite good, also correctly making the selection of the stream that U_c is closest to. At higher convective Mach numbers, however, the linear stability analysis calculations underestimate the departure of the convection velocity from the isentropically computed values (Eq. 3b). In fact, at the highest convective Mach number run of Papamoschou (1989a), the temporal, linear stability analysis predicts a U_c that is closer to U_2 than U_1, at variance with the data and the stream selection rule. This is as one would perhaps anticipate, *i.e.*, in keeping with the caveat that entropy (and total pressure) losses cannot be ignored at high (convective) Mach numbers, where finite amplitude wave effects are expected.

The situation in bounded, two-dimensional shear layers is more complicated, with many more unstable modes possible, some with $U_c > U_c^{(i)}$ and some with $U_c < U_c^{(i)}$. It is also not clear, in this case, how the convection velocity would be estimated using the neutral point phase velocity proposal of Sandham & Reynolds (1989b), as the dispersion relation solution branch of the most unstable mode typically crosses those of many other modes before reaching neutral stability.

Tam (1971) has reported the results of jet experiments and linear stability analysis of the cylindrical shear layer region of pressure-matched, supersonic jets ($M_1 = M_{jet}$). These include both nitrogen ($2.47 \leq M_{jet} \leq 2.92$) and helium ($1.44 \leq M_{jet} \leq 1.96$) jets exhausting in air. The agreement between observations and his stability analysis, which evaluated the wave angles away from the shear layer region directly, is very good and applies to both helium and nitrogen jets, corresponding to low and high Mach number core flows, respectively. These experiments, as well as other supersonic jet experiments (*e.g.*, Lowson & Ollerhead 1968, Oertel 1979), also support the empirical rule of a convection velocity U_c that is close to U_1, with shocks generated in the low speed stream, if $M_2 < 1$.

‡ It should be noted, however, that, for unbounded flows and as long as the convective Mach numbers are low, the differences in the actual values derived using these different estimates are not large.

It is noted, however, that Oertel (1979) reports that, at the highest jet Mach numbers he investigated, *two* sets of waves could be present, *i.e.*, one in each free stream, even though he recognizes that his experiments are not definitive on that score.

The convection velocity in the presence of shocks

To extend the estimation of the convection velocity to higher flow Mach numbers we must recognize that the (convective) Mach numbers, M_{c1} and M_{c2}, corresponding to the relative velocity of each of the free streams in the convective frame of the turbulent structures, *i.e.*,

$$M_{c1} = \frac{U_1 - U_c}{a_1} \qquad \text{and} \qquad M_{c2} = \frac{U_c - U_2}{a_2} \tag{4}$$

(Papamoschou & Roshko 1988), in which a_j denotes the speed of sound in the corresponding free stream, can approach, or exceed, unity. Under those conditions, the flow can support shocks across which the loss in total pressure may no longer be negligible. It can then be expected that the isentropic assumptions that were used to estimate the total pressure and, by extension, the convection velocity U_c at lower Mach numbers, will fail.

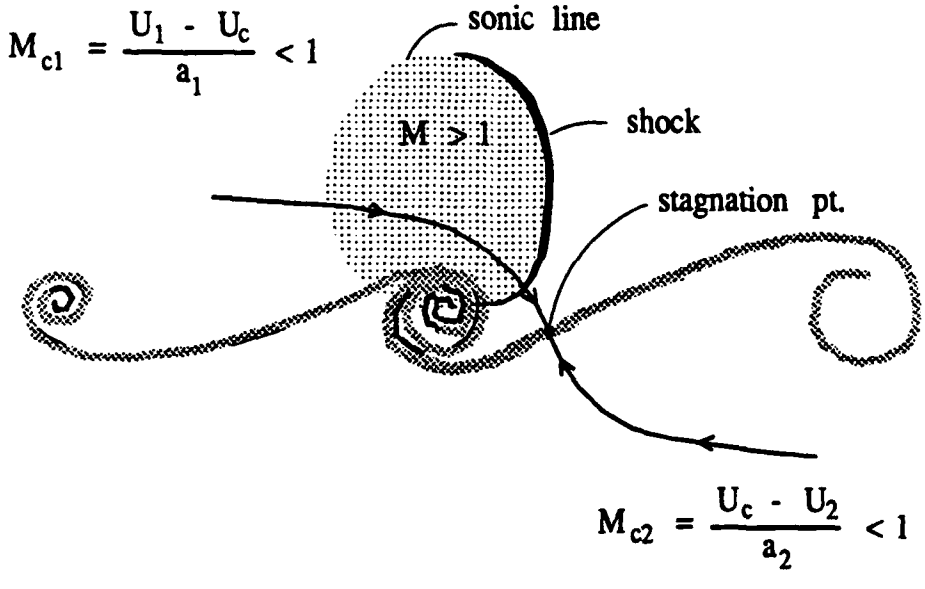

FIG. 1a Proposed vortex/shock configuration cartoon, sketched for a shock borne by the high speed stream and a transonic convective Mach number ($M_{c1} < 1$).

It has been argued that, to the extent that shocks can be borne on one side of the layer only, the large associated asymmetric losses in total pressure can be responsible for the large asymmetries in the observed behavior of the convection velocity U_c of the turbulent structures (Papamoschou 1989a, Dimotakis 1989). Evidence for the formation of shocks can be found in the calculations of Lele (1989), and Vandromme & Haminh (1989, *e.g.* Fig. 2), for example, for transonic convective Mach numbers where one expects weak shocks (dubbed "shocklets") confined to the vicinity of the shear zone. See Fig. 1a. No experimental evidence for these transonic shocklets is available at this writing.

For supersonic convective Mach numbers, experimental evidence has been available for turbulent-structure-generated shocks from the core region of supersonic jets, *i.e.*, Lowson & Ollerhead (1964), Tam (1971), and Oertel (1979). More recently such evidence has been documented for a two-dimensional, supersonic shear layer in Hall *et al.* (1991) and Hall (1991). In the Hall *et al.* experiments, a shock/expansion wave system extending into one of the free streams, as sketched in Fig. 1b, was found. An example of such a wave system, for a $M_1 = 1.5$ He high speed stream, over $M_2 = 0.35$ Ar low speed stream shear layer, is reproduced in Fig. 2 (from Hall *et al.* 1991, Fig. 5). See also Hall (1991, Fig. 4.11) for corresponding data for a $M_1 = 1.5$ He high speed stream, over $M_2 = 0.3$ N_2 low speed stream shear layer.

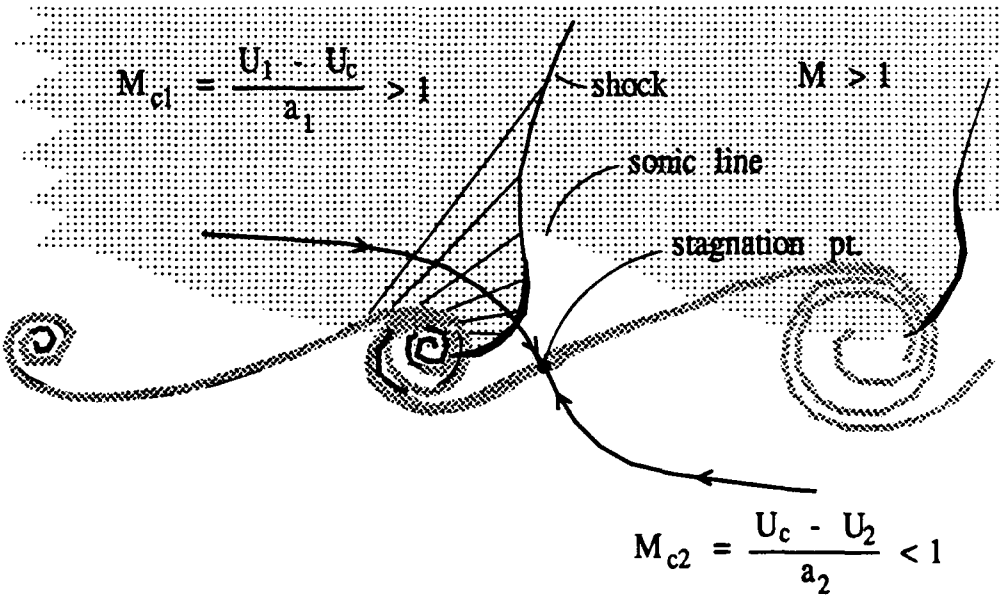

FIG. 1b Proposed supersonic vortex/shock configuration cartoon, sketched for a supersonic convective Mach number ($M_{c1} > 1$).

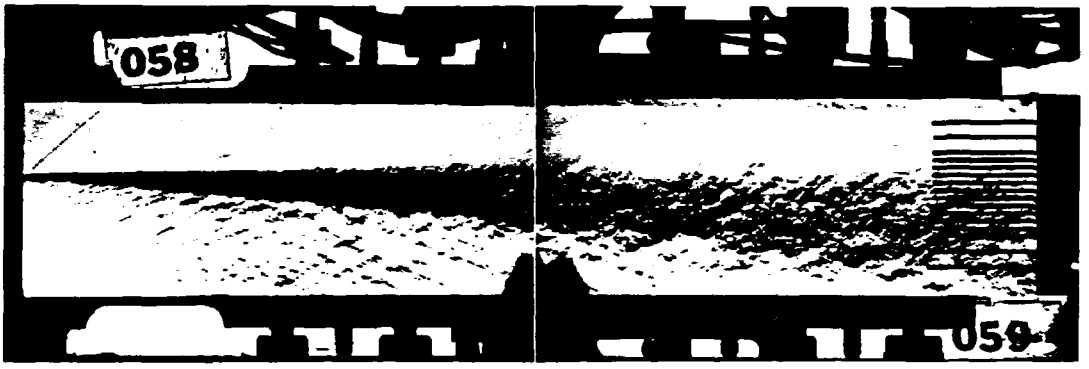

FIG. 2 Schlieren data for a $M_1 = 1.5$ [He] high speed stream, over $M_2 = 0.35$ [Ar] low speed stream shear layer. Note travelling oblique shock system in low speed stream (Hall *et al.* 1991, Fig. 5).

The difficulty with performing *ab initio* calculations of the convection velocity, including the effects of shocks, is that the results depend on the shock Mach number, M_s, corresponding to the normal velocity component before the shock, which cannot be estimated *a priori* (Papamoschou 1989a). It was suggested (Dimotakis 1989) that useful estimates could be made, at least of the qualitative behavior, by assuming that the normal shock Mach number could be approximated by the convective Mach number with respect to the corresponding free stream. Unfortunately, this assumption does not, in fact, explain the observed behavior.[‡] In the case of shocks, the problem of estimating the ratio X_j of the normal shock Mach number to the corresponding free stream Mach number in the j^{th} free stream, *i.e.*, $X_j = M_{sj}/M_{cj}$, where the subscript j denotes the stream that carries the shock(s), requires additional information.

‡ A coding error in the implementation of that proposal (Dimotakis 1989) masked the actual consequences of that assumption, yielding estimates for the convection velocity which happened to be qualitatively close to observations.

Estimating the shock Mach number

In what follows, it will be assumed that the fundamental turbulent structure in supersonic shear layers remains basically vortical. The presently available evidence suggests that the two-dimensional (spanwise coherent) structures of Brown & Roshko (1974) are not the prevalent mode under supersonic flow conditions. See, for example, results and discussion in Clemens *et al.* (1990) and Clemens & Mungal (1990), but also the analyses of Tam & Hu (1989) and Zhuang *et al.* (1990). Nevertheless, there is also evidence that the structure that is there is not small in scale, with a typical streamwise extent that is of the order of the local shear layer width. See Clemens *et al.* (1990), Fourguette *et al.* (1990), and Hall *et al.* (1991).* We will return to this issue later.

The proposed model will also be implemented assuming that the flow can be treated as unbounded. We will ignore, in other words, any influence on the convection velocity of the turbulent structures exerted by the presence of the guidewalls employed to confine the supersonic shear flow.

Finally, to repeat, it is not expected that an analysis based solely on the temporal behavior of the large scale structures in the convected frame can capture the (laboratory frame) empirical selection rule for the stream that carries the shocks suggested by the data to date. In particular, the empirical finding that shocks are carried by the low speed stream for ($M_1 > 1$, $M_2 < 1$), and by the high speed stream for ($M_1 > 1$, $M_2 > 1$). Pending further clarification of this issue, the proposed scheme should then be used when its results are in accord with this empirical rule.

In the case where the flow can support a shock in one of the two free streams, the flow ahead of the shock would be turned *via* an (almost) isentropic expansion before crossing the shock to enter the subsonic region in the neighborhood of the stagnation point ahead of the vortical structure. Two possibilities arise. For transonic convective Mach numbers, a supersonic bubble can exist in the vicinity of the vortical structure, as on the lifting side of a transonic airfoil, with a shock wave ahead of the stagnation point joining the sonic line to enclose the bubble. See cartoon in Fig. 1a. For supersonic Mach numbers, the region of supersonic flow — and the shock/expansion wave system — will extend to the far field, as noted in the cartoon in Fig. 1b and as seen in the schlieren data in Fig. 2.

As the velocities behind the shock(s) must be low — in fact zero at the stagnation point in the convective frame — the total pressure loss should be well approximated by

* Note that the characteristic spacing of the foot of the wave system local extent on the shear layer edge in Fig. 2 is comparable to the local shear layer width $\delta(x)$.

that of a normal shock. In that case, it should be possible to estimate p_s, the total pressure realized at the stagnation point, using the Rayleigh pitot tube formula, *i.e.*,

$$\frac{p_s}{p} = \left(\frac{\gamma+1}{2} M_s^2\right)^{\gamma/(\gamma-1)} \left(\frac{2\gamma}{\gamma+1} M_s^2 - \frac{\gamma-1}{\gamma+1}\right)^{-1/(\gamma-1)}$$

where p is the free stream static pressure and M_s is the shock Mach number (*e.g.*, Liepmann & Roshko 1957, p. 149). With these assumptions, the strength of the shock can be estimated if the angle $\Delta\theta$ through which the flow has been expanded is known. The turning angle $\Delta\theta_j$ in the j^{th} stream can be estimated, in turn, as the difference of the corresponding Prandtl-Meyer angles between the flow just ahead of the shock and the free stream (or sonic conditions), *i.e.*,

$$\Delta\theta_j = \theta_{\text{PM}}(M_{sj}) - \theta_{\text{PM}}(M_{cj}), \qquad \text{for} \qquad M_{cj} \geq 1 , \tag{5a}$$

where,

$$\theta_{\text{PM}}(M) \equiv \sqrt{\frac{\gamma+1}{\gamma-1}} \operatorname{atan}\left[\sqrt{\frac{\gamma-1}{\gamma+1}}\,(M^2-1)\right] - \operatorname{atan}\sqrt{M^2-1} \tag{5b}$$

defined for $M > 1$, is the Prandtl-Meyer angle function (*e.g.*, Liepmann & Roshko 1957, p. 99). If the convective Mach number M_{cj} in the j^{th} stream is close to, but less than, unity (transonic M_{cj}), the turning angle $\Delta\theta_j$ will be computed using

$$\Delta\theta_j = \theta_{\text{PM}}(M_{sj}) , \qquad \text{for} \qquad M_{cj} < 1 . \tag{5c}$$

The latter is equivalent to starting the calculation at the location where the streamline crosses the sonic line to enter the supersonic bubble. See Fig. 1a.

Depending on the flow parameters, the pressure matching condition can lead to several solution branches. Given the free stream that carries the shock and the shock strength, several branches will typically exist, with a continuum of solutions for the convection velocity U_c as a function of the shock strength parameter X. The ansatz proposed here is that *the convection velocity of the large scale structures is such as to render the flow stationary*. One can argue for this conjecture by noting that if the flow structure depicted in Figs. 1a,b is to represent a quasi-steady, convecting flow configuration, it must survive the small scale turbulent fluctuations which can be regarded as continuously disturbing it.

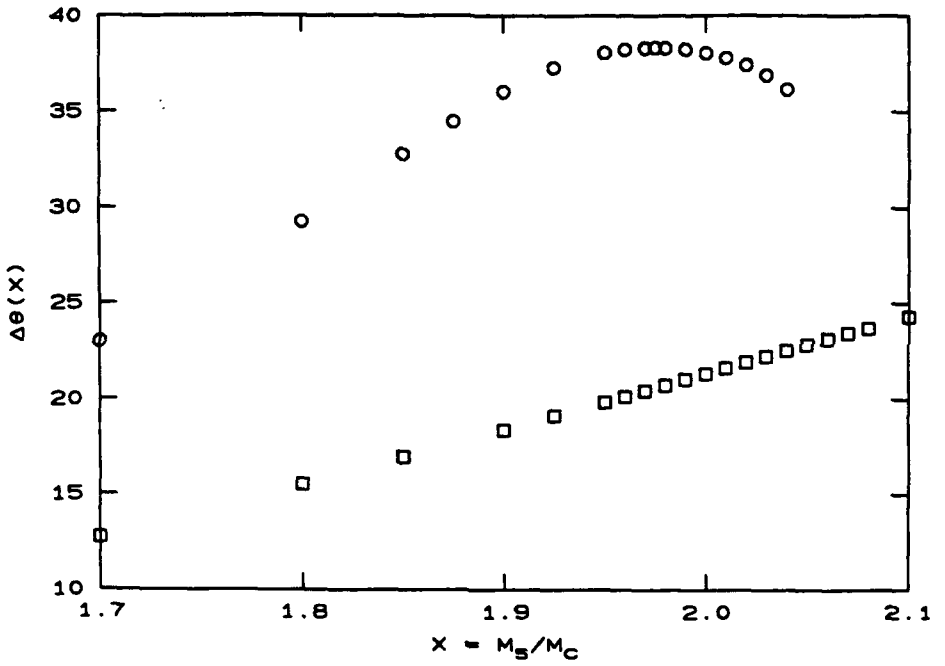

FIG. 3 Flow turning angle $\Delta\theta$, as a function of the shock strength parameter $X = M_s/M_c$. Squares: high speed stream shock. Circles: low speed stream shock. Flow parameters: $M_1 = 1.5\,[\mathrm{He}]$, $M_2 = 0.3\,[\mathrm{N_2}]$ (see Fig. 2) — Type I flow. Stationary solution ($\max\{\Delta\theta\}$) with low speed stream ($j = 2$) shock with $X_2 = 1.975$.

When the flow is computed as a function of the shock strength parameter $X_j = M_{sj}/M_{cj}$, corresponding to a shock in the j^{th} stream, one finds that the solution branches fall into two classes. In the first solution class, Type I flow, the turning angle $\Delta\theta$ can be computed by assuming that the flow chooses the stream j and the shock Mach number, *i.e.*, the shock strength parameter $X_j = M_{sj}/M_{cj}$, so as to render the turning angle $\Delta\theta_j$ stationary (a maximum). This corresponds to a stable flow configuration wherein small changes in the shock Mach number M_{sj} result in quadratically small changes in $\Delta\theta_j$. Alternatively, in Type II solutions, it is the shock strength parameter X_j that is stationary with respect to small changes in the turning angle $\Delta\theta$, corresponding to the maximum admissible value for X_j that yields a solution for U_c.

Satisfying the pressure matching condition as a function of the convection velocity U_c classifies the solutions as Type I or Type II. It is found, however, that both types of solutions can be admissible (in the same flow). In the latter case, one can argue for a selection rule which favors the Type I branch, over the Type II solution branch, as being the more robust configuration of the two. If more than one solution branch of the same type is possible, the proposed selection rule is that the branch that yields the *lower* total pressure is chosen by the flow. In other words, the flow will try to satisfy the pressure matching condition at the lowest stagnation pressure possible, generating the shock with the requisite strength.

Figure 3 depicts the results of sample calculations of $\Delta\theta$ as a function of the shock strength parameter X, for a supersonic shear layer with $M_1 = 1.5$[He] and $M_2 = 0.3$[N_2] (Case 2 in Hall 1991, Fig. 4.11). In this figure, the squares were computed assuming that a shock is present in the high speed stream, while the circles were computed for a shock in the low speed stream. It can be seen that, for these flow parameters, the solution corresponds to a stationary point in which the turning angle is a maximum, *i.e.*, a Type I flow, with a shock borne by the low speed stream ($j = 2$) and a shock/convective Mach number ratio of $X_2 = 1.975$.

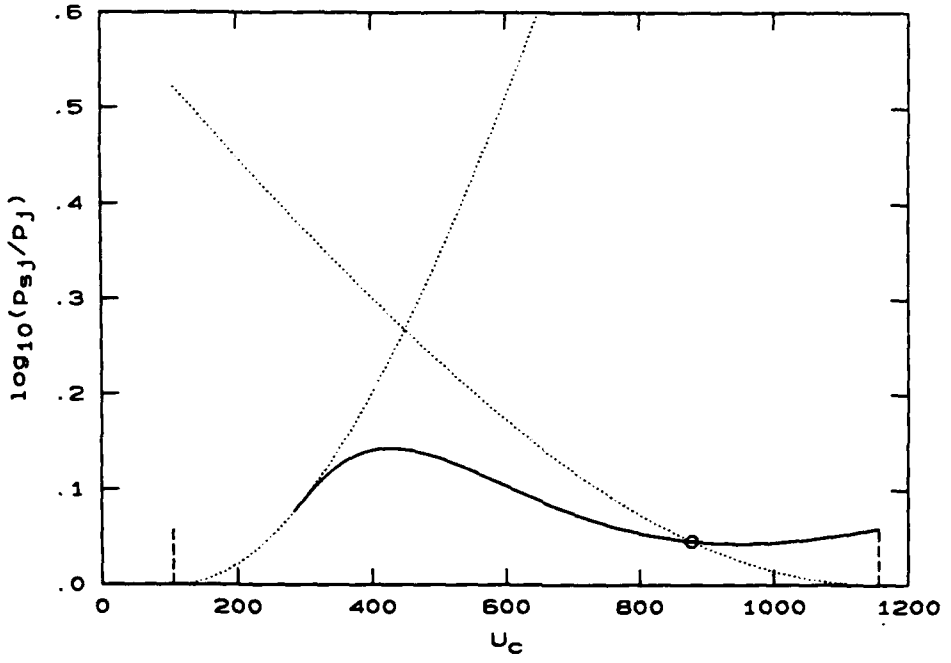

FIG. 4 Logarithm of total pressure from each stream as a function of convection velocity U_c. Dotted lines: isentropic recovery. Solid lines: pressure recovery through shocks. Flow conditions: $U_2/U_1 = 105/1160$ m/s and a low speed stream shock strength of $X_2 = 1.975$ (see Fig. 3). Solution of $U_c = 878$ m/s is indicated by circled point.

Figure 4 depicts the total pressure from each of the free streams, computed for this value of the shock strength parameter X_2. The dotted lines represent the isentropic pressure recovery from each free stream, while the solid lines represent the recovery pressure assuming shocks. The small vertical dashed line segments mark the free stream velocities $U_1 = 1160$ m/s and $U_2 = 105$ m/s. The solution point is indicated by the circled point of intersection of the two curves, yielding an estimate for the convection velocity of $U_c = 878$ m/s. This is much closer to the high speed stream velocity. The convective Mach numbers are $M_{c1} = 0.36$ and $M_{c2} = 2.2$.

These values are in good agreement with the Hall *et al.* (1991) observations of $2.1 \leq M_{c2} \leq 2.4$ for this flow, based on the shock angles in the schlieren flow visualization data (Fig. 2. In contrast, the convection velocity, as estimated from the isentropic relation for this flow, is given by $U_c^{(i)} = 449\,\mathrm{m/s}$, corresponding to a pair of much more closely matched (isentropically estimated) values of the convective Mach numbers ($M_{c1}^{(i)} = 0.917$ and $M_{c2}^{(i)} = 0.983$).

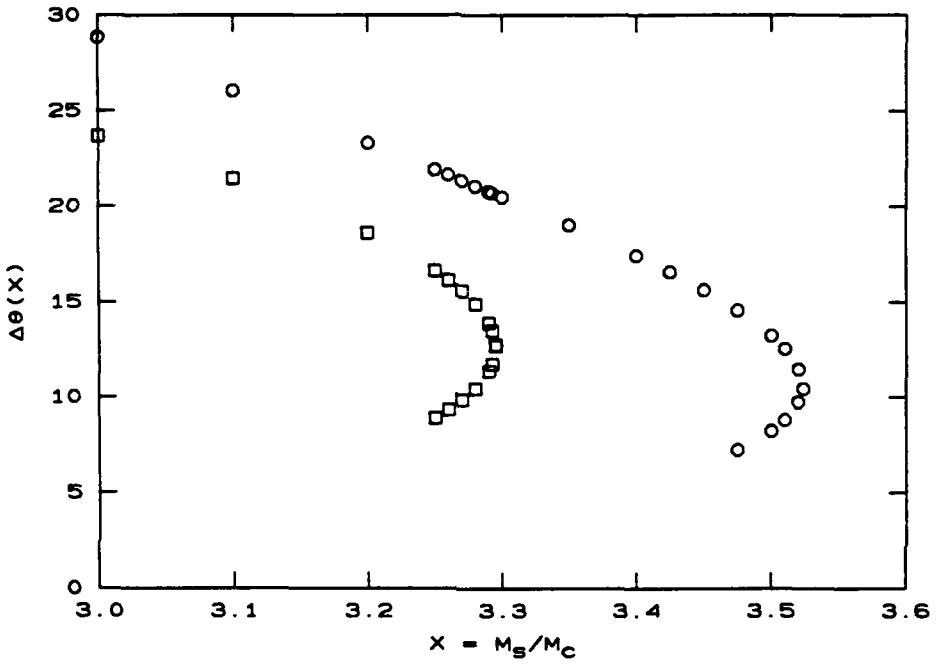

FIG. 5 Flow turning angle $\Delta\theta_j$, as a function of the shock strength parameter $X_j = M_{sj}/M_{cj}$. Supersonic shear layer: $M_1 = 2.8\,[\mathrm{N_2}]$, $M_2 = 2.6\,[\mathrm{Ar}]$. High speed stream shock denoted by squares and low speed stream shock by circles. Solution corresponds to the stationary point for a shock in the high speed stream ($j = 1$) at $X_1 = 3.295$ (Type II flow).

Figure 5 is computed for a supersonic shear layer with a $\mathrm{N_2}$, $M_1 = 2.8$, high speed stream and Ar, $M_2 = 2.6$, low speed stream (Papamoschou 1989a), as a second example. It can be seen that, in this case, two stationary points are possible, corresponding to maxima in the shock strength parameter with respect to the flow turning angle (Type II solutions). One derives from a shock wave in the high speed stream ($j = 1$) and a maximum in the shock strength parameter at $X_1 = 3.295$, while the other corresponds to a shock in the low speed stream ($j = 2$) and a shock strength parameter of $X_2 = 3.524$. Of these two, the solution with the shock in the high speed stream yields a lower stagnation (total) pressure ($p_s/p = 1.069$, *vs.* $p_s/p = 1.086$) and is the one accepted by the minimum stagnation pressure selection rule. This is also a transonic flow case (Fig. 1a), yielding values for the convective

Mach numbers of $M_{c1} = 0.47$ and $M_{c2} = 0.28$ differing by almost a factor of two, in good agreement with the values of 0.48 and 0.26, respectively, reported by Papamoschou (1989a). This represents an interesting flow. The isentropically estimated convective Mach numbers are, again, much closer to each other ($M_{c1}^{(i)} = 0.40$ and $M_{c2}^{(i)} = 0.36$) than the experimentally observed values. More significantly, they are rather low at these flow conditions. One might have argued that one should not expect any finite amplitude wave effects to speak of. Nevertheless, a Type II stationary solution exists with a rather large shock strength parameter ($X_1 = M_{s1}/M_{c1} \approx 3.3$), which the experiments suggest the flow has indeed availed itself of. Even so, the actual convective Mach numbers are in the transonic regime (Fig. 1a) with a shock Mach number estimated as $M_{s1} = X_1 M_{c1} \approx 1.5$. It should also be noted that the convective Mach numbers for this flow are also reasonably well accounted for by the Sandham & Reynolds (1989b, Fig. 2.25) stability analysis results.

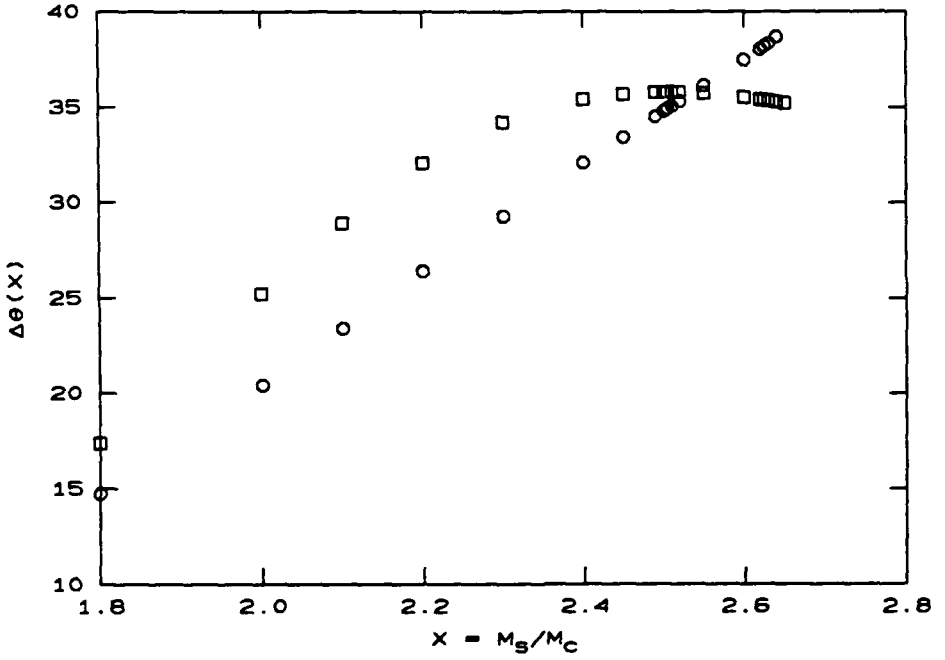

FIG. 6 Flow turning angle $\Delta\theta_j$, as a function of the shock strength parameter $X_j = M_{sj}/M_{cj}$. Supersonic shear layer: $M_1 = 3.2$[Ar], $M_2 = 0.2$[Ar]. High speed stream shock denoted by squares and low speed stream shock by circles. Predicted flow configuration corresponds to the stationary point with a shock in the high speed stream with $X_1 = 2.505$ (Type I flow). Experiments (Papamoschou 1989a) suggest that, for this flow, the shocks are borne by the *low* speed stream.

Finally, a case with a subsonic low speed stream will be discussed for which the proposed scheme predicts that the shock should be borne by the high speed stream, in contrast to the Papamoschou (1989a) data and the stream selection rule in this case. This is a supersonic shear layer with $M_1 = 3.2$[Ar] and $M_2 = 0.2$[Ar] for which Papamoschou reports

experimental estimates of $(M_{c1}, M_{c2})_{exp} = (0.39, 1.14)$. The $\Delta\theta_j(X_j)$ *vs.* $X_j = M_{sj}/M_{cj}$ plot computed for this flow is included in Fig. 6. It can be seen that this would suggest that a shock should be borne by the *high* speed stream (with a value for the shock strength parameter of $X_1 = 2.505$), corresponding to $(M_{c1}, M_{c2})_{th} = (1.94, 0.41)$. This is an interesting case because, as the $\Delta\theta_j(X_j)$ *vs.* $X_j = M_{sj}/M_{cj}$ plot would suggest, no other stationary configuration is predicted for this flow, other than the one with a high speed stream shock. One can only conclude that the elliptic nature of the flow in the low speed stream (Dimotakis 1989, Papamoschou 1989b) can impose additional constraints on the flow configuration. If such constraints are operative, they can, of course, not be accounted for in the temporal description (in a frame in which the flow structures are fixed) attempted here.

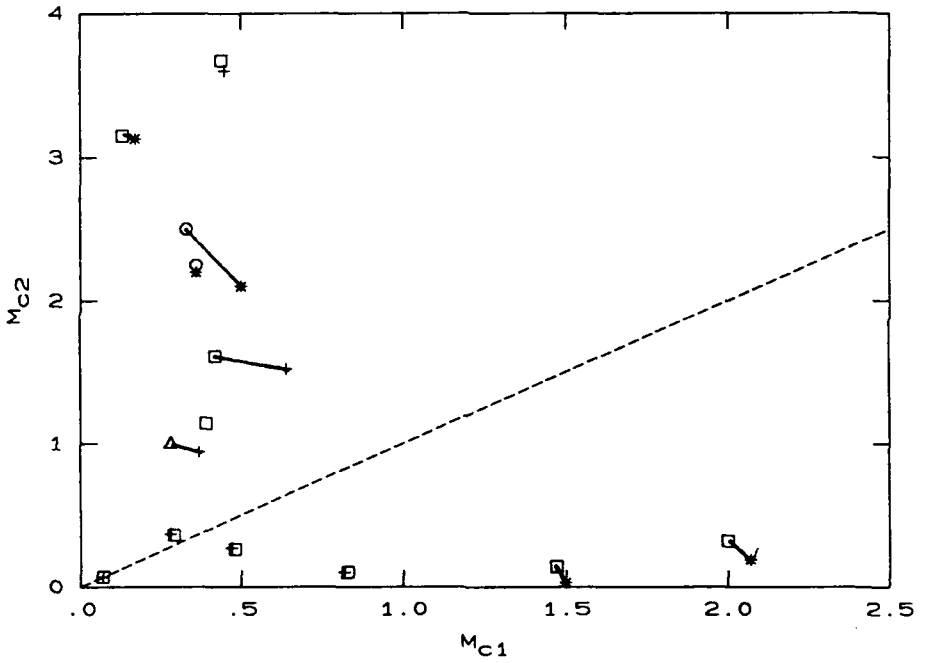

FIG. 7 Experimental data of (M_{c1}, M_{c2}) from Papamoschou (1989a, squares); Hall *et al.* (1991, circles); and Fourguette *et al.* (1990, triangle). Computed points are joined to corresponding flow data points by straight lines, corresponding to Type I (asterisks) and Type II (crosses) flows (see text).

The results of calculations based on the proposed scheme are summarized in Fig. 7, which is a composite plot of the (M_{c1}, M_{c2}) Papamoschou (1989a) data (squares), the Hall *et al.* (1991) data (circles), and the data point (triangle) by Fourguette *et al.* (1990)**. The estimates, based on the proposed scheme, for flows found to yield Type I solutions are

** The point (M_{c1}, M_{c2}) derived from the Fourguette *et al.* (1990) data was computed using the quoted (directly measured) value for the convection velocity of $U_c = 352\,\mathrm{m/s}$.

denoted by asterisks, while those corresponding to Type II solutions are denoted by crosses. If the computed values are found to fall outside the extent of the experimental data point symbols, they are joined to the corresponding data points by straight lines. The case where the stationary shock is borne by the stream not accord with the empirical stream selection rule is the $M_1 = 3.2\,[\mathrm{Ar}]$ and $M_2 = 0.2\,[\mathrm{Ar}]$ shear layer of Papamoschou (1989a) discussed above. No computed (M_{c1}, M_{c2}) point is indicated for it. It is interesting that the stability analysis of Sandham & Reynolds appears to predict the correct shock-bearing stream for this case, but predicts the wrong one for the flow with the highest M_{c2}. See Sandham & Reynolds (1989b, Fig. 2.25).

Discussion and conclusions

How can we reconcile the underlying thesis of the proposed theory based on the persistence of large-scale structures with interstitial stagnation points, with the experimental evidence (*cf.* Fig. 2)?

We first note that data of the type in Fig. 2 represent *spanwise* averages. Such data, in other words, do not preclude a flow structure that might *sectionally* be adequately approximated by the proposed cartoons. On the other hand, the little sectional (laser imaging) data presently available by Fourguette *et al.* (1990), some NO planar, laser-induced-fluorescence (PLIF) data by Clemens & Mungal (pvte. communication), as well as preliminary laser sheet Rayleigh imaging data in our laboratory (Rosemann *et al.*, unpublished) do suggest that the structure is indeed quite different from the pronounced two-dimensional vortical structure of Brown & Roshko (1984), as noted above.

If supersonic shear layer large scale structures can be described by the non-linear evolution of the superposition of *oblique* waves, we recognize that flow in the vicinity of the tip of the expected arrowhead-like structures, in that case, could be well approximated by stagnation point flow in the convected frame. The proposed analysis should then apply in that neighborhood and set the convection velocity of the resulting local "stagnation" region. Given that the rest of the structure can not overtake the arrowhead tip, the preceding analysis might then serve to define the convection velocity of the whole structure, even though the cartoon on which it is based may be unrepresentative of the flow as a whole.

In any event, it appears that the proposed cartoons, augmented with the ansatz of a shock strength that renders the flow stationary, coupled with the two selection rules, *i.e.*, of Type I over Type II branches (if both are present) and the choice of the solution that yields the lower stagnation pressure (if more than one solution is possible), can yield good quantitative estimates for the observed values of the convective Mach number, *provided it*

does not contradict the empirical stream selection rule that suggests that shocks will be borne by the low speed stream, if it is subsonic. The latter rule suggests that, for such flows, the existence of an elliptic region may be responsible for constraints which can override the principle of stationarity, as viewed in a vortex-fixed frame in which the dynamics can be described in terms of temporal growth. The proposal of stationarity for supersonic flow is also interesting in that it has no counterpart in subsonic, isentropic flow; the latter has no additional free parameter in satisfying the pressure matching condition.

Some of the implications of these results can be appreciated in the context of the discussion on shear layer entrainment outlined in the introduction. These points will be illustrated using the values derived from the experimental data and the results of these calculations for the Hall *et al.* (1991) supersonic shear layer data ($M_1 = 1.5\,[\mathrm{He}]$, $M_2 = 0.3\,[\mathrm{N_2}]$), as an example. For this shear layer, we might have predicted a relative velocity ratio, based on isentropic estimates†, of

$$\frac{U_1 - U_c^{(i)}}{U_c^{(i)} - U_2} \approx 2.1 \ . \tag{6a}$$

Instead, we have

$$\frac{U_1 - U_c}{U_c - U_2} \approx 0.36 \ , \tag{6b}$$

using the convection velocity estimate of $U_c \approx 880\,\mathrm{m/s}$ that is suggested by the data and also derived using the scheme proposed here. Ignoring, for the moment, the near unity $(1 + \ell/x)$ factor in Eq. 1, stemming from the spatial growth of the layer, this implies that such a layer, rather than being *high speed fluid rich* with a mean volumetric mixture ratio of high speed fluid to low speed fluid of roughly 2:1, can be expected to be *low speed fluid rich* with a volumetric ratio of roughly 1:3. There is almost a factor of 6 difference between the two estimates. Restoring the spatial growth factor in these calculations would result in small changes in the individual estimates, but would not substantially alter their ratio.

Before leaving this discussion, we should entertain the suggestion by Oertel (1979) that in supersonic jets at high enough Mach numbers one might expect shocks in both free streams (see also qualitative discussion in Dimotakis 1989). In this case, roughly symmetric turbulent structure convection velocities might be restored, with attendant implications for entrainment ratio, and supersonic shear layer mixing and combustion. Fortunately, this issue is likely to be resolved experimentally in the not-too-distant future. Several experimental efforts presently in progress, both in our laboratory and elsewhere, can be expected to yield supersonic shear layer data at higher relative free stream velocities yet.

---

† Recall Eq. 1 and related discussion and that $M_{c1}^{(i)}/M_{c2}^{(i)} = 0.917/0.983$ for this flow (see p. 13).

Accepting the proposed theoretical scheme, as well as the proposals on entrainment outlined in the introduction, at face value leads to some interesting implications for practical applications. Specifically, in addition to the asymmetries in entrainment that the data have already suggested should be anticipated, the proposed model further suggests that even small changes in the free stream parameters may be responsible for changing the stream that carries the shocks, under some flow conditions. Under these circumstances, gradual changes in the flow parameters can be expected to be potentially responsible for *jumps* in the flow configuration. In some cases, such large changes in the flow configuration can be expected to occur as a result of only small changes in flow velocity, composition, or stagnation temperature in one of the free streams. Such jumps would be responsible for correspondingly large changes in entrainment and, in turn, changes of the composition, chemical environment, chemical product formation and heat release in a combusting shear layer.

In closing, we should also note that the presence of turbulent-structure-generated shock waves in the free stream casts temporal evolution numerical simulations that utilize space-periodic boundary conditions in an interesting light. A moment's reflection over the cartoon in 1b will reveal that free stream particle paths that enter from the left to cross shock waves emerge and exit on the right with a different entropy. They can, therefore, not be reintroduced in a space-periodic fashion in the calculation if the simulation is to represent a quasi-stationary description of free stream conditions. In such a calculation, the entropy in the shock-bearing free stream will be continuously increasing. Such an increase will, of course, also occur in the spatially evolving flow. The point here is that temporally evolving, space-periodic flow of supersonic shear layers does not admit steady-state, *i.e.*, statistically quasi-time-independent, solutions. Spatially evolving flows have an important additional degree of freedom that can be exercised by tailoring the confining wall geometry so as to prescribe the local cross-sectional area available to the flow.

Acknowledgements

I would like to acknowledge many useful discussions with Prof. Dale Pullin that occurred in the course of the formulation of these ideas. I would also like to acknowledge the discussions with Jeff Hall and Henning Rosemann, that helped identify the coding error in the implementation of the previous analysis (Dimotakis 1989), the discussions and calculations with Chris Bond, as well as suggestions with the text by Paul Miller. This work was supported by the Air Breathing Propulsion program of the Air Force Office of Scientific Research, Grants 88–0155 and 90–0304.

References

BOGDANOFF, D. W. [1983] "Compressibility Effects in Turbulent Shear Layers," (TN) *AIAA J.* **21**(6), 926–927.

BROWN, G. L. and ROSHKO, A. [1974] "On Density Effects and Large Structure in Turbulent Mixing Layers," *J. Fluid Mech.* **64**(4), 775–816.

CLEMENS, N. T., MUNGAL, M. G., BERGER, T. E. and VANDSBURGER, U. [1990] "Visualizations of the structure of the turbulent mixing layer under compressible conditions," *AIAA* 28th *Aerospace Sciences Meeting*, 8–11 January 1990 (Reno, Nevada), paper AIAA–90–0500.

CLEMENS, N. T. and MUNGAL, M. G. [1990] "Two- and Three-Dimensional Effects in the Supersonic Mixing Layer," 26th *AIAA/SAE/ASME/ASEE Joint Propulsion Conference* (Orlando, FL), 10–12 July 1990, AIAA–90–1978.

COLES, D. [1981] "Prospects for Useful Research on Coherent Structure in Turbulent Shear Flow," *Proc. Indian Acad. Sci. (Eng. Sci.)* 4(2), 111–127.

COLES, D. [1985] "Dryden Lecture: The Uses of Coherent Structure," *AIAA* 23rd *Aerospace Sciences Meeting*, 14–17 January 1985 (Reno, Nevada), AIAA Paper 85–0506.

DIMOTAKIS, P. E. [1984] "Two-dimensional shear-layer entrainment," *AIAA* 22nd *Aerospace Sciences Meeting*, 9–12 January 1984 (Reno, Nevada), AIAA–84–0368. Published, *AIAA J.* **24**(11), 1791–1796 (1986).

DIMOTAKIS, P. E. [1989] "Turbulent Free Shear Layer Mixing," *AIAA* 27th *Aerospace Sciences Meeting*, 9–12 January 1989 (Reno, Nevada), AIAA–89–0262.

FERRI, A. [1973] "Mixing-Controlled Supersonic Combustion," *Ann. Rev. Fluid Mech.* **5**, 301–338.

FERRI, A., LIBBY, P. A. and ZAKKAY, V. [1962] "Theoretical and Experimental Investigation of Supersonic Combustion," Proc. 3rd *ICAS Congress, Stockholm*, (Spartan Books, Wash. DC), 1089–1155.

FOURGUETTE, D., MUNGAL, M. G. and DIBBLE, R. [1990] "Time Evolution of the Shear Layer of an Axisymmetric Supersonic Jet at Matched Conditions," *AIAA* 28th *Aerospace Sciences Meeting*, 8–11 January 1990 (Reno, Nevada), AIAA–90–0508.

JACKSON, T. L. and GROSCH, C. E. [1988] "Spatial Stability of a Compressible Mixing Layer," NASA ICASE Report No. 88–33.

JACKSON, T. L. and GROSCH, C. E. [1989] "Inviscid spatial stability of a compressible mixing layer," *J. Fluid Mech.* **208**, 609–637.

JACKSON, T. L. and GROSCH, C. E. [1990] "Absolute/convective instabilities and the convective mach number in a compressible mixing layer," *Phys. Fluids* A **2**(6), 949–954.

HALL, J. L. [1991] *An Experimental Investigation of Structure, Mixing and Combustion in Compressible Turbulent Shear Layers*, Ph.D. thesis, California Institute of Technology.

HALL, J. L., DIMOTAKIS, P. E. and ROSEMANN, H. [1991] "Experiments in non-reacting compressible shear layers," *AIAA* 29th *Aerospace Sciences Meeting*, 7–10 January 1991 (Reno, Nevada), AIAA Paper No. 91–0629.

LIEPMANN, H. W. and ROSHKO, A. [1957] *Elements of Gasdynamics* (GALCIT Aeronautical Series, John Wiley & Sons, Inc.).

LELE, S. K. [1989] "Direct Numerical Simulation of Compressible Free Shear Flows," *AIAA* 27th *Aerospace Sciences Meeting*, 9–12 January 1989 (Reno, Nevada), AIAA Paper 89–0374.

LOWSON, M. V. and OLLERHEAD, J. B. [1968] "Visualization of noise from cold supersonic jets," *J. Acoust. Soc. Am.* **44**, 624.

OERTEL, H. [1979] "Mach wave radiation of hot supersonic jets investigated by means of the shock tube and new optical techniques," 12th *Int. Symp. on Shock Tubes and Waves* (Jerusalem, 16–19 July 1979), 266–275.

PAPAMOSCHOU, D. [1989a] "Structure of the compressible turbulent shear layer," *AIAA* 27th *Aerospace Sciences Meeting*, 9–12 January 1989 (Reno, Nevada), AIAA–89–0126, published in *AIAA J.* **29**(5), 680–681 (1991).

PAPAMOSCHOU, D. [1989b] "Acoustic Paths in Compressible Shear Layers," *Bull. Am. Phys. Soc.* **34**(10), 2252.

PAPAMOSCHOU, D. and ROSHKO, A. [1988] "The Compressible Turbulent Shear Layer: An Experimental Study," *J. Fluid Mech.* **197**, 453–477.

RAGAB, S. A. and WU, J. L. [1989a] "Linear instabilities in two-dimensional compressible mixing layers," *Phys. Fluids* A **1**(6), 957–966.

RAGAB, S. A. and WU, J. L. [1989b] "Linear Instability Waves in Supersonic Turbulent Mixing Layers," *AIAA J.* **27**(6), 677–686.

SANDHAM, N. and REYNOLDS, W. C. [1989a] "The Compressible Mixing Layer: Linear Theory and Direct Simulation," *AIAA 27th Aerospace Sciences Meeting*, 9–12 January 1989 (Reno, Nevada), AIAA–89–0371.

SANDHAM, N. D. and REYNOLDS, W. C. [1989b] "A Numerical Investigation of the Compressible Mixing Layer," Stanford Report TF–45.

SANDHAM, N. D. and REYNOLDS, W. C. [1990] "Compressible Mixing Layer: Linear Theory and Direct Simulation," *AIAA J.* **28**(4), 618–624.

TAM, C. K. W. [1971] "Directional acoustic radiation from a supersonic jet," *J. Fluid Mech.* **46**(4), 757–768.

TAM, C. K. W. and HU, F. Q. [1988] "Instabilities of supersonic mixing layers inside a rectangular channel," Proceedings, *First National Fluid Dynamics Congress*, 25–28 July 1988 (Cincinnati, Ohio), **II**, 1073-1086.

TAM, C. K. W. and HU, F. Q. [1989] "The instability and acoustic wave modes of supersonic mixing layers inside a rectangular channel," *J. Fluid Mech.* **203**, 51–76.

VANDROMME, D. and HAMINH, H. [1989] "The compressible mixing layer," *Turbulence and Coherent Structures*, selected papers from "Turbulence 89: Organized Structures and Turbulence in Fluid Mechanics" (Grenoble, France), 18–21 September 1989, eds. O. Metais and M. Lesieur (Kluwer A.P., Dordrecht, Netherlands, 1991), 507–523.

ZHUANG, M., KUBOTA, T. and DIMOTAKIS, P. E. [1988] "On the Stability of Inviscid, Compressible Free Shear Layers," Proceedings, *First National Fluid Dynamics Congress*, 25–28 July 1988 (Cincinnati, Ohio), **II**, 768–773.

ZHUANG, M., DIMOTAKIS, P. E. and KUBOTA, T. [1990] "The Effect of Walls on a Spatially Growing Supersonic Shear Layer," *Phys. Fluids* A **2**(4), 599–604.

Appendix D

HALL, J. L., DIMOTAKIS, P. E. AND ROSEMANN, H. [1991] "Some measurements of molecular mixing in compressible turbulent mixing layers," *AIAA* 22nd *Fluid Dynamics, Plasma Dynamics and Lasers Conference*, Paper 91–1719.

AIAA-91-1719

Some Measurements of Molecular Mixing in Compressible Turbulent Shear Layers

J. L. Hall, P. E. Dimotakis and H. Rosemann
California Institute of Technology
Pasadena, CA

AIAA 22nd Fluid Dynamics, Plasma Dynamics & Lasers Conference
June 24-26, 1991 / Honolulu, Hawaii

SOME MEASUREMENTS OF MOLECULAR MIXING IN COMPRESSIBLE TURBULENT SHEAR LAYERS*

J. L. Hall**, P. E. Dimotakis† and H. Rosemann‡

Graduate Aeronautical Laboratories
California Institute of Technology
Pasadena, CA 91125

Abstract

A new blowdown wind tunnel facility is used to study reacting and non-reacting compressible, turbulent shear layers. In the reacting experiments reported here, low concentrations of hydrogen, fluorine and nitric oxide are carried by inert diluent gases, with the hydrogen and nitric oxide in the high-speed stream, and fluorine in the low-speed stream. The heat release associated with the resulting chemical reaction serves as a diagnostic for molecular mixing in the shear layer. This molecular mixing has been quantified at two compressibility levels by conducting 'flip' experiments in this new facility. The results indicate that the volume fraction of mixed fluid in the compressible shear layer is substantially reduced as compared to previous incompressible results. These same flip experiments also reveal that compressibility significantly reduces the entrainment ratio as compared to theoretical predictions extrapolated from incompressible models.

1. Introduction

Compressible turbulent shear layers have received considerable attention in recent years, on both the theoretical (Zhuang *et al.* 1988, Tam & Hu 1989, Lele 1989, Zhuang *et al.* 1990, Ragab & Sheen 1990, Sandham & Reynolds 1990, Chen 1991) and experimental levels (Chinzei *et al.* 1986, Papamoschou & Roshko 1988, Papamoschou 1991, Clemens *et al.* 1990, Clemens & Mungal 1990, Fourguette *et al.* 1990, Clark *et al.* 1990, Shau & Dolling 1990, Goebel & Dutton 1990, McIntyre & Settles 1991, Hall *et al.* 1991). This work has attempted to determine the effect of compressibility on the turbulent structure and growth rate of shear layers, as well as to assess the role that shock waves might play in such compressible flows. The results thus far have demonstrated that compressibility significantly reduces both the shear layer growth rate and the large-scale, two-dimensional structure content of the flow, and that travelling shock waves do exist in these flows at sufficiently high compressibility levels. The current work aims to extend these investigations by attempting to measure molecular mixing in compressible turbulent shear layers. The resultant mixing rates can then be compared to earlier incompressible data, thereby providing a measure of the effect of compressibility on the molecular mixing process.

** Research Engineer in Aeronautics, Member AIAA.

† Professor, Aeronautics & Applied Physics, Associate Fellow AIAA.

‡ Research Fellow in Aeronautics.

The methodology employed here is that of the 'flip' experiment. This technique has been used previously in water-based flows (Koochesfahani & Dimotakis 1986) and gas-phase flows (Mungal & Dimotakis 1984). The premise of this technique is that chemical reactions can be used to mark molecularly mixed fluid. In the present experiments, an exothermic reaction is employed so that the detection of higher than ambient temperature can be attributed to molecular mixing of the reactants and subsequent chemical reaction and heat release. Since the reactants are not pre-mixed, such temperature measurements can be related to the total amount of molecular mixing in the turbulent shear layer. This relationship can be precisely quantified by a flip experiment, provided that the chemical kinetics of the system are sufficiently fast. This requirement simply means that one wants to minimize the time lag between molecular mixing and chemical product formation, so that virtually all of the molecularly mixed fluid is tagged by the reaction signature (*e.g.*, by higher temperature). For this condition to be met, it is necessary to exceed some threshold value of the flow Damköhler number (Da), where

$$Da \equiv \frac{\tau_m}{\tau_c} \,. \tag{1}$$

Here, τ_m is the characteristic mixing timescale and τ_c is the characteristic chemical reaction timescale. Clearly, if $\tau_c \ll \tau_m$, then the time lag between mixing and reaction will be very small, and the flip experiment will yield quantitative estimates for the molecular mixing. Currently, the threshold value of Da for sufficiently fast chemical kinetics must be determined by experiment.

In the following sections, some background theory will be reviewed for the flip experiment and for the convective Mach number concept.

2. Background Theory

2.1 Flip Experiment

The flip experiment itself is perhaps best explained in the context of $p(\xi, y)$, the probability density function (pdf) which describes the distribution of fluid composition across the shear layer. Here, ξ is the mole fraction of high-speed fluid at transverse location y; therefore, $\xi = 1$ corresponds to pure high-speed fluid and $\xi = 0$ corresponds to pure low-speed fluid. Refer to Fig. 1 for the definition of the geometry and coordinate system used in this discussion. The pdf can be simplified by integrating across the shear layer; *i.e.*,

$$p(\xi) = \frac{1}{\delta} \int_0^\delta p(\xi, y) dy \,. \tag{2}$$

A sketch of $p(\xi)$ based on experiments with density-matched, *incompressible* shear layers is shown in Fig. 2 (Dimotakis 1989). Note that all compositions can be found in the shear layer, ranging from pure high-speed to pure low-speed fluid. Note also the central peak in the distribution, a peak thought to result from homogeneously mixed, large-scale vortex cores in the shear layer. More detailed discussions of this pdf can be found in the models of Broadwell & Breidenthal (1982), Dimotakis (1987) and Broadwell & Mungal (1988, 1990). For our current purposes, it suffices to recognize that in the absence of direct measurements of $p(\xi)$ in compressible shear layers, the pdf shown in Fig. 2 served as the basis for the analysis of the flip experiment data. A qualitative discussion of the sensitivity of the compressible flip experiment results to the precise form of $p(\xi)$ will be given later.

One goal of the flip experiment is to measure the *integral* of $p(\xi)$ without even knowing the functional form of $p(\xi)$. Specifically, the fraction of molecularly mixed fluid inside the shear layer is given by

$$\frac{\delta_m}{\delta} = \int_{\epsilon}^{1-\epsilon} p(\xi)\, d\xi \,, \tag{3}$$

where δ_m is the mixing thickness of the shear layer, and $\epsilon \ll 1$ so as to exclude the unmixed fluid. However, an experiment based on tagging molecularly mixed fluid with higher temperatures resulting from chemical reactions yields a different integral, one that is integrated *spatially* across the shear layer; *i.e.*,

$$\frac{\delta_p}{\delta} = \frac{1}{\delta} \int_0^{\delta} \frac{\Delta T(y)}{\Delta T_{ad}}\, dy \,, \tag{4}$$

where δ_p is the product thickness of the shear layer, ΔT_{ad} is the adiabatic flame temperature of the chemical system and $\Delta T(y)$ is the temperature rise due to chemical reactions at location y. The process of relating results in the form of Eq. 4 to the desired integral of Eq. 3 constitutes the methodology of the flip experiment. The key element consists of relating the local temperature rise $\Delta T(y)$ to the underlying distribution of mixture fractions $p(\xi, y)$ in the shear layer. This connection can be made in two steps.

First, one must find a functional relationship between chemical product formation and mixture fraction. This can be done in the fast-chemistry limit, because the lean reactant in the mixture will be completely consumed under these conditions. Note that 'lean' must be defined in reference to the stoichiometry of the chemical system. Typically, this is quantified in terms of the stoichiometric mixture ratio ϕ defined by

$$\phi \equiv \frac{X_2/X_1}{(X_2/X_1)_{st}} \tag{5}$$

where X_i is the free stream mole fraction of reactant i, and the subscript 'st' denotes a stoichiometric mixture. This special condition of complete lean reactant consumption enables the determination of chemical product formation. For example, in a stoichiometric mixture, all of the reactants will be consumed yielding 100% product formation. This product formation will linearly decrease to zero at $\xi = 0, 1$ corresponding to pure unmixed fluid (Dimotakis 1989). This behaviour is sketched in Fig. 3, where the product formation function $\theta(\xi, \xi_\phi)$ has been normalized so as to have a value of unity at the stoichiometric mixture fraction ξ_ϕ.

The second step is to realize that the normalized temperature rise measured in the experiment $(\Delta T(y)/\Delta T_{ad})$ can be related to the product formation function $\theta(\xi, \xi_\phi)$. For example, if all of the fluid at location y were mixed at the stoichiometric ratio, then

$$\frac{\Delta T(y)}{\Delta T_{ad}} = \theta(\xi = \xi_\phi) = 1 \,, \tag{6}$$

that is, one would measure the adiabatic flame temperature. However, in reality, a range of mixture fractions are found at any location inside the shear layer. Therefore, one must weight the product formation function $\theta(\xi, \xi_\phi)$ by the probability distribution function $p(\xi, y)$; *i.e.*,

$$\frac{\Delta T(y)}{\Delta T_{ad}} = \int_0^1 \theta(\xi, \xi_\phi)\, p(\xi, y)\, d\xi \,. \tag{7}$$

If this equation is integrated in y, one obtains

$$\frac{1}{\delta} \int_0^{\delta} \frac{\Delta T(y)}{\Delta T_{ad}}\, dy = \frac{1}{\delta} \int_0^{\delta} \int_0^1 \theta(\xi, \xi_\phi)\, p(\xi, y)\, d\xi\, dy \,. \tag{8}$$

Noting the definitions of δ_p/δ and $p(\xi)$ (Eqs. 2 and 4) this can be written as

$$\frac{\delta_p}{\delta} = \int_0^1 \theta(\xi,\xi_\phi)\, p(\xi)\, d\xi \,. \tag{9}$$

The integral on the right hand side of Eq. 9 is almost what is required to estimate the overall mixing (*cf.*, Eq. 3). If the triangular product-formation function $\theta(\xi,\xi_\phi)$ were replaced by a top-hat function that is unity in the range $\epsilon < \xi < (1-\epsilon)$ then the integral would be the overall molecular mixing. The final step in the flip experiment synthesis, therefore, is to manufacture a top-hat function from a *pair* of triangular product formation functions. This can be done by superimposing two product formation functions as shown in Fig. 4. Note that the two highly skewed triangles correspond to one very low and one very high stoichiometric mixture fractions, ξ_0 and $(1-\xi_0)$, where ξ_0 is small in some sense. The resultant function

$$F(\xi) = (1-\xi_0)\,[\theta(\xi,\xi_0) + \theta(\xi,1-\xi_0)] \tag{10}$$

therefore represents a close approximation to the desired top-hat function. In terms of measured product thicknesses, one obtains

$$\left[\frac{\delta_p(\xi_0)}{\delta} + \frac{\delta_p(1-\xi_0)}{\delta}\right] = \int_0^1 \theta(\xi,\xi_0)\, p(\xi)\, d\xi + \int_0^1 \theta(\xi,1-\xi_0)\, p(\xi)\, d\xi \,. \tag{11}$$

Now, if the pdf remains unchanged for the two experiments, then one can reduce the sum of the integrals as follows:

$$(1-\xi_0)\int_0^1 \{\theta(\xi,\xi_0) + \theta(\xi,1-\xi_0)\}\, p(\xi)\, d\xi = \int_0^1 F(\xi)\, p(\xi)\, d\xi \,. \tag{12}$$

The final integral, however, is an estimate for the molecular mixing in the shear layer (*cf.* Eq. 3). Therefore,

$$\frac{\delta_m}{\delta} \simeq \int_0^1 F(\xi) p(\xi) d\xi \,, \tag{13}$$

or in terms of product thicknesses,

$$\frac{\delta_m}{\delta} \simeq (1-\xi_0)\left[\frac{\delta_p(\xi_0)}{\delta} + \frac{\delta_p(1-\xi_0)}{\delta}\right] . \tag{14}$$

To summarize then, the volume fraction of molecularly mixed fluid in the shear layer, δ_m/δ, can be estimated from the spatial temperature-rise integrals from a pair of reacting flow experiments. These two experiments must consist of one very low and one very high stoichiometric mixture-ratio flows. In other words, one experiment must have the rich reactant in the high speed stream and the other must have the rich reactant in the low speed stream. Indeed, it is this 'flipping' of the rich reactant from one stream to the other that provides the name for the technique. Note that the preceding analysis assumes that the heat release associated with the chemical reaction does not change the flow, particularly with respect to the pdf and the overall growth rate.

The flip experiment can also yield information about the relative amounts of high- and low-speed fluid in the molecular mixture of the shear layer. In particular, in the limit of $\xi_\phi \rightarrow 0$, all of the molecularly mixed low-speed reactant will be consumed; therefore, the product thickness for this flow (Eq. 9) will be proportional to the total amount of low-speed fluid in the mixture. A similar situation prevails for the high-speed fluid in the limit of $\xi_\phi \rightarrow 1$. Therefore, the appropriate *ratio* of the product thicknesses from the flip experiment will yield an estimate for the mean mixture fraction $\bar{\xi}_m$; *i.e.*,

$$\bar{\xi}_m \simeq \frac{\delta_p(1-\xi_0)}{\delta_p(\xi_0)+\delta_p(1-\xi_0)} \,. \tag{15}$$

In terms of the pdf, this can be written as

$$\bar{\xi}_m = \int_\epsilon^{1-\epsilon} \xi\, p(\xi)\, d\xi \,. \tag{16}$$

This mean mixture fraction can also be re-written in terms of an entrainment ratio E_n, defined to be the amount of high-speed fluid per unit amount of low-speed fluid; *i.e.*,

$$E_n = \frac{\bar{\xi}_m}{1-\bar{\xi}_m} \,. \tag{17}$$

On the basis of incompressible shear layer experiments, Dimotakis (1984) proposed a model which would predict E_n on the basis of the free-stream parameters of the flow; *i.e.*,

$$E_n \simeq \frac{1}{s}\frac{w_2}{w_1}\frac{u_1-u_c}{u_c-u_2}\left(1+\frac{l}{x}\right) , \tag{18}$$

where s is the density ratio, w_i is the mean molecular weight of stream i, u_c is the large-scale structure convection velocity and l/x is the mean large-scale structure spacing to position ratio. Although it is not obvious that this formulation will be applicable to compressible shear layers, it does serve as a basis for comparison for the entrainment ratio estimates to be provided by the flip experiments.

2.2 Convective Mach Number

In order to assess compressibility effects on the molecular mixing in the turbulent shear layer, it is necessary to have a quantitative measure for compressibility. One such measure is the convective Mach number, a concept first applied to shear layers by Bogdanoff (1983) and used to correlate growth rate measurements (δ/x) with compressibility. This parameter is based on the idea that there exist large-scale structures in the shear layer that convect with a particular velocity, u_c. Given this, one can define two convective Mach numbers by taking the velocity differences of the free streams with respect to the motion of these turbulent structures; *i.e.*,

$$M_{c1} \equiv \frac{u_1-u_c}{a_1} \qquad \text{and} \qquad M_{c2} \equiv \frac{u_c-u_2}{a_2} \,, \tag{19}$$

where u_1 and u_2 are the free-stream velocities, and a_1 and a_2 are the free-stream sound speeds. Now, the convective Mach numbers for a given flow can be determined either by theoretical models or by direct measurement. The standard model (Coles 1981, Dimotakis 1984, Papamoschou & Roshko 1988) is based on the idea that there must exist interstitial stagnation points between large-scale shear layer structures in the convective frame of reference (Fig. 5). Assuming that an isentropic streamline can be traced from each free stream into the stagnation point, the requirement of a total pressure balance there produces an implicit equation for the convection velocity, u_c; *i.e.*,

$$p_1\left[1+\frac{\gamma_1-1}{2}\left(\frac{u_1-u_c}{a_1}\right)^2\right]^{\gamma_1/\gamma_1-1} = p_2\left[1+\frac{\gamma_2-1}{2}\left(\frac{u_c-u_2}{a_2}\right)^2\right]^{\gamma_2/\gamma_2-1} \tag{20}$$

Applying this model when $p_1 = p_2$, one finds that M_{c1} and M_{c2} are equal when $\gamma_1 = \gamma_2$ and that they are almost equal otherwise. Therefore, it has become conventional to consider the isentropic model value for M_{c1} (*i.e.* $M_{c1}^{(i)}$) to be "the" convective Mach number for a given flow.

This convective Mach number has proven important in correlating the effect of compressibility on the growth rate of the turbulent shear layer. Typically, the measured growth rate of a compressible flow is normalized by the theoretically estimated growth rate for an equivalent incompressible flow in order to isolate the effect of compressibility (*cf.* Papamoschou & Roshko 1988). Fig. 6 presents some accumulated data from Hall *et al.* (1991), in which it is seen that the collapse of the data is quite good except for a few cases at the low compressibility end of the plot. The reader is referred to Hall *et al.* (1991) for a discussion of these cases. This growth rate correlation problem aside, however, there are other difficulties that impede complete acceptance of the convective Mach number concept. The first is that it is unclear whether or not large-scale structures even exist in high-compressibility flows. Certainly, the existing Schlieren photographic data (Papamoschou & Roshko 1988, Chinzei *et al.*1986, Clemens & Mungal 1990, Hall *et al.* 1991) do not unambiguously show large-scale structures of the kind known to dominate incompressible turbulent shear layers (*e.g.* Brown & Roshko 1974). This is illustrated in Fig. 7, a typical Schlieren photograph of a medium-compressibility flow ($M_{c1}^{(i)} = 0.51$) taken from Hall *et al.* (1991). Another difficulty with the standard model is that the few direct measurements of u_c that exist (Papamoschou 1991, Hall *et al.* 1991) indicate that the actual convective Mach numbers are very different from the isentropic model predictions. Attempts to reconcile this discrepancy with non-isentropic (*i.e.*, shock-dissipative) models show promise (Dimotakis 1989, 1991), but they as yet lack experimental verification. The current situation is that there is no clear alternative to the standard model; therefore, the isentropic model parameter $M_{c1}^{(i)}$ will continue to be used to quantify compressibility in this paper, despite the growing recognition of its limitations.

3. Experimental Details

3.1 Facility Description

The current experiments were performed in the GALCIT Supersonic Shear Layer Combustion Facility (Fig. 8). This is a two-stream blowdown wind tunnel with a nominal run time of 3 sec. It is capable of producing chemically reacting flows based on $H_2/F_2/NO$ chemistry. For the current experiments, the facility was configured for a supersonic high-speed stream ($M_1 = 1.5$) and a subsonic low-speed stream ($M_2 < 0.5$). Different convective Mach numbers were generated by using different gases in the two free streams. The static pressure of the shear layer is nominally 1 atm.

The operation of the facility is straightforward. The desired gases or gas mixtures are loaded into a pair of storage tanks. At run-time, parallel piping networks deliver these gases to the test section via shutoff and flow regulating valves. Inside the test section, the gases flow through screens, honeycomb and appropriately contoured nozzles before coming into contact at the end of the splitter plate. The shear layer forms between two adjustable guidewalls on the top and bottom, and two windows on the sides. Upon exiting the test section, the shear layer gases enter a waste gas treatment system which is designed to neutralize the toxic and corrosive gases from $H_2/F_2/NO$ combustion experiments.

The primary diagnostic for the reacting flow experiments is a cross-stream rake of 16 exposed-junction thermocouples, each having a diameter of 0.001 in. These thermocouple provide time-averaged temperatures across the shear layer from which the product thickness (δ_p/δ) (Eq. 4) of the flow can be determined. These temperature measurements are supplemented by side-view Schlieren photography and guidewall static pressure measurements.

Further details on the facility design and operation can be found in Hall (1991).

3.2 Experiment Methodology

The reactants chosen for the compressible flip experiments were hydrogen and fluorine, with small quantities of nitric oxide added to the hydrogen stream to initiate the reaction. The main reason for this selection was that results from computer modelling (Dimotakis & Hall 1987) suggested that *only* this chemical system would be able to produce sufficiently fast chemical kinetics in a small laboratory facility at low stagnation temperatures. This system possesses the added advantage that the reaction is hypergolic even at ambient temperatures and below. Much the same reasoning led to the use of the $H_2/F_2/NO$ chemical system in the earlier incompressible experiments of Mungal & Dimotakis (1984) and Hermanson & Dimotakis (1989). The complete reaction mechanism thought to govern this system is listed in Table 1, where the coefficients A, β and E correspond to the standard Arrhenius formulation for the reaction rate; *i.e.*,

$$k_{f_j} = A_j T^{\beta_j} \exp[-E_j/R_o T] \ , \tag{21}$$

where, k_{f_j} is the molar production rate of species j, T is the temperature and R_o is the universal gas constant. A more detailed discussion of the chemical kinetics aspects of this experiment can be found in Hall (1991).

In the actual experiments, small concentrations of hydrogen and nitric oxide are added to an inert gas on the high-speed side, and small concentration of fluorine are added to an inert gas on the low speed side. This inert gas can be either nitrogen, argon or helium. Ideally, one would like these concentrations to be arbitrarily small so that the heat release will be negligible and therefore not perturb the underlying flow. However, the chemical reaction rate roughly scales with the *square* of the molecular number density (*cf.* Eq. 21 and Table 1), a feature that sets a minimum concentration requirement for sufficiently fast chemical kinetics. Practically speaking, this minimum concentration was determined in a series of kinetics experiments that preceeded each flip experiment. These experiments will be described in the next section.

In the flip experiments here, the definition of the stoichiometric mixture fraction ξ_ϕ was based only on the concentrations of the hydrogen and the fluorine, a simplification founded on the fact that only small amounts of nitric oxide were present in the flow. Ideally, one would like to have one experiment with ξ_ϕ close to zero ($[H_2] \gg [F_2]$) and the other experiment with ξ_ϕ close to unity ($[F_2] \gg [H_2]$), where [ ] denotes molar concentration. This will result in a better approximation of the flip experiment function $F(\xi)$ to the desired top-hat function in Fig. 4 (*cf.* Sec. 2.1). Unfortunately, this is generally limited by the combined requirements for fast kinetics and minimum heat release. Specifically, the lean reactant concentration must exceed a minimum value for fast kinetics, and the rich reactant concentration needs to be small in order to limit the heat release in the shear layer.

In addition, there were practical constraints on the allowable maximum concentrations of hydrogen and fluorine used in the laboratory which stemmed from safety considerations. The net result of all these limitations was to yield flip experiments with $\phi = 1/4, 4$ or $\phi = 1/3, 3$ ($\xi_\phi = 0.2, 0.8$ or $\xi_\phi = 0.25, 0.75$). These fairly low ratios will lead to underestimates for the molecular mixing fraction δ_m/δ, because the wings of the *pdf* will not be properly weighted by $F(\xi)$. An estimate of this error will be presented in the following section.

4. Results and Discussion

Table 2 lists all of the test cases for the current study. These experiments are divided into two groups: medium compressibility flows based on N_2/N_2 diluents (Cases 3a to 3e); and high compressibility flows based of He/N_2 diluents (Cases 2a to 2c) or He/Ar diluents (Cases 1a and 1b).[‡] The corresponding convective Mach numbers are $M_{c1}^{(i)} = 0.51, 0.91,$ and 0.96 respectively. Each compressibility regime can be sub-divided into a kinetics study at $\phi = 1$ and a flip experiment. In the table, δ_1 denotes the temperature thickness of the shear layer, with the edges of the layer defined by a normalized temperature rise of 1% of the maximum value. The normalized product thickness (Eq. 4) is therefore denoted by δ_p/δ_1. The Damköhler number was computed from Eq. 1, where τ_m was taken to be the time of flight through the test section, and τ_c was computed from a model based on the well-stirred reactor formulation (Dimotakis & Hall 1987, Hall 1991). Note that the high compressibility kinetics study employed He/N_2 diluents whereas the corresponding flip experiment employed He/Ar diluents. This is the result of a late recognition of the fact that the flip experiment requires constant molar heat capacity across the shear layer (*i.e.*, constant γ) in order to accurately relate temperature increases to chemical product formation. The use of He/Ar diluents satisfies this criterion, whereas He/N_2 does not. Nevertheless, it can be argued that the kinetics experiment with He/N_2 diluents represents an *upper* bound on the fast chemistry regime for He/Ar diluents because the molar heat capacity of nitrogen is higher than that of argon, leading to lower temperatures and slower kinetics.

Normalized temperature-rise profiles for the Case 3 kinetics experiment are presented in Fig. 9.* The solid lines are least-squares fitted curves for each experiment. It is seen that the curves for reactant concentrations of 2% and 4% virtually lie on top of each other. This is taken as evidence that *both* flows are in the kinetically fast regime; that is, doubling the reactant concentration did not more than double the chemical product formation. This result suggested that a 2% reactant concentration was the minimum threshold value for fast kinetics in the medium compressibility experiment. The corresponding results for the high-compressibility experiment are in shown in Fig. 10. Here, it is the 4% and 6% curves that nearly lie on top of each other, indicating that the minimum threshold value for fast kinetics in this flow was roughly 4%. Two other features from these plots should be noted. First, the temperature profile thicknesses, δ_1, are relatively insensitive to the effect of significant heat release inside the shear layer (ΔT_{flm} up to 633 K). Second, the peaks in the profiles lie roughly at $\Delta T/\Delta T_{\text{flm}} \sim 0.6$, which is close to the value found in the incompressible experiments of Mungal & Dimotakis (1984) and Hermanson & Dimotakis (1989).

---

‡ The cases are numbered in a consistent fashion with Hall *et al.* (1991). For example, Cases 1a and 1b here correspond to the non-reacting flow Case 1 in the earlier reference.

* Note that the temperature rise, ΔT, was based on a comparison between the reacting and non-reacting flows for the given diluent gases. Refer to Hall (1991) for a more complete discussion of the procedure.

Finally, a time-resolved, composite Schlieren photograph of the Case 3c reacting flow is presented in Fig. 11. The presence of significant heat release in the shear layer can be inferred from the pronounced banded structure seen in the photograph. Note, however, the absence of any large-scale vortical structure visible inside the shear layer, an observation consistent with results from earlier non-reacting experiments at high compressibility (Clemens & Mungal 1990, Hall *et al.* 1991).

Normalized temperature-rise profiles for the Case 3 flip experiment are presented in Fig. 12. These flows used a 2% lean reactant concentration as dictated by the kinetics experiment, and an 8% rich reactant concentration, a value selected to meet the twin constraints of minimized heat release and the safety threshold for the use of hydrogen and fluorine gas in the lab. This resulted in a flip experiment with $\phi = 1/4, 4$ ($\xi_0 = 0.2$). The behaviour of these profiles is seen to be qualitatively similar to the earlier incompressible flows (Mungal & Dimotakis 1984) in that the profile shifts toward the lean reactant, a feature that stems from the fact that the rich reactant will penetrate further into the other stream before being consumed. A second feature that has defied explanation thus far is the considerably larger temperature thickness for the $\phi = 1/4$ flow as compared to the other experiments. Note that it cannot be *solely* a heat release effect because $\Delta T_{\rm flm}$ is virtually the same for the $\phi = 1/4$ and $\phi = 4$ experiments. Whatever the cause, however, the existence of such a large perturbation on the base flow reduces the confidence of the results for this flip experiment. Given that uncertainty, one can proceed with the calculations in a straightforward manner. From Eqs. 14, and 15:

$$\frac{\delta_{\rm m}}{\delta} \simeq (1 - 0.2)(0.259 + 0.243) = 0.40\,, \tag{22a}$$

$$\bar{\xi} \simeq \frac{0.259}{0.243 + 0.259} = 0.52 \tag{23b}$$

and

$$E_n \simeq \frac{0.516}{1 - 0.516} = 1.07\,. \tag{24c}$$

The corresponding flip experiment results for the high-compressibility flow is presented in Fig. 13. Note that this flip experiment was based on a flip ratios of only $\phi = 1/3, 3$, corresponding to 3% and 9% reactant concentrations. This smaller ratio was dictated by the previously mentioned limitations on the maximum reactant concentrations that could be used in the lab. Note the implicit assumption that a 3%/9% mixture is as kinetically fast as a 4%/4% mixture. In Fig. 13, the shift of the temperature profile towards the lean reactant is quite evident. What is missing from this flow, however, is the curious layer thickening observed in the $\phi = 1/4$ flow at medium compressibility. Whatever the reason for this, the apparent reduction in flow perturbation increases the confidence of the results for this flip experiment. Proceeding with the calculations as before:

$$\frac{\delta_{\rm m}}{\delta} \simeq (1 - 0.25)(0.188 + 0.226) = 0.31\,, \tag{25a}$$

$$\bar{\xi} \simeq \frac{0.226}{0.226 + 0.188} = 0.55 \tag{26b}$$

and

$$E_n \simeq \frac{0.546}{1 - 0.546} = 1.2\,. \tag{27c}$$

The results just quoted indicate that at $M_{c1}^{(i)} = 0.51$, roughly 40% of the fluid inside the shear layer is molecularly mixed, whereas at $M_{c1}^{(i)} = 0.96$, roughly 31% of the fluid is molecularly mixed. These numbers can be compared to the value of 49% found in the previous work done with incompressible flows (Dimotakis 1989). This, by itself, suggests a strong compressibility effect which reduces the molecular mixing from 49% to 31% going from incompressible flow to $M_{c1}^{(i)} = 0.96$. However, it is possible that some of this reduction is a Reynolds number effect. More specifically, the incompressible experiments of Mungal *et al.* (1985) found that the product thickness decreased slightly with increasing Re_δ. Their data is plotted in Fig. 14, along with the current data. On the basis of this comparison, it is plausible that some of the reduced mixing measured in the current compressible experiments is, in fact, a Reynolds number effect. It should be noted, however, that more recent incompressible experiments by Frieler *et al.* (unpublished) suggest that the Reynolds number effect on mixing is much less than that found by Mungal *et al.* (1985) and may, in fact, be negligible. Furthermore, the extrapolation of these incompressible results to compressible flow must be considered highly speculative. Finally, note that such potential Reynolds number effects would seem to be unable to completely reconcile the difference between the two compressible flip experiments reported here. The highest compressibility case ($M_{c1}^{(i)} = 0.96$) has roughly 22% less molecular mixing than the medium compressibility case ($M_{c1}^{(i)} = 0.51$) even though it is only a factor of two higher in Reynolds number.

As mentioned previously, the low flip ratios used in the current experiments will result in underestimates for the molecular mixing because the wings of the pdf ($\xi \rightarrow 0, \xi \rightarrow 1$) will not be properly represented. However, if it is of the form of the incompressible pdf sketched in Fig. 2, then the underestimation will be small because very little mixed fluid will be mixed at the compositions that are under-counted. The magnitude of this error at $\phi = 1/4, 4$ is estimated to be -0.04 in δ_m/δ based on the incompressible experiments of Mungal & Dimotakis (1984). This is not sufficient to account for all of the observed difference between incompressible and compressible molecular mixing. It is possible, however, that compressibility will change the pdf and thereby change the error estimate. The same is true for the possible effect of the heat release on the base flow, a heat release which is significantly greater than that found in the incompressible experiments.

The results for E_n indicate that the molecular mixture has slightly more high-speed fluid than low-speed fluid. However, the values measured are somewhat lower than would be expected on the basis of the incompressible model of Dimotakis (1984) (Eq. 18) coupled with an isentropic model estimation of u_c (Eq. 20). For example, at $M_{c1}^{(i)} = 0.51$, the flip experiment yields $E_n = 1.07$ whereas the model predicts $E_n = 1.44$. The disparity is even more pronounced at $M_{c1}^{(i)} = 0.96$, namely a measurement of $E_n = 1.2$ versus a prediction of $E_n = 4.68$. One possible resolution of this difference is to recognize that the isentropic model prediction for u_c is almost certainly wrong at high compressibility (Papamoschou 1991, Hall *et al.* 1991). If higher values for u_c are adopted in the calculation, closer agreement between experiment and theory can be achieved (Hall 1991). Whatever the detailed reasoning, however, it seems apparent that compressibility drives the entrainment ratio towards unity as compared to incompressible results.

5. Conclusions

Flip experiments were conducted in medium- and high-compressibility shear layer flows in order to quantify the molecular mixing rates. It was found that compressibility reduces the fraction of molecularly mixed fluid inside the layer as compared to previously determined incompressible results. Specifically, it was found that roughly 31% of the fluid is molecularly mixed at an isentropic convective Mach number of 0.96, compared to a molecularly mixed fraction of 49% in incompressible flows. It is possible, however, that some of this reduction is due to the factor of ten increase in Reynolds number between the current compressible flows and the earlier incompressible ones. It should be emphasized that this reduction of molecularly mixed fluid inside the layer is ***in addition*** to the reduction in overall growth rate that has been demonstrated by many previous investigators. The flip experiments also indicated that the molecularly mixed fluid has slightly more high-speed fluid than low-speed fluid; however, this inequality is not nearly as large as would be expected based on extrapolations of previous incompressible models to these compressible flows. Finally, Schlieren photographs of these reacting flows do not show any large-scale vortex structures inside the shear layer.

Acknowledgements

The authors would like to acknowledge the many people at Caltech who contributed to the development and operation of the new facility used in this study. Particular thanks go to Earl Dahl for his many contributions above and beyond the call of duty, and to Chris Bond for his help in running the experiments. This work was sponsored by the Air Force Office of Scientific Research.

References

BAULCH, D. L., DUXBURY, G. J., GRANT, S. J. and MONTAGUE, D. C. [1981] "Evaluated Kinetic Data for High Temperature Reactions, Vol. 4," J. Phys. Chem. Ref. Data, Vol. 10, Suppl. 1.

BOGDANOFF, D. W. [1983] "Compressibility Effects in Turbulent Shear Layers," (TN) *AIAA J.* 21(6), 926–927.

BROADWELL, J. E. and BREIDENTHAL, R. E. [1982] "A Simple Model of Mixing and Chemical Reaction in a Turbulent Shear Layer," *J. Fluid Mech.* **125**, 397–410.

BROADWELL, J. E. and MUNGAL, M. G. [1988] "Molecular Mixing and Chemical Reactions in Turbulent Shear Layers," Proceedings, 22nd *Symposium (International) on Combustion* (The Combustion Institute), 579–587.

BROADWELL, J. E. and MUNGAL, M. G. [1990] "Large-scale Structures and Molecular Mixing," Presented, IUTAM Symposium of Fluid Mechanics of Stirring and Mixing (La Jolla, California), 20-24 August 1990.

BROWN, G. L. and ROSHKO, A. [1974] "On Density Effects and Large Structure in Turbulent Mixing Layers," *J. Fluid Mech.* 64(4), 775–816.

CHEN, J. H. [1991] "The Effect Of Compressibility On Conserved Scalar Mixing In A Plane Free Shear Layer," Sandia National Laboratories report WSS/CI 91-12.

CHINZEI, N., MASUA, G., KOMURO, T. MURAKAMI, A. and KUDOU, K. [1986] "Spreading of two-stream supersonic turbulent mixing layers," *Phys. Fluids* 29(5), 1345-1347.

CLARK, Jr. R. L., NG, W. F., WALKER, D. A. and SCHETZ, J. A. [1990] "Large-Scale Structure in a Supersonic Slot-Injected Flow field," *AIAA J.* 28(6), 1045–1051.

CLEMENS, N. T., MUNGAL, M. G., BERGER, T. E. and VANDSBURGER, U. [1990] "Visualizations of the structure of the turbulent mixing layer under compressible conditions," *AIAA* 28th *Aerospace Sciences Meeting*, 8–11 January 1990 (Reno, Nevada), paper AIAA–90–0500.

CLEMENS, N. T. and MUNGAL, M. G. [1990] "Two- and Three-Dimensional Effects in the Supersonic Mixing Layer," 26th *AIAA/SAE/ASME/ASEE Joint Propulsion Conference* (Orlando, FL), 10–12 July 1990, AIAA–90–1978.

COHEN, N. and BOTT, J. F. [1982] "Review of Rate Data for Reactions of Interest in HF and DF Lasers," AFWL Report SD–TR–82–86.

COLES, D. [1981] "Prospects for Useful Research on Coherent Structure in Turbulent Shear Flow," *Proc. Indian Acad. Sci. (Eng. Sci.)* 4(2), 111–127.

DIMOTAKIS, P. E. [1984] "Two-dimensional shear-layer entrainment," *AIAA* 22nd *Aerospace Sciences Meeting*, 9–12 January 1984 (Reno, Nevada), AIAA–84–0368. Published, *AIAA J.* 24(11), 1791–1796 (1986).

DIMOTAKIS, P. E. [1987] "Turbulent shear layer mixing with fast chemical reactions," US-France Workshop on Turbulent Reactive Flows (Rouen, France), 7–10 July 1987. Published: *Turbulent Reactive Flows*, (eds. R. Borghi and S. N. B. Murthy, *Lecture Notes in Engineering* 40, Springer-Verlag New York Inc., 1989), 417–485.

DIMOTAKIS, P. E. [1989] "Turbulent Free Shear Layer Mixing," *AIAA* 27th *Aerospace Sciences Meeting*, 9–12 January 1989 (Reno, Nevada), AIAA–89–0262.

DIMOTAKIS, P. E. [1991] "On the convection velocity of turbulent structures in supersonic shear layers," *AIAA* 22nd *Fluid Dynamics, Plasma Dynamics and Lasers Conference* (Honolulu, 24–26 June 1991), AIAA–91–1724.

DIMOTAKIS, P. E. and HALL, J. L. [1987] "A simple model for finite chemical kinetics analysis of supersonic turbulent shear layer combustion," AIAA/SAE/ASME/ASEE 23rd Joint Propulsion Meeting (La Jolla, CA), 29 June - 1 July 1987, AIAA Paper 87–1879.

FOURGUETTE, D., MUNGAL, M. G. and DIBBLE, R. [1990] "Time Evolution of the Shear Layer of an Axisymmetric Supersonic Jet at Matched Conditions," *AIAA* 28th *Aerospace Sciences Meeting*, 8–11 January 1990 (Reno, Nevada), AIAA Paper 90-0508.

GOEBEL, S. G. and DUTTON, J. C. [1990] "An Experimental Investigation of Compressible, Turbulent Mixing Layers," Technical Report Number UILU ENG 90-4005.

HALL, J. L. [1991] *An Experimental Investigation of Structure, Mixing and Combustion in Compressible Turbulent Shear Layers*, Ph.D. thesis, California Institute of Technology.

HALL, J. L., DIMOTAKIS, P. E. and ROSEMANN, H. [1991] "Experiments in Non-Reacting Compressible Shear Layers," *AIAA* 29th *Aerospace Sciences Meeting*, 7–10 January 1991 (Reno, Nevada), AIAA Paper 91-0629.

HERMANSON, J. C. and DIMOTAKIS, P. E. [1989] "Effects of heat release in a turbulent reacting shear layer," *J. Fluid Mech.* **199**, 333–375.

JACHIMOWSKI, C. J. [1988] "An Analytical Study of the Hydrogen-Air Reaction Mechanism With Application to Scramjet Combustion," NASA Tech. Paper 2791.

KOOCHESFAHANI, M. M. and DIMOTAKIS, P. E. [1986] "Mixing and chemical reactions in a turbulent liquid mixing layer," *J. Fluid Mech.* **170**, 83–112.

LELE, S. K. [1989] "Direct Numerical Simulation of Compressible Free Shear Flows," *AIAA* 27th *Aerospace Sciences Meeting*, 9–12 January 1989 (Reno, Nevada), AIAA Paper 89–0374.

MCINTYRE, S. S. and SETTLES, G. S. [1991] "Optical Experiments on Axisymmetric Compressible Turbulent Mixing Layers," *AIAA* 29th *Aerospace Sciences Meeting*, 7–10 January 1991 (Reno, Nevada), AIAA paper 91-0623.

MUNGAL, M. G. and DIMOTAKIS, P. E. [1984] "Mixing and combustion with low heat release in a turbulent mixing layer," *J. Fluid Mech.* **148**, 349-382.

MUNGAL, M. G, HERMANSON, J. C. and DIMOTAKIS, P. E. [1985] "Reynolds Number Effects on Mixing and Combustion in a Reacting Shear Layer," *AIAA J.* **23**(9), 1418–1423.

PAPAMOSCHOU, D. [1991] "Structure of the compressible turbulent shear layer," *AIAA J.* **29**(5), 680–681.

PAPAMOSCHOU, D. and ROSHKO, A. [1988] "The Compressible Turbulent Shear Layer: An Experimental Study," *J. Fluid Mech.* **197**, 453–477.

RAGAB, S. A. and SHEEN, S. [1990] "Numerical Simulation of a Compressible Mixing Layer," *AIAA* 21st *Fluid Dynamics, Plasma Dynamics and Lasers Conference* (Seattle, Washington), 18–20 June 1990, AIAA–90–1669.

SANDHAM, N. D. and REYNOLDS, W. C. [1990] "Compressible Mixing Layer: Linear Theory and Direct Simulation," *AIAA J.* **28**(4), 618–624.

SHAU, Y. R. and DOLLING, D. S. [1990] "The Detection of Large Scale Structure in Undisturbed and Disturbed Compressible Shear Layers," *AIAA* 28th *Aerospace Sciences Meeting*, 8–11 January 1990 (Reno, Nevada), AIAA–90–0711.

TAM, C. K. W. and HU, F. Q. [1989] "The instability and acoustic wave modes of supersonic mixing layers inside a rectangular channel," *J. Fluid Mech.* **203**, 51–76.

ZHUANG, M., KUBOTA, T. and DIMOTAKIS, P. E. [1988] "On the Stability of Inviscid, Compressible Free Shear Layers," Proceedings, *First National Fluid Dynamics Congress*, 25-28 July 1988 (Cincinnati, Ohio), **II**, 768–773.

ZHUANG, M., DIMOTAKIS, P. E. and KUBOTA, T. [1990] "The Effect of Walls on a Spatially Growing Supersonic Shear Layer," *Phys. Fluids* A **2**(4), 599–604.

Table 1: Description Of The Hydrogen-Fluorine-Nitric Oxide Chemical Reaction Mechanism

No.	Reaction	Source	A	β	E
1	$NO + F_2 \rightarrow NOF + F$	Baulch	4.2×10^{11}	0.0	2285
2	$NO + F + M \rightarrow NOF + M$	Baulch	3.0×10^{16}	0.0	0
3	$H + F_2 \rightarrow HF + F$	Cohen-Bott	2.9×10^{9}	1.4	1325
4	$F + H_2 \rightarrow HF + H$	Cohen-Bott	2.7×10^{12}	0.5	634
5	$F_2 + M \rightarrow F + F + M$	Baulch	2.1×10^{13}	0.0	33700
6	$H + F + M \rightarrow HF + M$	Baulch	7.5×10^{18}	−1.0	0
7	$H + H + M \rightarrow H_2 + M$	Jachimowski	6.4×10^{17}	−1.0	0
8	$H + NO + M \rightarrow HNC + M$	Jachimowski	5.4×10^{15}	0.0	−302
9	$H + HNO \rightarrow NO + H_2$	Jachimowski	4.8×10^{12}	0.0	0

The kinetics data listed here are given in cgs units. The use of the symbol M in the above chemical equations denotes *any* chemical species present in the reacting mixture.

Table 2: Summary Of Test Cases

Case	3a	3b	3c	3d	3e
Side 1 Gases	1% H_2 .25% NO 98.75% N_2	2% H_2 .25% NO 97.75% N_2	4% H_2 .25% NO 95.75% N_2	8% H_2 .25% NO 91.75% N_2	2% H_2 .25% NO 97.75% N_2
Side 2 Gases	1% F_2 99% N_2	2% F_2 98% N_2	4% F_2 96% N_2	2% F_2 98% N_2	8% F_2 92% N_2
ϕ	1	1	1	1/4	4
ΔT_{flm}	89 K	181 K	365 K	295 K	291 K
$(\Delta T/\Delta T_{flm})_{max}$	0.344	0.596	0.573	0.522	0.561
δ_1	45.5 mm	48.5 mm	49.8 mm	64.2 mm	48.7 mm
δ_P/δ_1	0.179	0.276	0.276	0.243	0.259
Da	0.23	1.4	5.3	1.7	18
β	2°	0.5°	−1°	0.5°	0.5°

Table 2 (Continued)

Case	2a	2b	2c	1a	1b
Side 1 Gases	2% H_2 .25% NO 97.75% He	4% H_2 .25% NO 95.75% He	6% H_2 .25% NO 93.75% He	9% H_2 .25% NO 90.75 He	3% H_2 .25% NO 96.75% He
Side 2 Gases	2% F_2 98% N_2	4% F_2 96% N_2	6% F_2 94% N_2	3% F_2 97% Ar	9% F_2 91% Ar
ϕ	1	1	1	1/3	3
ΔT_{flm}	214 K	425 K	633 K	578 K	575 K
$(\Delta T/\Delta T_{flm})_{max}$	0.534	0.627	0.664	0.471	0.620
δ_1	60.5 mm	54.7 mm	55.2 mm	54.3 mm	62.7 mm
δ_P/δ_1	0.198	0.252	0.262	0.188	0.226
Da	0.34 → 1.7	1.4 → 4.0	2.8 → 5.6	0.9 → 3.0	5.4 → 10.5
β	0.2°	−1°	−1.5°	−1.5°	−1.5°

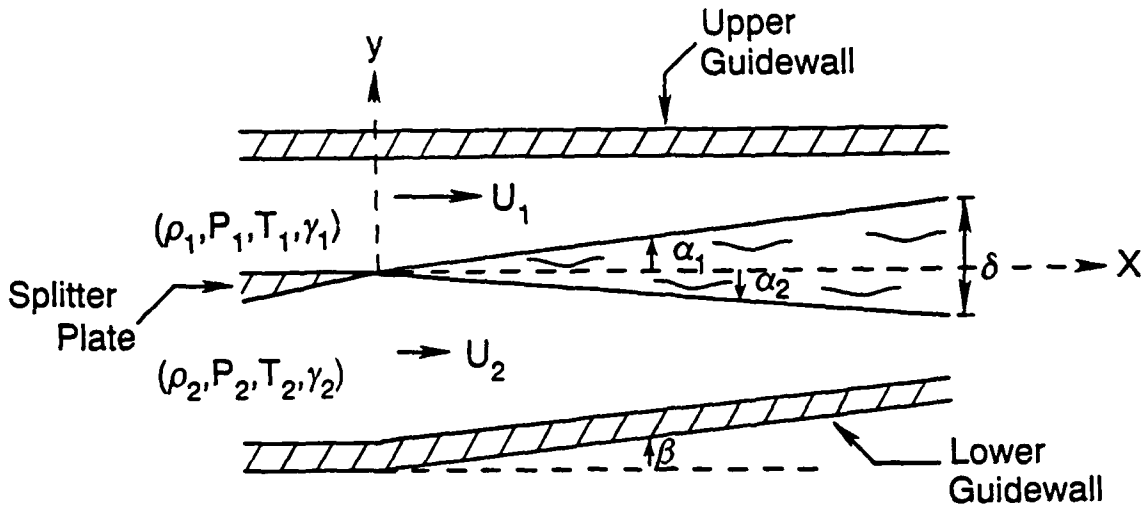

Fig. 1: Shear Layer Geometry

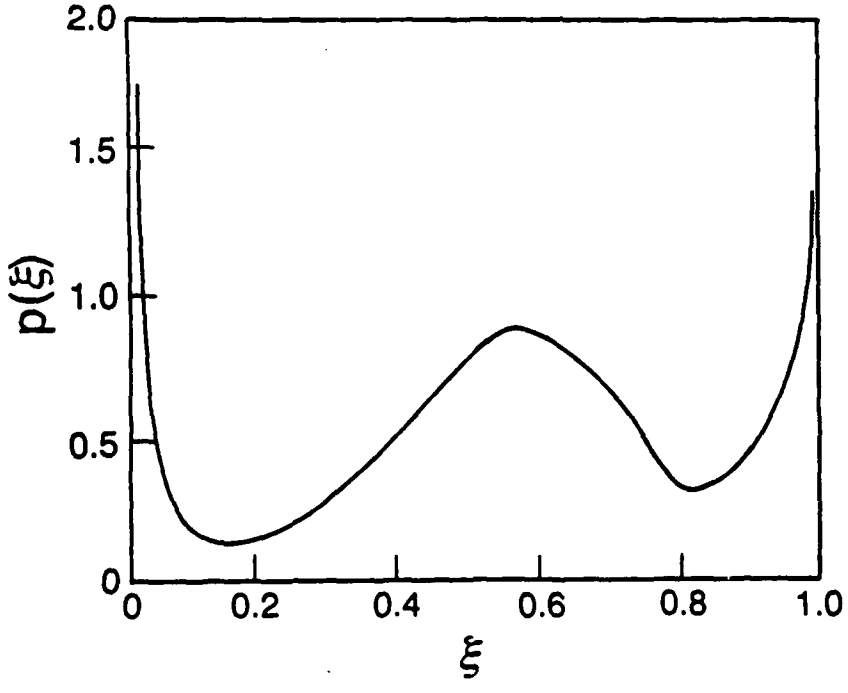

Fig. 2: Sketch Of The Mixture Ratio PDF For An Incompressible Shear Layer (Dimotakis 1989).

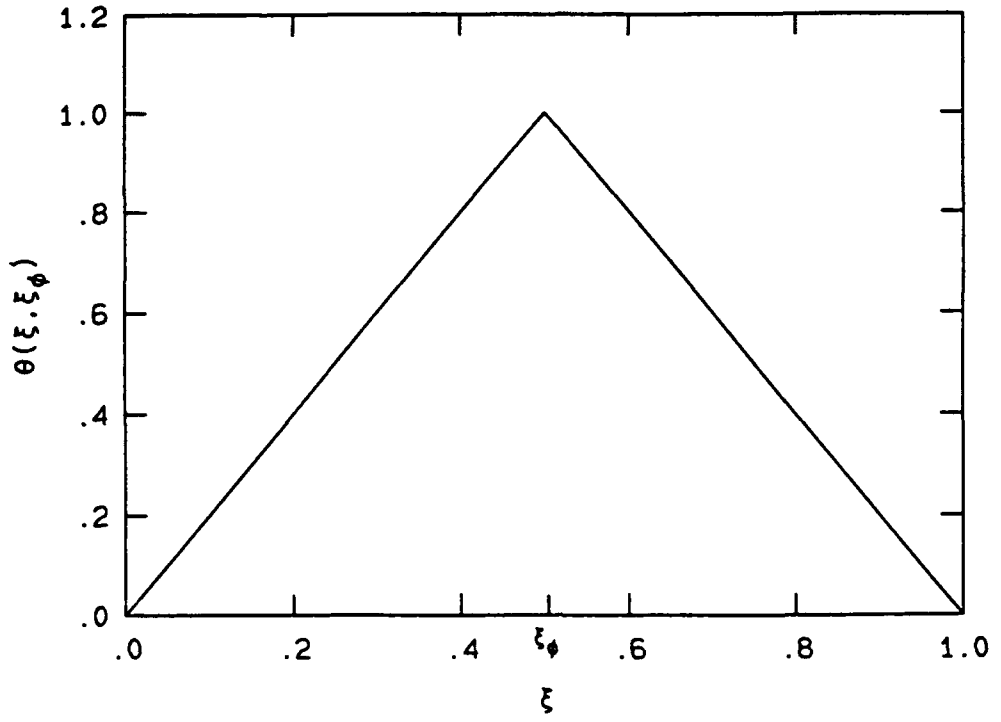

Fig. 3: Normalized Product Formation In The Fast-Chemistry Regime.

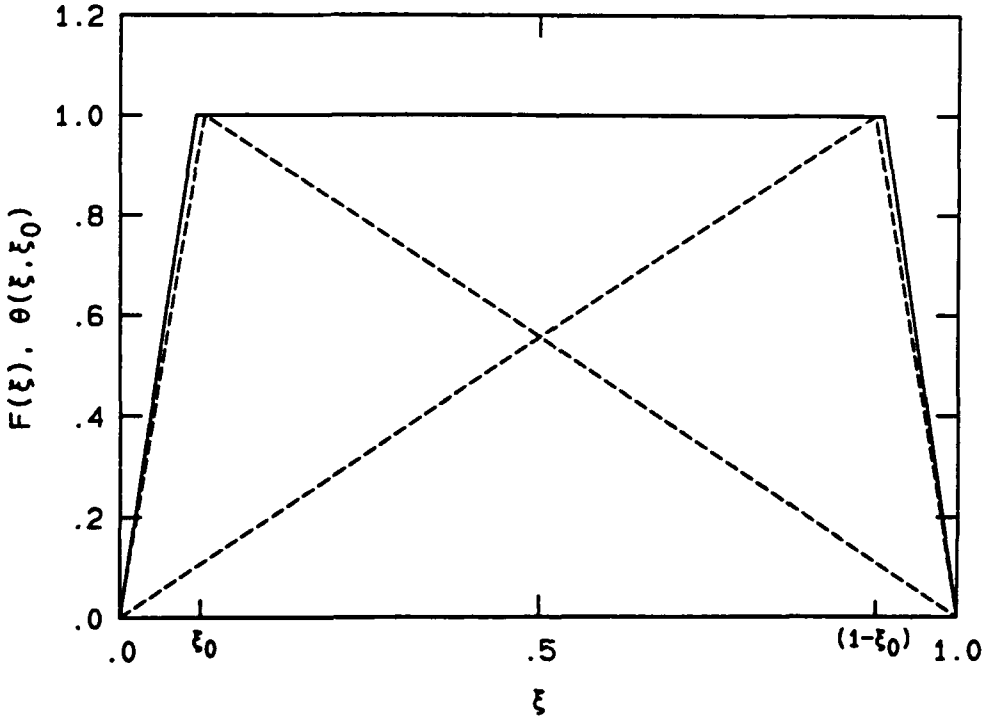

Fig. 4: Approximation Of The Top-Hat Profile Constructed By A Flip Experiment.

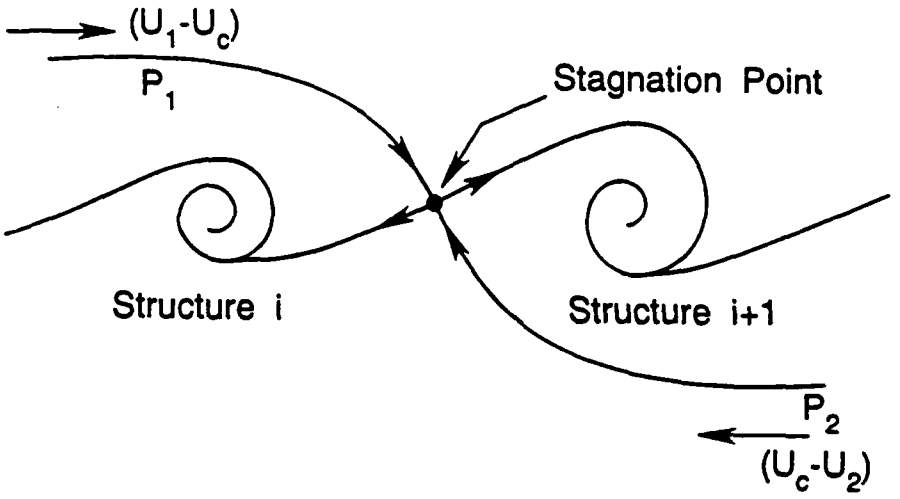

Fig. 5: Convective-Frame Isentropic Pressure-Matching Model For The Turbulent Shear Layer.

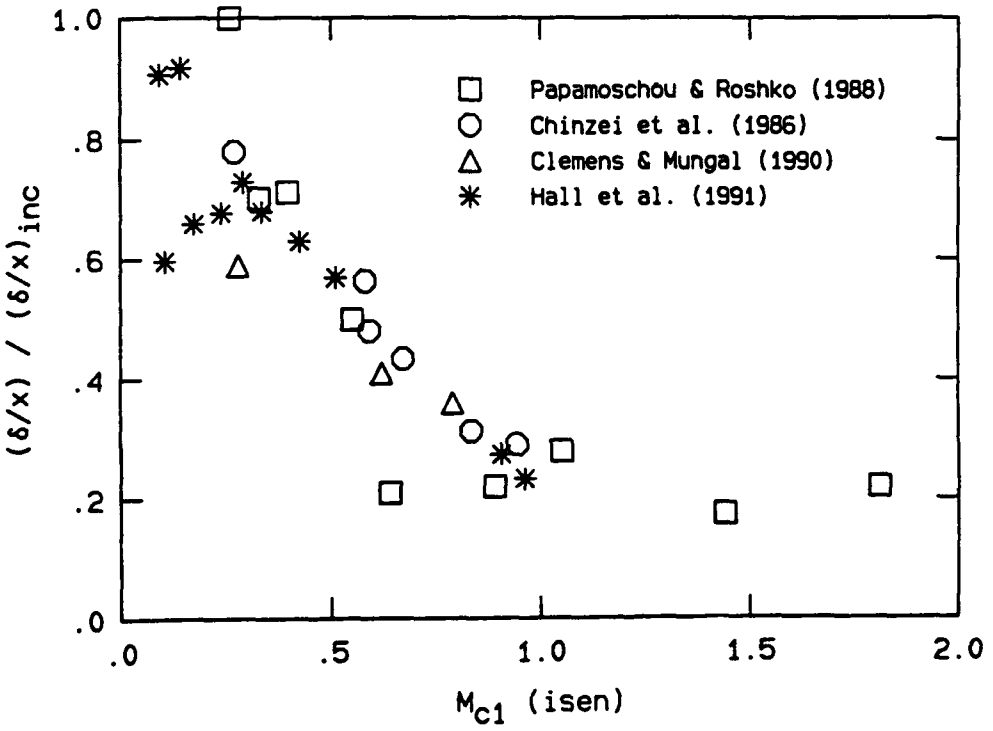

Fig. 6: Normalized Growth Rate Data Accumulated By Various Researchers.

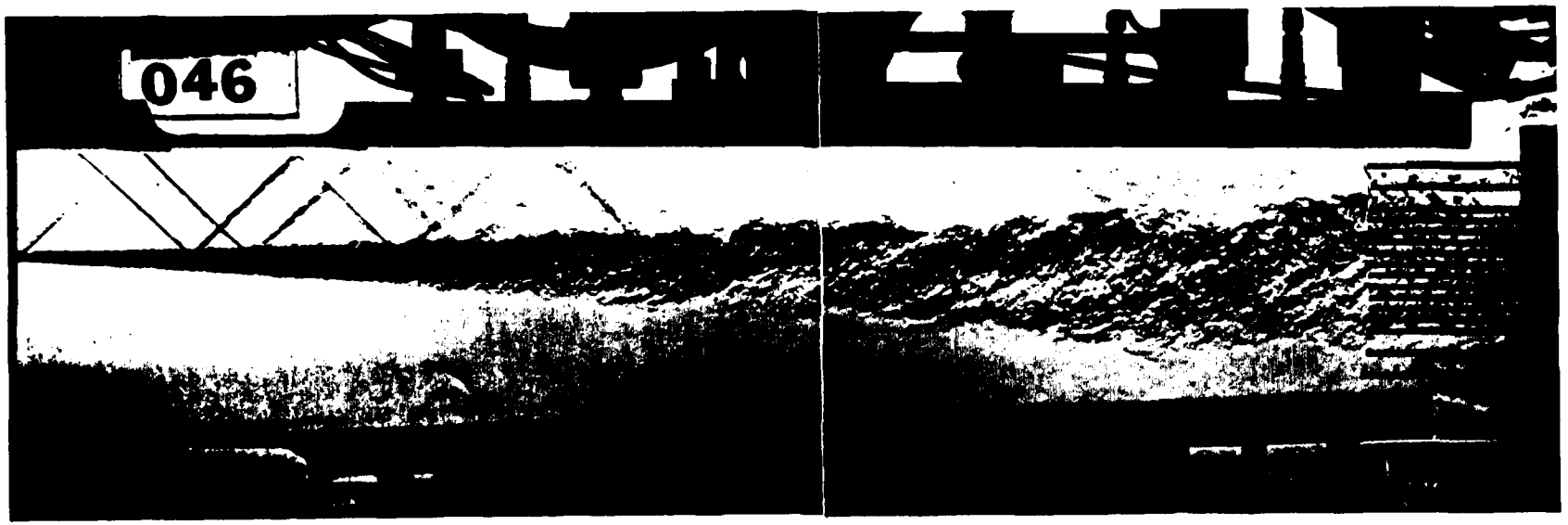

Fig. 7: Composite Schlieren Photograph Of Case 3 (N_2/N_2) Non-Reacting Flow.

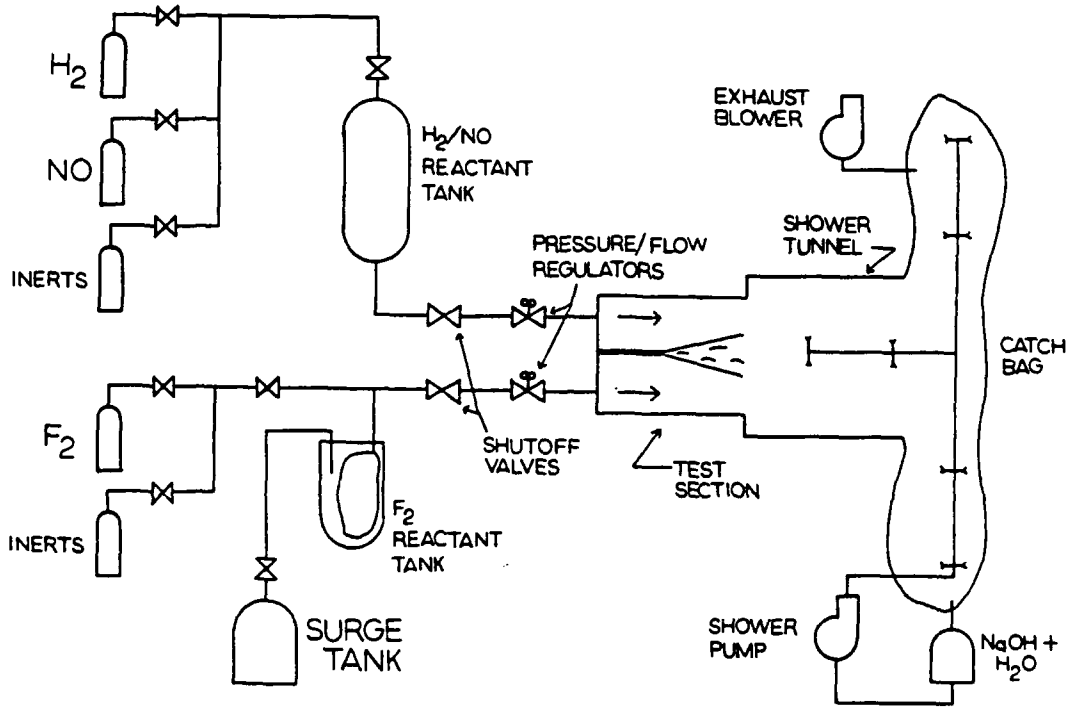

Fig. 8: Flow Schematic Of The Supersonic Hydrogen-Fluorine Shear Layer Combustion Facility.

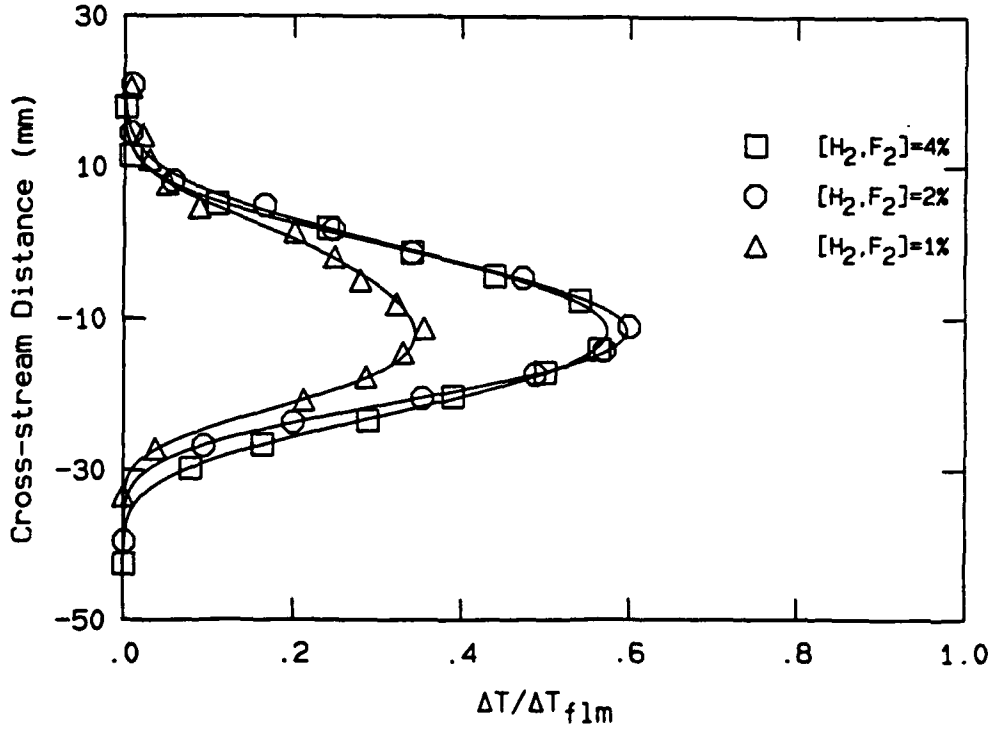

Fig. 9: Normalized Temperature Profiles For The Case 3 Kinetics Experiment.

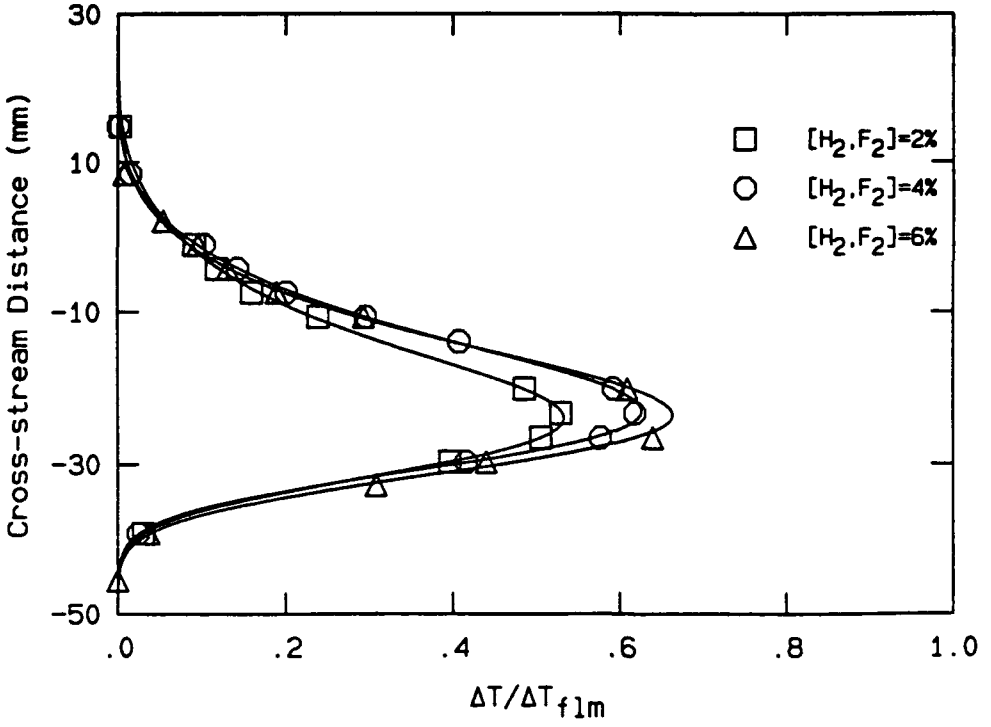

Fig. 10: Normalized Temperature Profiles For The Case 2 Kinetics Experiment.

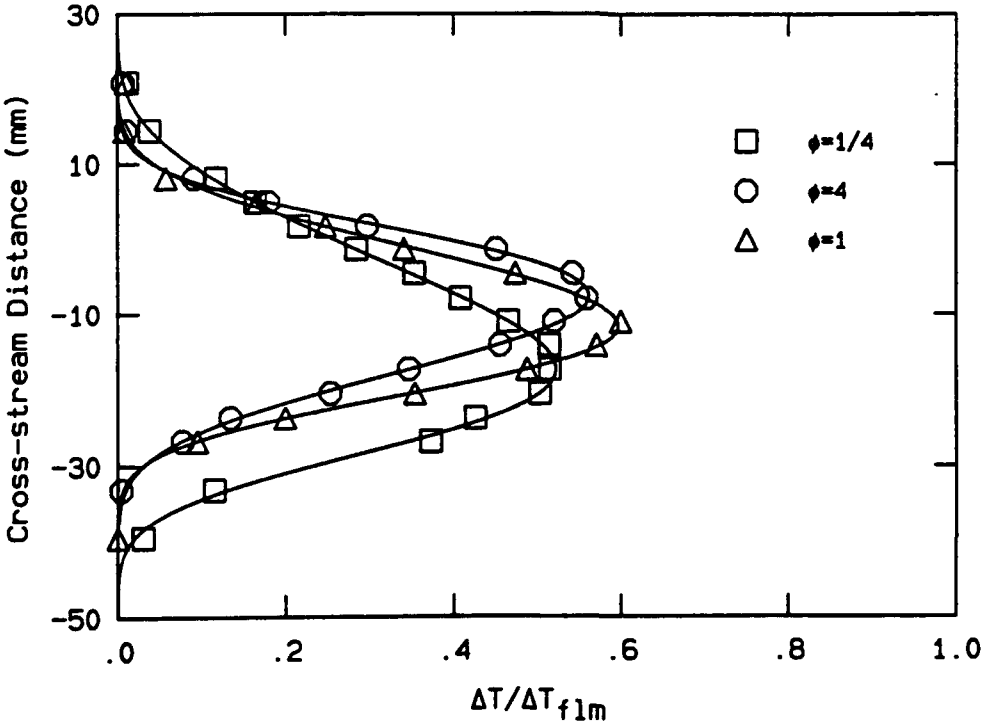

Fig. 12: Normalized Temperature Profiles For The Case 3 Flip Experiment.

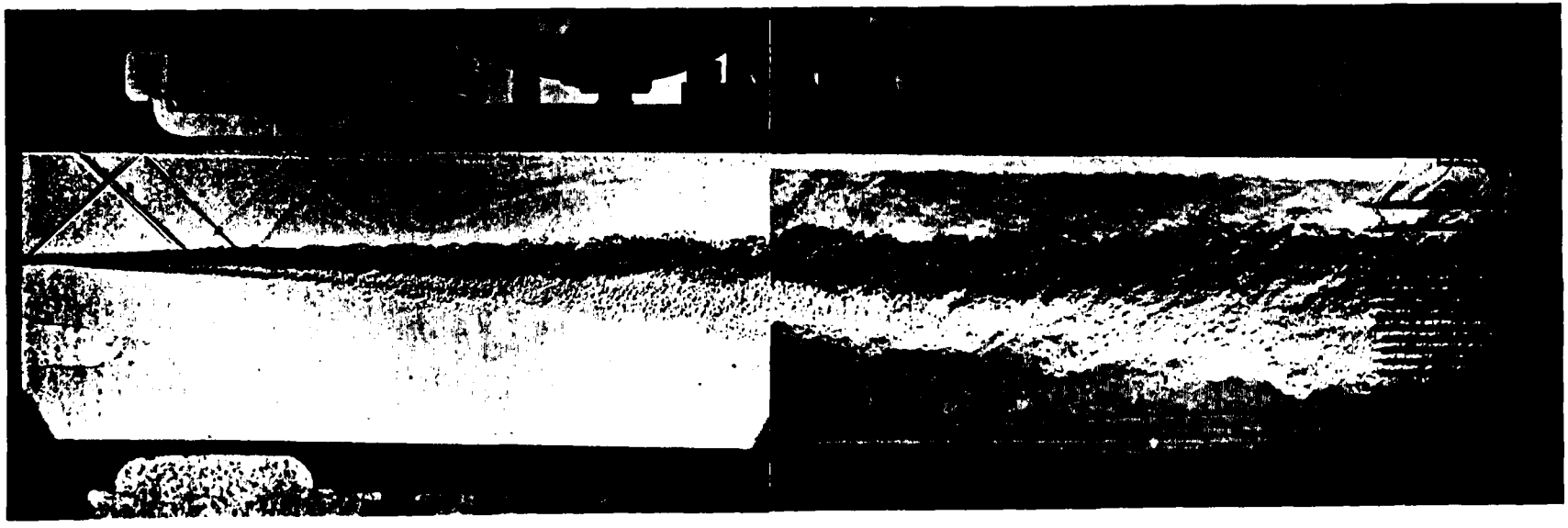

Fig. 11: Composite Schlieren Photograph Of Case 3c (N_2/N_2 Diluents) Reacting Flow.

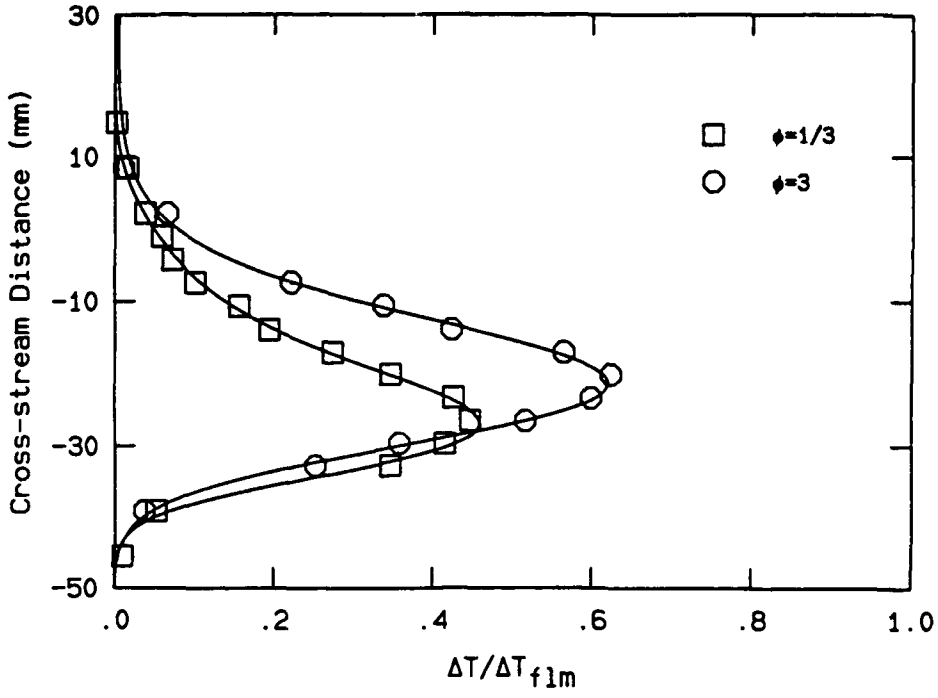

Fig. 13: Normalized Temperature Profiles For The Case 1 Flip Experiment.

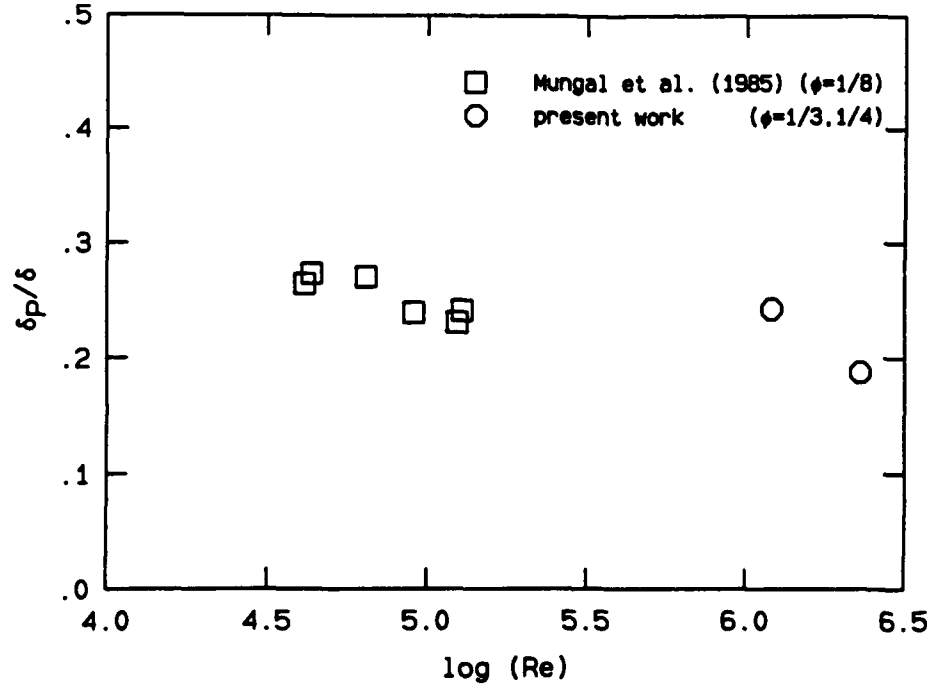

Fig. 14: Variation of Product Thickness With Reynolds Number At Low ϕ.

Appendix E

MILLER, P. L. AND DIMOTAKIS, P. E. [1991] "Stochastic geometric properties of scalar interfaces in turbulent jets," *Phys. Fluids A* **3**(1), 168–177.

Stochastic geometric properties of scalar interfaces in turbulent jets

Paul L. Miller and Paul E. Dimotakis
Graduate Aeronautical Laboratories, California Institute of Technology, Pasadena, California 91125

(Received 26 July 1989; accepted 14 September 1990)

Experiments were conducted in which the behavior of scalar interfaces in turbulent jets was examined, using laser-induced fluorescence (LIF) techniques. The experiments were carried out in a high Schmidt number fluid (water), on the jet centerline, over a jet Reynolds number range of 1000 < Re < 24 000. Both two-dimensional scalar data, $c(r,t)$ at fixed x/d, and one-dimensional scalar data, $c(t)$ at fixed x/d and r/x, were analyzed using standard one- and two-dimensional fractal box-counting algorithms. Careful treatment was given to the handling of noise. Both long and short records as well as off-centerline measurements were also investigated. The important effect of threshold upon the results is discussed. No evidence was found of a constant (power-law) fractal dimension over the range of Reynolds numbers studied. On the other hand, the results are consistent with the computed behavior of a simple stochastic model of interface geometry.

I. INTRODUCTION

The proposals of Mandelbrot[1-4] to account for the stochastic geometry of turbulent interfaces in terms of power-law fractal similarity generated considerable hope in the turbulence community. The proposed formalism held the promise of an alternate interpretation of a variety of important quantities in turbulence related to energy spectra and dissipation as well as a description of the behavior of the interfacial surface of scalars and mixing down to molecular diffusion scales (e.g., Gouldin[5] and Sreenivasan *et al.*[6]). The availability of scalar concentration and image data from several turbulent flows in our laboratory led us to a search for a power-law fractal description, i.e., a similarity scaling wherein the number of elements $N(\lambda)$, of an extent λ, required to cover the scalar interface would be given by

$$N(\lambda) \propto \lambda^{-D}. \tag{1}$$

In the work presented here, we report on the results of our investigations on the behavior of scalar interfaces in turbulent jets using laser induced fluorescence (LIF) techniques and a fractal box-counting algorithm to analyze the data. In the time since this work was begun, results have appeared in the literature of experimental measures of fractals in turbulent shear flows by several investigations. See, for example, Sreenivasan and Meneveau,[7] Sreenivasan *et al.*,[8] and Prasad and Sreenivasan.[9,10] They report that, in a variety of turbulent flows, including turbulent jets, scalar isoconcentration surfaces exhibit a constant fractal dimension in a small neighborhood of about $D = 2.36$.

II. APPARATUS AND PROCEDURE

The experiments were carried out utilizing the facility shown in Fig. 1. A large rectangular water tank of about two cubic meters volume acted as the (discharge) reservoir. Large windows on all sides of the tank provided optical access. To establish the flow, the jet plenum was filled with water tagged by a fluorescent laser dye (sodium fluorescein), and air was sonically metered to drive the jet fluid at constant velocity through a 2.54 mm (0.1 in.) diam nozzle at the base of the plenum. The beam from an argon ion laser was passed through appropriate optics and aligned radially through the centerline of the jet. A beam stop prevented reflections from the opposite window. In the two-dimensional measurements, a line segment centered on the jet axis, at $x/d = 300$, was imaged onto a linear photodiode array. The array was then scanned during a run, providing streak image data of concentration in one spatial dimension versus time (cf. Dimotakis *et al.*,[10] Dahm,[11] Green and Losi,[12] and Dahm and Dimotakis[13]).

For the single-point measurements, the laser beam optics were designed to generate a small Gaussian waist at the focus. A low laser power of 1.0 W was used to avoid heating of the dyed fluid in the very small focal volume and to prevent saturation. The plenum dye concentration was kept less than 10^{-6} M. Consequently, the much lower concentrations at the measuring station did not significantly attenuate or steer the beam. The resulting signal to noise was limited primarily by the 12-bit dynamic range of the A/D converter, rather than shot noise from the low fluorescence intensity.

The single-point measurements were made utilizing a low $f\#$ lens to collect light from a very short segment centered at the waist of the focused laser beam (on the jet centerline, at $x/d = 100$) onto a photomultiplier tube, yielding single-point concentration values versus time. An optical low-pass filter eliminated background laser light, passing only the frequency-shifted fluorescence. A slit spatial filter defined the length of the laser line segment sampled. The slit width was chosen such that the sampling volume was roughly cubic in shape, about 80 μm on each side. The use of the slit rather than a pinhole ensured that any small beam movements in the vertical direction did not alter the measurement volume. The long Rayleigh range and latitude in the depth of field minimized the effect of motion in either of the two horizontal directions. Data acquisition was computer controlled. The signal amplifier incorporated a three-pole Butterworth filter, with a cutoff frequency set slightly under 10 kHz. The data were sampled at 20 kHz for all the runs.

 0899-8213/91/010168-10$02.00

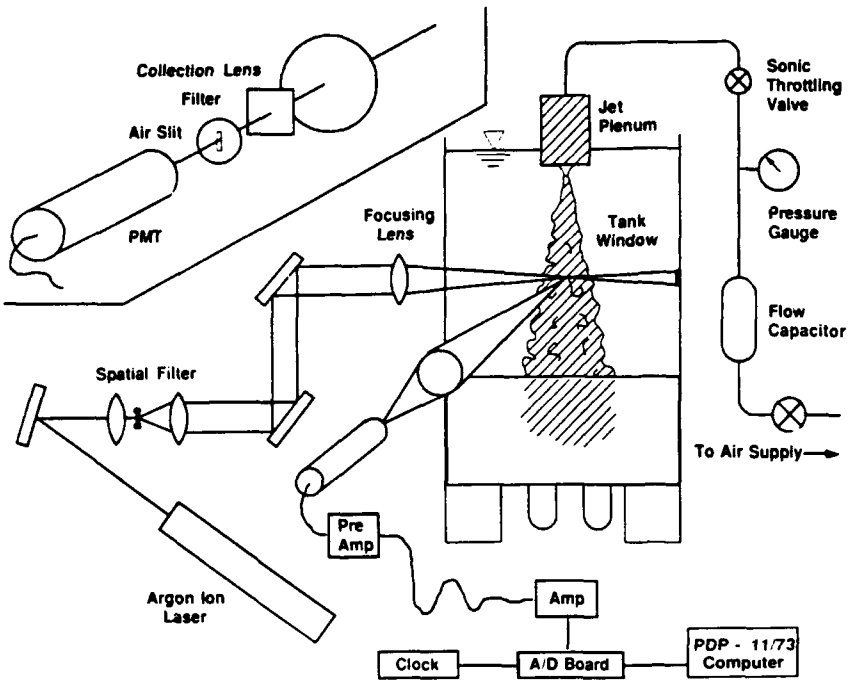

FIG. 1. Experimental apparatus

III. RESULTS AND DISCUSSION

The single-point scalar concentration measurements were made as a function of time on the jet centerline, for a range of Reynolds numbers from 2940 to 23 400. The Reynolds number used here is defined as

$$\mathrm{Re} = u_0 d/\nu, \tag{2}$$

where u_0 is the jet nozzle velocity, d is the jet nozzle diameter, and ν is the kinematic viscosity. Careful consideration was given to the treatment of noise. Specifically, power spectra of the data were calculated, allowing the optimal (least-mean-squared error) Wiener filter (Wiener,[14] Press *et al.*,[15] Dowling,[16] and Dowling *et al.*[17]) to be obtained. The data were then convolved with the Wiener kernel to obtain the optimally estimated signal, consistent with the detection noise level in each run. Sample concentration power spectra, $S_c(f)$, before and after the filtering process, are compared in Fig. 2. The normalization time τ_{LS} is the large scale passage time, δ/U_c, where δ is the local visual jet diameter and U_c is the mean centerline velocity calculated from the decay law reported by Chen and Rodi[18] (cf. Dowling[16]).

In order to apply the Wiener filter effectively, the data were intentionally oversampled. This is clearly seen by the extent of the noise floor in the unfiltered spectrum of Fig. 2. Note that the signal-to-noise ratio (SNR) is a function of frequency, since the total power spectrum increases with decreasing frequency, while the noise is well described as white, or of constant level. We recognize that there are not only requirements of spatial and temporal resolution on such measurements, but also what we could call "SNR resolution," located roughly at the intersection of the signal spectrum and the noise floor. In the single-point measurements discussed here, spatial resolution was typically the most restrictive of the three.

The Wiener-filtered data were subsequently thresholded and transitions, or crossings of the threshold value, were located. The threshold value chosen was the local mean concentration $\bar{c}$. This is an unambiguous choice: it is close to both the mode of the concentration PDF and the value where the most transitions are obtained. From the vantage point of scalar diffusion, $\bar{c}$ is also the value toward which the local scalar field is driven by the diffusion process (scalar dissipation). The effect of the choice of alternate thresholds on the results is, however, an important issue and is discussed below.

The resulting record of transition locations was then processed using a one-dimensional fractal box-counting algorithm. The box-counting algorithm determines the num-

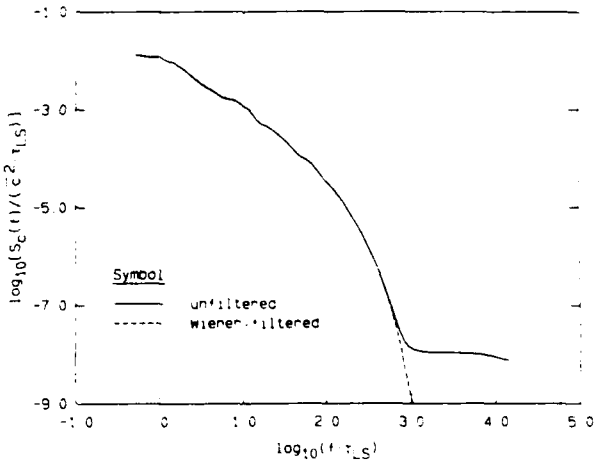

FIG. 2. Demonstration of the Wiener filter.

ber N of "tiles" (contiguous, constant length segments) required to cover the transition locations on a record, as a function of the tile size λ. The logarithm of $N(\lambda)$ may then be plotted as a function of $\log(\lambda)$. The logarithmic derivative,

$$D(\lambda) \equiv -d\log[N(\lambda)]/d\log(\lambda), \tag{3}$$

which is equal to minus the slope of the curve on this log–log plot, is then interpreted as the associated (local scale) fractal dimension.

As a demonstration of the box-counting algorithm utilized, a record was generated numerically of a Cantor set (with a necessarily finite range of scales) and processed. The result of the calculation is included in Fig. 3. The calculated points are connected with straight lines in the plots to aid the eye. The constant slope region is clearly visible, although there is some fluctuation about the expected analytic value of 0.631. This may correspond to the oscillations observed by Smith *et al.*[19] in numerical calculations of the fractal dimension for this set. The deviation at the smallest values of λ is attributable to the lack of smaller features in this representation of the Cantor set. At these smallest scales, transitions occupy an entire box on the line containing the set, while in a true Cantor set, the transitions have zero measure. Thus there are fewer transitions than there ought to be and this reduces $D(\lambda)$ for small λ. At the largest scales, with λ approaching the finite record length, there are no gaps between transitions of the size of the record or larger. As a result, large gaps are under-represented and $D(\lambda)$ rises. The deviations from the power-law fractal similarity behavior at the two extremes are therefore a consequence of the finite range of scales represented in the record and not an artifact of the processing.

The log–log plots of $N(\lambda)$ and plots of the resulting $D(\lambda)$ for our high resolution, single-point on-axis concentration measurements in the jet, using a threshold value equal to the mean concentration, are shown in Figs. 4 and 5. The length scale, estimated from the calculated mean (centerline) velocity, has been expressed in absolute length (meters).

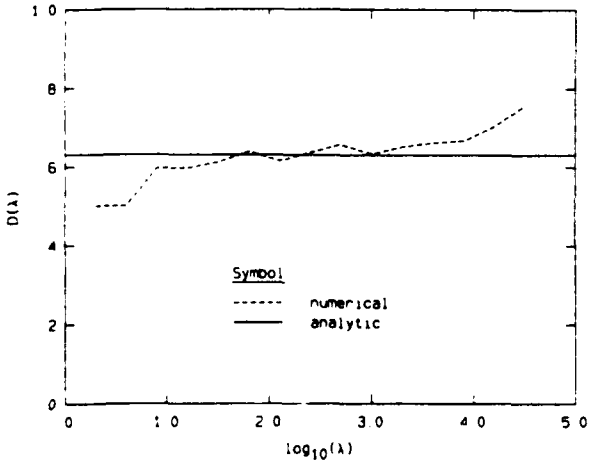

FIG. 3. Calculation for the Cantor set.

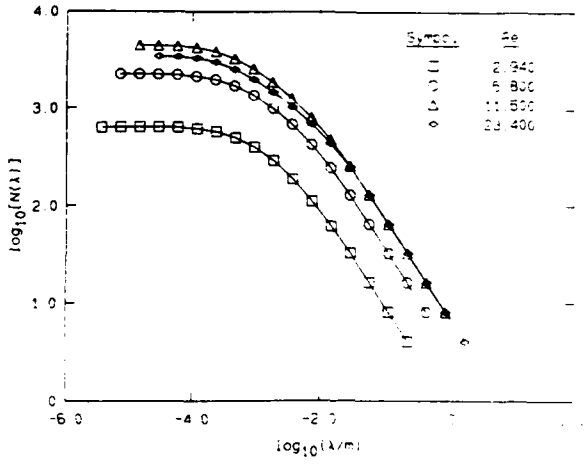

FIG. 4. Log–log tiling plots of centerline data for four Reynolds numbers ($x/d = 100$). Note that $\log_{10}(\delta/m) \simeq -1.0$.

If the data were characterized by a constant (power-law) fractal behavior, one would observe a horizontal region on the curves in Fig. 5. As can be seen, *there is no evidence of a constant value* on the $D(\lambda)$ plots, other than the limiting values of 0 and 1. It is for this reason that we denoted the logarithmic derivative of the $N(\lambda)$ curve by $D(\lambda)$ [Eq. (3)], rather than simply D. The observed smooth variation in $D(\lambda)$ occurs over a range of equivalent spatial scales from below the Kolmogorov scale (see the discussion below), up to the outer large scales of the flow. The limiting value of 1 at the large tile sizes indicates that every tile of sufficient length covers transitions. This is to be expected for scales on the order of the jet diameter (about 11 cm for the data in Fig. 5), or larger, since over such a distance (or corresponding time) a crossing of the mean concentration level is almost certain. Failure to reach an asymptotic value of unity would indicate that either the data record was of insufficient length to capture the largest scales of the flow, or that the processing

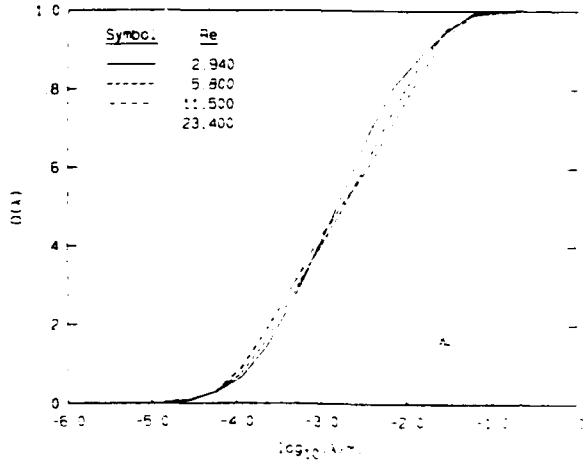

FIG. 5. Corresponding $D(\lambda)$ plots for Fig. 4. Here again $\log_{10}(\delta/m) \simeq -1.0$. For small scales, see the text.

algorithm stopped at a tile size shorter than the largest scales.

Note that all four curves in Fig. 5 merge in the vicinity of 80 μm. This is consistent with our estimate of the spatial resolution of these measurements. To see how this relates to the spatial resolution requirements for this flow, we can estimate the Kolmogorov[20] scale directly from its definition in terms of the mean energy dissipation rate, i.e.,

$$\lambda_K \equiv (\nu^3/\epsilon)^{1/4}. \tag{4}$$

Using the result of Friehe *et al.*[21] for the dissipation rate ϵ on the centerline of a turbulent jet (cf. Dowling[16]), i.e.,

$$\epsilon = 48(u_0^3/d)\left(\frac{(x - x_0)}{d}\right)^{-4}, \tag{5}$$

the Kolmogorov scales for these measurements are found to range from roughly 50 to 250 μm. By similarity arguments, the velocity field spatial scale where the action of viscosity will become important, say λ_v, will be some multiple of λ_K. Normalized energy spectra are found to break from a constant power law at a wave number k_v such that $k_v \lambda_K \simeq \frac{1}{8}$ (e.g., Chapman[22]). This yields an estimate of

$$\lambda_v = \pi/k_v \sim 25\lambda_K. \tag{6}$$

The smallest expected scalar diffusion (Batchelor[23]) scale λ_d is smaller yet by a factor of $Sc^{1/2}$, or 25–30 in this case, yielding an estimate for λ_d very close to λ_K (in water). These estimates are corroborated by the gas phase experiments of Dowling[16] as well as the measurements in water by Buch and Dahm[24] and suggest that the smallest diffusion scales may have been resolved in these experiments, at least at the lower Reynolds numbers.

As mentioned previously, earlier measurements were also made using a 512 pixel linear photodiode array, yielding line images versus time (two-dimensional streak data). The images were recorded at Reynolds numbers of 1000, 2000, and 3000, and were centered on the jet axis, spanning about a tenth of the local jet diameter (at $x/d = 300$). The local Kolmogorov scale was resolved in each case. These data were analyzed in several ways. First, the individual time records of each of the 512 pixels of the array were processed using the box-counting algorithm discussed previously. The results matched those of the single-point data. Next, the 512 element line images were processed separately, providing us with spatial results without invoking Taylor's hypothesis. Once again, while the dynamic range of the data is limited by the number of pixels in the array, we find a similar behavior (Fig. 6).

In addition to the one-dimensional box-counting algorithm, a two-dimensional tiling program was also employed on the streak image data. For those data, the data acquisition rate of the linear array was adjusted to be proportional to the local flow velocity, providing a two-dimensional streak image. This minimized changes in the stretching between the spatial and temporal dimensions with changes in Reynolds number. The results are shown in Fig. 7. Note that since this result uses two-dimensional tiling, $D(\lambda)$ is now bounded by the limiting values of 1 and 2. Qualitatively, the results from the line images and the full streak images are similar. Nevertheless, there is a small and systematic quantitative difference—the slopes of the higher-dimensional data are steeper. We believe that this difference is not an artifact.

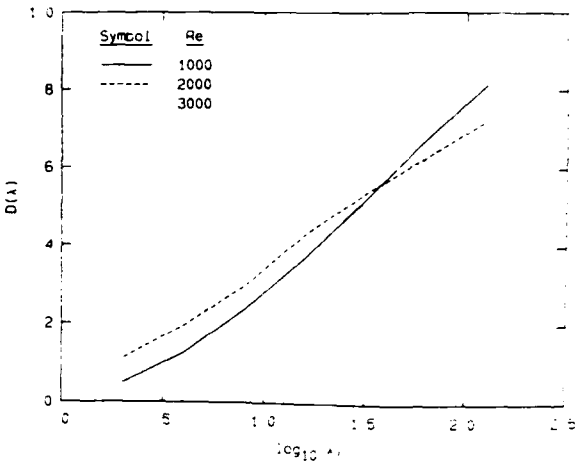

FIG. 6. Line image results.

Finally, single-point measurements were made off the jet centerline at $\eta = r/x$ of 0.06 and 0.13, at a Reynolds number of 8600. These results are shown in Fig. 8, with a corresponding centerline curve. The similarity in the three results is noteworthy.

This ensemble of on- and off-axis, one- and two-dimensional measurements is significant because it serves to examine the effect of analyzing temporal, rather than spatial, data. If one wishes to describe a spatial scalar interface, rather than an Eulerian point concentration history, some type of assumption is required, since we have insufficient information about the velocity field to make an exact conversion. We have used the calculated mean centerline velocity to convert the temporal data to spatial results in Fig. 5. Near the jet centerline, we feel this is acceptable, while near the edge of the jet, we recognize that the errors involved may not be negligible. Rather than open the issue of how accurate this

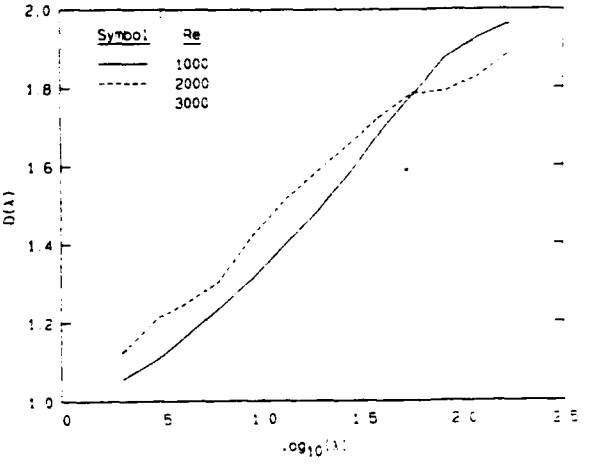

FIG. 7. Two-dimensional (streak image) results.

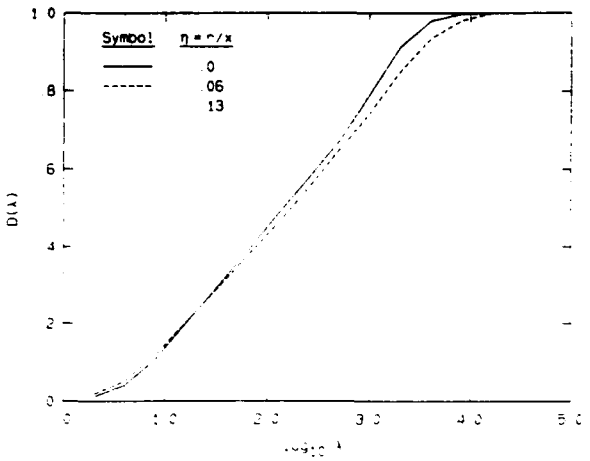

FIG. 8. Off-axis single-point results (Re = 8600, $\eta = r/x$).

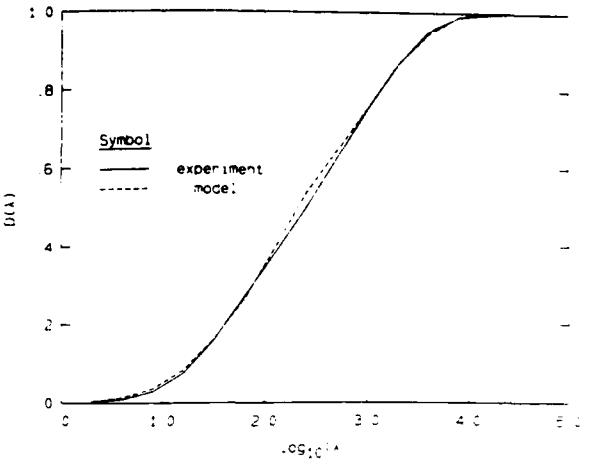

FIG. 9. Comparison of lognormal model and experiment (Re = 5800).

implementation of Taylor's hypothesis may be, we note *a posteriori* that the results are insensitive to its use. The behavior is qualitatively the same for the single-point measurements in Fig. 5, the off-axis results in Fig. 8, which could exhibit the greatest variance from Taylor's hypothesis, and the results in Fig. 6 from true (line image data). The latter, of course, do not utilize Taylor's hypothesis at all. The two-dimensional tiling algorithm and the corresponding results in Fig. 7 again demonstrate similar behavior.

It has been suggested (Sreenivasan and Meneveau[7]) that if long records are used in the box-counting algorithm, they may mask local power-law fractal behavior. We do not find this to be the case. This issue is discussed in the Appendix.

The persistence of these results may be traceable to a strong stochastic character of the interfaces. In an effort to model this behavior, we devised a simple Monte Carlo description of the threshold crossings. A program was written to produce a record of crossings that were randomly spaced with a lognormal distribution. PDF's of our measured crossing spacings independently show that the lognormal distribution is a good approximation. Two parameters, the location of the maximum and the width of the distribution, were allowed. Figure 9 includes the result for a Reynolds number of 5800. The agreement between model and experiment is good.

Finally, we wish to address the important issue of the choice of the value of the threshold. Recall that in the box-counting algorithm, a specific concentration value is chosen, and crossings of this threshold are located. These crossings correspond to the passage of an isoconcentration surface possessing the threshold value. For the results presented previously, the local mean concentration $\bar{c}$ was used as the threshold value. Recall that similar behavior is observed both on and off axis, despite the fact that the local (absolute) mean concentration changes significantly with $\eta = r/x$.

We examined the entire range of possible thresholds for our single-point data, both on axis and off axis at $\eta = 0.13$. Three-dimensional plots of $D(\lambda)$ versus threshold and $\log(\lambda)$ are shown in Figs. 10 and 11. A contour plot of the on-axis data offers an alternate representation of the results in Fig. 10 (Fig. 12). As can be seen, the continuous variation of the $D(\lambda)$ curves with λ persists for a rather large range of threshold values on either side of the local mean concentration. As the threshold is either increased or decreased, two effects are observed. The sloping region shifts position, achieving the asymptotic value of 1 at progressively larger scales, and a bump appears at smaller values of λ. While the

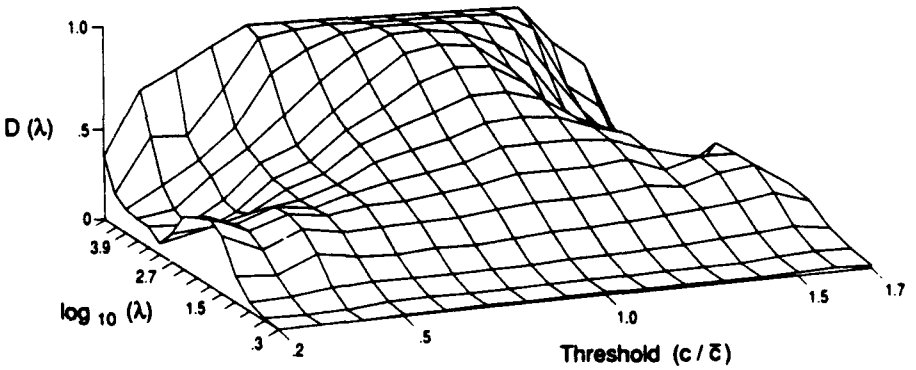

FIG. 10. Three-dimensional plot of $D(\lambda)$ versus threshold and λ for single-point, on-axis measurements (Re ≃ 10 000).

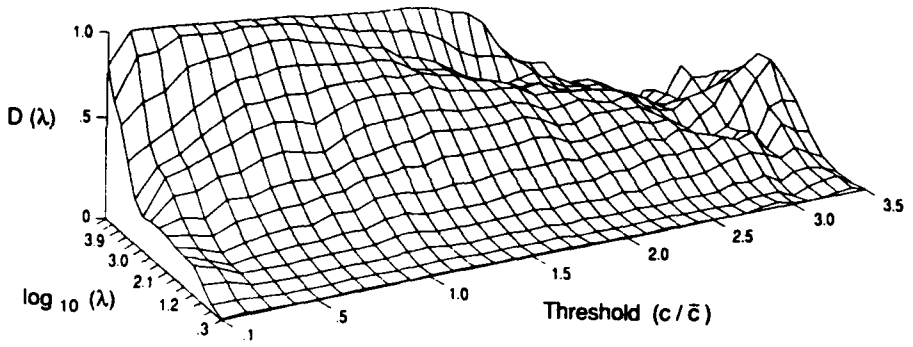

FIG. 11. Three-dimensional plot of $D(\lambda)$ versus threshold and λ for single-point, off-axis measurements ($Re \approx 10\,000$, $\eta = 0.13$).

linear scale may not make it clear, the off-axis data exhibit a similar bump at small scales as the on-axis data, when viewed at smaller values in logarithmic coordinates.

To investigate whether this behavior was a consequence of the random character of the concentration signal rather than the fluid dynamics of the turbulent jet, we processed data of laser light scattered from a very dilute, constant concentration solution. These data are essentially measurements of (shot) noise, possessing a white power spectrum. A narrow Gaussian filter was used as a cutoff to eliminate the highest frequencies. The corresponding three-dimensional plot of $D(\lambda)$ for these noise data is displayed as Fig. 13. The global behavior is very similar to Fig. 10, even though, for the noise data, no fluid mechanics are involved.

Note that, despite the qualitative similarities, there are several important quantitative differences between Fig. 10 and Fig. 13. The rise to the asymptotic value of 1 has a different slope in the two plots. This slope is a measure of the width of the distribution of scales. The scale at which the midpoint of the rise is found, which relates to the location of the maximum of the distribution, also varies. Finally, the range of normalized concentrations is much narrower in Fig. 13 than in Fig. 10, reflecting the very different transition PDF's in each case. While there is no particular relationship between these quantities for the noise data and the jet results, we do expect that they will provide useful information in the comparison of fluid flows. This topic, which is somewhat beyond the intent of the present paper, is left for future discussions.

To further understand the three-dimensional plots, we need to consider the nature of the concentration signal we are examining. The possible scalar values are bounded by zero and some upper limit, and the measured concentration time history exhibits many maxima and minima. Near the mean, relatively few of these extrema are encountered. On the other hand, for thresholds approaching the highest or lowest values detected, many such turning points are found, and they may dominate the statistics. Picture a local minimum in concentration, with a roughly parabolic dependence of $c(t)$ in its vicinity. Imagine then a threshold level that is slowly decreased toward the minimum value. Two threshold crossings are encountered, which, as the threshold is lowered, move closer together. These eventually (almost) join before the threshold drops below the minimum (recall that the signal is discretely sampled in time). Thus near the turning points there can be a separation of scales; one length is associated with the typical distance between extrema and the other is a much smaller scale associated with the spacing of crossings within pairs at each extremum.

This scale separation manifests itself in the $D(\lambda)$ plots in two primary ways. One is the appearance of a bump at the smallest scales, traceable to the double crossings at each extremum. This bump is indicative of a characteristic length at that scale. The second is that the rise of $D(\lambda)$ to its asymptotic value of unity is shifted to larger scales as the threshold is increased, or decreased, from the local mean. This is ascribable to what could be called conservation of spacing. Pairs of crossings drop out as the threshold moves past their extrema, producing a larger length scale associated with the distance between crossings to either side of the pair. This is enhanced by crossings within a pair coming closer together as the threshold approaches their extremum, causing the spaces between adjacent pairs to correspondingly increase.

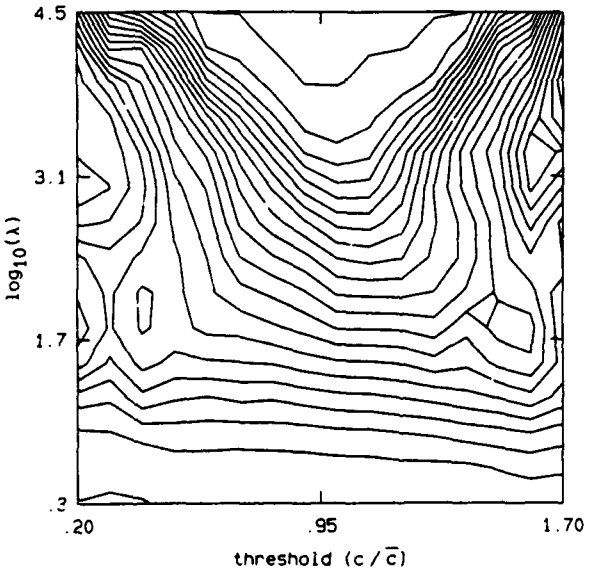

FIG. 12. Contour plot of data in Fig. 10.

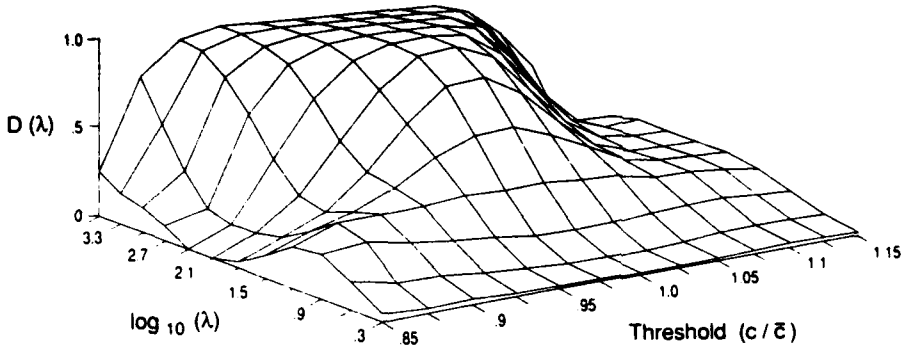

FIG. 13. Three-dimensional plot of $D(\lambda)$ for noise data.

Both the bump at small scales and the shift in the rise are evident in all of the three-dimensional $D(\lambda)$ plots.

IV. CONCLUSIONS

In this paper, we have discussed high resolution scalar field measurements conducted in the far field of a turbulent jet. We have examined single-point measurements, one-dimensional line images, two-dimensional streak images, ensembles of long records and short records, of on- and off-axis data in jet flows spanning over a decade in Reynolds number. We find no evidence that isoscalar surfaces are described by a fractal (power-law) similarity.

There have been a number of papers documenting experimental measurements of fractal dimension in turbulent flows, e.g., Sreenivasan and Meneveau,[7] Sreenivasan *et al.*,[6] Meneveau,[25] Prasad and Sreenivasan,[8] and Prasad and Sreenivasan,[9] among others. These authors have concluded that fractal (power-law) similarity *is* applicable to the description of scalar interfaces in a wide variety of turbulent flows, including jets.

We should state explicitly that our results are in direct disagreement with a significant portion of the previously cited papers. While those authors have increasingly cautioned against the use of one-dimensional data to search for fractal behavior, they have, at the same time, offered evidence in support of agreement between single-point measurements, line images, and two-dimensional images. Our examinations in this paper include the first two of the three methods, and do not support the notion of a constant fractal dimension. Instead, we found that, over a wide range of locations, thresholds, flow conditions, and different types of measurements, the behavior is well modeled by lognormal statistics.

We offer one possibility how previous researchers concluded that a constant fractal dimension is appropriate where we do not. As we have demonstrated previously, the influence of pairs of transitions near extrema may cause a bump or even a fairly level region in the $D(\lambda)$ curves at particular selections of the threshold. The thresholds used by Sreenivasan *et al.* are much lower than the local mean and may fall in such a region. It could be that the bump feature, particularly when finding the dimension by fitting a line to the log–log plots, gave the appearance of a constant dimension. It was only the direct differentiation of the curves that allowed us to generate plots such as Fig. 10, thereby discerning the bump.

Additionally, there is an issue concerning the two-dimensional results of Sreenivasan *et al.* and our findings. We have not analyzed two-dimensional spatial images at this time. Our use of two-dimensional streak images generated by the linear array, an approximation of spatial images, yielded results similar to those of our other data. However, we recognize the analysis of these data involves several assumptions which preclude exact comparison, and therefore we cannot directly confirm or deny the two-dimensional results.

Our data and analysis force us to conclude that, at least *in the far field of turbulent jets, scalar interface geometry cannot be described in terms of a constant fractal dimension*, under any of the flow conditions we have examined in our experiments. Further, we have found that the behavior of isoscalar surfaces with the local mean value agrees well with a simple, lognormal, stochastic model. For values substantially different than the local mean, similar behavior is observed if the boundedness of the signal is taken into account. This suggests to us that the notion of constant fractal dimension, if applicable to the jet scalar field at all, is something of a special case rather than the norm. These conclusions were the reason for avoiding the word "fractal" in our title, as that was originally coined by Mandelbrot to denote the power law of Eq. (1). In fact, Feder credits Mandelbrot as having retracted his original definition of a fractal. Mandelbrot's revised and more relaxed definition is not tied to a power law (Hausdorff–Besicovitch) dimension, but rather to a general geometric property of similarity (Feder,[26] p. 11). We appreciate that the flow in the far field of turbulent jets is characterized by a host of similarity properties, indeed spanning the full spectrum of scales (Dowling[16]). We note, however, that fractal (power law) behavior is not compelled by similarity.

This conclusion suggests that perhaps the premise for a constant (power-law) fractal dimension at moderate to high Reynolds numbers should be reexamined, i.e., the proposal that

$$N(\lambda) \propto \lambda^{-D} \tag{1}$$

can serve as the measure of the number of elements of scale λ required to cover the scalar interface, where D is a constant. In particular, we recognize that Eq. (1) is not dimensionally correct, at least as it stands; only a dimensionless group can be related to a pure number. Equation (1) could be made dimensionally correct using either inner variable scaling, i.e.,

$$N(\lambda) \propto (\lambda/\lambda_{\nu})^{-D}, \tag{7a}$$

where λ_{ν} is the scalar diffusion scale, or outer scaling, i.e.,

$$N(\lambda) \propto (\lambda/\delta)^{-D}, \tag{7b}$$

where δ is the local jet diameter, for example. There are difficulties with such proposals, however, especially for values of the fractal dimension D substantially different from the corresponding Euclidean values.

At least in the inertial range where one might expect the power-law fractal similarity to hold, it would imply either that the inner (Kolmogorov/Batchelor) scales [Eq. (7a)], or the outer scales [Eq. (7b)] are imposed on the dynamics. Yet, the high Reynolds number dimensional analysis and similarity scaling derived from the early Kolmogorov[27] hypotheses, which yield the $-\frac{5}{3}$ spectrum power laws, is equivalent with the assumption, among other things, that the only variables that enter in the inertial range cascade dynamics are the local scale λ (or wave number k) and the kinetic energy dissipation rate ϵ. The scaling laws implied by Eqs. (7a) and (7b) are inconsistent with this assumption, as no other length scale is derivable from λ and ϵ. While additional length scales are admissible in the subsequent turbulence similarity hypotheses that incorporate the intermittency corrections (e.g., Kolmogorov,[28] Oboukhov,[29] and Gurvich and Yaglom[30]), these enter through similarity laws that are much weaker than power laws, e.g., lognormal, and provide only small corrections to the originally proposed $-\frac{5}{3}$ spectrum power-law exponent. Alternatively, the original Kolmogorov similarity proposals of a scaleless cascade range are found to be *very nearly* correct (also see the related discussion in Dimotakis,[30] p. 482). In contrast, Eqs. (7) are equivalent to a *strong* dependence of the dynamics on outer, or inner, scales. Consequently, it would appear that a power-law description of the statistics at the high Reynolds numbers of interest is inappropriate, not only on the basis of the experimental data we have presented, but also on the basis of dimensional analysis and similarity arguments.

ACKNOWLEDGMENTS

We would like to acknowledge the assistance of D. Dowling and D. Lang with the experiments, helpful suggestions from W. Ashurst, as well as discussions with G. Losi. One of us (PD) would also like to acknowledge several conversations with B. Mandelbrot on the occasion of his visits at Caltech over the last ten years, or so, as well as with K. Sreenivasan during his stay at Caltech as a Visiting Professor a few years ago.

This work was performed under AFOSR Grants No. 83-0213 and No. 88-0155, and GRI Contract No. 5087-260-1467.

APPENDIX: ASPECTS OF THE FRACTAL ANALYSIS

This appendix expands upon several topics that we feel deserve a more detailed discussion, including aspects of the box-counting algorithm, the treatment of noise in the data, and the consequence of analyzing shorter data records.

There are subtle end effects that can occur with the box-counting algorithm. If the record submitted for box counting is a nonintegral number of a particular tile size in length, the last tile extends past the end of the record. Some type of weighting scheme for this fractional end tile may suggest itself, but such weighting requires the essentially *ad hoc* assignment of the corresponding probability of a transition. We have conducted numerical experiments utilizing the one-dimensional Cantor set, using nonintegral numbers of tiles. They displayed sawtooth oscillations that varied in wavelength as a function of tile size, consistent with end effects. We verified that various weighting schemes do not correct the difficulty. As a result, we decided that tile sizes should be exact factors of the total record length. This ensures that there is always an integral number of tiles in the record, and thus eliminates end effects of this type.

It is significant to note that, using only integral tiles, the $\log[N(\lambda)]$ curves must be nonincreasing with increasing tile size. *It cannot require more larger tiles than smaller ones to cover the same transitions.* Note, also, that local increases in the $\log[N(\lambda)]$ curve would yield a negative fractal dimension for the corresponding range of scales. This is, of course, inadmissible. As an example, imagine a record six elements long, in which the third and fourth elements contain transitions Fig. 14(a). If tiles of size 2 are placed on the record, the central tile will cover both transitions, and $N(\lambda)$ is 1. If two tiles of size 3 are laid down, then both the first tile, covering elements one through three, and the second tile, covering elements four through six, will cover transitions. In that case, $N(\lambda)$ will be 2. This example may appear to contradict the statement that the $\log[N(\lambda)]$ curves must be

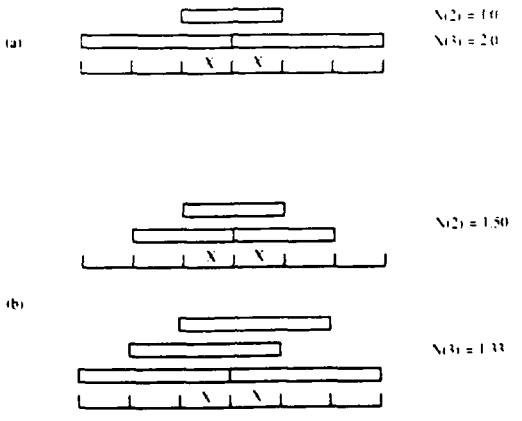

FIG. 14. Dependence on tile starting location. Tiles covering transitions, denoted by "X," are indicated by narrow rectangles. (a) Fixed starting location. (b) Weighted average over possible starting locations.

nonincreasing with tile size. It actually illustrates another issue.

We note that there is no preferred starting location or reference point when tiling a record. The apparent difficulty in the example is a consequence of the particular choice of starting location. If the tiling is done as many times as there are possible starting locations, all the information available is extracted. In the example, there are two possible starting locations for tiles of size 2, either on even or odd elements, and three for tiles of size 3 [Fig. 14(b)]. If the results with all possible starting locations are ensemble averaged, we find that $N(\lambda)$ is 1.5 for tiles of size 2, and 1.33 for tiles of size 3. The need to shift tile locations and the restriction of having an integral number of tiles in each record suggested the choice of tile sizes and record lengths that are powers of 2 of the sampling unit. We have found that using just eight different starting locations, equally spaced, does a reasonable job of reducing the effect illustrated in Fig. 14.

In addition to these end-effect difficulties, there is the issue of the influence of unavoidable noise in the data. It has been appreciated for some time that the presence of noise in a signal can profoundly affect the statistics of level crossings (e.g., Rice[11,12]). Since the box-counting algorithm utilizes level crossings or transitions, the issue of noise is important. To illustrate this, Fig. 15 displays a small segment of an unfiltered signal and the corresponding optimally (Wiener-) filtered signal. Bear in mind that the unfiltered signal appears as noisy as it does because it has been oversampled, as dictated for an effective implementation of the Wiener filter. It is apparent that noise grossly affects the crossings of the threshold (mean level), and that a proper treatment of this aspect of the data is an essential component of the signal and data processing. Note that noise can cause crossings where the signal *approaches* the threshold *but does not cross it*. By not only adding crossings in the vicinity of a true crossing, but also where there was no true crossing nearby, the noise contaminates the results at scales much larger than might be suspected, as well as at smaller scales.

The effect illustrated in Fig. 15 is accentuated because the signal is oversampled. Nevertheless, even a small addition of noise at the smallest scales can influence the results significantly. As a demonstration of this behavior, a data record from a particular run was processed unfiltered, with a variety of Gaussian filters of differing widths, as well as with the optimal (Wiener) filter. The Gaussian filter, if chosen with an appropriate width (which, however, is not known *a priori*), may serve as an approximation to the Wiener filter. Figure 16 shows the results for no filtering, insufficient filtering, optimal filtering, and overfiltering. It is evident that the presence of noise in the data may result in a region of nearly constant slope on the $\log[N(\lambda)]$ plots, which may even be interpreted as *two* regions of somewhat constant slope. In fact, the $D(\lambda)$ plots computed from these curves exhibit a "bump" at small scales, as previously discussed in the text. For these data, the slope at smaller scales is steeper than at larger scales, and there is a slight roll-off at the smallest values. When the noise is removed (the Wiener-filtered case), however, these constant slopes do not persist.

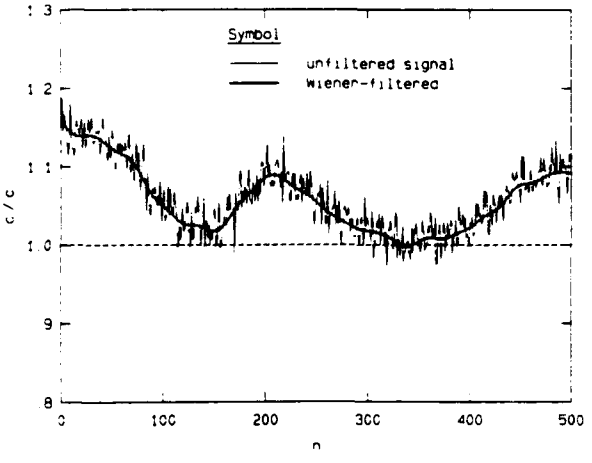

FIG. 15. Effect of noise on transitions (Re = 2940).

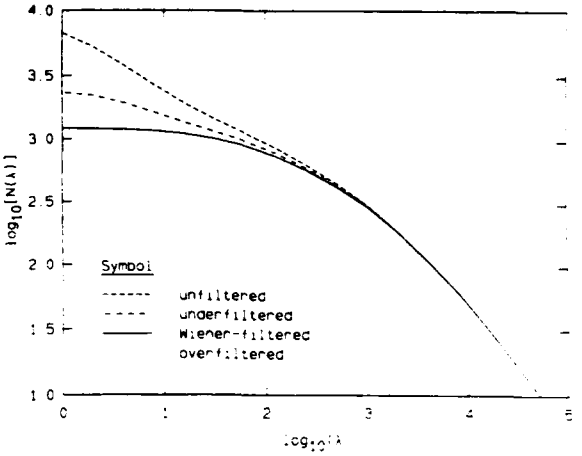

FIG. 16. Influence of noise on $\log[N(\lambda)]$ curves (Re = 2940).

Two additional points are illustrated by Fig. 16. First, as noted above, the contamination of the results is not limited to the small scales or high frequencies where the noise dominates. It extends to much larger scales. The various curves do not coincide until a scale of at least 500 or 1000 sampling units. This is larger, by a factor of 20–30, than the ratio of the signal spectrum intercept with the noise floor to the sampling frequency. We are forced to conclude that the influence of noise, if permitted, may encroach into scales that are well resolved with respect to space, time, and SNR. In short, a large SNR is not sufficient to ensure that noise has not affected the results. Additional care, such as use of the Wiener filter, is typically necessary. Second, it is evident from Fig. 16 that either too wide or too narrow a filter kernel can also affect the results. Filtering only the highest frequencies out of the noise is insufficient, yielding a similar rise in $N(\lambda)$ at the smallest scales as the unfiltered data. The overfiltered result, although similar in shape to the correct curve, has also been compromised. Thus very careful consideration must be given to the handling of noise in level crossing data that are analyzed for fractal behavior.

A final issue that should be assessed is the consequence

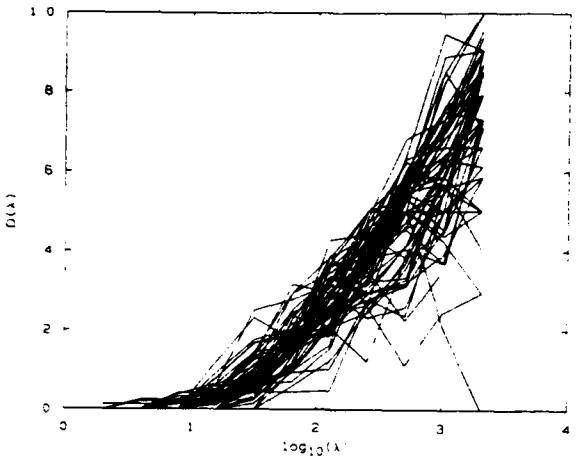

FIG. 17. Many individual short records (Re = 2940).

of analyzing shorter data records with the box-counting algorithm, as was mentioned in the text. Shorter records have been suggested (cf. Sreenivasan and Meneveau[7]) because of the possibility that scalar interfaces might display a particular power-law fractal behavior on a local length or time scale, but that over larger scales, fluctuations or variations in the local properties could smear it out. Our record lengths varied in length from about 8–70 large scale times. Such a number of large scales provided good statistics. We saw no indication the record lengths were influencing the results.

Nevertheless, we examined the behavior of shorter record lengths. Rather than ensemble averaging either the $\log[N(\lambda)]$ plots or the $D(\lambda)$ curves for many short records, we superimpose many separate realizations on one plot (Fig. 17). The results shown are for a Reynolds number of 2940. The individual curves do not exhibit a flat (horizontal) region, which would imply a constant fractal dimension. Additionally, the ensemble average, easily constructed by eye, resembles the result displayed in Fig. 5. Even shorter records were analyzed, for the entire range of Reynolds numbers, both on and off axis, and the outcome was the same for record lengths of all sizes. We conclude that record length is not a factor in our results.

[1] B. B. Mandelbrot, J. Fluid Mech. **72**, 401 (1975).
[2] B. B. Mandelbrot, *Fractals: Form, Chance, and Dimension* (Freeman, San Francisco, 1977).
[3] B. B. Mandelbrot, *Fractals and Turbulence: Attractors and Dispersion*, Lecture Notes in Mathematics (Springer, Berlin, 1977), Vol. 615, pp. 83–93.
[4] B. B. Mandelbrot, *The Fractal Geometry of Nature* (Freeman, San Francisco, 1983).
[5] F. C. Gouldin, AIAA J. **26**, 1405 (1988).
[6] K. R. Sreenivasan, R. Ramshankar, and C. Meneveau, Proc. R. Soc. London Ser. A **421**, 79 (1989).
[7] K. R. Sreenivasan, and C. Meneveau, J. Fluid Mech. **173**, 357 (1986).
[8] R. R. Prasad and K. R. Sreenivasan, Exp. Fluids **7**, 259 (1989).
[9] R. R. Prasad and K. R. Sreenivasan, Phys. Fluids A **2**, 792 (1990).
[10] P. E. Dimotakis, R. C. Miake-Lye, and D. A. Papantoniou, Phys. Fluids **26**, 3185 (1983).
[11] W. J. A. Dahm, Ph.D. thesis, California Institute of Technology, 1985.
[12] S. Green and G. Lost, California Institute of Technology, Ae104c Laboratory Report (unpublished).
[13] W. J. A. Dahm and P. E. Dimotakis, AIAA J. **25**, 1216 (1987).
[14] N. Wiener, *Extrapolation, Interpolation and Smoothing of Stationary Time Series* (Wiley, New York, 1949).
[15] W. H. Press, B. P. Flannery, A. A. Teukolsky, and W. T. Vetterling, *Numerical Recipes. The Art of Scientific Computing* (Cambridge U.P., Cambridge, 1986).
[16] D. R. Dowling, Ph.D. thesis, California Institute of Technology, 1988.
[17] D. R. Dowling, D. B. Lang, and P. E. Dimotakis, Exp. Fluids **7**, 435 (1988).
[18] C. J. Chen and W. Rodi, *Vertical Turbulent Buoyant Jets: A Review of Experimental Data* (Pergamon, New York, 1980).
[19] L. A. Smith, J-D. Fournier, and E. A. Spiegel, Phys. Lett. A **114**, 465 (1986).
[20] A. S. Gurvich and A. M. Yaglom, Phys. Fluids, **10**, Suppl., 59 (1967).
[21] C. A. Friehe, C. W. Van Atta, and C. H. Gibson, AGARD Turbulent Shear Flows Report No. CP-93, 1971, pp. 18.1–18.7.
[22] D. R. Chapman, AIAA J. **17**, 1293 (1979).
[23] G. K. Batchelor, J. Fluid Mech. **5**, 113 (1959).
[24] K. A. Buch and W. J. A. Dahm, Bull. Am. Phys. Soc. **34**, 2264 (1989).
[25] C. Meneveau, Ph.D. thesis, Yale University, 1989.
[26] J. Feder, *Fractals* (Plenum, New York, 1988).
[27] A. N. Kolmogorov, Dokl. Akad. Nauk SSSR **30**, 299 (1941); reprinted in Usp. Fiz. Nauk **93**, 476 (1967) [Sov. Phys. Usp. **10**, 734 (1968)].
[28] A. N. Kolmogorov, J. Fluid Mech. **13**, 82 (1962).
[29] A. M. Oboukhov, J. Fluid Mech. **13**, 77 (1962).
[30] P. E. Dimotakis, in *Turbulent Reactive Flows*, Lecture Notes in Engineering (Springer, Berlin, 1989), Vol. 4, pp. 417–485.
[31] S. O. Rice, Bell Syst. Tech. J. **23**, 282 (1944).
[32] S. O. Rice, Bell Syst. Tech. J. **24**, 46 (1945).

Appendix F

DOWLING, D. R. AND DIMOTAKIS, P. E. [1990] "Similarity of the concentration field of gas-phase turbulent jets," *J. Fluid Mech.* **218**, 109.

J. Fluid Mech. (1990), *vol.* 218, *pp.* 109–141
Printed in Great Britain

Similarity of the concentration field of gas-phase turbulent jets

By DAVID R. DOWLING† AND PAUL E. DIMOTAKIS
Graduate Aeronautical Laboratories, California Institute of Technology,
Pasadena, CA 91125, USA

(Received 1 June 1989 and in revised form 9 December 1989)

This work is an experimental investigation of the turbulent concentration field formed when the nozzle gas from a round, momentum-driven, free turbulent jet mixes with gas entrained from a quiescent reservoir. The measurements, which were made with a non-intrusive laser-Rayleigh scattering diagnostic at Reynolds numbers of 5000, 16000, and 40000, cover the axial range from 20 to 90 jet exit diameters and resolve the full range of temporal and spatial concentration scales. Reynolds-number-independent and Reynolds-number-dependent similarities are investigated. The mean and r.m.s. values of the concentration are found to be consistent with jet similarity laws. Concentration fluctuation power spectra are found to be self-similar along rays emanating from the virtual origin of the jet. The probability density function for the concentration is also found to be self-similar along rays. Near the centreline of the jet, the scaled probability density function of jet fluid concentration is found to be nearly independent of the Reynolds number.

1. Introduction

The round, momentum-driven, free turbulent jet, a small source of high-speed fluid issuing into a large quiescent reservoir, is one of the classical free shear flows. This simple geometry has wide engineering application and has attracted investigators for more than 50 years (Ruden 1933; Kuethe 1935). It is a special turbulent flow for several reasons, and two of its unique far-field properties are important elements of this investigation. First, the mean concentration field of a passive scalar that issues from the jet nozzle displays a distinct self-similarity with increasing downstream distance, and second, the evolution of the maximum mean velocity and the largest scale of motion conspire to give the flow a single Reynolds number independent of the distance from the jet nozzle (e.g. Landau & Lifshitz 1959). Properties of the convected concentration (scalar) field, formed downstream of the jet nozzle, should depend only on the Reynolds number of the jet, the Schmidt number (kinematic viscosity divided by species diffusivity) of the jet/reservoir fluid pair, and the location of the observation point with respect to the nozzle exit. This paper explores these dependences by describing the results of an experimental investigation in gas-phase turbulent jets, and comparing the findings with previous jet studies.

Two concepts of similarity are addressed and it is necessary to explain the terminology that is used in each case. *Specific similarity* is applied to the properties of the jet's turbulent concentration field that allow a collapse of its statistical measures

† Present address: Applied Physics Laboratory, University of Washington, Seattle, WA 98105, USA.

with downstream distance *at a fixed Reynolds number and Schmidt number. General similarity* is used to describe properties of the jet's turbulent concentration field that are *independent of Reynolds number.*

The measured mean profile of jet fluid concentration is similar in *general*, and collapses on rays that emanate from the virtual origin of the jet (Wilson & Danckwerts 1964; Becker, Hottel & Williams 1967: Townsend 1976; Birch *et al.* 1978: Lockwood & Moneib 1980; Chen & Rodi 1980 and the references cited therein, plus figure 6). In the cylindrical coordinates used in this paper. this *general* similarity profile of the mean concentration of jet fluid. $\bar{C}$, takes the following form:

$$\bar{C}(x,r) = \kappa \frac{C_0 d^*}{x - x_0} g\left(\frac{r}{x - x_0}\right) \equiv \kappa \frac{C_0}{\chi} g(\eta). \tag{1}$$

where κ is a parameter determined by experiment. d^* is the momentum diameter of the nozzle exit. C_0 is the jet exit concentration. $g(\eta)$ is a smooth function that has a maximum value of one at $\eta = 0$ and is determined by experiment. x is the distance from the jet nozzle along the axis of the jet. r is the radial distance from the axis of the jet. and x_0 is the virtual origin of the jet flow in the far field. A schematic of this coordinate system is given as figure 1.

The momentum diameter that appears in (1) is defined by

$$d^* = \frac{2\dot{m}_0}{(\pi \rho_\infty J_0)^{\frac{1}{2}}}, \tag{2}$$

where ρ_∞ *is the density of the reservoir fluid.* $\dot{m}_0$ is the nozzle mass flux. and J_0 is the nozzle thrust. It was introduced in a limited way by Thring & Newby (1953), used by Avery & Facth (1974), and modified to the present form by Dahm & Dimotakis (1987). The momentum diameter has been used to collapse the results of a wide variety of jet experiments (see Dahm & Dimotakis 1987). Note that d^* reduces to the geometrical nozzle exit diameter, d, for density-matched jet and reservoir fluids and a perfect 'top-hat' exit velocity profile.

While the similarity of the mean profile is well supported by experimental results. there is substantial conflict between the results of different investigations regarding the similarity of concentration fluctuations in the turbulent jet (Chen & Rodi 1980: Lockwood & Moneib 1980; Dahm 1985). The reported discrepancies between investigations (see figure 10) could arise from many sources. including insufficient resolution of all of the fluctuating scales. contamination of the flow by buoyancy forces. unsteadiness in the jet source or quiescent reservoir. variations in molecular Schmidt number ($\nu_\infty / D_{j\infty}$) and Reynolds number between experiments, and differences in experimental configurations.

Recent work at a Reynolds number of 5000 by Dowling & Dimotakis (1988) suggests that many statistical properties of the jet's fluctuating concentration field follow the same similarity law as the mean concentration. Their main finding was that the concentration field of the jet. downstream of $x/d = 20$. was statistically self-similar in every detail along rays that emanate from the virtual origin of the jet. This paper examines the extent to which this concept of detailed similarity applies to turbulent jets at different Reynolds numbers. The available experimental information in liquid-phase jet flows is not as well developed as that of gas-phase flows. Therefore, the role of the Schmidt number in jet similarity is not addressed at length and is mentioned only where appropriate. The conclusions of this paper are based on comparisons of new and previously reported results for the mean concentration, $\bar{C}$.

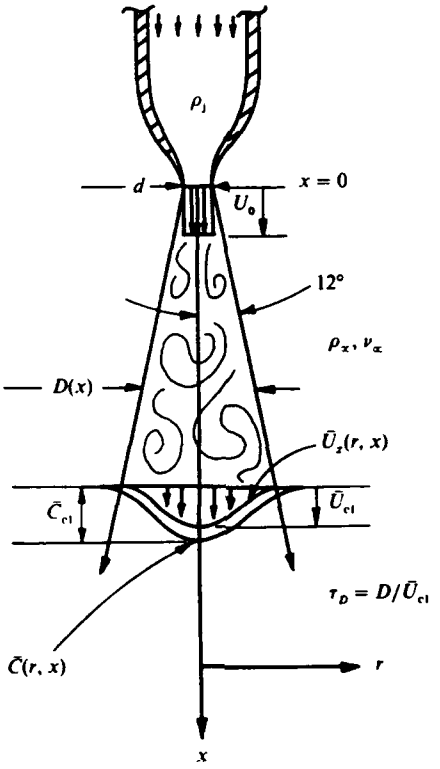

FIGURE 1. Turbulent jet coordinates.

the root-mean-square (r.m.s.) concentration fluctuation, C'_{rms}, the probability density function (PDF) of concentration, and the power spectrum of concentration fluctuations, $E_c(f)$. While this list of statistical parameters is certainly not exhaustive, it forms a useful basis for describing the fluctuating character of the jet flow.

The measurements reported here – single-point, concentration time-histories – were made using a non-intrusive laser-Rayleigh scattering diagnostic in a steady, gas-phase, axisymmetric, momentum-driven jet that issued into a large enclosure. The diagnostic was sensitive to the number-weighted concentration of jet gas molecules but the results are presented in terms of the mass-weighted concentration, since that is the quantity that best represents constant-density conditions (see Pitts 1986). Special effort was expended to eliminate and/or quantify the possible sources of experimental contamination mentioned above so that the natural state of the jet's turbulent concentration field could be investigated. These precautions are summarized at the beginning of the next section.

The new results are presented at three jet exit Reynolds numbers: 5000, 16000 and 40000. These Reynolds numbers were computed from the jet exit velocity, U_0 (taken as uniform across the nozzle exit), the geometrical nozzle exit diameter, d, and the reservoir kinematic viscosity, ν_∞, i.e.

$$Re_0 = \frac{U_0 d}{\nu_\infty}. \tag{3}$$

The experimental design, apparatus, and diagnostic technique are described in the

next section. They are the same ones employed by Dowling & Dimotakis (1988), and are described in detail in Dowling (1988), and Dowling, Lang & Dimotakis (1989). The experimental findings, with comparisons and discussion, are presented in §3. The conclusions are given in §4.

It is worth emphasizing that the results and comparisons presented in §3 are specialized to the concentration field of the round, momentum-driven, free turbulent jet. Comparisons of the current results with concentration or velocity measurements from other shear flows, which do not possess the same special similarity properties as the jet, are not included. Additionally, the chosen allocation of resources did not allow for measurements of both concentration and velocity in a manner that was suitable, so the current experiments can only be considered to address properties of the jet's velocity field which can be inferred from concentration measurements. The only velocity scale, besides U_0, that is referenced throughout the manuscript is the mean centreline velocity, $\bar{U}_{\rm cl}$, which was computed from the empirical decay law suggested by Chen & Rodi (1980). As discussed in §3.2, this does not affect the conclusions drawn from this research, nor impose any significant penalty on the presentation of the results.

2. Experimental design, apparatus, and technique

The experiment was designed to resolve the entire range of spatial and temporal concentration scales while mitigating the influences from the previously mentioned contamination sources. The spatial resolution requirement was that the measurement volume had to be smaller than the local Batchelor scale, $\lambda_{\rm B}$ (Batchelor 1959), in each dimension. The temporal resolution requirement was that the bandwidth of the data acquisition system had to comfortably exceed the mean passage frequency, $f_{\rm B}$, of lengthscales the size of $\lambda_{\rm B}$. Actual lengths and frequencies were estimated, for design purposes, from classical turbulence formulae and published experimental results.

For the chosen gas pairs, the Schmidt number, Sc, was near unity so the Batchelor and Kolmogorov scales were assumed to be about equal (Batchelor 1959; Monin & Yaglom 1975).

$$\lambda_{\rm B} \equiv \frac{\lambda_{\rm K}}{Sc^{\frac{1}{2}}} \approx \lambda_{\rm K} = \beta\left\{\frac{\nu_x^3}{\bar{\epsilon}}\right\}^{\frac{1}{4}} \propto DRe_0^{-\frac{3}{4}}. \tag{4}$$

Here, $\lambda_{\rm K}$ is the Kolmogorov scale, β is a dimensionless constant, $\bar{\epsilon}$ is the mean energy dissipation rate, and D is the local jet diameter (see figure 1). Actual values of $\lambda_{\rm B}$ used to design the experiment were calculated using the results of Friehe, Van Atta & Gibson (1971) for the mean centreline energy dissipation rate in the jet,

$$\bar{\epsilon} = 48\frac{U_0^3}{d}\left(\frac{x-x_0}{d}\right)^{-4}, \tag{5}$$

and a conservative value of $\beta\,(=1)$. The mean Batchelor-scale passage frequency, $f_{\rm B}$, was calculated from the mean centreline velocity decay law suggested by Chen & Rodi (1980) and (4), i.e.

$$f_{\rm B} \approx \frac{\bar{U}_{\rm cl}}{\lambda_{\rm K}} = \bar{U}_{\rm cl}\left(\frac{\bar{\epsilon}}{\nu_x^3}\right)^{\frac{1}{4}}. \tag{6}$$

where

$$\bar{U}_{\rm cl} = 6.2\,U_0\left(\frac{x-x_0}{d}\right)^{-1}. \tag{7}$$

The effect of buoyancy forces was estimated using the buoyancy-lengthscale

formalism developed in Fischer *et al.* (1979). The measurements of Papanicolaou & List (1987, 1988) show that the jet is momentum dominated for x/l_b less than one; l_b is a buoyancy lengthscale defined by

$$l_b = \left(\frac{(J_0/\rho_\infty)^3}{(B/\rho_\infty)^2}\right)^{\frac{1}{4}}, \tag{8}$$

where

$$B = \int_{A_0} (\rho_j - \rho_\infty)\, U_j \, \mathrm{d}A, \tag{9}$$

ρ_j is the density of pure jet gas, U_j is the jet nozzle exit velocity profile, and A_0 refers to the jet nozzle exit area (for a 'top-hat' exit velocity profile $U_j = U_0$). Chen & Rodi (1980) propose a more restrictive criterion of $x/l_b \leqslant 0.53$, for momentum-dominated flow. The present measurements all satisfy $x/l_b \leqslant 0.4$.

To accommodate the diagnostic chosen, the experiments were performed inside a special enclosure. To prevent reverse flow inside this chamber, a mild coflowing velocity was imposed on the reservoir gas. The effect of this mild coflow on the evolution of the jet was estimated from the results of Reichardt (1964) who measured the velocity half-width of coflowing jets as a function of x/l_c, where l_c is the momentum lengthscale associated with a jet in a coflowing stream,

$$l_c^2 = \frac{4}{\pi \rho_\infty U_c^2}\left\{\int_{A_0} \rho_j (U_j - U_c)\, U_j \, \mathrm{d}A\right\} \tag{10}$$

(also see Hinze 1975). Reichardt's work suggests that the coflow has little effect on the jet for x/l_c less than about one. All of the present measurements satisfy $x/l_c \leqslant 0.5$.

To assure that the jet and coflow were stable during an experiment, the measured mean concentration was checked during the first, middle, and final thirds of a run to make sure that there was less than $\pm 10\%$ to 20% variation. The repeatability of runs was also checked and found satisfactory. To ensure that adequate statistics were collected, an experiment was required to last many times longer than the mean convection time of the local jet diameter. This timescale, τ_D, was estimated from the half-angle of the jet's turbulent cone, about 12° (White 1974), and (7):

$$\tau_D = D(x)\bar{C}_{cl}^{-1}. \quad \text{where} \quad D(x) = 2(x - x_0)\tan(12°) \approx 0.43(x - x_0). \tag{11}$$

The time interval of data collection varied from $16\tau_D$ to $180\tau_D$. This sampling interval proved to be adequate for the central region of the jet, but may not have been long enough to accurately determine the statistics of the flow near the edges of the jet where the mean velocity is smaller, the relevant convection timescale is longer than τ_D, and the flow is intermittent.

The Schmidt number for each of the gas pairs used was estimated from the empirical correlations for the diffusivity of gases found in Reid, Prausnitz & Sherwood (1977). These correlations are accurate to within about 5 or 10%.

The three Reynolds numbers explored here were chosen in accordance with the performance of the experimental apparatus and diagnostic. At $Re_0 = 5000$, all of the design criteria were met and measurements were made at $x/d = 20$, 40, 60, and 80. However, these results showed that the resolution criteria were conservative and had been met by a very wide margin. The second Reynolds number, 16000, was chosen to take better advantage of the diagnostic capabilities while still resolving all of the fluctuating concentration scales in the flow at different downstream distances from the jet nozzle. At $Re_0 = 16000$, measurements were made at $x/d = 30$ and 90. The

	(a) For $Re_0 = 5000$ ($x_0 = -3.7d$)			
	$x/d = 20$	$x/d = 40$	$x/d = 60$	$x/d = 80$
λ_B(μm)	(290)	(530)	(780)	(1020)
Diode size (μm)	200, 500	500	500	1000
f_B(kHz)	(3.7)	(1.08)	(0.51)	(0.29)
Digitization rate (kHz)	96, 40	20	10	5
τ_D (s)	(0.18)	(0.62)	(1.31)	(2.3)
No. of τ_D during a run	40, 100	40	30	16

	(b) For $Re_0 = 16000$ ($x_0 = 0.5d$)		(c) For $Re_0 = 40000$ (x_0 taken to be zero)
	$x/d = 30$	$x/d = 90$	$x/d = 60$
λ_B(μm)	(60)	(180)	(61)
Diode size (μm)	200	500	200
f_B (kHz)	(99)	(10.9)	(120)
Digitization rate (kHz)	180	30	240
τ_D (s)	(0.016)	(0.146)	(0.026)
No. of τ_D during a run	180	120	80

TABLE 1. Resolution and parameter summary at each Reynolds number. Calculated values appear in parentheses.

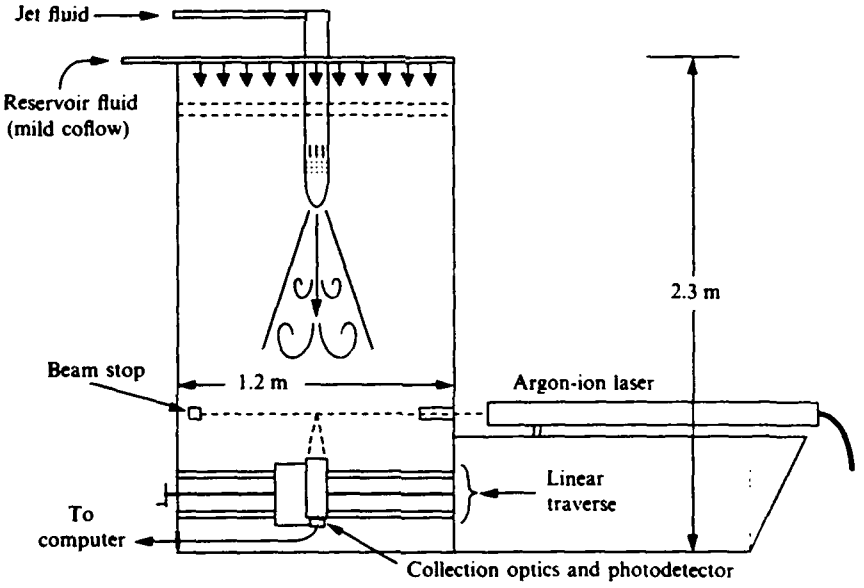

FIGURE 2. Schematic of the experimental apparatus in cross-section.

final Reynolds number, 40000, was the highest at which data could be collected with the present experimental arrangement while still meeting the resolution requirements. This meant that only one downstream location was explored, $x/d = 60$. A summary of the calculated and actual resolution of each set of experiments is given in table 1. The Taylor Reynolds number, Re_λ, along the centreline of the jet was estimated from the formulae in Hinze (1975), (5) and (7), and a typical value of the

centreline r.m.s. velocity fluctuation, $u'_{\rm rms} \approx 0.25\bar{U}_{\rm cl}$. The results are: $Re_\lambda \approx 100$, 180, 280 for $Re_0 = 5000$, 16000, and 40000 respectively.

The experiments were conducted in a large enclosure ($1.2 \times 1.2 \times 2.3$ m) that was used to isolate the jet and reservoir gases from dust particles, laboratory lighting, and air currents (see figure 2). The jet was produced by a vertically adjustable nozzle with $d = 19.0$ mm for the experiments at $Re_0 = 5000$, and $d = 7.62$ mm for the experiments at $Re_0 = 16000$ and 40000. Both nozzles had smooth inner contours and their measured exit turbulence levels were less than 0.2% at the experiment Reynolds numbers. A uniform coflowing velocity, typically less than 0.006 of the jet exit velocity was produced over the entire cross-section of the large enclosure. The volume flux of the coflow was chosen to provide the jet entrainment needs to a point below the farthest measuring station (Ricou & Spalding 1961). Plexiglas windows (1×1.5 m) were used for shadowgraph imaging of the jet. The exhaust gases exited through the bottom of the enclosure.

For the experiments at $Re_0 = 5000$, the jet gas was ethylene, C_2H_4, and the reservoir gas was nitrogen. This gas pair has a jet/reservoir density ratio of 1.0015 and a molecular Schmidt number of 1.0. For the experiments at $Re_0 = 16000$ and 40000, the jet gas was propylene, C_3H_6, and the reservoir gas was argon. This gas pair has a jet/reservoir density ratio of 1.053 and a Schmidt number of 1.2. In both cases, the dynamic head at the nozzle exit was measured to determine U_0. An axisymmetric boundary-layer calculation was used to estimate boundary-layer thicknesses at the nozzle exit in order to calculate d^* for each Reynolds number. The results were $d^* = 0.96d$ at $Re_0 = 5000$, $d^* = 1.005d$ at $Re_0 = 16000$, and $d^* = 1.01d$ at $Re_0 = 40000$.

Laser-Rayleigh scattering was used to determine the instantaneous concentration of the binary mixture of jet and reservoir gases in a small focal volume within the turbulent cone of the jet. Laser-Rayleigh scattering has been successfully used and documented in many previous studies (see discussion and citations in Dowling *et al.* 1989), and is only described briefly here. The technique makes use of the fact that gas molecules elastically scatter photons, and that different molecules have different Rayleigh-scattering cross-sections. Rayleigh scattering from a binary gas mixture can be described by an extinction coefficient, α_T, that is related to the mole fraction, X_1, of one of the gases of the mixture.

$$\alpha_T = \alpha_1 X_1 + \alpha_2 (1 - X_1). \tag{12}$$

where α_1 and α_2 are the extinction coefficients of the pure gases which compose the binary mixture under consideration. The amount of scattered light that can be collected, and converted to a single current using a photodetector, is proportional to α_T. Hence, the magnitude of the detected current is related in a linear manner to X_1. In practice, the two end points, $X_1 = 0$ and 1, of this linear relationship are recorded for the purposes of calibration, and the conversion from signal current to mole fraction is accomplished by linear interpolation.

For these experiments, the Rayleigh-scattered light from a short segment of a nominally 20 W argon-ion laser beam was imaged one-to-one onto a small aperture photodiode. The diameter of the sensitive area of the photodiode was between 0.20 and 1.00 mm; the local resolution requirements of the jet dictating the size used for each experimental run (see table 1). The signal current from the photodiode was amplified, filtered, and sent to an LSI-PDP-11/73 based computer system where it was digitized and stored for subsequent processing. The sampling frequency and filter bandwidth were chosen to ensure that the temporal resolution requirements

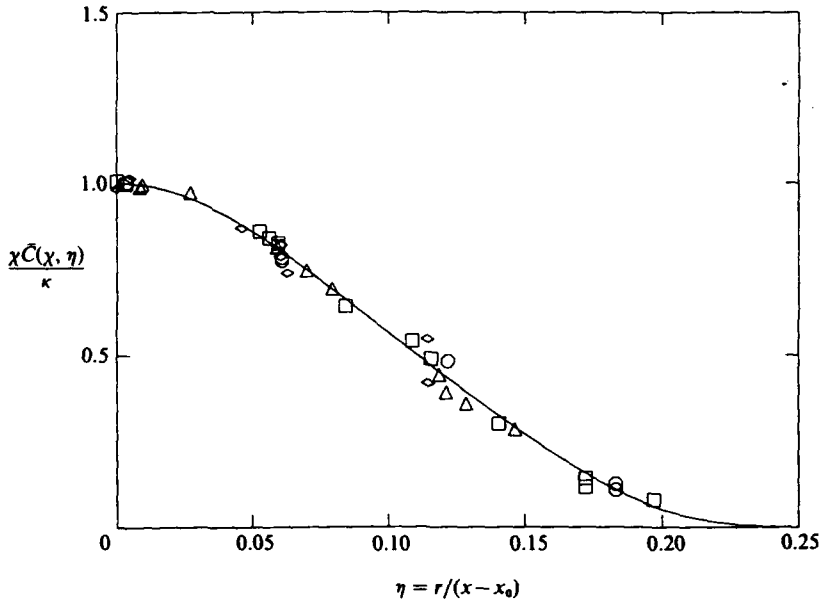

FIGURE 3. Scaled mean concentration (using the parameters of (1)), $\chi\bar{C}(\chi,\eta)/\kappa$, versus the scaled radial coordinate, $\eta = r/(x-x_0)$, at $Re_0 = 5000$ with $\kappa = 5.11$, $x_0 = -3.7d$, and $d^* = 0.96d$ ($\square$, $x/d = 20$; $\circ$, 40; $\triangle$, 60; $\diamond$, 80).

were easily met in all cases, with the possible exception of the highest Reynolds number runs.

The experimental methodology was quite simple in principle. The large enclosure was filled with pure reservoir gas. When residual velocities from the filling process had dissipated, the coflow and the jet were started together. The start of data acquisition was delayed until the jet had established a steady state. Runs lasted from a few seconds to almost a minute. The total number of individual concentration measurements in a single run was typically 2^{19} (> 500000). The sensitivity of the whole system was calibrated before and/or after each run by introducing pure jet and reservoir gases into the focal volume. The absolute accuracy of the calibration was about ± 1 parts per 10^3, which resulted from mild drift in the laser power and electronics. The techniques used for data processing and data reduction are described in Dowling (1988), and Dowling *et al.* (1989).

3. Results

3.1. *Basic properties of the concentration field of the jet*

The mean value of concentration from each run was computed by simple averaging, and plotted using the axis scaling suggested by (1). The results are displayed on figure 3 for the data at $Re_0 = 5000$ with $\kappa = 5.11 \pm 0.05$ and $x_0 = -3.7d$, on figure 4 for the data at $Re_0 = 16000$ with $\kappa = 4.73 \pm 0.1$ and $x_0 = 0.5d$, and on figure 5 for the data at $Re_0 = 40000$. It was not possible to obtain precise values for κ and x_0 at $Re_0 = 40000$ because measurements were only made at $x/d = 60$, so there is no scaling of the vertical axis on figure 5. The value of κ at $Re_0 = 40000$ is estimated to be between 5.1 and 5.2. It is important to note that the axis scaling on figures 3 and 4 is based only on the fitted values of κ and x_0 at each Reynolds number. There is no

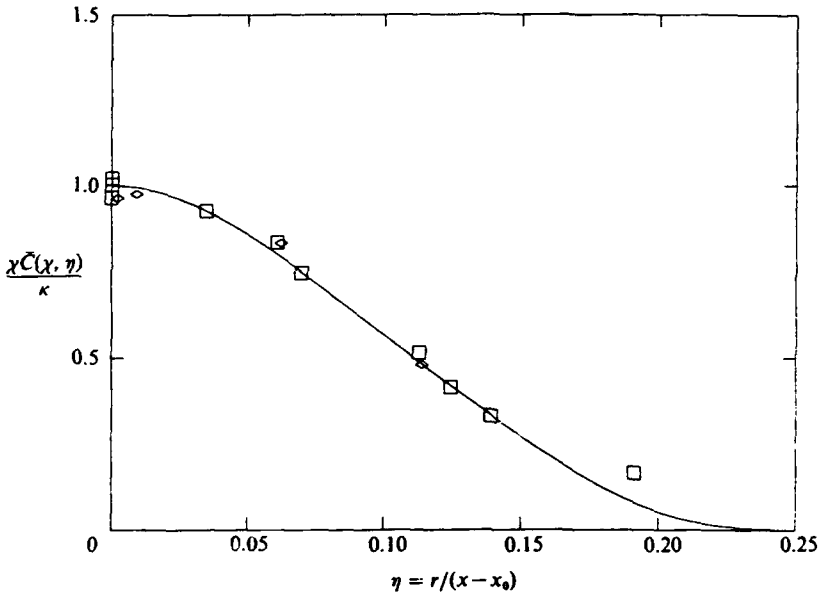

FIGURE 4 Scaled mean concentration (using the parameters of (1)), $\chi\bar{C}(\chi,\eta)/\kappa$, versus the scaled radial coordinate, $\eta = r/(x-x_0)$, at $Re_0 = 16000$ with $\kappa = 4.73$, $x_0 = 0.5d$, $d^* = 1.005d$, and the fitted mean profile from the data at $Re_0 = 5000$ (□, $x/d = 30$; ◇, 90).

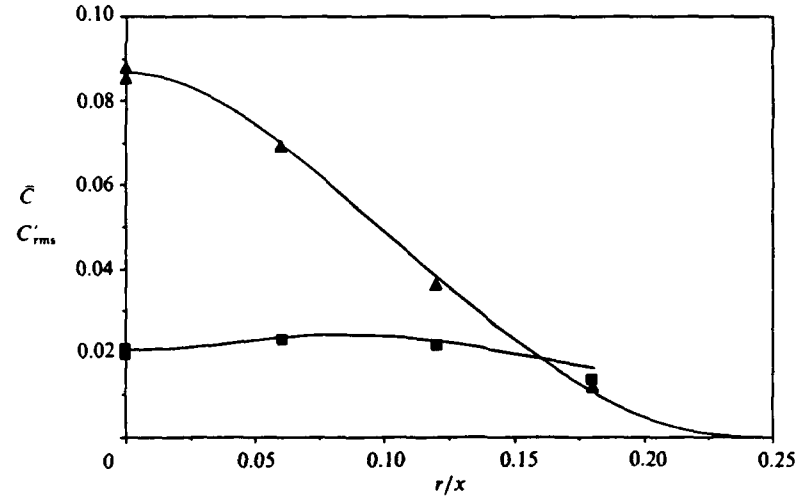

FIGURE 5. Mean (▲) and r.m.s. (■) concentration at $Re_0 = 40000$ and $x/d = 60$, with fitted mean profile from the data at $Re_0 = 5000$, and r.m.s. profile from the data at $Re_0 = 16000$.

'self-normalization' of the data on either of these figures. For example, separate normalizations by the local centreline mean, or concentration profile radius at half-maximum were not necessary. The fact that the profile function $g(\eta)$ emerges in these plots testifies to the *specific* similarity of $\bar{C}$, and the proper selection of κ and x_0 at each Reynolds number. Figures 3, 4 and 5 show that the experimental apparatus and technique produced a turbulent jet with the accepted *general* similarity form for $\bar{C}$. The mean concentration profile curve on figures 3, 4, and 5 is a least-squares fit to the data at $Re_0 = 5000$.

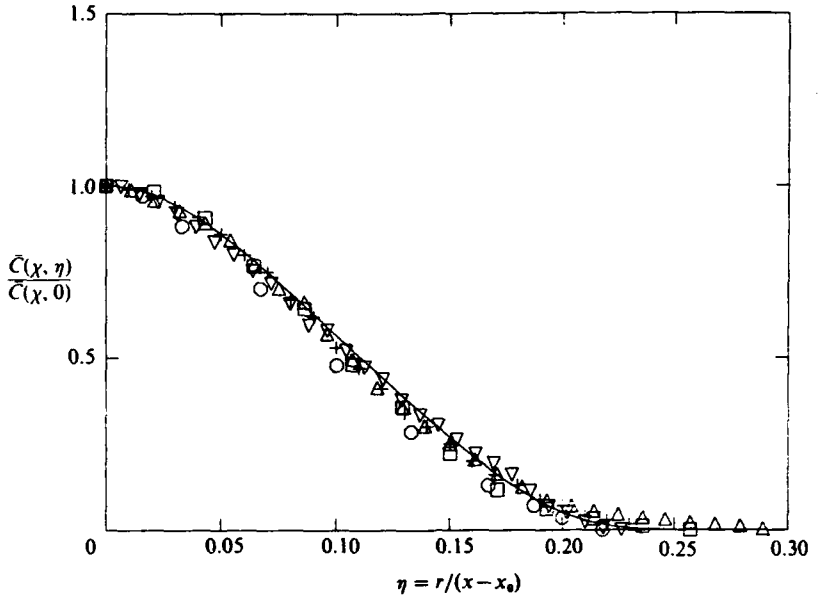

FIGURE 6. Comparison of the fitted mean concentration profile. $\bar{C}(\chi,\eta)/\bar{C}(\chi,0)$, with the results of other experiments (○, Lockwood & Moneib 1980; □, Corrsin & Uberoi 1950; △, Birch *et al.* 1978; +, Becker *et al.* 1967; ▽, Dahm 1985; ——, current profile).

Author	Re_0	Sc or Pr	Diagnostic
Becker *et al.* (1967)	54000	38000	Smoke scattering
Birch *et al.* (1978)	16000	0.70	Raman scattering
Clay (1973)	800000	0.70	Thermometry (air)
Corrsin & Uberoi (1950)	33000 and up	0.7	Thermometry (air)
Dahm (1985)	5000	600–800	Laser-induced fluorescence
Lockwood & Moneib (1980)	50000	0.7	Thermometry (air)
Wilson & Danckwerts (1964)	20000–60000	0.7	Thermometry (air)
Papanicolaou & List (1987)	10000–16000	7.0	Thermometry (H_2O)
Papanicolaou & List (1988)	2600–3600	$\approx 10^3$	Laser-induced fluorescence
Papantoniou (1985)	5600	600–800	Laser-induced fluorescence
Present study	5000	1.0	Rayleigh scattering
	16000	1.2	
	40000	1.2	

TABLE 2. Turbulent jet mixing experiments

A comparison of this fitted profile with the published profiles of other experiments is given on figure 6. The agreement between profiles is good and the small differences can probably be attributed to the differing experimental conditions and techniques of each experiment. Table 2 lists some of the important parameters of the experiments used for comparison with the current studies. All of these studies are of turbulent jets beyond $x/d = 20$, above $Re_0 = 2500$. and estimated to be free of serious influence from buoyancy forces or a coflowing stream. Detailed comparison with any larger body of work is beyond the scope of this paper.

A comparison of the current and previous experimental results for the mean centreline concentration, $\bar{C}(\chi, 0)$, is provided on figure 7. The vertical axis is scaled so that the measured data will fall on horizontal lines when the far-field behaviour

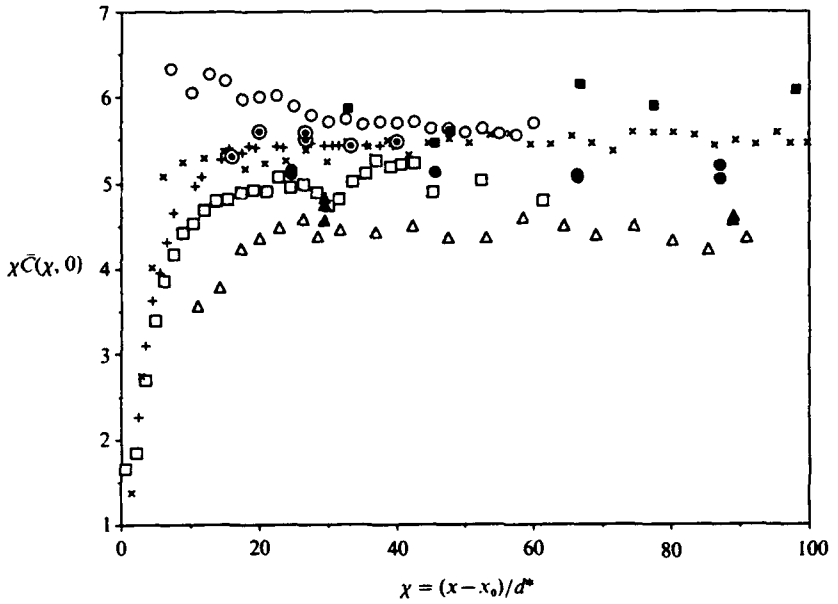

FIGURE 7. Comparison of current results with the results of previous experiments for the scaled mean centreline concentration, $\chi\bar{C}(\chi,0)$, versus the scaled downstream coordinate, $\chi = (x-x_0)/d^*$ (□, Lockwood & Moneib 1980; ○, Wilson & Danckwerts 1964: △, Birch *et al.* 1978; +, Becker *et al.* 1967, ×, Dahm 1985; ⊙, Papanicolaou & List 1987: ■, Papanicolaou & List 1988; ●, present data $Re_0 = 5000$; ▲, present data $Re_0 = 16000$).

of the jet is attained. The ordinate of the horizontal portion of the curves is the value of κ for each experimental effort. The current data fall within the scatter of the results of the other experiments.

The reported variation in κ is, perhaps, interesting and unexpected. It could result from improper calculation of d^*, miscalibration of experimental diagnostics, or Reynolds-number effects. For example, the value of κ differs by about 8% in the current studies at 5000 and 16000. Different nozzles were used for each set of experiments. It is possible that the design of the smaller nozzle could have caused the maximum momentum flux to occur slightly beyond the nozzle's exit plane in an effective area smaller than $\frac{1}{4}\pi d^2$ (vena contracta). This would produce a slightly smaller value of d^* than the result of the axisymmetric boundary-layer calculation. A correction of this type would bring the current results for κ closer together. It is unlikely, however, that miscalculation and/or miscalibration could account for the entire range of variation in κ seen on figure 7 ($4 < \kappa < 6$). Reynolds-number effects cannot be ruled out, but an examination of table 2 and figure 7 does not reveal a simple monotonic trend in κ with Re_0. Other possible sources for the reported variation in κ can be ruled out. Misalignment of measurement points with respect to the true jet axis could cause the reported discrepancies, but to account for the 8% change in κ the misalignment would have to be about $\pm 1.5°$, almost an order of magnitude greater than the estimated angular location error (about $\pm 0.2°$) of the current experiments. Initial density differences between the jet and reservoir fluids are accounted for in the far field through d^*. Additionally, there does not appear to be a physical mechanism which would allow differences in the Schmidt (Prandtl) number between experiments to change the jet's bulk entrainment rate of reservoir fluid, and thus influence the value of κ. At low and moderate Reynolds numbers,

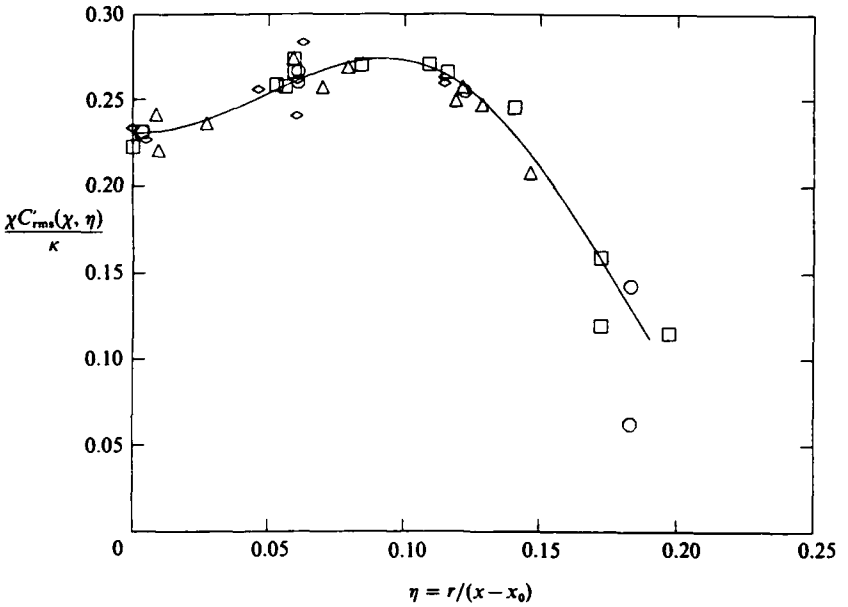

FIGURE 8. Root-mean-square concentration fluctuation level plotted versus $\eta = r/(x-x_0)$, with the same scaling of the vertical axis that collapses the mean concentration at $Re_0 = 5000$ (□, $x/d = 20$; ○, 40; △, 60; ◇, 80).

Niwa *et al.* (1984) have demonstrated the dependence of κ on Re_0. The recent article on self-preservation in turbulent flows by George (1989) suggests that details of the jet nozzle exit conditions play a role in determining κ.

The root-mean-square (r.m.s.) concentration fluctuation level, $C'_{\rm rms}$, was computed directly from each time series after optimal filtering (Wiener 1949, described in Press *et al.* 1986, illustrated in Dowling *et al.* 1989). This filtering was performed to remove noise from the measured time series. For any of the current data sets, the difference in the computed value of $C'_{\rm rms}$ before and after optimal filtering was a small percentage ($\approx 0.1\%$ and always $< 2\%$) of the final value of $C'_{\rm rms}$ computed after filtering. The results for $C'_{\rm rms}$ are plotted on figures 5, 8 and 9 for $Re_0 = 40000$, 5000 and 16000, respectively. The axis scaling employed on figures 8 and 9 is exactly the same as that used on figures 3 and 4 for $\bar{C}$ at the same Reynolds numbers. As before, no 'self-normalization' of the data was necessary. Note that the vertical axes on figures 8 and 9 are not scaled by the centreline r.m.s. fluctuation level. The profile curve for $C'_{\rm rms}$ on figure 5 is the same as the one on figure 9. The fact that the r.m.s. fluctuation level data cluster about a single curve, in the *specific* similarity coordinates of the mean concentration, at $Re_0 = 5000$, and 16000, implies that $C'_{\rm rms}$ and $\bar{C}$ conform to the same *specific* similarity law, and that $C'_{\rm rms}/\bar{C}$ is a *general* similarity variable for the jet. This issue is further addressed in the next section.

As noted in the Introduction, this behaviour was not found in many previous investigations. Figure 10 is a plot of $C'_{\rm rms}/\bar{C}$ on the centreline of the jet for several experiments. The present data at $Re_0 = 5000$ and 16000 fall on horizontal lines, indicating that $C'_{\rm rms}$ and $\bar{C}$ follow the same *specific* similarity laws based on the values of κ and x_0 at each Reynolds number. The value of $C'_{\rm rms}/\bar{C}$ on the centreline for the current studies is 0.230 ± 0.007 at $Re_0 = 5000$, 0.237 ± 0.005 at $Re_0 = 16000$, and 0.23 ± 0.01 at $Re_0 = 40000$. The failure of many previous studies to find a constant value of $C'_{\rm rms}/\bar{C}$ on the centreline of the jet may be attributable to

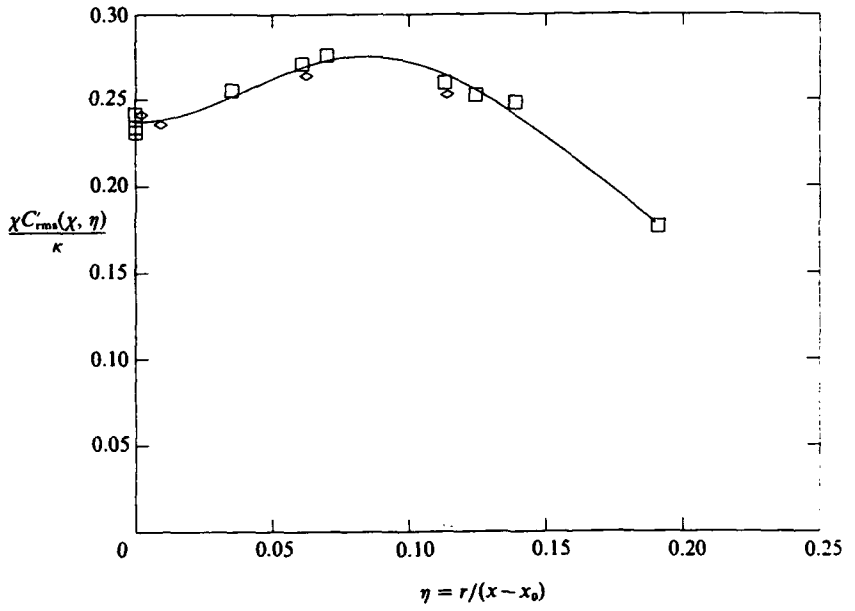

FIGURE 9. Root-mean-square concentration fluctuation level plotted versus $\eta = r/(x-x_0)$. with the same scaling of the vertical axis that collapses the mean concentration at $Re_0 = 16000$ (□. $x/d = 30$: ◇, 90).

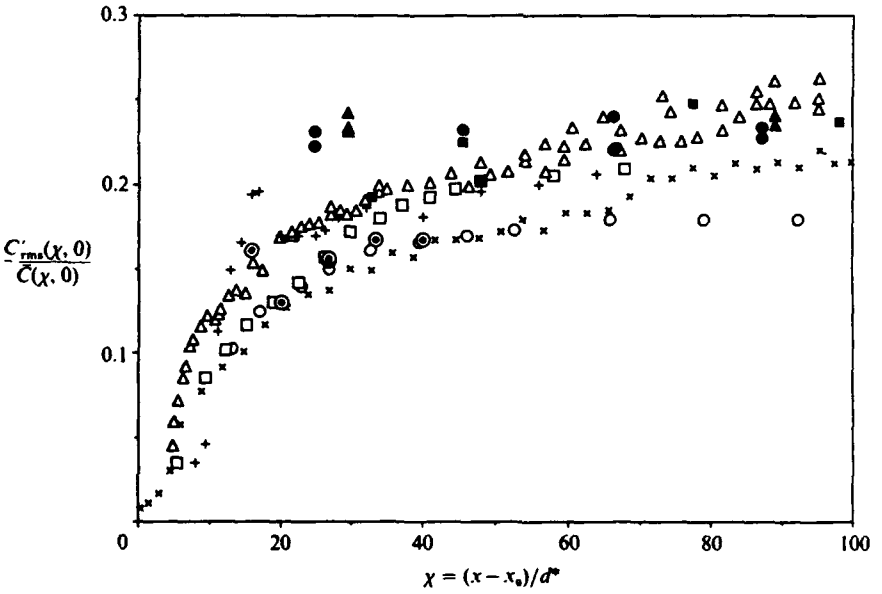

FIGURE 10. Comparison of current results with the results of previous experiments for the centreline ratio of the r.m.s. to mean concentration. $C'_{rms}(\chi.0)/\bar{C}(\chi.0)$. versus the scaled downstream coordinate, $\chi = (x-x_0)/d^*$ (□, Lockwood & Moneib 1980; ○. Wilson & Danckwerts 1964; △. Birch *et al.* 1978; +. Becker *et al.* 1967; ×, Dahm 1985; ⊙. Papanicolaou & List 1987; ■. Papanicolaou & List 1988; ●. present data $Re_0 = 5000$; ▲. present data $Re_0 = 16000$).

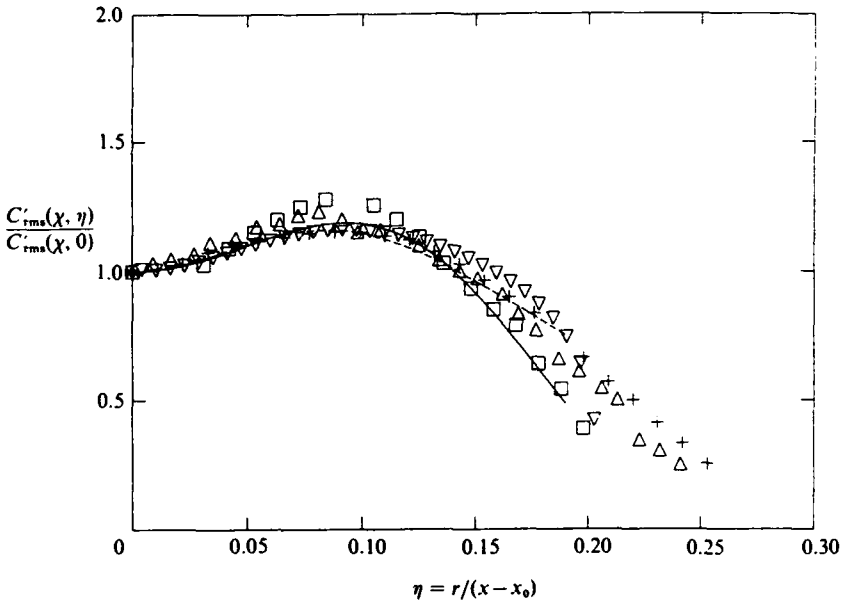

FIGURE 11. Comparison of the current results with the results of previous experiments for the r.m.s. concentration fluctuation level, divided by its centreline value, versus $r/(x-x_0)$ (□, Lockwood & Moneib 1980; △, Birch *et al.* 1978; +, Becker *et al.* 1967; ▽, Dahm 1985; ——, current profile at $Re_0 = 5000$; – – – –, current profile at $Re_0 = 16000$). Reynolds and Schmidt number information for the plotted data is available in table 2.

inadequate temporal, spatial, or dynamic resolution of concentration fluctuations nearer to the jet nozzle. Because the process of computing an r.m.s. does not commute with averaging, a measurement probe that performs a fixed amount of averaging in time or space may not produce consistent r.m.s. measurements when placed in a flow with resolution requirements that vary with downstream distance. For the jet, f_B is proportional to $(x-x_0)^{-2}$, and λ_B is proportional to $(x-x_0)$: as a result, the resolution requirements are more difficult to satisfy at lower values of $(x-x_0)/d$. Additionally, if the measurement noise is large enough to obscure a significant portion of the signal's power spectrum, then filtering this noise may lead to an underestimation of $C'_{\rm rms}$ because part of the signal spectrum may be filtered too. Recall that $C'_{\rm rms}$ is the square root of the area under the power spectral curve (see (15) for the definition used in this study). If the noise is not filtered, then $C'_{\rm rms}$ may be overestimated because it may include contributions from the noise. The spatial and temporal resolution of the present experiments was adjusted at each downstream measurement location to prevent direct resolution difficulties, and the measurement diagnostic had sufficient dynamic range to effectively eliminate the influence of noise. Concentration fluctuation power spectra of the current data are described in §3.2, and the results presented there support these contentions concerning the resolution of the current measurements.

If the fluctuation levels of all the experiments are normalized by their centreline value, the r.m.s. profiles can be compared. Figure 11 is a plot of the fitted curves from this study with the results from other experiments. The less than perfect collapse is not surprising since the six experiments shown were performed at different Reynolds and Schmidt numbers, using different diagnostics with varying resolution.

An interesting comparison can be made between the present data at $Re_0 = 5000$

and 16000 on figure 11. The increase in Reynolds number causes a broadening of the r.m.s. profile. This effect might be explained by a simple argument concerning timescales near the edge of the jet. Consider parcels of high-concentration fluid that are ejected to the edge of the jet by the turbulent velocity field. As r is increased for a fixed value of x, there should be some radial location beyond which smoothing of concentration fluctuations (i.e. mixing) is only weakly influenced by turbulent stirring. In this region, smoothing proceeds at the diffusion rate alone, since the production rate of new interface between fluid constituents is not an important factor. The timescale over which diffusion can act in this outlying region is the timescale associated with re-entrainment by the Biot–Savart induced motions from the jet's largest scales. In a jet flow with a self-similar velocity field, the re-entrainment time, t_r, should be proportional to the local rotation time for a large vortex in the flow (i.e. $t_r \propto D/\bar{U}_{cl}$), and the mean size of the high-concentration parcels, l_h, tossed to the edge of the jet should be proportional to D which is proportional to $(x-x_0)$:

$$t_r \propto \frac{D}{\bar{U}_{cl}} \propto \frac{(x-x_0)^2}{U_0 d} = \frac{(x-x_0)^2}{\nu_\infty} Re_0^{-1}. \tag{13}$$

An indication of the relative amount of smoothing due to pure diffusion in a typical high-concentration parcel before re-entrainment, can be obtained from the ratio of the diffusion lengthscale associated with t_r, i.e. $(D_{j\infty} t_r)^{\frac{1}{2}}$, to the lengthscale of the high-concentration parcel.

$$\frac{(D_{j\infty} t_r)^{\frac{1}{2}}}{l_h} \propto \frac{(D_{j\infty}(x-x_0)^2/\nu_\infty Re_0)^{\frac{1}{2}}}{(x-x_0)} = \frac{1}{(Sc\, Re_0)^{\frac{1}{2}}}. \tag{14}$$

An increase in this ratio indicates an increase in the effectiveness of purely diffusive smoothing of the concentration field at the edge of the jet. As indicated by (14), increasing the Reynolds or Schmidt number should decrease the amount of diffusion, and increase the local concentration fluctuation level at the edge of the jet. The proposed effect of Re_0 can be seen on figure 11 for $r/(x-x_0) \geqslant 0.15$ by comparing the current results at $Re_0 = 5000$ and 16000. The proposed effect of Sc is illustrated on the same figure by the current results at $Re_0 = 5000$ and the measurements of Dahm (1985) ($Re_0 = 5000$ and $Sc \approx 600$–800). Even though (14) is speculative and not quantitative, note that the result depends only on d and U_0 in a combination that gives Re_0.

The region of validity of (14) appears to depend on Re_0 since the measurements at $Re_0 = 16000$ and 40000 of C'_{rms} are essentially identical (see figures 5 and 9, recalling that the smooth profile curve for r.m.s. measurements is the same on both figures). Hence, (14) may only be relevant for Re_0 less than roughly 10^4. Above this value, turbulent stirring may be important all the way to the edge of the jet. Examination of table 2 and figure 11 shows that for $Re_0 > 10^4$, higher concentration fluctuations near the edge of the jet are not well correlated with larger experimental values of $ScRe_0$.

Another comparison worth making is between the current results at $Re_0 = 16000$ and those of Birch *et al.* (1978) at the same Reynolds number and nearly the same Schmidt number. The mean profiles agree reasonably well but the r.m.s. profiles do not. The disagreement in the r.m.s. profile (see figure 11) might be the result of resolution problems (see discussion below). The mismatch of the centreline r.m.s. levels at the farthest downstream location (see figure 10) might be the result of buoyancy in the experiments of Birch *et al.* When the buoyancy lengthscale is

estimated for their experiments, the result is $l_b \approx 55d$, which suggests that their jet may not be momentum dominated beyond $x/d \approx 55$. For comparison, l_b for the present work at $Re_0 = 16000$ is about $440d$.

Returning to figure 11, it can be seen that the peak values of the r.m.s. profiles do not coincide. While this might be the result of Reynolds-number effects, it might also partially result from resolution difficulties near the centreline. At a given downstream location, the mean passage frequency of concentration scales is greatest at the jet centreline. As the measurement point is moved toward the edge of the jet, the convection velocity decreases, so the bandwidth necessary to capture all of the fluctuations is smaller. If the estimated r.m.s. value of the centreline is low, possible because of insufficient time–space resolution, the rest of the r.m.s. profile is elevated when normalized by the artificially lower value. This centreline resolution difficulty should be most apparent in flows at high Schmidt number because of the smaller size of λ_B (see (4)).

3.2. *Power spectra of concentration fluctuations*

The power spectrum of concentration fluctuations, $E_c(f)$, was calculated from each of the data sets before optimal filtering using the method described in Appendix C of Dowling (1988). The overall normalization was chosen such that

$$\left\{2\int_0^\infty E_c(f)\,\mathrm{d}f\right\}^{\frac{1}{2}} = C'_{\mathrm{rms}}. \tag{15}$$

The independent variable is the frequency, f (in Hz).

If $E_c(f)$ has the same similarity as $\bar{C}$, then it should collapse along rays that emanate from the virtual origin of the jet when scaled by $\bar{C}$ and an appropriate timescale of the jet flow. In this study, the timescale chosen was τ_D (see (11)) which is certainly appropriate for the centreline of the jet flow. Even though a longer timescale should be used for rays off the centreline, τ_D has been used on all of the plots to simplify the presentation of the spectral results. In the far field, the local jet diameter grows linearly with $(x-x_0)$, and the mean centreline velocity decays like $(x-x_0)^{-1}$, so τ_D is proportional to $(x-x_0)^2$. Because a single Reynolds number is associated with the far field of the jet, the *general* mean-flow similarity actually requires that all jet timescales, which are related by a power of the Reynolds number, will have a quadratic dependence on $(x-x_0)$. The passage time of the Kolmogorov scale, for example, increases like $(x-x_0)^2$, and is related to τ_D by a factor of $Re_0^{-\frac{3}{4}}$.

The figures discussed in this section depict $E_c(f)$ on the vertical axis, scaled by the local value of $\tau_D\bar{C}^2$, and f on the horizontal axis multiplied by τ_D. The spectra are plotted in log-log coordinates, so the numerical factors involved in computing the timescale τ_D (the tangent of the jet half-angle ≈ 0.213, and the constant from Chen & Rodi's mean centreline velocity decay law = 6.2) only shift the plots relative to the numerical values on the axes and do not affect the spectral shapes. Consequently, other timescales with the same quadratic dependence on the downstream coordinate will produce the same collapse seen in the spectra presented on figures 12–17. All of the spectra in these figures were smoothed with a one-tenth decade filter.

It should be emphasized at the outset of this section that the spectral collapse obtained using τ_D, and $\bar{C}$ does not require any knowledge of either the kinetic-energy dissipation rate or the scalar fluctuation dissipation rate as would be the case for collapsing scalar spectra with Kolmogorov normalization (Gibson 1968). The spectral collapse displayed here is based on the estimates of the largest (and not the smallest) features of the flow. The spectral presentation on figures 12–20 is aimed at

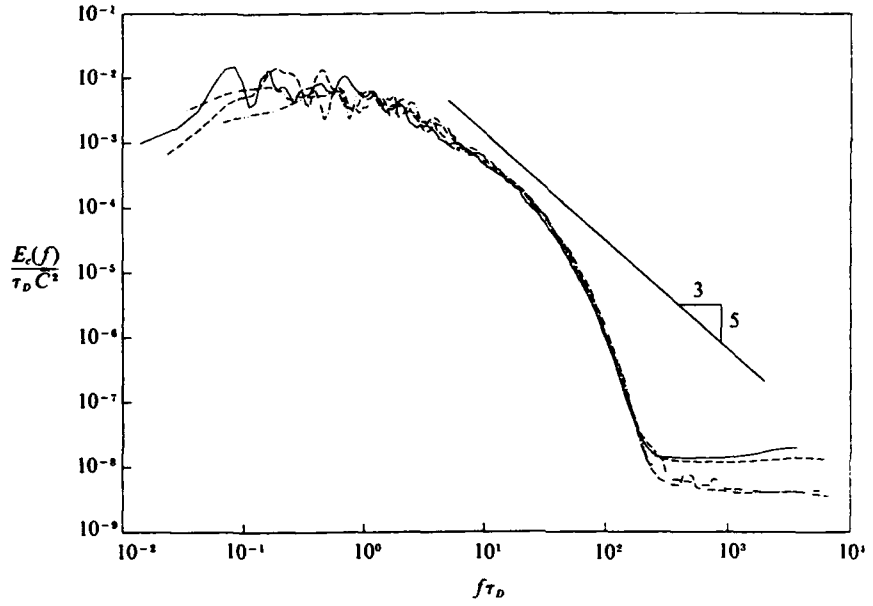

FIGURE 12. Scaled power spectra of the concentration fluctuations, $E_c(f)/\bar{C}^2\tau_D$, versus dimensionless frequency, $f\tau_D$, on the jet centreline at $Re_0 = 5000$ (——, $x/d = 20$; – – – –, 40; – · – · –, 60; – · · – · · –, 80).

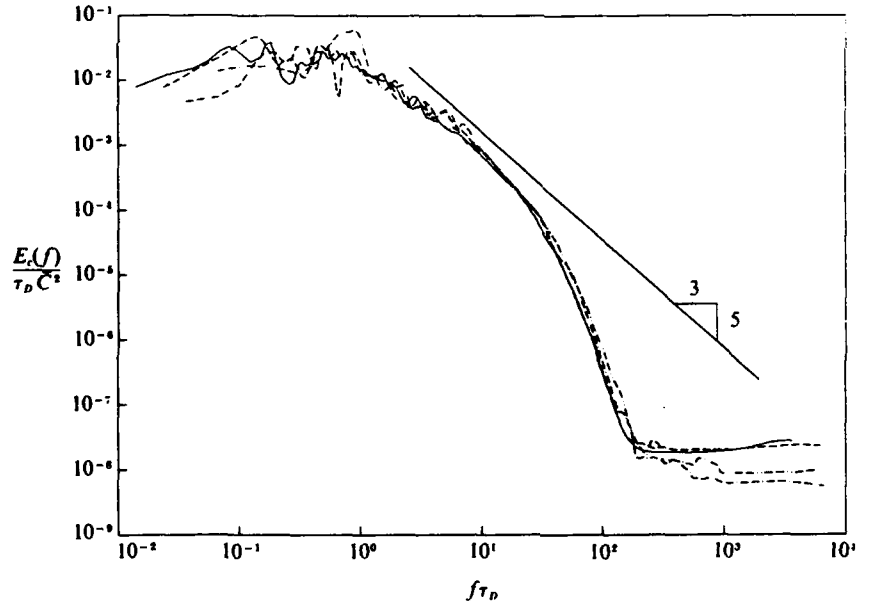

FIGURE 13. Scaled power spectra of the concentration fluctuations, $E_c(f)/\bar{C}^2\tau_D$, versus dimensionless frequency, $f\tau_D$, 3.4° off the jet centreline at $Re_0 = 5000$ (——, $x/d = 20$; – – – –, 40; – · – · –, 60; – · · – · · –, 80).

determining the extent of self-similarity of $E_c(f)$ using natural scaling parameters of the turbulent jet. A presentation and discussion of these spectra in Kolmogorov-normalized form is given in Dowling (1988).

Figures 12, 13 and 14 are plots of the scaled values of $E_c(f)$ from the measurements

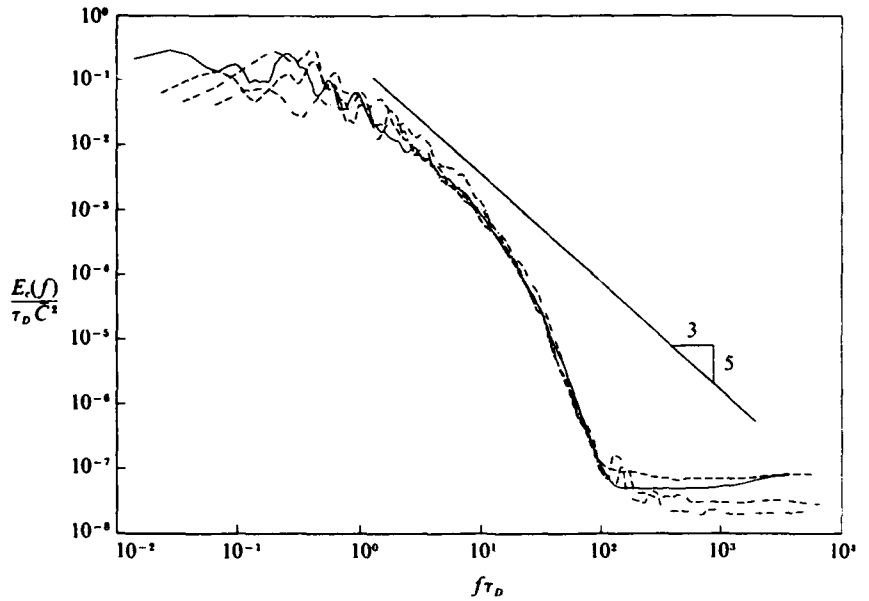

FIGURE 14. Scaled power spectra of the concentration fluctuations, $E_c(f)/\bar{C}^2\tau_D$, versus dimensionless frequency, $f\tau_D$. 7° off the jet centreline at $Re_0 = 5000$ (——, $x/d = 20$; – – –, 40; – · – · –, 60; – · · – · · –, 80).

at $Re_0 = 5000$ along the three rays $r/(x-x_0) \approx 0$ (centreline), $r/(x-x_0) \approx 0.06$ (3.4° off the centreline), and $r/(x-x_0) \approx 0.12$ (7° off the centreline) for $x/d = 20, 40, 60$, and 80. The nearly horizontal region of the spectra at high values of $f\tau_D$ is the noise floor produced by the measurement technique. The small bumps that occur in the noise floor are the scaled values of 60 Hz, 120 Hz, and 360 Hz. The diagnostic system that allowed these spectra to be measured with a dynamic range of nearly seven decades is described in Dowling *et al.* (1989).

The spectra collapse well in spite of the modest Reynolds number of the flow. Deviations from a perfect collapse, which are more evident as the edge of the jet is approached, are probably attributable to decreased statistical convergence. In particular, for a fixed run time at a given downstream location, the total effective sample size is smaller near the edge of the jet, where the mean velocity is lower, the turbulence is intermittent, and there is less mixed fluid to sample. Other reasons for the deviations could be small variations in Re_0 from run to run, and minor angular differences ($\pm 0.2°$) between the actual measurement locations and exact alignment along a given ray. The quality of the collapse displayed on figures 12, 13 and 14 for $E_c(f)$, and on figure 8 for $C'_{\rm rms}$ is strong verification that $C'_{\rm rms}$ and $\bar{C}$ follow the same *specific* similarity law throughout the jet. Recall that $E_c(f)$ and $C'_{\rm rms}$ are related through (15), so figure 8 is an integral measure of the *specific* similarity of $E_c(f)$ at $Re_0 = 5000$.

The adequacy of the sampling rate of the measurements is evident through the length of the portion of each measured spectra that is devoted to the noise floor. Clearly, any further increase in the sampling rate for these runs would not have 'uncovered' any more of the turbulent concentration signal spectra. The adequacy of the spatial resolution can also be ascertained from the spectra. These experiments were designed to resolve a calculated value of λ_B ((4), with $\beta = 1$). At $Re_0 = 5000$, the calculated value of $f_B \tau_D$ is about 670. If there were any effect on the measurements

from the finite spatial resolution of the detection system, it would be manifest in the spectra for $f_B \tau_D$ near and above 670. Because this region of the spectra falls below the noise floor for all of the plotted results, the portion of the measured spectra at frequencies below $f_B \tau_D \approx 670$, and above the noise floor can be regarded as free of any resolution difficulties. More importantly, however, the collapse of the spectra at different axial stations at high frequency supports the claim of no resolution difficulties.

For locally isotropic turbulent flow at high Reynolds number with Schmidt number of order unity, the spectrum of turbulent scalar fluctuations is expected to display a $-\frac{5}{3}$ power-law region (Batchelor 1959; Gibson 1968; Monin & Yaglom 1975). The Kolmogorov (Batchelor) lengthscale passage frequency should correspond to the high-frequency end of this region when a proper value of β is used in (4) to compute λ_K. Previous spectral investigations by Clay (1973), Chapmann (1979) and others put the actual value of β at little more than 10. While the spectra plotted on figures 12–14 are clearly not from a high-Reynolds-number flow, the scaled frequency range in which they begin to fall more rapidly than a constant power law is close to the value of $f_B \tau_D$ (≈ 54) calculated with $\beta = 12.5$. This figure for β was suggested by Professor Carl Friehe (personal correspondence, 1988). Clay and Friehe worked on a heated, and perhaps slightly buoyant, jet flow at a Reynolds number of almost 10^6. On figures 12–14, the choice of the same timescale for each ray causes the numerical location of the spectral break point (if one can be considered to exist on these plots) to decrease with increasing $r/(x-x_0)$.

At the low-frequency end, $f\tau_D \leqslant 1$, the spectra on figures 12–14 are approximately flat or show a mild peak in the range $0.1 \leqslant f\tau_D \leqslant 1.0$. While this behaviour is consistent with the passage of structures whose scale is approximately the same as the local diameter, the most general conclusion to be drawn is that the fluctuations that occur at frequencies below $1/\tau_D$ do not have a greater amplitude than those that occur near $1/\tau_D$. Consequently, one can think of the turbulent cascade at this Re_0 as starting at a lengthscale which is approximately the size of the local jet diameter.

Although the spectra collapse along rays when scaled by τ_D and $\bar{C}$, the spectra are *different* from ray to ray in ways that cannot be corrected by changing the timescale used to non-dimensionalize the axes of the plots. In particular, the spectra along the ray at 7° show a longer power-law region with a slope closer to $-\frac{5}{3}$ than those from the inner rays. This latter behaviour is also apparent in the spectra reported by Lockwood & Moneib (1980) at $x/d = 20$ in a heated air jet at $Re_0 \approx 50000$.

For the data recorded at $Re_0 = 16000$, the resolution requirements were relaxed by a factor of three. This choice was made because it put the value of $\frac{1}{3} f_B \tau_D$ ($\approx 1600/3$ with $\beta = 1$) right at the point where the signal contribution to the measured spectra met the noise floor, thereby making the best use of the available experimental bandwidth. Figures 15, 16 and 17 are plots of the scaled values of $F_c(f)$ from the measurements at $Re_0 = 16000$ along the three rays $r/(x-x_0) \approx 0$ (centreline), 0.06 (3.4° off the centreline) and 0.11 (6.3° off the centreline) for $x/d = 30$ and 90. The slopes of the diagonal lines on these figures do not have a theoretical basis and were drawn only to aid the eye. The quality of the collapse shown on figures 15–17 implies that all of the conclusions from the lower Reynolds number concerning the *specific* similarity of C'_{rms} and $E_c(f)$ remain valid at $Re_0 = 16000$. As before, incomplete statistical convergence, the intermittent character if the flow near the edge of the jet, small differences in Re_0, and imperfect angular alignment may well be responsible for the small deviations from a perfect collapse.

These spectra show the same general shape as those at $Re_0 = 5000$ except for the

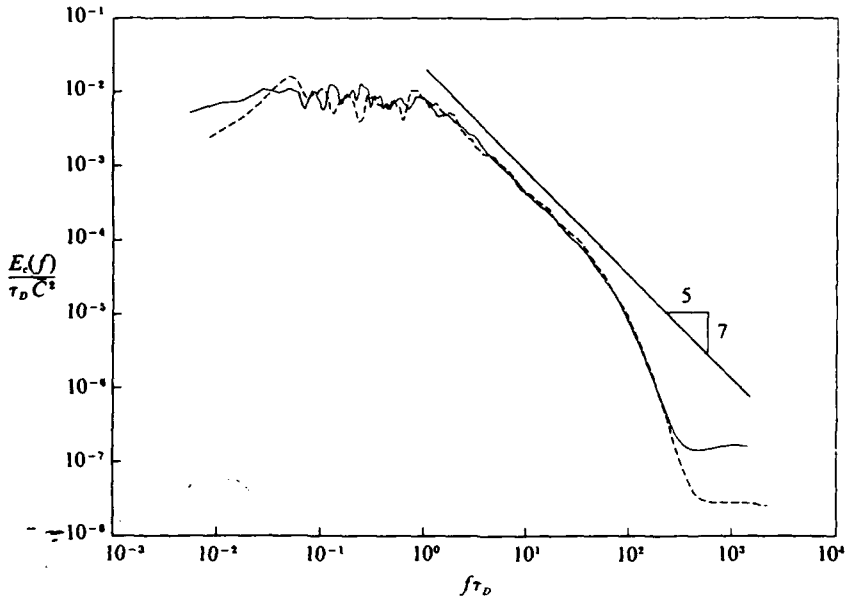

FIGURE 15. Scaled power spectra of the concentration fluctuations, $E_c(f)/\bar{C}^2\tau_D$, versus dimensionless frequency, $f\tau_D$, on the jet centreline at $Re_0 = 16000$ (——, $x/d = 30$; – – – –, 90).

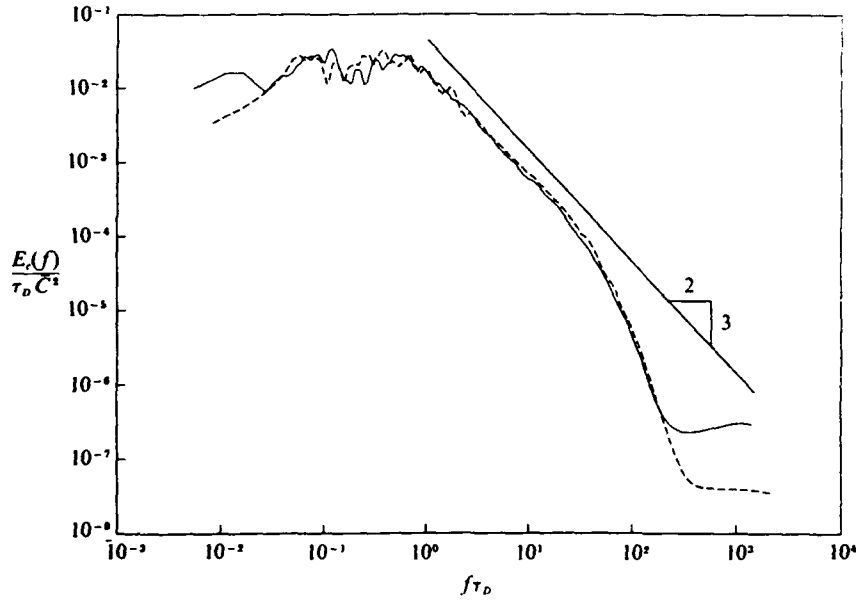

FIGURE 16. Scaled power spectra of the concentration fluctuations, $E_c(f)/\bar{C}^2\tau_D$, versus dimensionless frequency, $f\tau_D$, 3.4° off the jet centreline at $Re_0 = 16000$ (——, $x/d = 30$; – – – –, 90).

appearance of longer power-law regions, which extend the high-frequency range of the spectra. The slope of the power-law region steepens as the edge of the jet is approached. The spectra from the centreline appear have a slope of about -1.4, which decreases to -1.5 on the ray 3.4° off the centreline, while the straightest part of the spectra from the ray 6.3° off the centreline has a slope close to $-\frac{5}{3}$. The low-

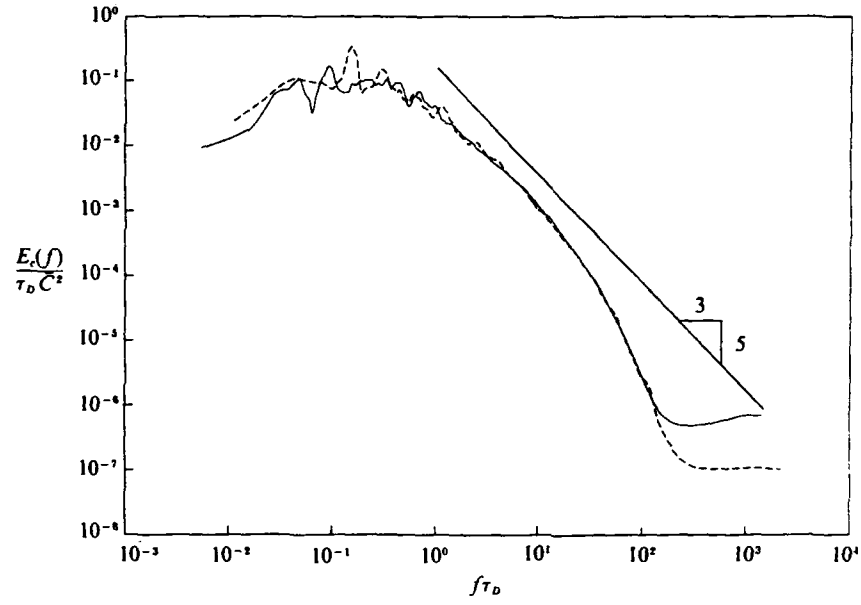

FIGURE 17. Scaled power spectra of the concentration fluctuations, $E_c(f)/\bar{C}^2\tau_D$, versus dimensionless frequency, $f\tau_D$. 6.3° off the jet centreline at $Re_0 = 16000$ (——, $x/d = 30$; – – – –, 90).

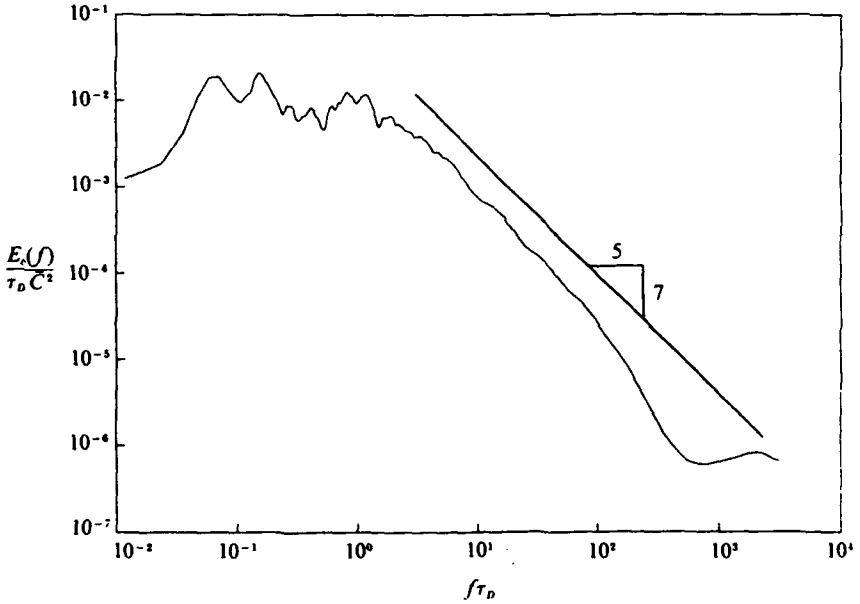

FIGURE 18. Scaled power spectra of the concentration fluctuations, $E_c(f)/\bar{C}^2\tau_D$, versus dimensionless frequency, $f\tau_D$, on the jet centreline at $Re_0 = 40000$ and $x/d = 60$.

frequency ends of the spectra at $Re_0 = 16000$ have the same behaviour as the spectra at $Re_0 = 5000$.

Figures 18 and 19 depict $E_c(f)$ at $Re_0 = 40000$, $x/d = 60$ and $r/(x-x_0) \approx 0$ and 0.12. The axis scaling is the same as before except that here x_0 was taken to be zero. In both cases, the full, high-frequency behaviour of the jet is partially masked by the measurement noise. The power-law regions are slightly longer than those at

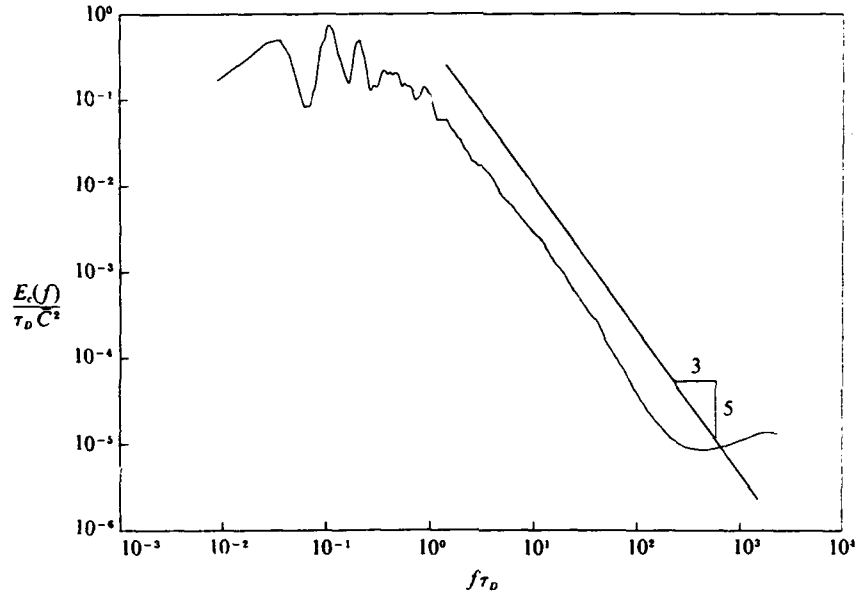

FIGURE 19. Scaled power spectra of the concentration fluctuations. $E_c(f)/\bar{C}^2\tau_D$, versus dimensionless frequency, $f\tau_D$, 7° off the jet centreline at $Re_0 = 40000$ and $x/d = 60$.

$Re_0 = 16000$, and the slopes are consistent with those displayed by the same rays at the lower Reynolds numbers. It is possible that the observed spatial variation of exponents for the measured spectra are not peculiar to the Reynolds-number range investigated here, and might persist at higher Reynolds numbers. Therefore, the exponent of the spectral power-law region along a particular ray might be a *general* similarity property of the jet concentration field. The low-frequency ends of the spectra on figures 18 and 19 have the same behaviour as that of the spectra at the smaller Reynolds numbers.

The physical reasons for the differences in power-law-region exponents, and their deviation from $-\frac{5}{3}$, are unknown. Yakhot, She & Orszag (1989) argue that the inertial-range velocity spectra of homogeneous turbulence might produce spectral power-law exponents that differ from $-\frac{5}{3}$, so perhaps the turbulent scalar field might also produce spectra with power-law exponents that differ from $-\frac{5}{3}$. The spectral differences found seem to indicate that jet turbulence is statistically different from ray to ray.

A comparison of previously reported scalar spectra from the jet centreline with the current results is given on figure 20. The parameters necessary to scale the spectra from other experiments and make them satisfy the overall normalization (equation (15)) were taken from the author's papers in all but one case. The vertical location of the spectrum of Clay (1973) could not be determined because he did not include C'_{rms} among his results. Its vertical location on figure 20 was chosen to match that of the spectrum of Becker *et al.* (1967), whose Reynolds number of 54000 was closest to that of Clay.

The current results and those of Becker *et al.* (1967) agree quite well for $f\tau_D$ less than unity. This implies that the concentration fluctuation energy associated with the largest scales is independent of Reynolds number for $Re_0 \geqslant 5000$. The centreline spectrum of Lockwood & Moneib (1980) probably falls below the others in this frequency range because their reported centreline r.m.s. level, at the downstream location of their spectral measurement ($x/d = 20$), is low ($C'_{rms} = 0.16\,\bar{C}$) when

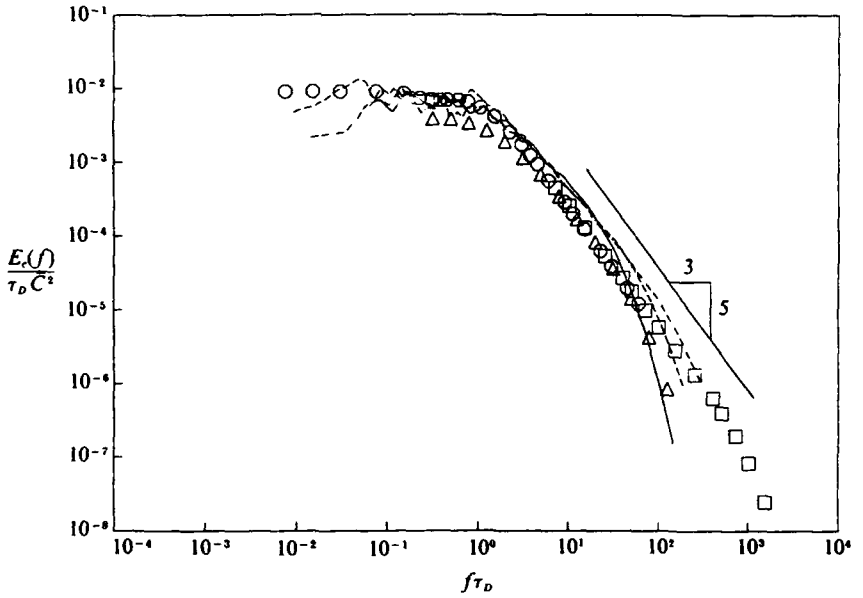

FIGURE 20. Comparison of the current results to previous experiments for the scaled centreline concentration fluctuation power spectra, $E_c(f)/\bar{C}^2\tau_D$. versus dimensionless frequency, $f\tau_D$ (□, Clay 1973: ○, Becker *et al.* 1967; △, Lockwood & Moneib 1980; present results——, $Re_0 = 5000$; – – – –, $Re_0 = 16000$; – · – · –, $Re_0 = 40000$). Reynolds and Schmidt number information for the plotted data is available in table 2.

compared to that of the other experiments. Hence, the behaviour of the largest concentration scales is likely to be a *general* similarity property of the jet. This contention has some backing, at present, from the liquid-phase (i.e. Schmidt number ≈ 600) measurements of Weddell (1953) and Dahm. Dimotakis & Broadwell (1984). They showed that the flame length in reacting jet flows becomes independent of Reynolds number above $Re_0 \approx 3000$. Because the largest scales of motion dominate the entrainment process in shear layers and jets (Brown & Roshko 1974; Dimotakis, Miake-Lye & Papantoniou 1983; Dahm & Dimotakis 1987), the Reynolds-number independence of the largest concentration scales is consistent with these flame-length observations.

The centreline spectra of Becker *et al.* (1967) and Clay (1973) closely follow a $-\frac{5}{3}$ power law over a significant range, whereas the current centreline results do not. This might result from the influence of buoyancy in the Clay's heated jet which discharged horizontally. Buoyancy may have deflected the effective centreline of the jet from the geometrical centreline, thereby altering the jet's character, and complicating the proper geometrical placement of the measurement probe with respect to the nozzle exit. The reasons for the difference in the spectral exponent between the current centreline spectrum at $Re_0 = 40000$ and that of Becker *et al.* are unknown. Note also that the spectrum of Lockwood & Moneib (1980) does not entirely coincide with that of Becker *et al.* either, even though the Reynolds numbers of these two studies were very close. However, if the centreline spectrum of Lockwood & Moneib is raised so that its level is the same as that of the other spectra at $f\tau_D \approx 1$, it would be a close match with the current spectra at $Re_0 = 16000$ and 40000.

These differences do not appear to have a simple explanation. From the currently accepted theoretical standpoint (Batchelor 1959; Gibson 1968; see also Monin &

Yaglom 1975), it is unlikely that the differences in Schmidt (Prandtl) number between experiments could have any effect on the spectral content of the scalar field at frequencies below the passage frequency of the Kolmogorov scale, which is of order 10^2 or greater on the scaled abscissa for all the experimental results shown on figure 20. It also seems unlikely that there would be a significant Reynolds-number effect confined to the small range between 40000 (the highest of the current study) and 54000 (the Reynolds number of Becker *et al.*). It would appear that the source of these spectral differences must lie in experimental differences between these investigations which effect the character of the jet's concentration field either directly, or through the turbulent velocity field which convects the measured scalars.

Regardless of the exact shape or levels, one Reynolds-number effect can be seen in figure 20. This is the movement to higher frequency, with increasing Reynolds number, of the break point at which a spectrum starts to fall faster than a constant power law. This observation was, of course, anticipated since $f_B \tau_D \propto \lambda_K^{-1} \propto Re_0^{\frac{3}{4}}$. The spectrum from Lockwood & Moneib was computed from data that were filtered at frequencies higher than $f\tau_D \approx 50$, and therefore breaks from the constant-power-law behaviour at a lower frequency than expected. Taken all together, this observation, the above discussion, and figures 12–20, lead to the conclusion that the exact shape of the jet's concentration fluctuation power spectrum is *specifically* self-similar, but not *generally* self-similar.

3.3 *Probability density function of concentration*

After each data set was optimally filtered, a histogram of the instantaneous concentration divided by the local mean concentration, $C/\bar{C}$, was compiled by sorting the data into bins. This histogram was normalized; i.e.

$$\int_0^\infty \mathrm{PDF}\,(C/\bar{C})\,\mathrm{d}(C/\bar{C}) = 1. \tag{16}$$

to form a probability density, PDF $(C/\bar{C})$. The independent variable, $C/\bar{C}$, was chosen because dividing C by $\bar{C}$ should remove the effects of the downstream decay of the mean concentration. For fixed Re_0, the probability density function of $C/\bar{C}$ should depend only on $r/(x-x_0)$ if the statistical properties (higher moments) of the distribution of concentration fluctuations in the jet follow the same *specific* similarity law as the first moment, $\bar{C}$. Additionally, the PDFs presented below are plotted with a linear abscissa and a linear ordinate to determine the extent to which they can be considered self-similar. Logarithmic axes or additional self-normalization with anything besides $\bar{C}$ would only obscure the main conclusion to be drawn from this section: the PDF of $C/\bar{C}$ is self-similar along rays that emanate from the jet's virtual origin.

Figures 21, 22 and 23 display the measured PDFs of $C/\bar{C}$ along the three rays at $r/(x-x_0) \approx 0$, 0.06 and 0.12 for $x/d = 20$, 40, 60 and 80 at $Re_0 = 5000$. The quality of the collapse of the distributions along rays implies that $C/\bar{C}$ is the proper *specific* similarity variable, and that the higher moments of the PDF of $C/\bar{C}$ are independent of the downstream position in the jet. For example, the square root of the second moment of the PDF of $C/\bar{C}$, taken about $C/\bar{C} = 1$, is $C'_{\mathrm{rms}}/\bar{C}$, which was previously found to depend only on $r/(x-x_0)$ for fixed Re_0 (see §3.1). Slight imperfections in the collapse are believed to be the consequence of incomplete statistical convergence, the intermittent character of the flow at the larger values of $r/(x-x_0)$, and possibly

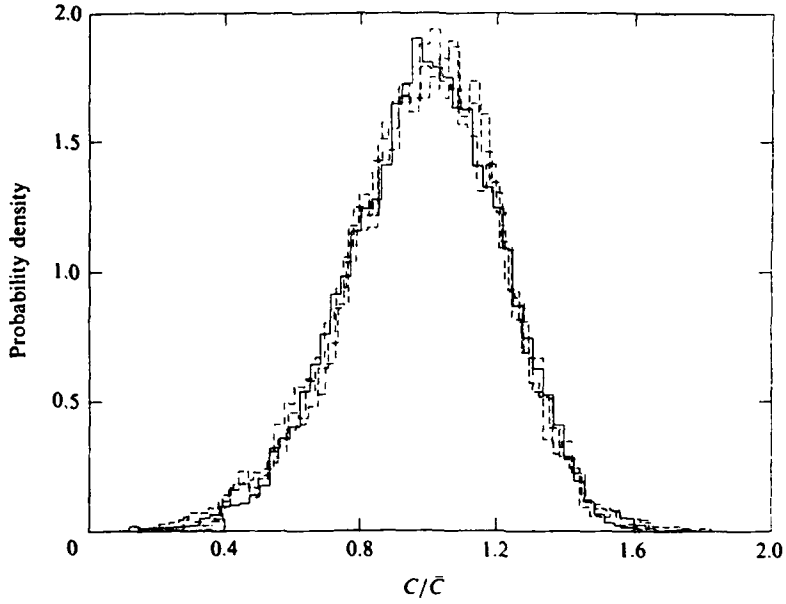

FIGURE 21. Probability density function of the scaled concentration, $C/\bar{C}$, on the jet centreline at $Re_0 = 5000$ (——, $x/d = 20$; – – – –, 40; – · – · –, 60; – · · – · · –, 80).

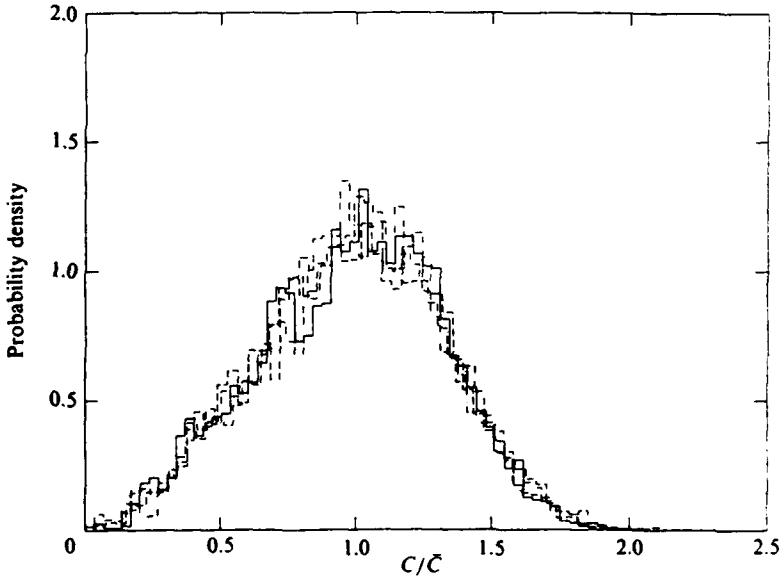

FIGURE 22. Probability density function of the scaled concentration, $C/\bar{C}$, 3.4° off the jet centreline at $Re_0 = 5000$ (——, $x/d = 20$; – – – –, 40; – · – · –, 60; – · · – · · –, 80).

imperfect alignment of individual measurement points with respect to the chosen ray (note the difference between the PDFs at $\eta = 0.11$ and $\eta = 0.12$ on figure 26).

Figures 24, 25 and 26 depict the measured probability density functions of $C/\bar{C}$ along the three rays at $r/(x-x_0) \approx 0$, 0.06 and 0.11 to 0.12, for $x/d = 30$ and 90, at $Re_0 = 16000$. The quality of the collapse is good, implying that the proposed *specific*

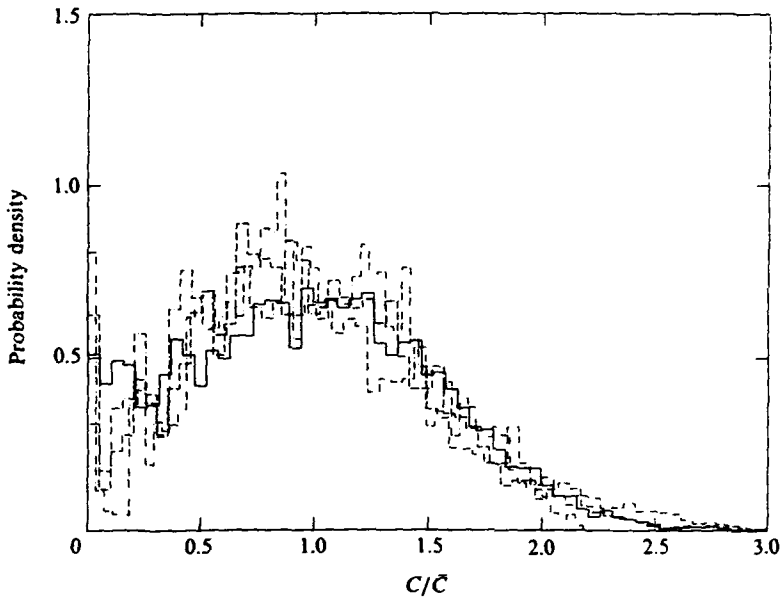

FIGURE 23. Probability density function of the scaled concentration, $C/\bar{C}$, 7° off the jet centreline at $Re_0 = 5000$ (——, $x/d = 20$; – – –, 40; – · – · –, 60; – · · – · · –, 80).

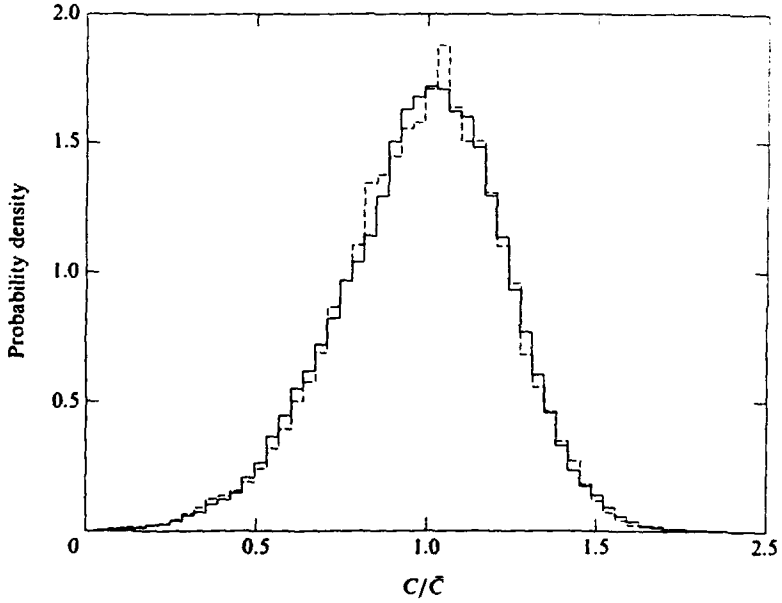

FIGURE 24. Probability density function of the scaled concentration, $C/\bar{C}$, on the jet centreline at $Re_0 = 16000$ (——, $x/d = 30$; – – –, 90).

similarity variable, $C/\bar{C}$, for the PDF of concentration fluctuations is a *general* similarity variable, even though the actual shapes of the PDFs of $C/\bar{C}$ might depend on Re_0. Imperfections in the collapse at this Reynolds number may be attributable to the same problems mentioned in the previous paragraph.

The area contained in the first bin ($C \approx 0$) of the plotted PDFs corresponds to unmixed fluid from the reservoir. Its contribution to the whole PDF must increase

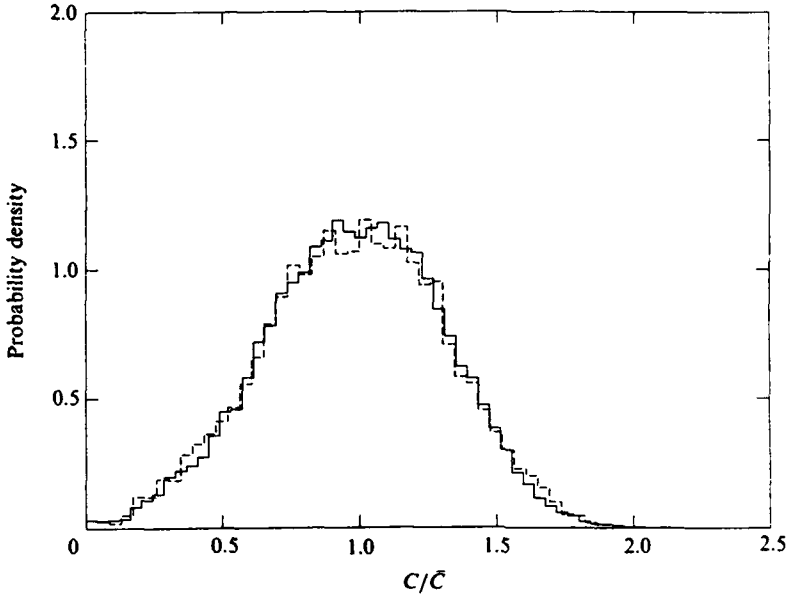

FIGURE 25. Probability density function of the scaled concentration, $C/\bar{C}$. 3.4° off the jet centreline at $Re_0 = 16000$ (——, $x/d = 30$; - - - -. 90).

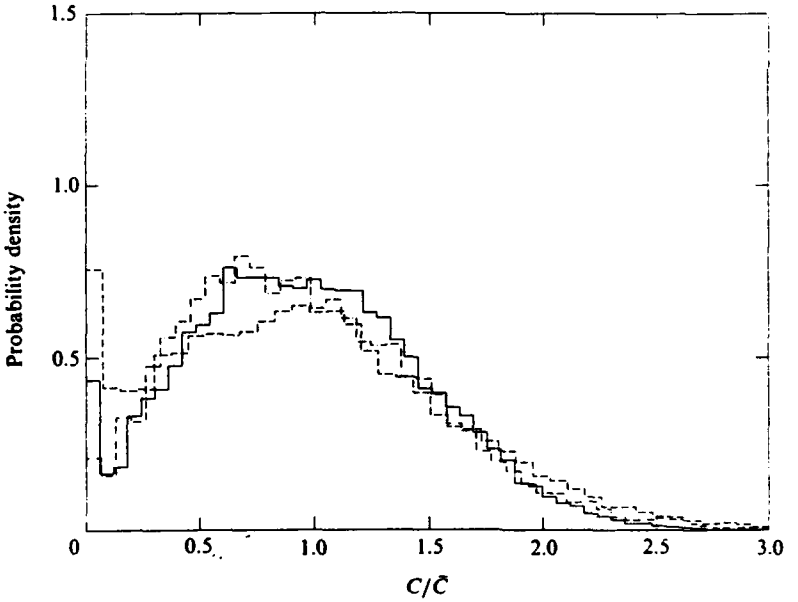

FIGURE 26. Probability density function of the scaled concentration, $C/\bar{C}$. 6.3° to 7° off the jet centreline at $Re_0 = 16000$ (——, $x/d = 30$, $\eta \approx 0.11$; - - - -, $x/d = 30$, $\eta \approx 0.12$; - · - · -, $x/d = 90$, $\eta \approx 0.11$).

as $\gamma/(x-x_0)$ increases until the measurement point is completely outside the jet, and the probability of finding reservoir fluid is unity. Therefore, the area of the first bin of the PDF can be taken as a measure of one minus the intermittency of the jet's concentration field, where the intermittency is understood to be the fraction of the time that the concentration field at a point can be considered turbulent. Figures 23

and 26 appear to show that one minus the intermittency, by this measure, varies by as much as factor of three. While this could certainly result from a sampling interval that was too short in comparison with the timescales of the flow, the basis for the above intermittency observation is put in further doubt when the finite precision of the experimental calibration is accounted for. Unlike the bulk of the PDF, the absolute accuracy of the calibration (about ± 1 part per 10^3) is an important limit in the interpretation of concentration measurements near $C = 0$. For example, the mean concentration value of the run at $x/d = 90$ that was used to create figure 26 was about 0.025, which means that each plotted PDF bin covers a range of only 0.0005 (roughly half the calibration error). Additionally, because it is possible to find smooth regions of the jet's concentration field near its edge with $C \neq 0$, the distinction between turbulent and non-turbulent fluid should perhaps be based on a threshold for $|\mathrm{d}C/\mathrm{d}t|$ and not just a threshold on $C/\bar{C}$. To conclude, the limitations of the finite sampling interval, the calibration accuracy, and the lack of a proper turbulent/non-turbulent distinction criterion prevent the inclusion of any quantitative statements concerning the intermittency inferred from the reported PDFs of $C/\bar{C}$. Chatwin & Sullivan (1989) discuss the shortcomings of the standard definition of the intermittency for a dispersing scalar in turbulent flow.

At this point, one direct Schmidt-number comparison can be made with the results of Dahm (1985) at $Re_0 = 5000$ and $Sc \approx 600$–800. He found pure reservoir fluid on the centreline of the jet at least 3% of the time. In the current study at $Re_0 = 5000$, pure reservoir fluid was not found on the jet centreline (see figure 21 near $C = 0$). While this difference could result from calibration inaccuracy, which makes the $C = 0$ level of the data uncertain, the size of the observed discrepancy between $Sc = 1.0$ and $Sc \approx 600$–800 is larger than that which can be produced from the current calibration uncertainty alone. Hence, the reservoir fluid's lateral turbulent diffusivity appears to have an 'inverted' dependence on the molecular diffusivity, because pure reservoir fluid reaches the jet centreline at $Sc \approx 600$–800 ($D_{\mathrm{j}\infty} \ll \nu_\infty$), but not at $Sc = 1.0$ ($D_{\mathrm{j}\infty} = \nu_\infty$). This inverse behaviour of the effective diffusivity of a scalar in the presence of both molecular and convective transport has also been noted by Taylor (1953) for flow through a tube.

Figure 27 is a comparison of the averaged and smoothed centreline PDFs of $C/\bar{C}$ at $Re_0 = 5000$, 16000 and 40000. The PDFs for $Re_0 = 5000$ and 16000 plotted on this figure were obtained by combining those on figures 21 and 24, respectively. The distribution for $Re_0 = 16000$ is a little shorter and a little wider than the others. This is consistent with the slightly higher value of $C'_{\mathrm{rms}}/\bar{C}$ on the centreline at this Reynolds number (see figure 10). The differences in the three distributions on figure 27 are small, which implies that the PDF of $C/\bar{C}$ on figure 27 is a good candidate for a *general* centreline similarity PDF.

This contention is supported, for the most part, by a comparison of this research with other investigations (see figure 28). The bulk of the measurements, including all of the gas-phase results, collapse well. Two investigations in liquid-phase jets at high Schmidt number (Dahm 1985, axial measurements; and Papantoniou 1985; both in dark symbols on figure 28), produce PDFs that are significantly broader than the rest of the investigations. It is unlikely that these two PDFs differ from the rest because of Schmidt-number effects since other high-Schmidt-number efforts (Dahm 1985, radial measurements; and Papanicolaou & List 1988) agree with the lower Schmidt and Prandtl-number results. It is also unlikely that the observed differences are the result of Reynolds-number effects since the shape of the centreline PDF of $C/\bar{C}$ from investigations at Reynolds numbers from 3000 (Papanicolaou & List 1988) to 52000

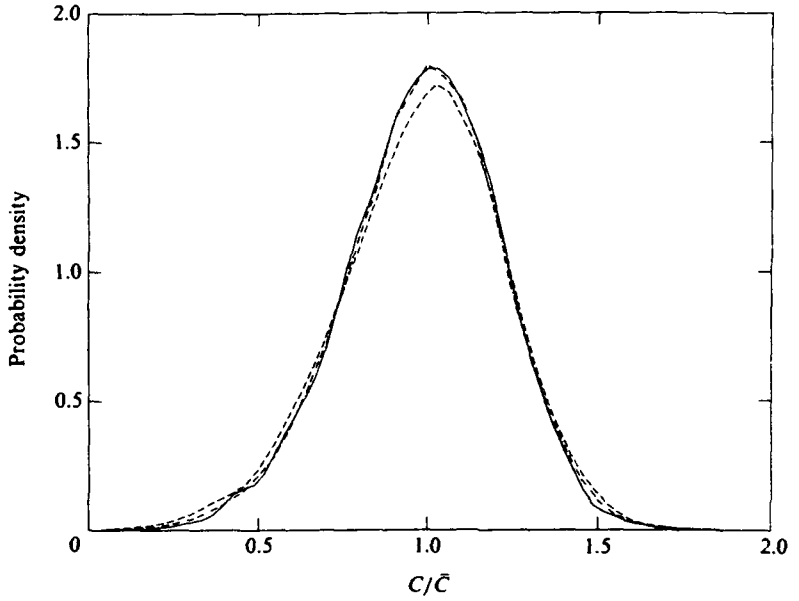

FIGURE 27. Averaged probability density functions of the scaled concentrations, $C/\bar{C}$, on the jet centreline (——, $Re_0 = 5000$; – – – –, 16000; – · – · –40000).

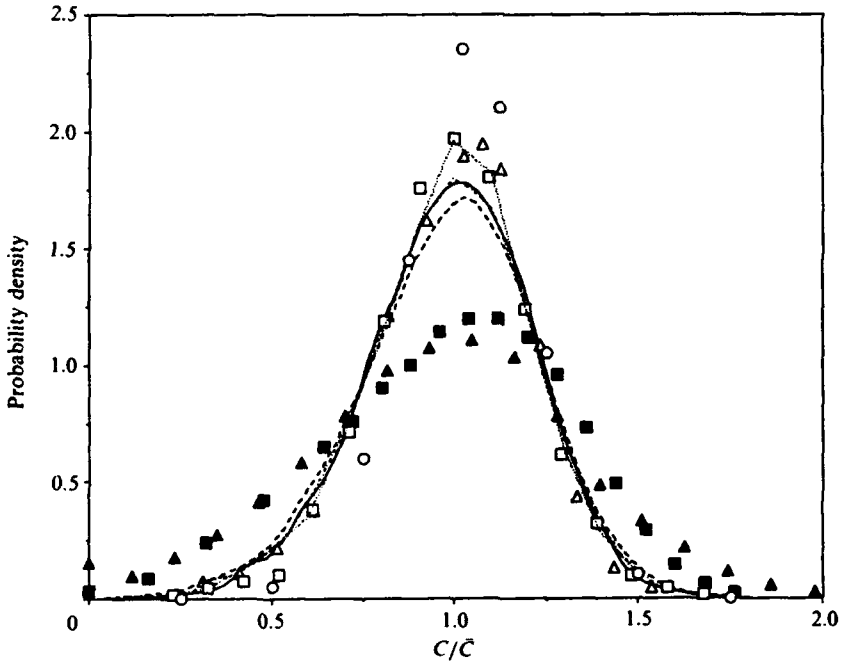

FIGURE 28. Comparison of reported centreline probability density functions of concentration with the concentration axis scaled by the local mean concentration (△, Dahm 1985, radial measurements; ■, Dahm 1985, axial measurements; □, Lockwood & Moneib 1980; ▲, Papantoniou 1985; ○, Papanicolaou & List 1987; · · · · · · · , Papanicolaou & List 1988; ——, current results at $Re_0 = 5000$; – – – –, current results at $Re_0 = 16000$; – · – ·, current results at $Re_0 = 40000$). Reynolds and Schmidt number information for the plotted data is available in table 2.

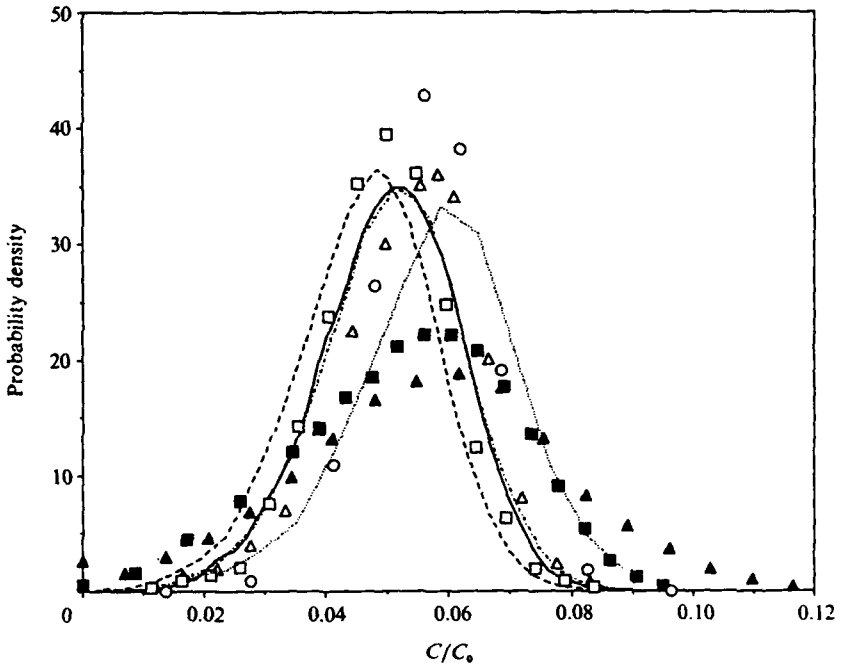

FIGURE 29. Comparison of reported centreline probability density functions of concentration without scaling the concentration axis by the local mean concentration (△, Dahm 1985, radial measurements; ■, Dahm 1985, axial measurements; □ Lockwood & Moneib 1980; ▲, Papantoniou 1985; ○, Papanicolaou & List 1987; ·····, Papanicolaou & List 1988; ——, current results at $Re_0 = 5000$; – – –, current results at $Re_0 = 16000$; – · – · –, current results at $Re_0 = 40000$). C_0 is the jet exit concentration. Reynolds and Schmidt number information for the plotted data is available in table 2. All PDFs are referenced to $\chi = 100$.

(Lockwood & Moneib 1980) is essentially the same. The difference in the two groupings on figure 28 is probably too large to be caused by resolution differences between experiments. However, resolution differences could result in the comparatively mild scatter in the 'preferred' PDF-shape grouping (open symbols and dashed/dotted lines on figure 28).

The scaling of the abscissa in figures 21–28 hides a major problem in the understanding of jet similarity: there is no precise and accepted value for κ (the mean centreline concentration decay parameter, see §3.1). The demonstrated *general* similarity variable of the jet's concentration field, $C/\bar{C}$, removes any dependence on the value of κ. Figures 28 and 29 illustrate this point. Both figures depict the same data. The difference is the abscissa of figure 29, which is the *absolute* relative concentration, C/C_0, for a particular *downstream position* (C_0 is the jet exit concentration). All of the PDFs on figure 29 have been referenced to $(x-x_0)/d^* = 100$ for the purposes of comparison, using the mean centreline concentration decay law from each experiment, and the assumption that the PDF of $C/\bar{C}$ was specifically self-similar in each experiment. The difference in the quality of the collapse between figure 28 and 29 is entirely the result of the variation in κ (see (1) and figure 7).

Another important point that should be emphasized is that figures 27 and 28 are for the centreline *only*. Since the r.m.s. profile of concentration fluctuations may depend on Reynolds number and/or Schmidt number near the edge of the jet (see discussion in §3.1), the PDF of $C/\bar{C}$ may also. In fact, the evidence of figure 11 for

$Re_0 \approx 10^4$ suggests that the width of the PDF of $C/\bar{C}$ on a given ray near the edge of the jet ($r/(x-x_0) > 0.15$) should increase with increasing Re_0 or Sc. Hence, while it appears that the PDF of $C/\bar{C}$ is *generally* self-similar near the centreline, and perhaps out as far as $r/(x-x_0) \approx 0.12$ (compare figures 22 with 25, and 23 with 26), PDFs of $C/\bar{C}$ significantly off the jet centreline may only be *specifically* self-similar along rays.

A final matter that should be discussed involves the statistical coupling of the PDF of $C/\bar{C}$ and $E_c(f)$ through the r.m.s. concentration fluctuation, $C'_{\rm rms}$, i.e.

$$\bar{C}^2 \int_0^\infty (C/\bar{C}-1)^2 \,\mathrm{PDF}\,(C/\bar{C})\,\mathrm{d}(C/\bar{C}) = 2\int_0^\infty E_c(f)\,\mathrm{d}f = C'^2_{\rm rms}. \tag{17}$$

This relation suggests that $C'_{\rm rms}$ on the centreline, and therefore the centreline PDF of $C/\bar{C}$, should depend on Re_0 since the length of the power-law region of $E_c(f)$ is found to depend on Re_0 (see final paragraph of §3.2). While this is mathematically correct, we note that as the Reynolds number is raised above $Re_0 \approx 5000$, the integrated contribution from the extended portion of $E_c(f)$ is a small fraction of the total r.m.s. fluctuation level, an amount perhaps too small to detect in the background of other experimental uncertainties in the present Reynolds-number range from 5000 to 40000. The largest contributions to the r.m.s. fluctuation level comes from the spectral region near $f\tau_D \approx 1$, which has been found to be independent of Re_0 above $Re_0 = 5000$.

4. Conclusions

This work leads to several conclusions. For a fixed Reynolds number and Schmidt number, the jet's turbulent concentration field is not only self-similar along rays in the mean, but is statistically self-similar along rays at every time- and lengthscale as demonstrated by the collapse of the power spectrum of concentration fluctuations. This detailed similarity along rays appears to be a *general* similarity property of the jet because it was found at two values of Re_0 (5000 and 16000). One set of *general* similarity parameters for the turbulent jet's concentration field appears to be $\bar{C}$ and τ_D (or any lengthscale that has a quadratic dependence on downstream distance). Use of these should effect a collapse of the statistical measures of the fluctuating concentration field in the jet at any turbulent Reynolds number. The shape of the PDF of $C/\bar{C}$ near the *centreline* in gas-phase jets appears to be self-similar in *general* (except for the small caveat mentioned at the end of §3.3), which implies that $C'_{\rm rms}/\bar{C}$ has a *general* self-similar value on the centreline between 0.23 and 0.24. Results to date suggest that the PDF of $C/\bar{C}$ may only be *specifically* self-similar away from the jet centreline. And finally, the contribution of the largest concentration scales to the strength of the concentration fluctuations in the jet is *generally* self-similar above $Re_0 = 5000$.

This work also points out the clear need for further experimentation to determine the factors that control the decay parameter, κ. Such an investigation will likely require extensive measurements of the jet's velocity field, which regrettably were beyond the scope of this study.

The authors wish to acknowledge useful discussions with Dr J. E. Broadwell, and thank Professor W. A. Dahm for providing the digitized values of the 'pre-1986' experimental results for figures 6, 7, 10, and 11. These experiments would not have been possible without the electronic wizardry of Dr Dan Lang. Thanks also to Paul Miller for his insightful suggestions, and proof reading of the text. This work was

supported by the Gas Research Institute under grants 5083-260-0878 and 5087-260-1467, and the Air Force Office of Scientific Research under grants 83-0213 and 88-0155.

REFERENCES

AVERY, J. F. & FAETH, G. M. 1974 Combustion of a submerged gaseous oxidizer jet in liquid metal. *Fifteenth Intl Symp. on Combustion*, pp. 501–512. The Combustion Institute, Pittsburgh, Pennsylvania.

BATCHELOR, G. K. 1959 Small scale variation of convected quantities like temperature in turbulent fluid. *J. Fluid Mech.* **5**, 113–139.

BECKER, H. A., HOTTEL, H. C. & WILLIAMS, G. C. 1967 The nozzle fluid concentration field of the round turbulent jet. *J. Fluid Mech.* **30**, 285–303.

BIRCH, A. D., BROWN, D. R., DODSON, M. D. & THOMAS, J. R. 1978 The turbulent concentration field of a methane jet. *J. Fluid Mech.* **88**, 431–449.

BROWN, G. L. & ROSHKO, A. 1974 On density effects and large structure in turbulent mixing layers. *J. Fluid Mech.* **64**, 775–816.

CHAPMANN, D. R. 1979 Computational aerodynamics development and outlook. *AIAA J.* **17**, p. 1293–1313.

CHATWIN, P. C. & SULLIVAN, P. J. 1989 The intermittency factor of scalars in turbulence. *Phys. Fluids* A **1**, 761–763.

CHEN, C. J. & RODI, W. 1980 *Vertical Turbulent Buoyant Jets: A Review of the Experimental Data*. Pergamon.

CLAY, J. P. 1973 Turbulent mixing of temperature in air, water, and mercury. Ph.D. thesis, University of California San Diego, La Jolla Ca.

CORRSIN, S. & UBEROI, M. S. 1950 Further experiments on the flow and heat transfer in a heated turbulent air jet. *NACA Rep.* 998.

DAHM, W. A. 1985 Experiments on entrainment, mixing, and chemical reactions in turbulent jets at high Schmidt number. Ph.D. thesis, California Institute of Technology, Pasadena, CA.

DAHM, W. A. & DIMOTAKIS, P. E. 1987 Measurements of entrainment and mixing in turbulent jets. *AIAA J.* **25**, 1216–1223.

DAHM, W. A., DIMOTAKIS, P. E. & BROADWELL, J. E. 1984 Non-premixed turbulent jet flames. *AIAA paper* 84-0369.

DIMOTAKIS, P. E., MIAKE-LYE, R. C. & PAPANTONIOU, D. A. 1983 Structure and dynamics of round turbulent jets. *Phys. Fluids* **26**, 3185–3192.

DOWLING, D. R. 1988 Mixing in gas phase turbulent jets. Ph.D. thesis, California Institute of Technology, Pasadena CA.

DOWLING, D. R. & DIMOTAKIS, P. E. 1988 On mixing and structure of concentration field of turbulent jets. In *Proc. First National Congress on Fluid Dynamics, 25–28 July 1988 Cincinnati, Ohio. Part 2*, pp. 982–988. AIAA.

DOWLING, D. R., LANG, D. B. & DIMOTAKIS, P. E. 1989 An improved laser-Rayleigh scattering photodetection system. *Exp. Fluids* **7**, 435–440.

FISCHER, H. G., LIST, E. J., KOH, R. C. Y., IMBERGER, J. & BROOKS, N. H. 1979 *Mixing in Inland and Coastal Waters*. Academic.

FRIEHE, C. A., VAN ATTA, C. W. & GIBSON, C. H. 1971 Jet turbulence: dissipation rate measurements and correlations. *AGARD Turbulent Shear Flows*, CP-93, pp. 18-1 to 18-7.

GEORGE, W. K. 1989 The self-preservation of turbulent flows and its relation to initial conditions and coherent structures. In *Advances in Turbulence* (ed. W. K. George & R. Arndt), pp. 39–73. Hemisphere.

GIBSON, C. H. 1968 Fine structure of scalar fields mixed by turbulence. II Spectral theory. *Phys. Fluids* **11**, 2316–2317.

HINZE, J. O. 1975 *Turbulence*, 2nd edn., pp. 224–225, 520–523. McGraw-Hill.

KUETHE, A. M. 1935 Investigations of the turbulent mixing regions formed by jets. *Trans. ASME E: J. Appl. Mech.* **1**, 87–95.

LANDAU, L. D. & LIFSHITZ, E. M. 1959 *Fluid Mechanics*. Pergamon.

LOCKWOOD, F. C. & MONEIB, H. A. 1980 Fluctuating temperature measurements in a heated round free jet. *Combust. Sci. Tech.* **22**, 63–81.

MONIN, A. S. & YAGLOM, A. M. 1975 *Statistical Fluid Mechanics*, vol. II, Chap. 8. MIT Press.

NIWA, C., ICHIZAWA, J., YOSHIKAWA, N. & OHTAKE, K. 1984 Time-resolved concentration measurements of jets by laser Rayleigh method – comparison of He, CO_2, and CCl_2F_2 jets. *Proc. Fourteenth Intl Symp. on Space Technology and Science, Tokyo.*

PAPANICOLAOU, P. N. & LIST, E. J. 1987 Statistical and spectral properties of the tracer concentration in round buoyant jets. *Intl J. Heat Mass Transfer* **30**, 2059–2071.

PAPANICOLAOU, P. N. & LIST, E. J. 1988 Investigations of round turbulent buoyant jets. *J. Fluid Mech.* **195**, 341–391.

PAPANTONIOU, D. 1985 Observations in turbulent buoyant jets by use of laser-induced fluorescence. Ph.D. thesis, California Institute of Technology, Pasadena, Ca.

PITTS, W. M. 1986 Effects of global density difference and Reynolds number variations on mixing in turbulent axisymmetric jets. *Natl Bur. Stand. Internal Rep.* 86-3340.

PRESS, W. H., FLANNERY, B. P., TEUKOLSKY, S. A. & VETTERLING, W. T. 1986 *Numerical Recipes*, pp. 417–419. Cambridge University Press.

REICHARDT, H. 1965 Turbulenten Strahlausbreitung in Gleichgerichteter Grundstromung. *Forsh. Ing.-Wes.* **30**, 133–139; topic developed in: Zur problematik der turbulenten Strahlausbreitung in einer Grundstromung, *Mitt. MPI und AVA. Gottingen.* Nr. 35.

REID, R. C., PRAUSNITZ, J. M. & SHERWOOD, T. K. 1977 *The Properties of Gases and Liquids*, 3rd edn, p. 554. McGraw Hill.

RICOU, F. P. & SPALDING, D. B. 1961 Measurements of the entrainment by axisymmetrical turbulent jets. *J. Fluid Mech.* **11**, 21–32.

RUDEN, P. 1933 Turbulente Aurbreitungsvorgänge im Freistrahl. *Naturwissenshaften* (Jahrg. 21) **21/23**, 375–378.

TAYLOR, G. I. 1953 Dispersion of soluble matter in a solvent flowing slowly through a tube. *Proc. R. Soc. Lond.* A **219**, 186–203.

THRING, M. W. & NEWBY, M. P. 1953 Combustion length of enclosed turbulent jet flames. *Fourth (Intl) Symp. Combustion*, pp. 789–796. The William & Wilkins Co., Baltimore, Maryland.

TOWNSEND, A. A. 1976 *The Structure of Turbulent Shear Flow*. 2nd edn. Cambridge University Press.

WEDDELL, D. S. 1953 in Hottel, H. C. Burning in laminar and turbulent fuel jets. *Fourth (Intl) Symp. Combustion*, pp. 97–113. The William & Wilkins Co., Baltimore, Maryland.

WHITE, F. M. 1974 *Viscous Fluid Flow*, pp. 505–510. McGraw-Hill.

WIENER, N. 1949 *Extrapolation, Interpolation, and Smoothing of Stationary Time Series*. Technology Press (MIT and John Wiley).

WILSON, R. A. M. & DANCKWERTS, P. V. 1964 Studies in turbulent mixing – II, A hot air jet. *Chem. Engr. Sci.* **19**, 885–895.

YAKHOT, V., SHE, Z. S. & ORSZAG, S. A. 1989 Deviations from the classical Kolmogorov theory of the inertial range of homogeneous turbulence. *Phys. Fluids* A **1**, 289–293.

Appendix G

DIMOTAKIS, P. E. AND MILLER, P. L. [1990] "Some consequences of the boundedness of scalar fluctuations," *Phys. Fluids A* **2**(11), 1919–1920.

LETTERS

The purpose of this Letters section is to provide rapid dissemination of important new results in the fields regularly covered by Physics of Fluids A. Results of extended research should not be presented as a series of letters in place of comprehensive articles. Letters cannot exceed three printed pages in length, including space allowed for title, figures, tables, references and an abstract limited to about 100 words. There is a three-month time limit, from date of receipt to acceptance, for processing Letter manuscripts. Authors must also submit a brief statement justifying rapid publication in the Letters section.

Some consequences of the boundedness of scalar fluctuations

Paul E. Dimotakis and Paul L. Miller
Graduate Aeronautical Laboratories, California Institute of Technology, Pasadena, California 91125

(Received 24 August 1990; accepted 11 September 1990)

Values of the scalar field $c(\mathbf{x},t)$, if initially bounded, will always be bounded by the limits set by the initial conditions. This observation permits the maximum variance $\overline{c'^2}$ to be computed as a function of the mean value $\bar{c}$. It is argued that this maximum should be expected in the limit of infinite Schmidt numbers (zero scalar species diffusivity). This suggests that $c'/\bar{c}$ on the axis of turbulent jets, for example, may not tend to a constant, i.e., independent of x/d, in the limit of very large Schmidt numbers. It also underscores a difficulty with the k^{-1} scalar spectrum proposed by Batchelor [J. Fluid Mech. **5**, 113 (1959)].

In contrast to velocity fluctuations in a three-dimensional flow, a turbulent flow cannot generate passive scalar fluctuaton values outside the initial bounds. Consequently, the values of the scalar field $c(\mathbf{x},t)$, if initially within 0 and 1, for example, will always be bounded by these limits. This can be shown to be a direct result of the scalar transport equation,

$$\frac{\partial c}{\partial t} + \mathbf{u}\cdot\nabla c = \mathscr{D}\nabla^2 c, \tag{1}$$

in which the scalar species diffusivity $\mathscr{D}$ must be positive, as directed by thermodynamic considerations.

A useful measure of the scalar fluctuations is the scalar variance $\overline{c'^2}$, which equals the second moment of $p(c)$, the probability density function (pdf) of the scalar, i.e.,

$$\overline{c'^2} = \int_0^1 (c-\bar{c})^2 p(c)\,dc, \tag{2}$$

where the scalar values specified by the initial/boundary conditions have been scaled such that $0 \leqslant c \leqslant 1$ and where

$$\bar{c} = \int_0^1 c\,p(c)\,dc \tag{3}$$

is the mean (expectation) value of the scalar field (pdf).

As a consequence of the boundedness of the values of the scalar field, the variance is maximized when the pdf realizes its integral as far away from the mean as possible. In other words, as

$$p(c) \to (1-\bar{c})\delta(c) + \bar{c}\,\delta(1-c), \tag{4}$$

where $\delta(c)$ denotes the Dirac delta function. This pdf should describe the behavior in the limit of $\mathscr{D} \to 0$, corresponding to $\mathrm{Sc} \equiv \nu/\mathscr{D} \to \infty$, where Sc is the Schmidt number of the diffusing species and ν is the kinematic viscosity. In such a flow, the turbulence will be stirring, but not mixing, $\bar{c}$ parts of $c = 1$ fluid per $(1-\bar{c})$ parts of $c = 0$ fluid. This yields

$$\overline{c'^2} \to \bar{c}(1-\bar{c}) \quad \text{as} \quad \mathrm{Sc} \to \infty, \tag{5}$$

for the limiting value for the variance, which attains its maximum of $\overline{c'^2} = \frac{1}{4}$ at $\bar{c} = \frac{1}{2}$. The foregoing suggests that the ratio Ξ,

$$0 < \Xi = \frac{\overline{c'^2}}{\bar{c}(1-\bar{c})} < 1, \tag{6}$$

is an appropriate unmixedness parameter, with zero attained in the limit of perfect mixing, i.e., as $p(c) \to \delta(c-\bar{c})$, and unity corresponding to stirring but no mixing [Eqs. (4) and (5)] in the limit of $\mathrm{Sc} \to \infty$. The quantity Ξ of Eq. (6) was proposed by Danckwerts,[1] in the context of estimating the rate of a chemical reaction of imperfectly mixed reactants, who dubbed it "intensity of segregation" and recognized its limits. In contrast, the more conventional normalization of the variance of the scalar fluctuations yields

$$\overline{c'^2}/\bar{c}^2 \to (1-\bar{c})/\bar{c} \quad \text{as} \quad \mathrm{Sc} \to \infty, \tag{7}$$

and can realize any value between zero and infinity depending on the value of $\bar{c}$.

These relations imply that, in the limit of $\mathrm{Sc} \to \infty$, the normalized root mean square scalar fluctuations on the axis of a momentum-driven, axisymmetric, turbulent jet, for example, should tend to infinity as $x/d \to \infty$, where d is the jet nozzle diameter and x is the distance from the jet nozzle (measured from a virtual origin). In particular, at finite Reynolds number and large x/d we should expect

$$\frac{c'}{\bar{c}} < \left(\frac{1-\bar{c}}{\bar{c}}\right)^{1/2} \sim \mathrm{const}\left(\frac{x}{d}\right)^{1/2} \quad \text{as} \quad \mathrm{Sc} \to \infty, \tag{8}$$

since $\bar{c} \propto d/x$ in this case. This should be compared to the assumption that, at large x/d, $c'/\bar{c}$ can be taken as a constant on the jet axis; often accepted as valid independently of the Schmidt number.

A second consequence of the limiting behavior of $\overline{c'^2}$ concerns the spectrum of the scalar fluctuations at high Schmidt numbers. Specifically, it was proposed by Batchelor[2] that at high Reynolds numbers and for spatial scales

 0899-8213/90/111919-02$02.00

below the Kolmogorov dissipation scale[3]

$$\lambda_K \equiv (\nu^3/\epsilon)^{1/4}, \tag{9a}$$

where ϵ denotes the dissipation rate of the kinetic energy per unit mass, the spectrum $E_c(k)$ of a passive conserved scalar $c(\mathbf{x},t)$ should obey a k^{-1} power law. This regime was predicted to extend to spatial scales down to the scalar diffusion (Batchelor) scale

$$\lambda_B \equiv \lambda_K \, \mathrm{Sc}^{-1/2}. \tag{9b}$$

It would appear that the arguments leading to this conclusion become more robust as the separation between the Kolmogorov and Batchelor scales increases, i.e., in the limit of large Schmidt numbers.

Now, the variance of the scalar fluctuations can also be computed as the integral of the scalar spectrum over the range of wave numbers, i.e.,

$$\overline{c'^2} = \frac{1}{\pi}\int_0^\infty E_c(k)dk \simeq \frac{1}{\pi}\int_0^{1/\lambda_B} E_c(k)dk. \tag{10}$$

As a consequence, as Sc becomes large, the Batchelor proposal yields at high Reynolds numbers (Moffatt[4])

$$\overline{c'^2} \sim \frac{\chi}{U/L}\left(A + \frac{B}{2}\mathrm{Re}^{-1/2}\ln(\mathrm{Sc})\right), \tag{11a}$$

where

$$\chi \equiv \overline{\mathscr{D}|\nabla c|^2} \sim \frac{(\Delta c)^2}{L/U} \tag{11b}$$

is the scalar dissipation rate, $\mathrm{Re} = LU/\nu$ is the flow Reynolds number, A and B are constants, and $\Delta c = 1$ is the scalar diference specified by the initial/boundary conditions. This estimate of the variance can be seen to diverge (logarithmically) as the Schmidt number is increased.

The difficulty with the logarithmic divergence was recognized by Batchelor,[2] who stated that the k^{-1} spectrum would be established throughout the viscous-convective range, $1/\lambda_K < k < 1/\lambda_B$, only if sufficient variance $\overline{c'^2}$ was supplied from the larger scales (also see the discussion in Monin and Yaglom,[5] p. 437). Moffatt[4] points to the logarithmic divergence, but observes that, at high Reynolds numbers, the contribution from the Batchelor spectrum [the second term in Eq. (11a)] is typically negligible.

We appreciate that to establish the logarithmic divergence of Eq. (11) may require a time t in excess of the Batchelor diffusion time t_B, which, for high Reynolds number flow, would be scaled by[2]

$$t_B = (t_K/2)\ln(\mathrm{Sc}), \tag{12a}$$

where

$$t_K \equiv (\nu/\epsilon)^{1/2} \propto (L/U)\mathrm{Re}^{-1/2} \tag{12b}$$

is the Kolmogorov dissipation time.[3] A time t_B may be required for the diffusion interface thickness to decrease to the Batchelor diffusion scale λ_B, under the action of the sub-Kolmogorov scale strain rate, and for the spectrum to extend to $k \simeq 1/\lambda_B$. At fixed Reynolds number, the limiting behavior can be studied by increasing the Schmidt number, with an attendant increase in the time t allowed for the diffusion process to attain dynamic equilibrium, such that $t > t_B$, as necessary.

Comparing Eqs. (11) and (12), we see that the contribution to the variance from the k^{-1} portion of the scalar spectrum is proportional to the product $\chi t_B \sim \mathrm{Re}^{-1/2}\ln(\sqrt{\mathrm{Sc}})$. It would appear that, provided the time available for diffusion is larger than t_B as $\mathrm{Sc} \to \infty$, the k^{-1} spectrum yields a scalar fluctuation variance that is inconsistent with the upper bound of Eq. (5).

Finally, we should note that a correction to the k^{-1} power law that would increase the negative exponent of k, or the application of an integrating factor in that regime, would permit the integral over wave numbers to converge in the limit of high Schmidt number. We also recognize, however, that convergence alone would not be sufficient to resolve the difficulty; the scalar variance, as estimated by the scalar spectrum [Eq. (10)], must be bounded by its maximum [Eq. (5)].

ACKNOWLEDGMENTS

We would like to acknowledge our discussions with P. Saffman, D. Meiron, and H. K. Moffatt.

This work is part of a larger effort on turbulent mixing supported by AFOSR Grant No. 88-0155 and GRI Contract No. 5087-260-1467.

[1] P. V. Danckwerts, Appl. Sci. Res. Sec. A 3, 279 (1952).
[2] G. K. Batchelor, J. Fluid Mech. 5, 113 (1959).
[3] A. N. Kolmogorov, Dokl. Akad. Nauk SSSR 30, 299 (1941).
[4] H. K. Moffat, Rep. Prog. Phys. 46, 621 (1983).
[5] A. S. Monin and A. M. Yaglom, *Statistical Fluid Mechanics: Mechanics of Turbulence*, edited by J. Lumley (MIT Press, Cambridge, MA, 1975), Vol. II.

Appendix H

BROADWELL, J. E. AND MUNGAL, M. G. [1991] "Large-scale structures and molecular mixing," *Phys. Fluids* A **3**(5), Pt. 2, 1193–1206.

Large-scale structures and molecular mixing

James E. Broadwell
Graduate Aeronautical Laboratories, California Institute of Technology, Pasadena, California 91125

M. Godfrey Mungal
Department of Mechanical Engineering, Stanford University, Stanford, California 94305

(Received 28 August 1990; accepted 20 December 1990)

Scalar mixing and chemical reactions in turbulent shear layers and jets are examined with emphasis on experimental results of high spatial and temporal resolution. Such measurements show that the notion of distinguishing fluids that are molecularly mixed from those that are simply stirred is valid and useful. Two models that seem especially suitable for implementing mixing analyses from this viewpoint are described and speculations on possible connections with the idea of chaotic advection offered.

I. INTRODUCTION

A paragraph taken from Ref. 1, by Aref and Jones, will make clear that the title of this Symposium, *The Fluid Mechanics of Stirring and Mixing*, contains, by implication, many of the major points that we wish to make in this paper. They write the following:

"For convenience we shall follow a terminology suggested by Eckart in which *stirring* signifies the mechanical process whereby fluids are distributed more uniformly within a given domain, i.e., stirring is a process of stretching of intermaterial area. *Mixing*, on the other hand, is the process of diffusion of substances across intermaterial surfaces. Stirring can promote mixing by creating more intermaterial surface area. Mixing depends on material properties, such as diffusivities, whereas stirring is a purely kinematical aspect dependent on flow parameters. Indeed, it is possible to stir fluids that do not mix at all."

A primary objective of this paper is to show that scalar mixing in free turbulent shear flows is well described in these terms and that it is the existence of large-scale structures in these flows that makes such a description useful. More specifically, evidence is cited showing that (1) large-scale motions associated with the structures lead to mean concentration distributions that differ markedly from those of the mean mixed fluid, and (2) the overall mixing rate is influenced by the value of the molecular diffusivities even at what are considered to be high Reynolds numbers.

In the paper, we follow the advice of Leonardo da Vinci, who wrote "Remember, when discoursing about water, to induce first experience, then reason." Today this would perhaps be written as follows: In discussing turbulence, consider first experiment, physical or numerical, and then theory. The paper, consists therefore, mainly of discussions of experimental results and their implications concerning the path to the molecularly mixed state. The paper includes, nevertheless, a discussion of models of this path and some speculations about the relevance of the ideas from chaotic advection to stirring and mixing in turbulent shear flows. For simplicity, only constant, or near constant, density flows are considered. Likewise, though many of the ideas apply to other free shear flows such as wakes and jets in cross flow, only jets and shear layers will be discussed.

The outline of the remainder of the paper is as follows. In Sec. II evidence of the persistence of structures to high Reynolds numbers is presented. In Sec. III scalar mixing and chemical reaction experiments are described. In Sec. IV two models are discussed: a two-stage Lagrangian model: and the linear eddy model. Section V contains speculations about shear flow mixing and chaotic advection and Sec. VI contains some concluding remarks.

II. EVIDENCE OF PERSISTENCE OF STRUCTURES TO HIGH REYNOLDS NUMBERS

This section is a short review of some of the evidence for the existence of large-scale structures in shear flows. We begin first with the findings in two-dimensional mixing layers and conclude with the observations for jets. Of particular interest is the persistence of large-scale motions to high Reynolds numbers.

A. Shear layers

Perhaps the most important photo for evidence of large-scale structures in mixing layers was also the first. Most readers are familiar with the classic shadowgraph photos of Brown and Roshko[2] of the mixing layer formed between a high-speed stream of helium–argon and an equal density, low-speed stream of nitrogen. Their photos clearly show the two-dimensional rollers as well as the fine-scale structure which exist throughout the mixed fluid regions. An important point to note here is that their photos are of the *scalar* field, and not the velocity field. As will be seen in Sec. III, the sharp edges in the visualizations are consistent with the concentration fields to be described later. Such edges are not present in the velocity field.

The issue of existence of the organized structure at high Reynolds number was addressed by several researchers, including Dimotakis and Brown[3] using water as the working medium and Mungal *et al.*[4] using high-speed gases. More recent evidence of the Brown–Roshko structure at very high Reynolds number has been provided by Clemens and Mun-

 0899-8213/91/051193-14$02.00

gal[5] (Fig. 1). The mixing layer seen here was formed between two airstreams at speeds of 430 and 275 m/sec. This composite photo is a schlieren image together with "cuts" through the flow that avoids the spatial integration inherent in shadow–schlieren photos. In this case, a laser sheet was passed through the flow and scattered light from fine alcohol droplets which mark the mixed fluid region. The Brown–Roshko structure and connecting braid regions are visible in the side view, while the two-dimensionality of the structure is seen in the plan view. Also visible is the smaller scale, secondary structure that has been described by Bernal and Roshko.[6] The important point is that the structure seen here is observed at Reynolds numbers, based on local shear layer thickness, velocity difference, and mean kinematic viscosity of 230 000 that is an order of magnitude greater than the studies of Brown and Roshko. Furthermore, the exit of the test section is about 3000 initial boundary-layer momentum thicknesses downstream of the splitter plate. Note also that in Ref. 7 the Brown–Roshko structure was seen to persist to values of the Reynolds number as high as 600 000. When taken together with other studies at lower Reynolds numbers,[8-14] these results are compelling evidence that the large-scale motions are essentially inviscid in nature and exist for all Reynolds numbers beyond some critical value.

The secondary structure seen in Fig. 1 was originally investigated by Bernal and Roshko.[6] They propose that it consists of a series of smaller scale vortices of alternating sign which partially wrap around the primary structure and corrugate the braid region. That the structures are vortices has been verified in the low Reynolds number experiments of Lasheras and Choi,[15] and in high Reynolds number flow by the work of O'Hern.[16] In O'Hern's work, cavitation in the low pressure cores of the streamwise vortices produced a natural flow visualization. Another interesting feature of his configuration is that the shear layer forms between a free stream and a recirculating region behind a vertical plate–not a particularly "clean" flow. Thus the structure appears to be quite robust to external disturbances.

This issue of the robustness of the structures has been the subject of at least two studies which attempted to disrupt them. Breidenthal[17] investigated the influence of the wake of a thick splitter plate as well as that of a significant change in the planform shape, whereby alternate sections of the plate were removed. Wygnanski *et al.*[18] studied the effects of tripping the boundary layer, vortex generators, and high free-stream (grid) turbulence. In every case, the layer is found to recover toward the Brown–Roshko picture, usually after a transition distance where the effects of the disturbance are first felt and then forgotten.

The evidence presented in this section can be summarized as follows. The Brown–Roshko structure in mixing layers is believed to result from inviscid instability and, as such, exists for high Reynolds number flows. Figure 2 (from Coles[19]) is a cartoon (using the terminology of Corcos[20]) of the resulting fluid motion. In a frame of reference moving with the structure, fluid from both free streams is drawn toward the braid region and is sketched as a stagnation region. The outflow from this region then moves toward the cores of the spanwise structures where mixed fluid accumulates. This cartoon will be discussed later in Sec. IV.

B. Jets

While evidence for organization in two-dimensional mixing layers is abundant, the story for jets is much less direct, as will be seen below. However, modern diagnostic and visualization approaches are beginning to reveal the underlying large-scale structures in jets.

The first difficulty is that shadow/schlieren images of jets do not reveal obvious organization as was the case for the mixing layer. This is now believed to be a consequence of the increased complexity of the jet. The experimental evidence suggests that structures in jets are more three dimensional with one structure often partially nested within the other so that laser sheet-cutting techniques are important to finding structure. Additionally, the use of movie sequences and of

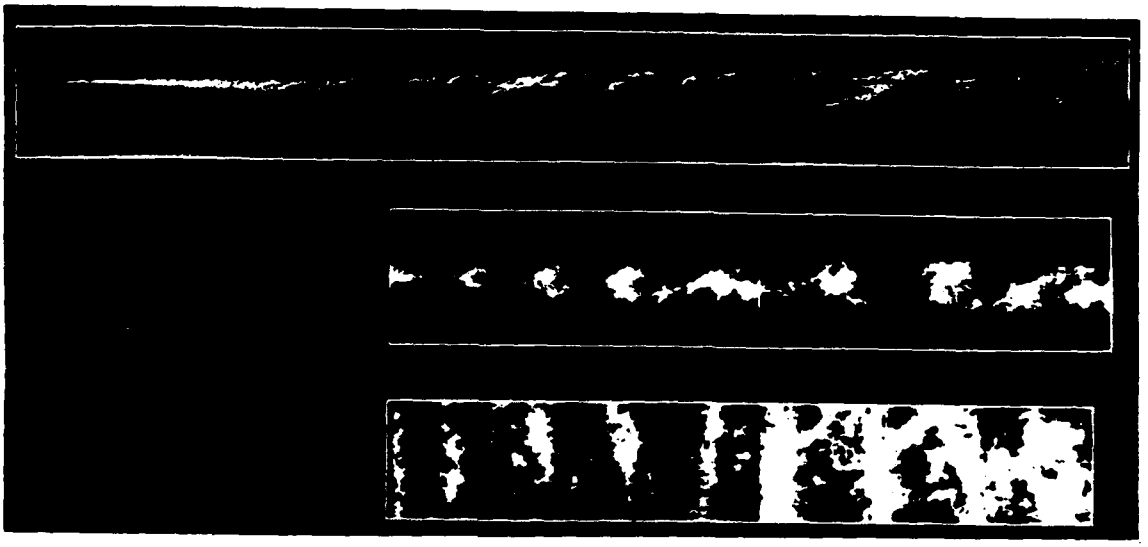

FIG. 1. High Reynolds number shear layer.[5] Top image shows schlieren photographs from $x = 0$–45 cm downstream. Planar side and plan views shown from $x = 15$–45 cm. Re at exit plane = 230 000.

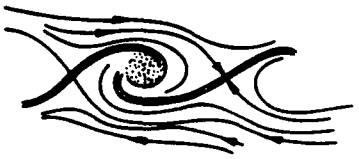

FIG. 2. Cartoon of mean streamlines and molecular mixing zones in the shear layer.[19]

chemical reactions to allow fuel bearing structures to "burn out" and hence become invisible has also proven especially helpful.

Dahm and Dimotakis[21] used a chemical reaction (in water) and a movie sequence to investigate the spatial and temporal evolution of a turbulent jet at a Reynolds number of 10 000. In this case the chemical reactions in their study simulate zero heat release combustion and provide an instantaneous view of the spatial concentration field. At about 150 diameters downstream (their "flame tip") the movie sequences show that the jet fluid reactant is consumed by the reservoir fluid reactant in a quasiperiodic fashion at a frequency that scales with the local large-scale variables. Careful examination of the movie sequence shows that the jet consists of organized structures that convect downstream and burn out quasiperiodically at the tip.

Figure 3 contains results of van Cruyningen *et al.*[22] and shows a planar cut through the centerline of a nonreacting Re = 8000 jet. The structure of the jet is revealed as regions of distinct concentration which decrease in the downstream direction, but in a stepwise fashion, a characteristic first observed by Dahm and Dimotakis[21] (the decrease in discrete steps in Fig. 3 is obscured by the rescaling). It is these large regions of similar concentration that "burn out" quasiperiodically in the study of Dahm and Dimotakis.

To illustrate the jet dynamics in a compact fashion, Mungal *et al.*[23] have used the technique of volume rendering[24] to present many frames of data from a movie sequence simultaneously. Here x-y frames from the movie are stacked sequentially as a function of time, t, to produce a solid object in x-y-t space. A virtual line source of light to the left of the stack provides illumination. Surfaces that would be hidden on the rear face of the stack are removed from view. With this display technique many frames of data can be presented simultaneously, with further examples shown in Ref. 25. In addition, a large-scale structure which convects downstream is revealed as a traveling "bump" in the rendered surface. Figure 4 shows the result of applying the technique to a $\mathrm{Re} = 2\times 10^8$ momentum-driven jet. Several features of the large-scale motion are visible; the structures are seen to grow as they progress downstream, decay in speed, and occasionally pair. This photo establishes the presence of large-scale structure in jets to very high Reynolds numbers, and again

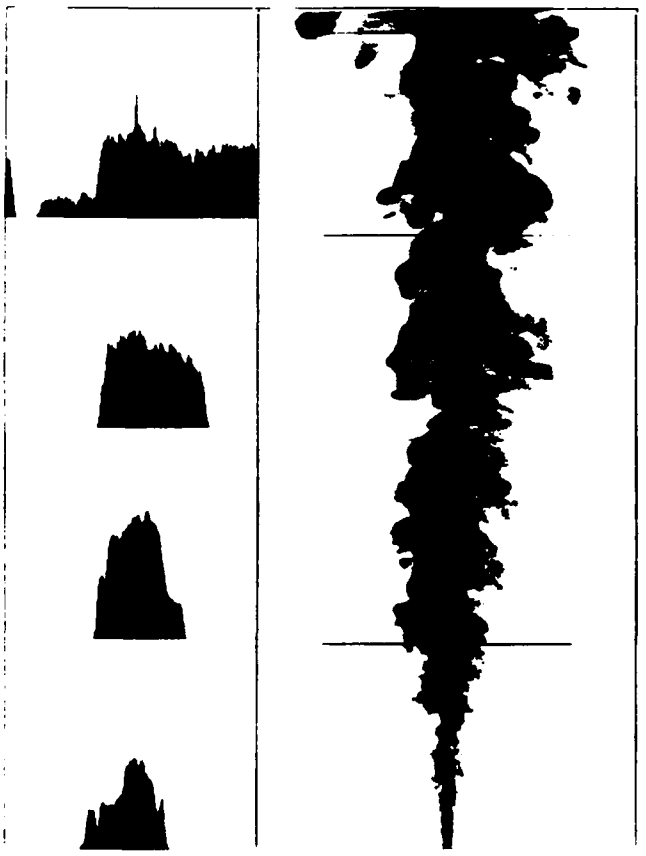

FIG. 3. Planar laser-induced fluorescence cut through the centerline of the Re = 8000 jet.[22] Concentration field rescaled to remove $1/x$ decay. Four instantaneous profiles are shown at the stations indicated.

FIG. 4. An x-y-t volume rendering of the $\mathrm{Re} = 2\times 10^8$ momentum-driven jet.[23] View extends from x = 400–2000 ft vertically. Time axis covers t = 0–21 sec. Note the presence of organized large-scale structures which convect downstream.

when taken together with previous lower Reynolds number studies,[26-32] suggests that the presence of the large-scale structures is Reynolds number independent.

The organized structure in the round turbulent jet is thus viewed as resulting in motion by which external fluid is entrained and mixed into the main jet body. The entrainment occurs primarily from the upstream boundary of the structures while fluid from deep within the jet is pushed toward the outer jet edges, such motion causing the bumps seen in Fig. 4. Some direct evidence for the large-scale motion is seen in the color photos of Shlien.[33] Here, a thin stream of dye was allowed to enter the jet far field and thus mark the entrained fluid. The dye streamer is seen to enter deep into the jet, cross the centerline, and eventually appear at the outer jet edge, usually within 1 or 2 local jet diameters. Figure 5, from Ref. 34, is a schematic of this type of entrained fluid motion resulting from the large scales. The arrows suggest the type of stirring that results when viewed from the laboratory frame. As can be seen, the recently entrained fluid travels toward the centerline of the jet while the (older) jet fluid is pushed toward the outer edges, and is later reentrained. The instantaneous motion is to be compared with the time-averaged motion seen in Fig. 5(b) which differ from the stirring motions seen instantaneously. This schematic is the analog of that shown for the mixing layer (Fig. 2), and will be used later in Sec. IV.

III. SCALAR MIXING AND CHEMICAL REACTION EXPERIMENTS

Having established in Sec. II that large-scale structures are present in shear layers and jets, we proceed to examine their influence on mixing and chemical reactions in such flows.

A. Shear layers

The first point has to do with the distribution and composition of the fluid that is entrained and mixed in the two-dimensional shear layer. Figure 6, containing results for both gases (Schmidt number, Sc~0.7) and liquids (Sc~600), shows the distribution of fluid that is both stirred and mixed, the mean composition, and the distribution of that which is mixed. The mean composition consists therefore of both unmixed free-stream fluid and mixed fluid. In this figure, the mean composition comes from measurements in water but is similar to those observed in gases.

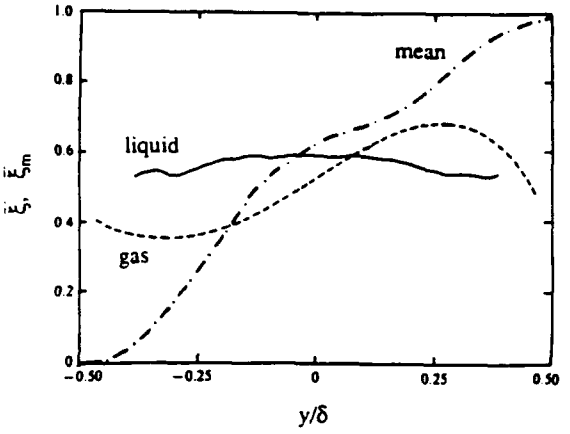

FIG. 6. Mean and mean mixed fluid concentration in the turbulent mixing layer: -·-, mean, liquid,[35] Re = 23 000; ——, mean mixed fluid, liquid,[35] Re = 23 000; ---, mean mixed fluid, gas,[42] Re = 65 000.

Notice first the striking difference between the mean mixed composition and the mean values. This difference is especially clear for the water experiment where it can be seen that there is virtually no lateral variation in the mixed composition while the mean values follow the S-shaped curve that has been known for many years. Since the (volume) ratio of the high-speed to low-speed fluid mixed in the layer (the entrainment ratio E) is about 1.3 for the present density and speed ratio,[10,35-37] the mixed fluid concentration exceeds one-half.

Next, observe that although the mixed composition in gases also departs markedly from the mean curve, it differs also from the mixed liquid distribution. This is the first indication of what is to be a second theme of this paper, i.e., that the molecular diffusion coefficient influences mixing even at so-called high Reynolds numbers.

Consider next Fig. 7, where four probability density functions (pdf's) of concentration are plotted: (a) for liquids from Koochesfahani and Dimotakis,[38] (b) for gases, from Konrad,[35] (c) a theoretical result from Kollman and Janicka[39] using Reynolds-averaged equations, and (d) the experimental results from Batt.[40] (With respect to theoretical predictions, Batt's results have also been reproduced by the analysis of Pope.[41]) We see that in Figs. 7(a) and 7(b) the peak concentration varies little with the lateral coordinate, again, especially for the liquid experiment. For Fig. 7(c), however, the peak values move as would be expected from the mean curve in Fig. 6. The similar shape of the experimental results of Fig. 7(d) is due to the low resolution of the measuring probe: when the resolution is such that mixed and unmixed fluid cannot be distinguished the shape is consistent with the mean values. The similarity between these latter results is therefore understandable, for when the Navier–Stokes equations are averaged and the diffusion terms

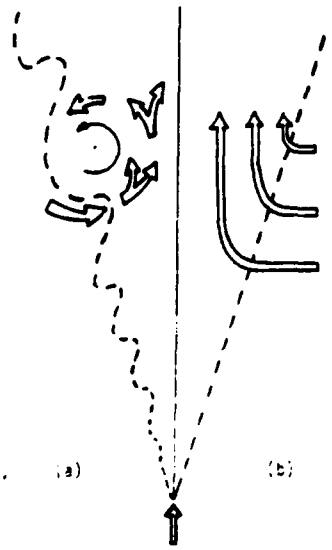

FIG. 5. Schematic of entrained flow into a turbulent jet.[34] (a) Instantaneous flow; (b) time-averaged flow.

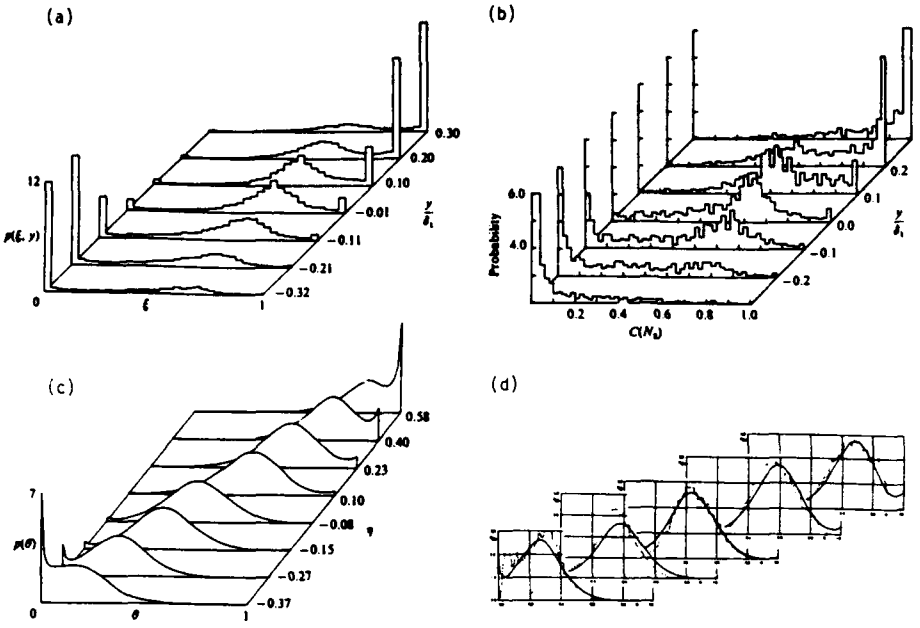

FIG. 7. Probability density function (pdf) of mixture fraction in the turbulent shear layer (a) Koochesfahani and Dimotakis,[38] liquid, Re = 23 000; (b) Konrad,[35] gas, Re = 25 000; (c) Kollman and Janicka,[39] calculations (independent of Sc, Re); (d) comparison of Kollman and Janicka with experimental results of Batt,[40] gas, Re = 80 000.

dropped, again the distinction between mixed and stirred fluid is lost.

The resolution requirements are severe, approaching dimensions the order of the Batchelor scale. In the experiments yielding Fig. 7(a), the liquid pdf, the resolution was approximately the Kolmogorov scale, and hence these results are slightly in error. The effect of resolution limitations is discussed thoroughly in Ref. 38 as is the method for obtaining the results in Fig. 6 that are free from these difficulties. For reasons given later, the gas pdf, Fig. 7(b), is believed to be accurate.

While the emphasis of the present paper is upon mixing, it is clear that one of the primary applications of the ideas is to chemical reactions, and conversely, that much can be learned about mixing from chemical reaction experiments, particularly those in which the reaction cause little, if any, change in the flow. Several such experiments, some associated with the above-mentioned work, are discussed next.

One such investigation involving reactions in water was carried out in the same facility in which the pdf in Fig. 7(a) was measured. For present purposes, the details of the reaction are not important; only the fact that it is fast relative to the mixing rate is required. In this and the following discussions the symbol ϕ denotes the equivalence ratio of a reaction, and means the mass of high-speed fluid required to completely react unit mass of low-speed fluid. Figure 8 shows the distribution of product for two experiments, one with $\phi = 10$ and the other for $\phi = \frac{1}{10}$, such conditions being realized by simply interchanging the fluids of fixed composition from one side to the other. (This has come to be called a flip experiment.) When $\phi = 10$ more product is generated because the "lean" reactant is carried on the high-speed side in this case. The characteristic of the distributions that is emphasized here, however, is their *symmetry*. Although one reactant is almost ten times richer than the other, the product distribution carries little evidence of that fact. It is the nearly flat mixed fluid composition in Fig. 6 that is the source of the symmetry.

Consider next a similar experiment at about the same Reynolds number in gases.[42] The results are shown in Fig. 9, where the flip is made for a range of ϕ's. Here the nitrogen stream carried dilute concentrations of hydrogen and fluorine and traces of nitric oxide sufficient for the reactions to be fast, i.e., mixing limited. The time mean temperature was determined from time traces at eight stations across the layer. Focusing on $\phi = 8$ and $\frac{1}{8}$ we see again higher temperature (or more product) for $\phi = 8$ and that in this case the profiles are not quite symmetric albeit the deviation is small, in accordance with the small slope of mean mixed composition in gases plotted in Fig. 6.

As was mentioned, the mean temperature profiles in Fig. 9 came from temperature–time traces taken at eight stations across the shear layer, Fig. 10 being an example for $\phi = 1$. These traces provide a clear explanation for the differ-

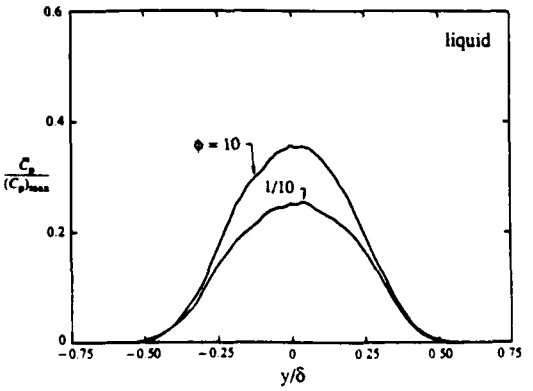

FIG. 8. Mean product profiles for fast chemical reaction in liquid.[38] $\phi = 10$ and $\frac{1}{10}$ from top to bottom; Re = 23 000.

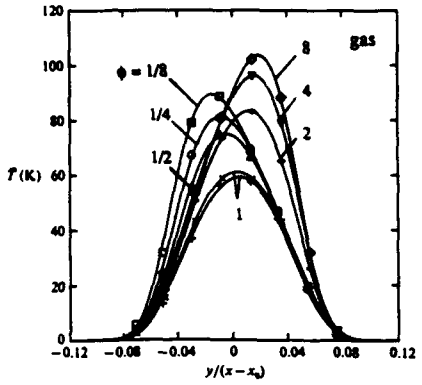

FIG. 9. Mean temperature (product) profiles for fast chemical reaction in gases.[42] Left curves $\phi = \frac{1}{8}, \frac{1}{4}, \frac{1}{2}, 1$ from top to bottom. Right curves $\phi = 8, 4, 2, 1$ from top to bottom; Re = 65 000.

ence in the mean and the mean mixed profiles that has been emphasized in the preceding discussion. Observe that the maximum temperature is of similar magnitude at the eight stations indicating that the mixed composition likewise, is nearly the same. The approximately Gaussian shape in Fig. 9 arises from the relative times that the various probes spend in mixed and unmixed fluid. Similar concentration–time traces from both passive and chemical reaction experiments in the water shear layer experiment (Ref. 38) exhibit the same characteristics and lead to the same conclusions concerning the mean concentration distribution in Fig. 8.

When the Konrad pdf, Fig. 7(b), is used to compute the mean temperature for the hydrogen–fluorine experiment, the results are in good agreement with those shown in Fig. 9 for $\phi = 8, 1, \frac{1}{8}$ (Mungal, unpublished). (A different conclusion drawn in Ref. 42 arose from the use of a nominal layer width for normalizing y, the lateral coordinate. This now seems improper in view of the large variation in layer widths that have since been observed.) It is this computation that establishes the accuracy of this pdf.

Next of interest are several (unpublished) instantaneous product profiles (Fig. 11) for the liquid experiment

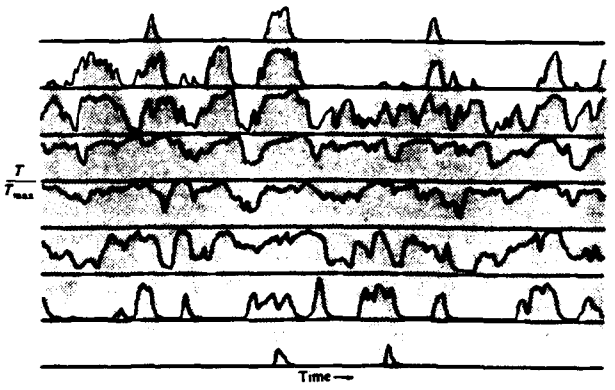

FIG. 10. Temperature–time traces measured simultaneously at eight transverse locations for fast chemical reaction in gases.[42] High speed on top. Time axis = 51.2 msec. $\phi = 1$, Re = 65 000.

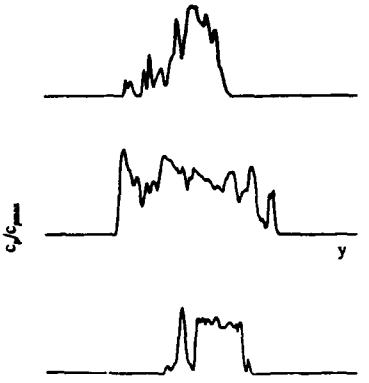

FIG. 11. Instantaneous product profiles in a reacting, liquid mixing layer, and as a function of lateral coordinate, Re = 23 000, from Koochesfahani (unpublished).

kindly furnished to the authors by M. Koochesfahani. The shapes of these profiles are to be contrasted with the mean values plotted in Fig. 8. What is to be noted particularly, are the remarkably steep sides and large interior fluctuations in these shapes. The significance of these features will be discussed in Sec. IV after additional profiles, such as those in Fig. 3, have been presented for jets.

When the product concentrations and temperature profiles in Figs. 8 and 9 are integrated and normalized to obtain total reaction product amounts that can be compared, it is found that about twice as much product is generated in the gas flow as in the liquid—the results are given in Sec. IV, where the significance of the difference is discussed.

It is instructive to examine next the effect on the mean temperature profiles of another parameter, the Damköhler number (Da), defined here as the ratio of the flow time to the measuring station to the chemical reaction time. Figure 12, from Ref. 43, shows the result for $\phi = \frac{1}{8}$ in gases where it is noted that as the reaction rate coefficient is reduced from that yielding mixing limited conditions to slow values, not only does the amount of product drop, but the profiles become symmetric (becomes liquidlike as we say). Recall that the liquid reaction product profiles are symmetric, but that the gas is not. The similarity of the effects of such unrelated

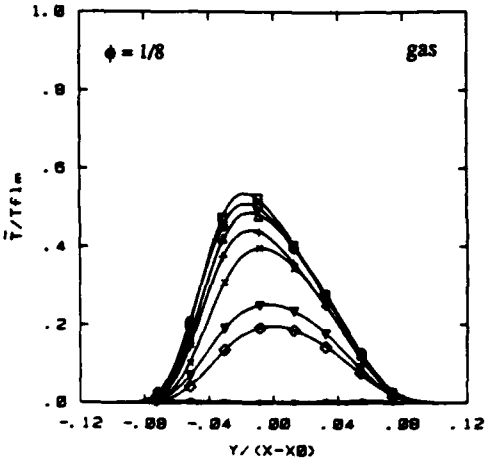

FIG. 12. Mean temperature (product) profiles for variable reaction rate in gases.[43] $\phi = \frac{1}{8}$ for all cases. Reaction rate decreases from top to bottom; Re = 65 000.

parameters (Sc, Da) provides, we believe, an important clue to the nature of stirring and mixing in the turbulent shear layer. An explanation for the similarity is offered in Sec. IV.

B. Jets

We take up next results from turbulent jets, both axisymmetric and two dimensional, where, in contrast to the shear layer, a finite flux of one fluid, the jet flux, mixes with an (effectively) infinite extent of reservoir fluid. This difference provides data with a different set of clues concerning the nature of stirring and mixing in turbulent shear flows.

The first of these clues is in the results of an experiment carried out in the 1940s by Hottel[44] and co-workers at MIT. There, Weddell studied jets consisting of an alkali solution marked with phenophthalein discharging into an acid reservoir. The jet, which is initially red, becomes colorless when it entrains and mixes with sufficient acid. Dahm *et al.*[21,45] have repeated this experiment using fluorescence of the jet fluid as the pH indicator. In the experiments, the reservoir–jet normality ratio, or ϕ, is the mass of reservoir fluid required to cause the color or fluorescence to vanish from a unit mass of jet fluid when the two are mixed homogeneously. These investigators studied the "flame length" dependence on Reynolds number and on ϕ, where flame length means the distance for the color or fluorescence to disappear. At the flame end, *every* element of jet fluid is mixed with at least ϕ parts of reservoir fluid.

Their results, from Ref. 45, are collected in Figs. 13 and 14 and constitute two remarkable findings. First, beyond $\mathrm{Re} \sim 3000$ the mean flame length becomes independent of the Reynolds number, and second, this length varies linearly with ϕ.

It is established by dimensional reasoning and experiment that the mass flux of a jet rises linearly with the axial distance,[46] and, consistently, the mean concentration falls like $1/x$. The Weddell–Dahm experiment provides information about the rate of molecular mixing. In particular, it shows that *every element* of jet fluid is mixed with at least ϕ parts of reservoir fluid at the location $x = 10\phi$ (Fig. 14); i.e., that the highest concentrations of jet fluid also fall like $1/x$. Evidence that this same conclusion holds for gaseous flames (when jet diameter d is properly redefined) is discussed in Dahm[47] and in the jet model of Broadwell.[48] This conclusion, suggesting that the mixed concentration *on the jet centerline*, where the concentration is highest, is independent of both Schmidt number and Reynolds number, has been confirmed by the recent highly resolved concentration measurements of Dowling and Dimotakis[49] in a gas jet discharging into a reservoir of equal density. Figure 15 shows the resulting pdf's together with those of other investigators. We speculate that the solid symbols represent data influenced by buoyancy and are thus ignored here. To repeat, the data of Fig. 15 is evidence that neither Reynolds nor Schmidt numbers influence the composition of fluid on the jet centerline. This remarkable result, in apparent contradiction with those for the shear layer, is discussed further in Sec. IV.

The preceding discussions have dealt with the mean flame length and its implications for the mean molecular mixing rate. An important discovery of Dahm and Dimotakis was the large-scale fluctuation in this quantity. It is, of course, the intrinsic nature of turbulent flows to exhibit fluctuations, but what was discovered in these experiments was an almost periodic, nearly constant, large fluctuation. The data, showing that the length fluctuations scale with the local jet diameter δ and the frequency with u/δ (where u is the

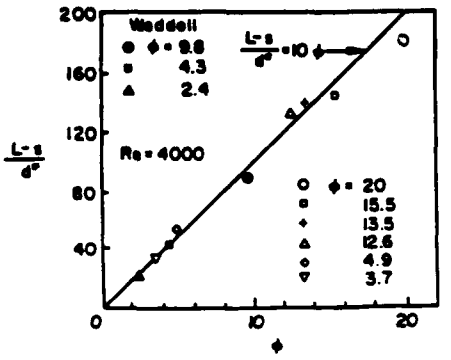

FIG. 14. Mean turbulent flame length at high Reynolds number versus equivalence ratio.[45]

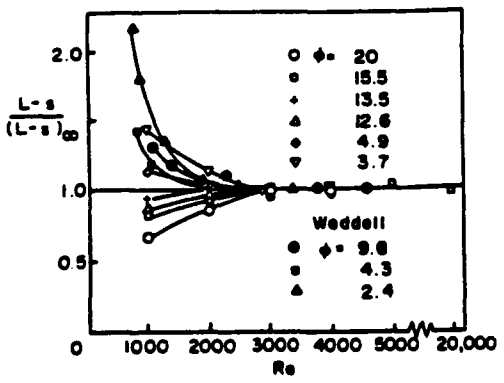

FIG. 13. Mean turbulent flame length normalized by its asymptotic value versus Reynolds number and equivalence ratio.[45]

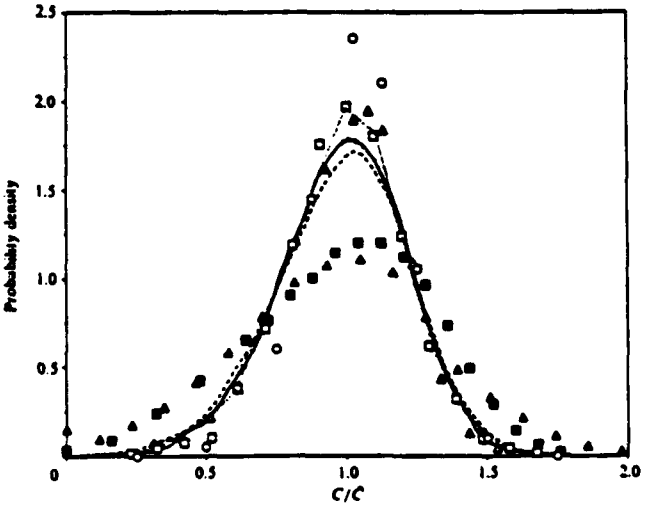

FIG. 15. Probability density function (pdf) of mixture fraction along the jet centerline.[49] ——, Re = 5000; ---, Re = 16 000; - - -, Re = 40 000.

local mean centerline velocity), appears in Refs. 21 and 47.

Mungal and O'Neil[50] and Mungal *et al.*[51] followed up the above work by performing similar experiments to those of Dahm but using burning (gaseous) systems. Volume rendering shows the orderly progression of burning large-scale structures up through the jet body which burn out quasiperiodically at the flame tip.[51] To first order the appearance of the liquid and gaseous flame are found to be remarkably similar.

The shear layer section began with a discussion of the lateral concentration profiles: this section takes up the nature of such profiles in jets. Corresponding to Fig. 6 is Fig. 16 for jets from the study of Papantoniou and List[52] (similar findings were reported earlier by Dahm[47]). Here, although the difference is not as striking as in Fig. 6, the mean mixed concentration departs significantly from the mean value near the edges of the jet. (References 52 and 27 show that for buoyant jets and jets in coflow the departure is larger.)

Several instantaneous profiles from Refs. 22, 47, and 52 appear in Figs. 3 and 17. Similar shapes have been observed by Dibble *et al.*[53] Perhaps the first of such observations is that of Uberoi and Singh[54] from their study of the temperature distribution in a slightly heated two-dimensional jet. Note the similarity between these instantaneous profiles and those in Fig. 11 for the shear layer. The significant common features of the instantaneous profiles are the large fluctuations about nearly constant values and the sharp drop at the edges. Such features in various cumulus cloud profiles, such as droplet density, are reported in Ref. 55. See Figs. 1(a) and 8(b) of this work and the accompanying discussion.

A difference between the shear layer and the axisymmetric jet profiles is the occasional presence of two mixed fluid concentration levels in the latter case. A possible explanation for this difference, mentioned in Sec. II, was proposed in Ref. 21, where it was pointed out that two structures of different compositions are often nested.

It is relevant at this point to discuss a result from the study of Antonia *et al.*[56] of a heated two-dimensional jet. Figure 18 contains temperature and velocity time traces at $x/d = 40$ and at the velocity half-width lateral station. The numbers in parentheses denote locations along the span of the jet. The simultaneity of the temperature fronts, marked by the arrows, indicates the nearly two-dimensional nature of the structures. The temperature ramps, the sharp rise followed by a gradual decline, have also been observed in axisymmetric jets by many others including Gibson *et al.*,[57] Dowling,[58] van Cruyningen,[59] Antonia *et al.*,[27] and in water by Dahm.[47] In shear layers they have been noticed and analyzed by Fiedler,[10] Konrad,[35] Mungal and Dimotakis,[42] and Mungal and Frieler.[43] In boundary layers, ramps have been reported by Chen and Blackwelder.[60] Intriguingly, such temperature and humidity ramps have been reported in the atmospheric boundary layer, where, of course, the Reynolds number is very high: Van Atta estimates values of Re_λ of the order of 5×10^3. See Refs. 61 and 62, for instance, for a discussion of these observations.

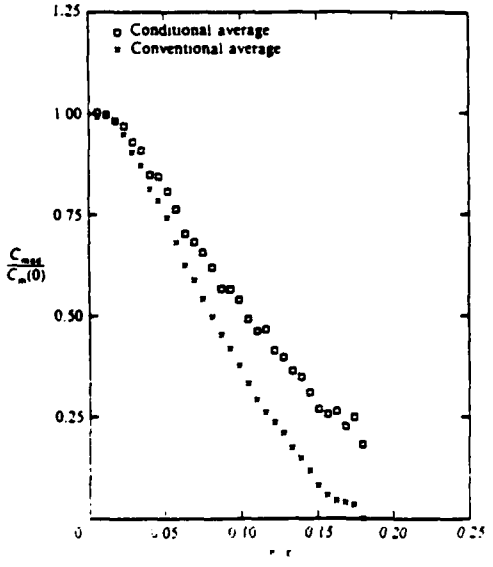

FIG. 16. Radial profile of mean and mean mixed concentration in a turbulent jet.[52]

IV. MODELS

This section provides a fairly extensive discussion of two models and brief remarks about several other modeling approaches.

A. A two-stage Lagrangian model

The early experiments on shear layers and jets at high Reynolds numbers that revealed large-scale structures, together with results from the Weddell flame simulation in water, suggested a simple model[63] of mixing and chemical reactions in these flows. The model, as subsequently modified and extended,[64] is described next. As will be seen, it provides a framework for interpreting the above discussed observations.

It is easier for present purposes to restrict attention to cases for which the Schmidt number is $Sc \geq 1$ and to start with the shear layer. The model is based upon a Lagrangian picture of the flow in which the large-scale unsteadiness is an essential feature and in which discrete quantities of free-stream fluids enter the layer at large scale (Roshko's gulping[2]). These streams flow into the braids, Fig. 2, begin to intertwine, and enter the spanwise structures. During this time, the interface is stretched at an ever increasing rate until the motions reach the Kolmogorov viscous scale $\lambda_k \sim \delta/\mathrm{Re}^{3/4}$, where δ is the local width and $\mathrm{Re} = \delta\Delta u/\nu$ the local Reynolds number. The time for this inviscid "cascade" scales with $\delta/\Delta u$ and initially the interface is subjected to the large-scale strain $\Delta u/\delta$. At this initial condition, the viscous layer thickness is the Taylor scale, $\lambda_t \sim \delta/\mathrm{Re}^{1/2}$ and the embedded scalar thickness is $\delta/(\mathrm{Re\,Sc})^{1/2} = \delta/\mathrm{Pe}^{1/2}$, where Pe is the Péclet number. Batchelor[65] shows that the local straining reduces λ_k to $\delta/(\mathrm{Re}^{1/4}\mathrm{Sc}^{1/2})$ in a time $(\delta/\Delta u)(1/\mathrm{Re}^{1/2})\ln \mathrm{Sc}$. Then, since the time for scalar diffusion across this reduced (Batchelor) scale is only $(\delta/\Delta u)/\mathrm{Re}^{1/2}$, when $\mathrm{Re}^{1/2} \gg \ln \mathrm{Sc}$, this scalar diffusion time is negligible compared to $\delta/\Delta u$, the cascade time. This argument leads to the simplifying assumption that the inter-

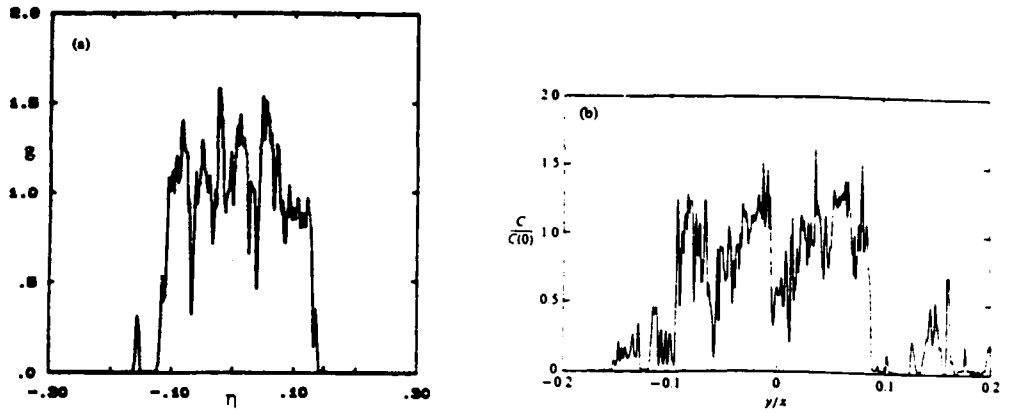

FIG. 17. Instantaneous concentration profiles in a turbulent jet. (a) Dahm and Dimotakis,[21] Re = 5000, $x/d = 300$; (b) Papantoniou and List,[52] Re = 5600, $x/d = 150$. Note the similarity to Fig. 3.

twined fluids mix instantaneously when the scale λ_k is reached.

Next we make use of the intuitive notion that the interfacial area per unit volume grows slowly at first, then with increasing rapidity as λ_k is approached. (Some support for this idea is found in chaotic advection studies where even for two-dimensional motions such interfaces grow exponentially.) Combination of this picture with the above discussion of the diffusion time suggests the following simplifying approximation. The diffusion layer thickness is λ_t for the time $\delta/\Delta u$ after which the entangled fluids mix instantaneously. As fluids continue to enter the layer farther downstream, the process repeats.

The same description is taken to apply to the jet (Fig. 5), where now the Taylor layers form between the entering reservoir fluid and the jet plus reservoir fluid mixture, the composition of which changes with downstream distance.

In both flows, the above-mentioned events take place at random times and locations; the model is intended to describe the averaged consequences of such events. Taking S to be the average surface area per unit volume at the large scale, equal to B/δ, with B a constant, we find that the contribution resulting from the Taylor layers to the mixed volume per unit volume of the layer is

$$\lambda_t \cdot S = \frac{\delta}{(\mathrm{Re\,Sc})^{1/2}} \cdot \frac{B}{\delta} = \frac{B}{(\mathrm{Re\,Sc})^{1/2}}.$$

At any axial station then the molecularly mixed fluid volume fraction V_m can be written

$$V_m = A + B/(\mathrm{Re\,Sc})^{1/2}$$

in which A is the average mixed volume fraction generated when the entrained fluid reaches λ_k. The constants A and B are determined from experiments as described later.

In the application of these ideas, the mixture formed instantaneously at λ_k is taken, as a further simplification, to be at a single composition and is hence called the homogeneous mixture. In both the shear layer and the jet, the continual stirring by the large-scale motions makes a more complex treatment of doubtful value. This stirring also implies that it would be difficult to justify any other than a one-dimensional assumption for the mixed fluid composition. Figure 6, of course, helps justify this approximation. The averaged flows as described above can be represented schematically as in Fig. 19.

In the models, the mean fluid motions are taken from standard similarity laws with their empirically determined constants.

In Ref. 64, this analysis is applied to a low-speed shear layer between two nitrogen streams, one carrying hydrogen and the other fluorine, both in dilute concentrations. Flux equations are derived for the reactants in the two mixed streams. They show that when $x/\bar{u}$ is replaced by time in the homogeneous mixture equations, these equations describe exactly the fluorine and hydrogen equations in a perfectly stirred reactor to which the Taylor streams are steadily added. It is helpful, therefore, to represent the flows as in Fig. 19. In this study, the Taylor layers are represented as stagnation point flows formed between the two free streams and treated by a boundary-layer integral analysis. At this level of approximation, the result is again a set of equations for a perfectly stirred reactor. These approximations combined with

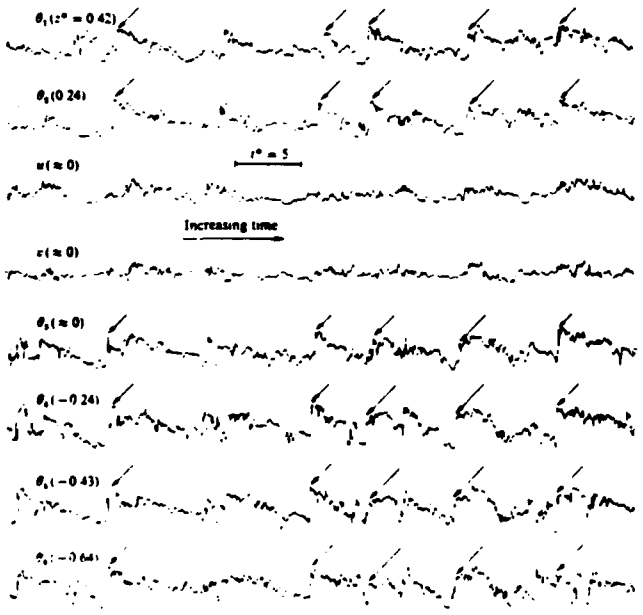

FIG. 18. Time traces of temperature and velocity fluctuations obtained with a spanwise rake of cold wires in a turbulent plane jet.[70]

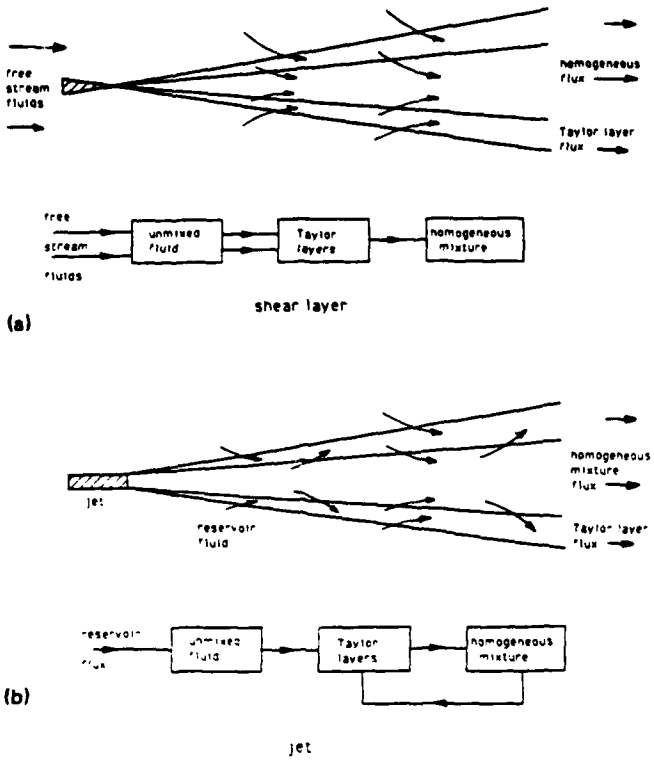

FIG. 19. Sketch of mixed fluid flux and the model schematic for (a) shear layer and (b) jet.

the simplification of the hydrogen–fluorine chemical kinetics allowed an analytical treatment of the problem. The analysis was applied to four sets of experiments, Refs. 38 (liquid), 42 (gas), 43 (Da effect), and 4 (Re effect), as described next.

In the chemical reaction experiments the amount of product was characterized by the "product thickness" defined by

$$\delta_P = \int_{-\infty}^{\infty} \frac{c_P(y)}{c_\infty}\, dy$$

where c_P is the molar product concentration and c_∞ is the fluorine concentration in the low-speed stream. The equivalence ratio ϕ is the ratio of the free-stream fluorine concentration to that of the hydrogen. Figure 20 shows the dependence of δ_P, normalized by the layer thickness, on ϕ for both the H_2–F_2 reaction and a reaction in water where ϕ is equivalently defined. In both experiments conditions are such that the reactions are fast enough to cause them to be mixing limited. The two solid symbols are experimental points from which the constants A and B were determined. Observe first as noted above that approximately twice as much product comes from the gas reaction as from that in water.

The form of the plot illustrates the nature of the model. In water, the Sc = 600 results, where the contribution to δ_P from the Taylor layers is negligible, the amount of product rises with increasing high-speed concentration at fixed concentration in the low-speed stream, i.e., with $1/\phi$ to the value $1/E$ at which condition all the low-speed reactant has been converted to product. (Recall that E is the entrainment ratio.) The dashed line for gases comes from adding at each ϕ the Taylor layer product to that of the homogeneous mixture.

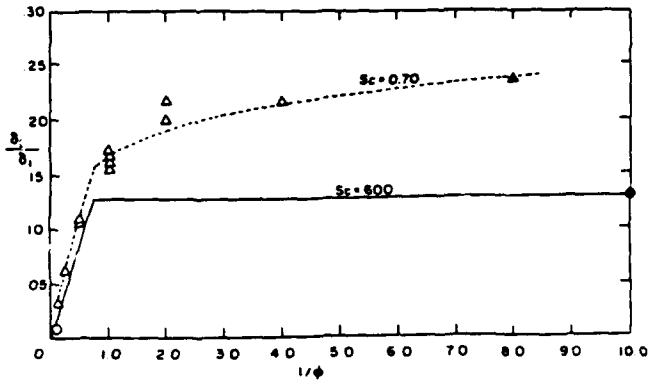

FIG. 20. Normalized product versus equivalence ratio showing model predictions for gases and liquids.[44] Triangles correspond to data of Fig. 9, circles to data of Fig. 8.

As is described in Ref. 43, the overall reaction rate of the H_2–F_2 reaction could be varied by adjustment of the trace nitric oxide concentration required to initiate the reaction. In this way a Damköhler number, $\mathrm{Da} = k(c_H)_\infty x/\bar{u}$, that arises in the analysis could be varied from zero to the mixing limited conditions. Here k is the global reaction rate coefficient, $(c_H)_\infty$, is the hydrogen free-stream concentration, x is the distance to the measuring station from the location of the mixing transition, and $\bar{u}$ is the mean speed. Figure 21 shows the results with the contributions from the Taylor layers [here marked $(\delta_P)_f$] and the homogeneous zone [here marked $(\delta_P)_h$] indicated separately.

It is useful next to discuss the effects of the Reynolds number since when Re is changed by changing the velocities, as was done in the experiments,[4] there is an accompanying change in the Damköhler number. Figure 22 compares the theoretical results for gases with several reaction rates to the experimental values of Ref. 4 mentioned above (denoted by circles). The solid symbols mark the same conditions as in Fig. 20 and the curve $k/k^* = 1$ is to be compared to the

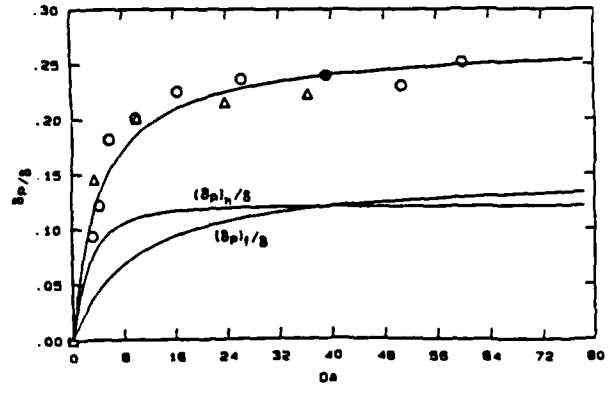

FIG. 21. Normalized product versus Damköhler number, compared to experimental results.[44] Lower lines show contributions to total from homogeneous mixture (h) and Taylor layers (f). Circles, Re = 65 000; triangles, Re = 130 000.

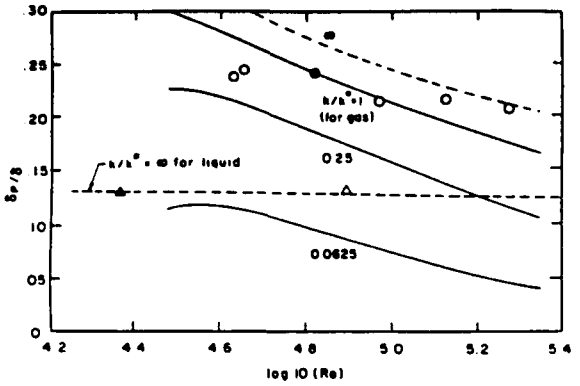

FIG. 22. Normalized product thickness versus Reynolds number.[64] Circles are experimental results in gas. Triangles are results in water. Dashed lines for infinite reaction rates. Solid lines for finite reaction rate.

experimental H_2–F_2 values. The agreement is only qualitative. For the liquid reaction, however, the agreement is good.

The curves for the infinite reaction rate illustrate the effect of Reynolds numbers alone, showing the gas value asymptoting to that of the liquid as $\mathrm{Re} \to \infty$. It is instructive at this point to sketch the model behavior as it approaches this limit. It is clear that at any fixed, finite Reynolds number, the product thickness can be reduced arbitrarily by increasing the Schmidt number. Thus we speculate that the behavior is as sketched in Fig. 23. The finite value for δ_p/δ for $\mathrm{Re} \to \infty$ would seem, intuitively, to imply that the interface becomes a volume filling surface at this condition. A finite flame length for a jet, for fixed ϕ as $\mathrm{Re} \to \infty$, implied by Fig. 23 leads to a similar conclusion. [In the sketch, the curves below the asymptotic value are outside the range of the model as presently formulated: they do not meet the condition $\mathrm{Re} \gg (\ln \mathrm{Sc})^2$.] We note at this point that Dimotakis[66] has formulated a model for this flow which, agreeing similarly with the H_2–F_2 and water reaction data discussed above, yields the limit $\delta_p/\delta = 0$ for $\mathrm{Re} \to \infty$ at fixed Schmidt number.

In Refs. 63 and 64 the Taylor layers were also referred to as flame sheets, a nomenclature that has proved confusing. In the combustion literature, the latter term refers to the zone within which chemical reactions take place and for fast reactions would be a thin sheet occupying only a small fraction of the diffusion zone (the Taylor layer). Of course, if only mixing and not chemical reactions are under discussion, the term flame sheet would be entirely inappropriate. Next it is interesting to note that in Ref. 67 Saffman wrote, "As is well known, viscous effects in motions at large Reynolds numbers are confined in laminar flows to boundary layers and vortex sheets whose thickness is proportional to the $\frac{1}{2}$ power of the viscosity. It is a mystery why turbulence has $\nu^{3/4}$ rather than $\nu^{1/2}$ dependence for the length scale of the viscous effects." The picture of the flow on which the present model is based implies that viscous effects would be felt at the $\nu^{1/2}$ scale as well as the smaller scales generated by the interface stretching.

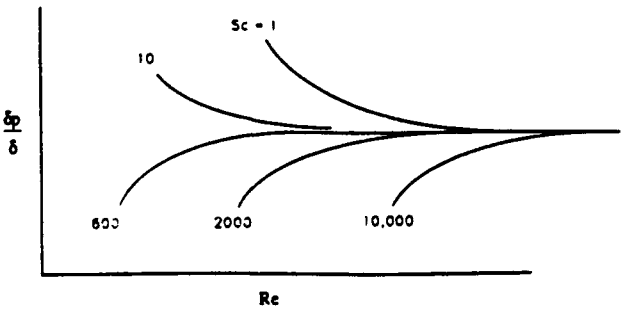

FIG. 23. Model prediction of limiting normalized product as a function of Sc and Re for the shear layer

Several matters left unexplained in Sec. III are taken up next, the first being the similarity of the effects on product profiles in the shear layer of changes in the Schmidt number and Damköhler numbers. The ideas underlying the model provide a straightforward explanation. When the diffusion coefficient is low ($\mathrm{Sc} \gg 1$) there is negligible reaction in the Taylor layers, hence a delay after the reactants enter the shear layer before product is generated, and hence a symmetric profile. A reaction rate reduction has the same consequences. There is even crude quantitative support for this argument. Recall that in the gas experiment approximately one-half the reaction products lie in the Taylor layers and note that the temperature profiles become symmetric when the average temperature is reduced by about one-half.

Another point has to do with the independence of the jet centerline pdf from the Schmidt and Reynolds numbers in contrast to the shear layer mixing dependence on these parameters. Other observations from the Dowling and Dimotakis[49] jet study provide a plausible explanation. They find no pure (unmixed) reservoir fluid on or within a few degrees of the centerline but toward the jet edge, of course, a rising amount. Furthermore, although the data are sparse, the pdf in this region does depend on both the Schmidt and Reynolds numbers and in a way consistent with the thinning of the Taylor layers there as these parameters increase. All these results are consistent with the idea that the jet "core" constitutes the "homogeneous" mixture of the model while the outer regions consist of both this mixture and the Taylor layers.

Note also that the picture of successive cascades to a Kolmogorov scale in the jet, in a distance that scales with the jet diameter at which the cascade begins, explains both the dependence of the pdf on x/d and the large-scale fluctuations in flame length.

The simplicity of the model is sufficient to permit treatment of complete chemical kinetic system even for such reactants as methane–air where as many as 250 reactions may be involved. Since the study of the pollutant formation in many fuel–air systems may require the use of such complete chemical systems, the jet model, Ref. 48, is particularly suited for this application. Reference 68 describes an initial step in a continuing program of such studies. On the other hand, the ideas on which the model is based allow a simple treatment of flame blowout of jets[69] and jets in coflow,[70] in which the chemistry is highly simplified.

Another application of the shear layer model in which

the complete chemical kinetics set needs to be considered is the hydrogen–air reaction in supersonic flow (Miller *et al.*[71]). A noteworthy feature of this study is the critical effect of the reaction in the Taylor layers on the time or distance required for completion of the reaction.

Other models having some elements in common with the above-described approach include that of Dimotakis[66] mentioned above, but one in particular, that of Effelsberg and Peters,[72] has considerable similarity. They, in examining the data of LaRue and Libby[73] for the wake of a heated cylinder, find that the temperature pdf measured at each transverse location can be divided into three parts (1) unmixed fluid, (2) internal "superlayer," and (3) fully mixed fluid. Making a best fit to data with these three components, they also find a mixed fluid contribution with a peak that does not vary with the transverse coordinate. A difference from the above-described model is that the scale of the superlayer is identified with the Kolmogorov scale instead of the Taylor scale.

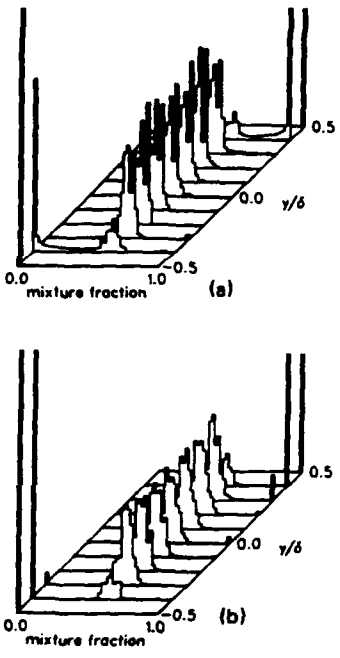

FIG. 24. Probability density function of mixture fraction versus transverse distance as predicted by the linear eddy model.[75] (a) Gas (Sc = 0.7), Re = 10 000. (b) Liquid (Sc = 600) Re = 10 000.

B. The linear eddy model

Another original and intriguing way of incorporating the large-scale motions into a model of scalar mixing in turbulent flows is described in a series of papers by Kerstein. The procedure, called the linear eddy model, has been applied to scalar mixing in homogeneous turbulence,[74] the planar shear layer,[75] homogeneous round jets,[76] and inhomogeneous round jets.[77] While the basic concepts underlying the model are the same in these cases, one of the strengths of the model, the brief discussion here will be confined to the shear layer. To quote from Ref. 75: "The linear eddy modeling approach involves the representation of a spatially developing flow by a simulation of the time development along a transverse line moving with the mean flow. Scalar quantities evolve by Fickian (molecular) diffusion and by randomly occurring spatial rearrangements, representing turbulent convection." Thus, in the language of the Symposium, stirring is simulated by the spatial rearrangements and mixing by the exact computation of molecular diffusion subsequent to the rearrangement. The model thus deals explicitly with the effects of Reynolds and Schmidt numbers and can also treat various Damköhler numbers.

Results from varying only the first two parameters are reproduced here from Ref. 75. Figure 24 shows the spatially resolved pdf of the concentration field in the shear layer for gases and liquids at two Reynolds numbers. Comparison of Figs. 24 and 7 indicate that the model correctly reproduces both the invariance of the peak concentrations with y/δ in both gases and liquids as well as the (Reynolds number dependent) wings in gases and their absence in liquids. Significantly, when the spatial rearrangements are only small scale, the peak of the pdf is found to vary with y/δ.

Figure 25 shows the agreement between the model results and the experimentally observed dependence of the product thickness on the Schmidt and Reynolds numbers. There is also an extensive discussion of the Damköhler number influence and of its correct formulation. In summary, this new approach to the analysis of scalar mixing and chemical reaction shows considerable promise of yielding new insight into these processes.

V. SPECULATIONS ABOUT SHEAR FLOW MIXING AND CHAOTIC ADVECTION

This section contains some tentative thoughts about the connections between the concepts of chaotic advection and turbulent shear flow mixing. For extensive discussions of the subject see for instance, the papers (and their references) of Aref,[78] Ottino,[79] Leonard *et al.*,[80] and the editors' discussion of Ref. 81. Here we wish only to draw attention to the similarity of the scalar fields observed by Dahm and Buch[82] in a coflowing jet to those generated by Leong and Ottino[83] in a closed chaotic flow apparatus, and to comment on the study of Aref and Jones.[1]

This latter study, concerning the separation of particles by chaotic advection, seems relevant to the subject of the mixing transition in the shear layer and perhaps to shear flows in general. Aref and Jones investigate by computation

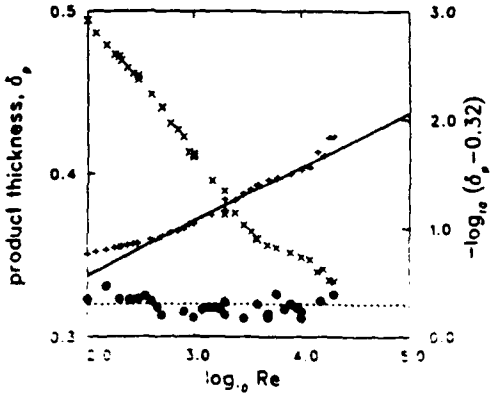

FIG. 25. Product thickness versus Re for gas ○ and liquid ● from the linear eddy model.[75] Gas results replotted ▲ as the difference between gas and liquid. A solid line slope of $-\frac{1}{3}$ is shown for comparison.

a scheme for separating particles, but the results can be used to infer some of the characteristics of mixing in such flows. They examine the configuration shown in Fig. 26 in which the dark spot marks the initial location of a set of diffusing particles. The cylinders are rotated so as to cause Stokes flow in the background fluid in which the particles diffuse. After prescribed rotation schedules, one steady, the other unsteady, the motion is reversed and the background fluid returned to its initial state. The focus of the paper is upon the large difference in the degree of return of the diffusing particles to their initial state in the two cases, the steady flow causing integrable advection and the unsteady, chaotic advection.

We identify a fall in the percent return with enhanced mixing and look at only two cases, Figs. 27(a) and 27(b) [Figs. 2(b) and 2(d) of the original paper]. For the smallest diffusivity, there is little mixing in the integrable case, but for chaotic advection, a steep rise follows the initially flat region. At the highest diffusivity, the mixing begins immediately and there is almost no difference in the two cases.

The relationships that we see in the above work to the mixing transition in the two-dimensional shear layer may be summarized as follows.

First, in the shear layer, the sudden rise in the degree of mixing at the transition[17,35] takes place in a small number of pairings, perhaps one or two. This is observed in both experiments[84] and in direct numerical simulations.[85] In the Aref–Jones work, the fall in the degree of return occurs after only a few cycles, and, for small diffusivity, is also abrupt.

In the shear layer, the increase in mixedness at the transition is large for small diffusivity, as in water, but much smaller when diffusivity is large, as in air. A similar effect is seen in comparing Figs. 27(a) and 27(b). Here, for small diffusivity the difference in the return between integrable and nonintegrable motion is large, but negligible when diffusivity is sufficiently large. In other words, in air the diffusion coefficient is large enough to cause considerable mixedness even before the chaotic motion arises, but for water, this motion is needed to produce the asymptotic degree of mixing.

Another relationship between the two flows is suggested by the Aref–Jones correlation of their numerical data. They find that the number of cycles to reach the steep fall-off can be scaled by equating the striation thickness generated by the chaotic motion to the diffusion thickness. We speculate that the mixing transition takes place when the chaotic motion leads to a state where the Taylor layers begin to overlap.

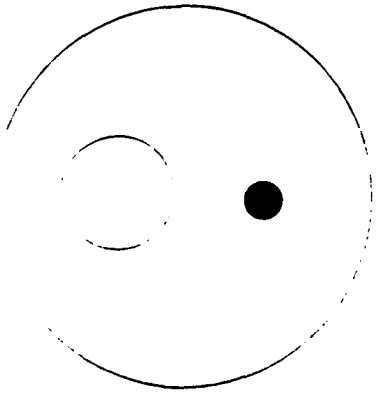

FIG. 26. Definition sketch for numerical stirring experiments of Aref and Jones.[1] Two-cylinder geometry is shown. The black dot represents the initial location of advected particles.

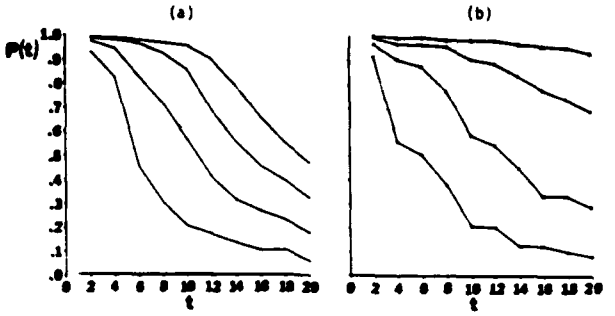

FIG. 27. Graphs of return percentage $P(t)$ versus stirring time t for decreasing diffusivity (bottom to top): (a) Chaotic advection, (b) integrable advection; from Aref and Jones.[1]

These possible connections are recognized to be tenuous, for instance the Aref–Jones flow is two dimensional and slow, whereas at transition the flow is already three dimensional. Furthermore, in the shear layer flow the fluid motions themselves are free to evolve in time.

VI. CONCLUDING REMARKS

Since the major conclusions were anticipated in the Introduction, they need not be repeated here. The following are several closing comments. Independently of the validity or usefulness of the modeling approaches discussed here, the experimental data presented in the opening sections suggest the need for additional experimental and numerical investigations in which all relevant scales can be resolved for a range of Reynolds and Schmidt numbers. Effects of changes in Schmidt number are especially revealing, and, as the preceding sections indicate, the data are limited. The consequences of changes in these parameters observed in the experiments also imply that their variation in chaotic advection studies could be important, as the Aref–Jones study illustrates.

Perhaps one of the more interesting questions raised in the paper is the nature of the singularity $\mathrm{Re} \to \infty$ at fixed Schmidt number. The proposed behavior discussed in the text is based largely on intuitive arguments; a rigorous treatment would be most instructive.

Note added in proof. The stirring–mixing distinction was suggested by C. Eckart in Journal of Marine Research, VII, 3, 265 (1948). The da Vinci quotation in the Introduction appears in *An Introduction to Hydrodynamics and Water Waves*, by B. Le Méhauté (Springer-Verlag, New York, 1976).

ACKNOWLEDGMENTS

The authors are pleased to acknowledge helpful discussions with R. W. Dibble, A. R. Kerstein, and with their colleagues and students at Caltech and Stanford. They also thank M. Koochesfahani for providing the unpublished data in Fig. 11.

J. E. B. was supported under AFOSR Contract No. 90-

0304, ONR Grant No. N-00014-89-J-1991, and by the Gas Research Institute under Grant No. 5087-260-1467.

[1] H. Aref and S. W. Jones, Phys. Fluids A **1**, 470 (1989).
[2] G. L. Brown and A. Roshko, J. Fluid Mech. **64**, 775 (1974).
[3] P. E. Dimotakis and G. L. Brown, J. Fluid Mech. **78**, 535 (1976).
[4] M. G. Mungal, J. C. Hermanson, and P. E. Dimotakis, AIAA J. **23**, 1418 (1985).
[5] N. T. Clemens and M. G. Mungal, AIAA Paper No. AIAA-90-1978, 1990.
[6] L. P. Bernal and A. Roshko, J. Fluid Mech. **170**, 499 (1986).
[7] N. T. Clemens, Ph. D. thesis, Stanford University, Stanford, California, 1991.
[8] C. D. Winant and F. K. Browand, J. Fluid Mech. **63**, 237 (1974).
[9] A. K. M. F. Hussain, J. Fluid Mech. **173**, 303 (1986).
[10] H. E. Fiedler, Adv. Geophys. **18A**, 93 (1974).
[11] D. Oster and I. Wygnanski, J. Fluid Mech. **123**, 91 (1982).
[12] R. E. Breidenthal, J. Fluid Mech. **109**, 1 (1981).
[13] S. M. Masutani and C. T. Bowman, J. Fluid Mech. **172**, 93 (1986).
[14] C.-M. Ho and L. S. Huang, J. Fluid Mech. **119**, 443 (1982).
[15] J. C. Lasheras and H. Choi, J. Fluid Mech. **189**, 53 (1988).
[16] T. J. O'Hern, J. Fluid Mech. **215**, 365 (1990).
[17] R. E. Breidenthal, Phys. Fluids **23**, 1929 (1980).
[18] I. Wygnanski, D. Oster, H. Fiedler, and B. Dziomba, J. Fluid Mech. **93**, 325 (1979).
[19] D. Coles, Proc. Ind. Acad. Sci. (Eng. Sci.) **4**, 111 (1981).
[20] G. M. Corcos, in *Perspectives in Fluid Mechanics, Lecture Notes in Physics*, edited by D. Coles (Springer, Berlin, 1988), Vol. 320, p. 48.
[21] W. J. A. Dahm and P. E. Dimotakis, AIAA J. **25**, 1216 (1987).
[22] I. van Cruyningen, A. Lozano, and R. K. Hanson, Exp. Fluids, **10**, 41 (1990).
[23] M. G. Mungal, A. Lozano, and I. van Cruyningen, to appear in Exp. Fluids.
[24] R. A. Drebin, L. Carpenter, and P. Hanrahan, Comput. Graphics, **22**, 65 (1988).
[25] I. van Cruyningen, A. Lozano, M. G. Mungal, and R. K. Hanson, AIAA J. **29**, 479 (1991).
[26] A. E. Perry and T. T. Lim, J. Fluid Mech. **88**, 451 (1978).
[27] R. A. Antonia, A. Prabhu, and S. E. Stephenson, J. Fluid Mech. **72**, 455 (1975).
[28] R. Chevray and N. K. Tutu, J. Fluid Mech. **88**, 133 (1978).
[29] S. Komori and H. Ueda, J. Fluid Mech. **152**, 337 (1985).
[30] J. Tso, L. S. G. Kovasznay, and A. K. M. F. Hussain, J. Fluids Eng. **103**, 503 (1981).
[31] W. M. Pitts, Combust. Flame **76**, 197 (1989).
[32] P. E. Dimotakis, R. Miake-Lye, and D. A. Papantoniou, Phys. Fluids **26**, 3185 (1983).
[33] D. J. Shlien, J. Fluid. Mech. **183**, 163 (1987).
[34] M. G. Mungal and D. K. Hollingsworth, Phys. Fluids A **1**, 1615 (1989).
[35] J. H. Konrad, Ph. D. thesis, California Institute of Technology, Pasadena, California, 1976.
[36] G. L. Brown, *Fifth Australasian Conference on Hydraulics and Fluid Mechanics* (University of Canterbury, New Zealand, 1974), p. 352.
[37] P. E. Dimotakis, AIAA J. **24**, 1791 (1986).
[38] M. M. Koochesfahani and P. E. Dimotakis, J. Fluid Mech. **170**, 83 (1986).
[39] W. Kollmann and J. Janicka, Phys. Fluids **25**, 1755 (1982).
[40] R. G. Batt, J. Fluid Mech **82**, 53 (1977).
[41] S. B. Pope, Combust. Sci. Technol. **25**, 159 (1981).
[42] M. G. Mungal and P. E. Dimotakis, J. Fluid Mech. **148**, 349 (1984).
[43] M. G. Mungal and C. E. Frieler, Combust. Flame **71**, 23 (1988).
[44] H. C. Hottel, *Proceedings of 4th Symposium (International) on Combustion* (The Combustion Institute, Pittsburgh, PA, 1953), p. 97.
[45] W. J. A. Dahm, P. E. Dimotakis, and J. E. Broadwell, AIAA Paper No. 84-0369, 1984.
[46] F. P. Ricou and D. B. Spalding, J. Fluid Mech. **11**, 21 (1961).
[47] W. J. A. Dahm, Ph. D. thesis, California Institute of Technology, Pasadena, California, 1985.
[48] J. E. Broadwell, in *Turbulent Reactive Flows, Lecture Notes in Engineering*, edited by R. Borghi and S. N. B. Murthy (Springer, Berlin, 1989), Vol. 40, p. 257.
[49] D. R. Dowling and P. E. Dimotakis, J. Fluid Mech. **218**, 109 (1990).
[50] M. G. Mungal and J. M. O'Neil, Combust. Flame **78**, 377 (1989).
[51] M. G. Mungal, P. S. Karasso, and A. Lozano, Combust. Sci. and Technol. **76**, 165 (1991).
[52] D. A. Papantoniou and E. J. List, J. Fluid Mech. **209**, 151 (1989).
[53] R. W. Dibble, M. B. Long, and K. Lyons (private communication).
[54] M. S. Uberoi and P. I. Singh, Phys. Fluids **18**, 764 (1975).
[55] P. H. Austin, M. B. Baker, A. M. Blyth, and J. B. Jensen, J. Atmos. Sci. **42**, 1123 (1985).
[56] R. A. Antonia, A. J. Chambers, D. Britz, and L. W. B. Browne, J. Fluid Mech. **172**, 211 (1986).
[57] C. H. Gibson, C. A. Friehe, and S. O. McConnell, Phys. Fluids **20**, S156 (1977).
[58] D. R. Dowling, Ph. D. thesis, California Institute of Technology, Pasadena, California, 1988.
[59] I. van Cruyningen, Ph. D. thesis, Stanford University, Stanford, California, 1990.
[60] C.-H. P. Chen and R. F. Blackwelder, J. Fluid Mech. **89**, 1 (1978).
[61] C. W. Van Atta, Arch. Mech. **29**, 161 (1977).
[62] C. W. Van Atta, in *Structure and Mechanisms of Turbulence II, Lecture Notes in Physics*, edited by H. Fiedler (Springer, Berlin, 1978), Vol. 76, p. 138.
[63] J. E. Broadwell and R. E. Breidenthal, J. Fluid Mech. **125**, 397 (1982).
[64] J. E. Broadwell and M. G. Mungal, *22nd (International) Symposium on Combustion* (The Combustion Institute, Pittsburgh, PA, 1988), p. 579.
[65] G. K. Batchelor, J. Fluid Mech. **5**, 113 (1959).
[66] P. E. Dimotakis, in Ref. 48, p. 417.
[67] P. G. Saffman, in *Topics in Nonlinear Physics*, edited by N. J. Zabusky (Springer, Berlin, 1968), p. 567.
[68] A. E. Lutz, R. W. Dibble, R. J. Kee, and J. E. Broadwell, AIAA Paper No. 91-0478, 1991.
[69] J. E. Broadwell, W. J. A. Dahm and M. G. Mungal, *20th (International) Symposium on Combustion* (The Combustion Institute, Pittsburgh, PA, 1984), p. 303.
[70] W. J. A. Dahm and R. W. Dibble, in Ref. 64, p. 801.
[71] M. F. Miller, C. T. Bowman, J. A. Miller, and R. J. Kee, Paper No. 89-110, Western States Section/The Combustion Institute, Fall Meeting, 1989.
[72] E. Effelsberg and N. Peters, Combust. Flame **50**, 351 (1983).
[73] J. C. LaRue and P. A. Libby, Phys. Fluids **17**, 1956 (1974).
[74] A. R. Kerstein, Combust. Sci. Technol. **60**, 392 (1988).
[75] A. R. Kerstein, Combust. Flame **75**, 397 (1989).
[76] A. R. Kerstein, J. Fluid Mech. **216**, 411 (1990).
[77] A. R. Kerstein, R. W. Dibble, M. B. Long, B. Yip, and K. Lyons, in *Seventh Symposium on Turbulent Shear Flows* (Stanford University, Stanford, 1989), Paper No. 14-2.
[78] H. Aref, J. Fluid Mech. **143**, 1 (1984).
[79] J. M. Ottino, *The Kinematics of Mixing: Stretching, Chaos and Transport* (Cambridge U.P., Cambridge, 1989).
[80] A. Leonard, V. Rom-Kedar, and S. Wiggins, Nucl. Phys. B (Proc Suppl.) **2**, 179 (1987).
[81] *Disorder and Mixing*, NATO ASI Series E: Applied Sciences, edited by E. Guyon, J.-P. Nadal, and Y. Pomeau (Kluwer Academic, Dordrecht, The Netherlands, 1988), Vol. 152, p. 339.
[82] W. J. A. Dahm and K. A. Buch, in Ref. 77, Paper No. 14-1.
[83] C. W. Leong and J. M. Ottino, J. Fluid Mech. **209**, 463 (1989).
[84] L.-S. Huang and C.-M. Ho, J. Fluid Mech. **210**, 475 (1990).
[85] R. D. Moser and M. M. Rogers, Phys. Fluids A **3**, 1128 (1991).

Appendix I

LUTZ, A. E., KEE, R. J., DIBBLE, R. W. AND BROADWELL, J. E. [1991] "A Model for Detailed Chemical Kinetics in Turbulent Nonpremixed Jet Flames," *AIAA* 29th *Aerospace Sciences Meeting*, AIAA 91-0478.

AIAA 91-0478

A Model for Detailed Chemical Kinetics in Turbulent Nonpremixed Jet Flames

A. E. Lutz, R. J. Kee
Sandia National Laboratories
Livermore, CA
R. W. Dibble
University of California
Berkeley, CA
J. E. Broadwell
California Institute of Technology
Pasadena, CA

29th Aerospace Sciences Meeting
January 7-10, 1991/Reno, Nevada

A MODEL FOR DETAILED CHEMICAL KINETICS IN TURBULENT NONPREMIXED JET FLAMES

Andrew E. Lutz* and Robert J. Kee**
Sandia National Laboratories
Livermore, CA

Robert W. Dibble†
University of California
Berkeley, CA

James E. Broadwell‡
California Institute of Technology
Pasadena, CA

Abstract

This paper describes a model that predicts detailed chemical kinetic behavior in turbulent nonpremixed jet flames. The model uses two perfectly stirred reactors to represent regions of uniformly mixed fluid and strained-flames in the jet. Entrainment into these reactors and exchange of fluid between them is governed by relatively simple jet mixing rules that come from dimensional analysis and experimental observations. With the mixing described by these rules, the model can include extensive chemical kinetics at very low computational cost. First, we use the model to predict the kinetically controlled super-equilibrium concentrations of OH in a hydrogen flame and compare the results with measurements. Then, we compare predictions of NO_x production in turbulent hydrogen and propane flames with measurements. Although the model predicts NO_x emissions higher than observed, the trends with respect to velocity, diameter, and fuel are correct. Furthermore, the model helps identify the separate effects of radiation, buoyancy, and residence time.

Introduction

Many practical combustors rely on injection of fuel in turbulent, chemically reacting jets. Unfortunately, because of the overwhelming difficulties of a first-principles approach to simulating a comprehensive chemical-kinetic system in a turbulent flow environment, it has been impractical to predict chemically controlled phenomena in turbulent flows. Conventionally, investigators have developed increasingly complex turbulence models, but have left the chemistry to be simulated by various simplifications such as partial equilibrium assumptions or reduced reaction mechanisms (see, for example, Whitelaw and Jones,[1] Chen, et al.,[2] or Pope[3]). These approaches have found some success in predicting global behavior of flames, but are deficient in their ability to predict the complex chemical kinetic behavior that is required to understand pollutant formation.

The approach used here follows the ideas introduced by Broadwell, Breidenthal, and Mungal,[4-7] and others[8,9] which view a turbulent nonpremixed jet as an ensemble of well-mixed zones that are separated by diffusion layers. Based on these ideas, we develop a simple fluid mechanics model for an axisymmetric turbulent jet. The simplicity of this model allows us to include a comprehensive chemical kinetics model, using a relatively large set of elementary chemical reactions.

The Model

We consider a turbulent jet with density ρ_J, discharging into quiescent surrounding air with density ρ_S. The surrounding fluid is entrained into the jet by large-scale vortical motions. A conceptual sketch of the model is shown in Fig. 1. At any position in the jet we imagine eddies of homogeneously mixed fluid that are separated from the entrained but as yet unmixed fluid by diffusion layers. Subsequently, these diffusion layers stretch, roll up, and eventually merge to form a new homogeneous mixture with a lower nozzle-fluid concentration. (A similar view of the structure of a turbulent

* Senior Staff Member, Computational Mechanics Division
** Supervisor, Computational Mechanics Division
† Associate Professor, Department of Mechanical Engineering, Member, AIAA
‡ Senior Scientist, GALCIT, Fellow, AIAA

wake was proposed by Effelsberg and Peters.[9]) Early in the jet the combustion occurs primarily in the diffusion layers. In time, the homogeneous eddies become sufficiently hot and contain a combustible mixture, so they ignite.

The chemical kinetic model considers the diffusive layers and the homogeneous regions as two separate zones. The homogeneous regions are represented by one perfectly stirred reacter, the *homogeneous reactor*. The diffusion layers could be modeled in several ways with various degrees of complexity: (1) an opposed-flow, strained, nonpremixed flame,[6,10] (2) an inhomogeneous well-stirred reactor,[11] (3) a perfectly stirred reactor, or (4) simply neglected. We expect that option (1) provides the best physical representation over the widest range of conditions, but it will be computationally expensive. Perhaps suprisingly, even approach (4) is valid under some circumstances.[12] Here, we develop approach (3), and use a second stirred reactor, the *flame sheet reactor*, to represent the portion of fluid within the diffusive layers that is reacting.

Mixing and Entrainment Correlations

Momentum Dominated Flow

In the far field of the turbulent jet, the total axial mass flow rate $m(x) = \rho u A$ through a plane normal to the jet scales linearly with the distance from the nozzle,[13]

$$m(z) = C_1 z m_o, \; z = x/d^*, \; d^* = d_o\sqrt{\rho_J/\rho_S}. \quad (1)$$

where m_o is the mass flow rate at the nozzle, d_o is the nozzle diameter, x is the distance downstream of the nozzle, and z is the dimensionless location that accounts for the density differences between the fluids via the adjusted diameter d^*. The experiments of Ricou and Spalding established $C_1 = 0.32$.[13]

The average velocity, $\bar{u}$ decreases with distance from the nozzle as quiesent fluid from the surroundings is entrained into the jet. As long as the velocity is large enough, the total momentum of the jet is conserved. $m\bar{u} = m_o u_o$. The entrainment follows Eq. (1) until the fluid has slowed to the point where buoyant forces become important.

The linear entrainment correlation in Eq. (1) comes from observations in the far field of the jet, and must approach the condition $m(0) = m_o$ through some transition region near the nozzle. However, rather than modify the correlation so that it obeys this condition, we neglect the region near the nozzle, and establish initial conditions at a location beyond $z = 1/C_1$, where $m > m_o$.

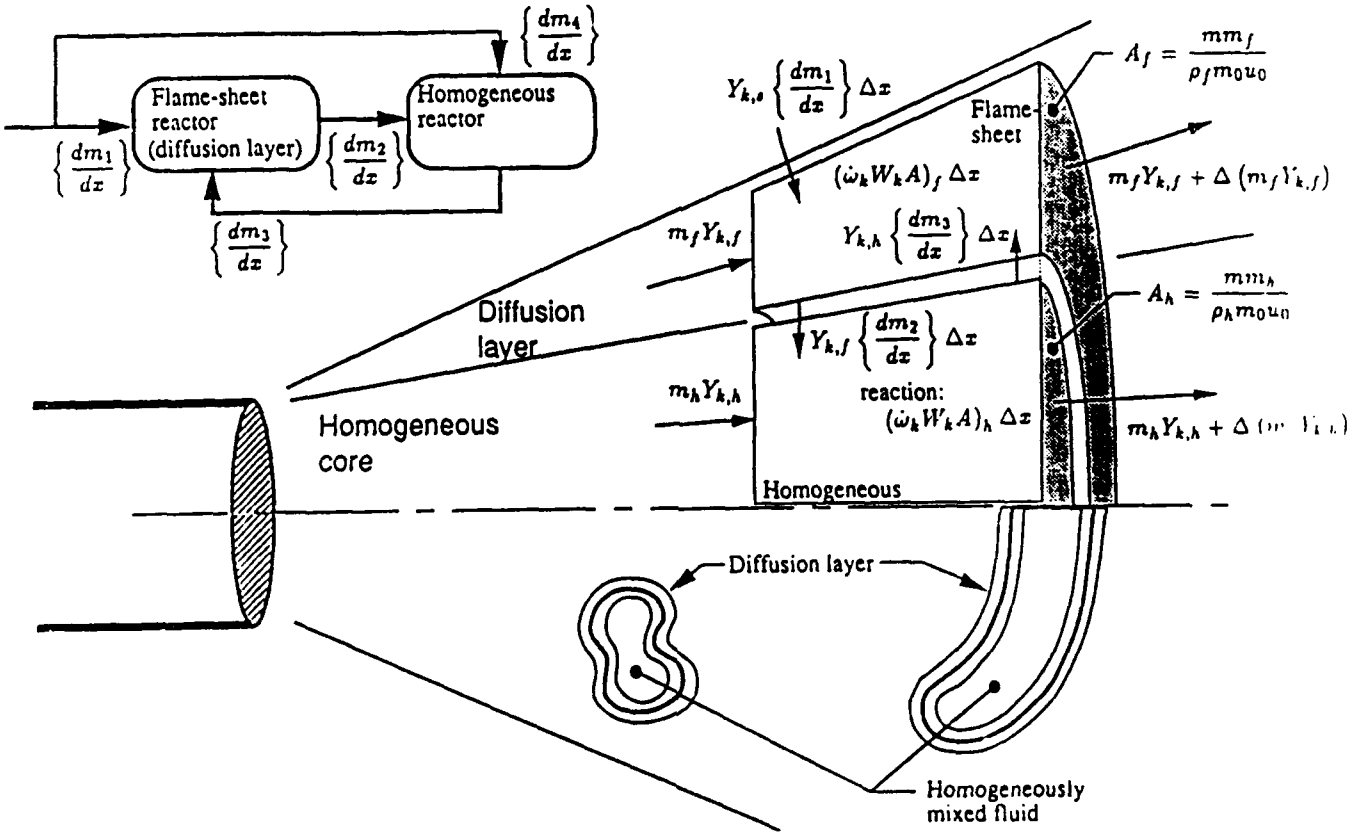

Figure 1. The schematic of a turbulent jet model shows the homogneous eddies surrounded by diffusion layers that separate them from the surrounding fluid. The control volume in the upper half of the sketch describes the mass fluxes into and between the reactors.

At any axial location, only a fraction of the total mass flux is mixed to the molecular level. Flame-length investigations[14] and analogous liquid-into-liquid studies[15] were used to establish that the mass flux of molecularly mixed fluid m_h^∞ is roughly one third of the total axial mass flux $m(z)$ and grows linearly with distance,

$$m_h^\infty(z) = C_2 z m_o. \tag{2}$$

The superscript ∞ denotes that this is the mass flow rate through the homogeneous region in the limit of infinite Reynolds number (when the diffusion layers are negligible). The regions of homogeneously mixed fluid are surrounded by a diffusion layer that separates them from the moving, but unmixed, ambient fluid. The mass flux in these diffusion layers is growing at a rate specified by

$$m_d(z) = C_3 z m_o. \tag{3}$$

Arguments are presented[4] that C_3 should scale as $1/\sqrt{(\mathrm{Re\ Sc})}$. The model includes the option of a dependence $C_3 = C_2\sqrt{(\mathrm{Re})_{\mathrm{ref}}/\mathrm{Re}}$; in the gaseous jets we consider, $\mathrm{Sc} \approx 1$. Note that in the limit of large Reynolds number, the time for growth of the diffusion layer decreases, so C_3 approaches zero. However, in the calculations presented here we have neglected this Reynolds number dependence, because preliminary calculations showed that its effect on the emission index is relatively small. For all the calculations presented here, we let $C_2 = C_3 = 0.05$, which sets the flame length.

Buoyancy Dominated Flow

The velocity of the jet fluid decreases with distance from the nozzle. Eventually, buoyant forces become important in the entrainment process. Becker and Yamazaki[16] performed experiments in propane jet flames, which provide correlations for the mass flow rate and momentum in the buoyant regime. The total mass flow rate grows according to

$$\frac{dm}{dz} = \begin{cases} C_1 m_o, & \text{for } z < z_B, \\ \frac{2}{5} C_4 m_o \mathrm{Ri}^{1/2} z^{3/2}, & \text{for } z > z_B, \end{cases} \tag{4}$$

where the Richardson number, $\mathrm{Ri} = g d^*/u_o^2$ is the inverse of the Froude number and g is the acceleration of gravity. Momentum conservation now includes a buoyancy term in the form

$$\frac{m\bar{u}}{m_o u_o} = \begin{cases} 1, & \text{for } z < z_B, \\ 1 + C_5\ \mathrm{Ri}\ z^3, & \text{for } z > z_B, \end{cases} \tag{5}$$

This momentum relation enters the conservation equations through the average velocity, $\bar{u}$. Becker and Yamazaki[16] report $C_4 = 0.08$ and $C_5 = 0.048$.

The data of Becker and Yamazaki[16] could perhaps be used in the integration of a momentum equation in the model. However, since we have not been able to produce a momentum formulation that reproduces their original data, we incorporate their correlations directly from the experimental measurements. The disadvantage of this procdure is that the correlations in Eqs. (4) and (5) contain discontinuities at the point z_B, where they switch from momentum-dominated to buoyancy-dominated flow. According to the data for propane flames, this switch occurs at the normalized location $\xi_B = 1.59$, where the normalized coordinate ξ is defined by Becker and Yamazaki as $\xi = \mathrm{Ri}^{1/3} z$. We suggest that this switch may occur at some other value for other fuels, because the Richardson number does not include the influence of the local density difference in the flame. The force of the initial jet is $\rho_o u_o^2 d_o^2$, while the buoyant force is $(\rho_\infty - \bar{\rho}) g V$, where $\bar{\rho}$ is an average density over the volume V. If $V \sim d_o^3$, then the ratio of the buoyant force to the jet momentum is

$$\frac{(\rho_\infty - \bar{\rho}) g d_o}{\rho_o u_o^2}.$$

This ratio includes information about the density difference that is not included in the Richardson number. Becker and Yamazaki suggest that the local density $\bar{\rho}$ is roughly one half the surrounding density ρ_∞, and neglect the density difference. However, the density difference in the flame zone will vary for different fuels. Furthermore, the lower density of hydrogen leads to jet Reynolds numbers small enough that there could be effects of the laminar-to-turbulent transition. For these reasons, we do not expect the Richardson number at which the flow becomes buoyancy-dominated to be the same for hydrogen as it is for propane.

Since we do not have the kind of careful measurments of the buoyancy effects for hydrogen that Becker and Yamazaki produced for propane at high Reynolds numbers, we simply chose different values of ξ_B to match the behavior of the hydrogen data of Chen and Driscoll.[17]

Conservation Equations

Mass balances for the two control volumes shown in Fig. 1 lead to

$$\frac{dm_h}{dz} = \left\{\frac{dm_2}{dz}\right\} - \left\{\frac{dm_3}{dz}\right\} + \left\{\frac{dm_4}{dz}\right\} \tag{6}$$

$$\frac{dm_f}{dz} = \left\{\frac{dm_1}{dz}\right\} - \left\{\frac{dm_2}{dz}\right\} + \left\{\frac{dm_3}{dz}\right\} \tag{7}$$

where the flow rates between the reactors (e.g., $\left\{\frac{dm_1}{dz}\right\}$) are defined by the mixing rules given in the next section. Species and energy balances for the homogeneous reactor are as follows (the equations for the

flame sheet reactor are the same, except for the subscripts).

$$\frac{dY_{k,h}}{dz} = \frac{1}{m_h}\left\{\frac{dm_2}{dz}\right\}(Y_{k,f} - Y_{k,h}) + \frac{1}{m_h}\left\{\frac{dm_4}{dz}\right\}(Y_{k,s} - Y_{k,h}) + \frac{d^*}{\bar{u}}\left(\frac{\dot{\omega}_k W_k}{\rho}\right)_h \quad (8)$$

$$c_{ph}\frac{dT_h}{dz} = \frac{1}{m_h}\left\{\frac{dm_2}{dz}\right\}\sum_{k=1}^{K} Y_{k,f}(h_{k,f} - h_{k,h}) + \frac{1}{m_h}\left\{\frac{dm_4}{dz}\right\}\sum_{k=1}^{K} Y_{k,s}(h_{k,s} - h_{k,h}) - \frac{d^*}{\bar{u}}\sum_{k=1}^{K}\left(\frac{\dot{\omega}_k W_k h_k}{\rho}\right)_h - \frac{\pi d^* d_{\rm eff}\epsilon\sigma}{m_h}(T_h^4 - T_o^4) \quad (9)$$

In these ordinary differential equations the independent variable is the axial distance from the nozzle, z. The dependent variables are the temperature T, the mass fractions Y_k, and the total mass flow rates through the reactors, m_h and m_f. The subscripts f, h, and s refer to the flame sheet and homogeneous reactors, and the surroundings, respectively. The subscript o refers to the fluid as it flows from the nozzle. Other variables are h_k the specific enthalpies, W_k the molecular weights, and c_p the mean specific heat. The pressure is assumed to be constant, and the mass density ρ is evaluated using the ideal gas equation-of-state. The species production rates by chemical reaction are given by $\dot{\omega}_k$. The thermal radiation model considers emission from the surface of a cylinder, defined by the emissivity of a gray gas ϵ, the Stefan-Boltzmann constant σ, and an effective diameter $d_{\rm eff} = d_o + C_2 x$.

To help identify the controlling parameters, we present a dimensionless form of the energy equation (9). For momentum-dominated flow, we write (ignoring for the moment the first two mixing terms on the right hand side of Eq. (9))

$$\frac{d\hat{T}}{dz} = \cdots + C_1 z \Delta\hat{q}\frac{\tau_o}{\tau_c} - \frac{1}{\rho_o u_o}\left(\frac{\epsilon\sigma\hat{T}^3}{r c_p}\right)\left(\hat{T}^4 - 1\right) \quad (10)$$

where $\hat{T} = T/T_o$. We have defined two time scales: a nominal residence time based upon the nozzle conditions, $\tau_o = d_o/u_o$, and a reaction time scale, τ_c that comes from the approximating the chemical heat release by $(\Delta q/\tau_c) \approx \sum(\dot{\omega}_k W_k h_k)$. This form of the equation shows that the chemistry depends on a Damköhler number, $\mathrm{Da} = \tau_o/\tau_c$, while the radiation energy loss scales with the inverse of the jet velocity, u_o. Therefore, if the flow is momentum-dominated and nearly adiabatic, the solutions scale with the nominal residence time τ_o.

Flux Definitions

The essence of the mixing model is embodied in the specification of mass fluxes to and between the reactors. The total mass flow rate, m_t that can react in either of the reactors is the homogeneously mixed fluid m_h^∞ plus half the mass flux in the diffusion layer, m_d, so $m_t = m_h^\infty + m_d/2$. We presume that the diffusion layer grows into the ambient and homogeneous fluid at equal rates. Diffusion into the ambient fluid increases the flux of fluid that can potentially react. However, while diffusion into the homogeneously mixed fluid can change the reaction chemistry, it does not introduce new mass into the system.

Physically, diffusion layers are established by concentration gradients in the flow. If there is combustion, most of the reaction occurs in thin, hot zones located at the stoichiometric point. To model these layers, we represent the reactive regions by the flame-sheet reactor. In order to produce flame-sheet behavior from a perfectly stirred reactor, we must control both the size and stoichiometry of the reactor.

With this picture in mind, we let the mass flow rate through the flame-sheet reactor be a fraction of the mass flow rate into the diffusion layer, $m_f = r m_d$, where $r = 0.15$ was chosen for all calculations presented here. The remaining fluid from the fuel-rich and fuel-lean sides of the stoichiometric zone passes into the homogeneous reactor. The mass flow rate through the homogeneous reactor is then $m_h = m_h^\infty + (1/2 - r)m_d$.

The stoichiometry of the flame-sheet reactor is controlled by the parameters α and β which are the fractions of the fluid from the surroundings and homogeneous reactor, respectively, that pass through the diffusion layer into the homogeneous reactor. The values of α and β are adjusted dynamically during the integration (see the appendix for details).

The four flux terms that appear in the conservation equations are

$$\left\{\frac{dm_1}{dz}\right\} = (1-\alpha)\frac{dm_t}{dz} \quad (11)$$

$$\left\{\frac{dm_2}{dz}\right\} = [2 - (\alpha+\beta)]\frac{dm_t}{dz} - r\frac{dm_d}{dz} \quad (12)$$

$$\left\{\frac{dm_3}{dz}\right\} = (1-\beta)\frac{dm_t}{dz} \quad (13)$$

$$\left\{\frac{dm_4}{dz}\right\} = \alpha\frac{dm_t}{dz} \quad (14)$$

where

$$\frac{dm_t}{dz} = \frac{dm_h^\infty}{dz} + \frac{1}{2}\frac{dm_d}{dz}$$

is the total mass flux into the two-reactor system. We assume, with some support from the experiments of Johari,[18] that the molecular mixing rate scales with the entrainment rate in buoyant flows as it does in the momentum-dominated regime (see Eq. (2)). Therefore, we write the mass fluxes of both the homogeneous fluid and diffusion layers in terms of the total entrainment:

$$\frac{dm_h^\infty}{dz} = \frac{C_2}{C_1}\frac{dm}{dz}$$

$$\frac{dm_h^\infty}{dz} = \frac{C_3}{C_1}\frac{dm}{dz} \qquad (15)$$

The system of Eqns. (4)-(9) with the flux definitions in Eqs. (11)-(14) for the two reactors form an initial value problem in terms of the downstream location z. The system is integrated using standard ordinary differential equation methods.[19] The initial conditions for the problem are established at a location $z_1 = 1/(C_2 + C_3(1/2 - r))$, because as noted above, the model is based on entrainment correlations that are not valid at the nozzle. We chose this form for z_1, because at this point, the mass flow rate in the homogeneous reactor is equal to the initial flow rate of the nozzle, m_o. The initial flame-sheet reactor has the composition of an equilibrium mixture at the adiabatic flame temperature. The initial homogeneous-reactor composition is pure nozzle fluid at ambient temperature.

Although the equations are derived in a fixed coordinate system, it is sometimes convenient to view the reactions as taking place in constant-pressure reactors of increasing volume (as sketched in Fig. 1). In this view, the reactors are moving downstream with the average velocity, $\bar{u}(z)$.

Results

OH concentration in a Hydrogen Flame

Recent experiments in a turbulent nonpremixed jet flame by Barlow et al.[20] provide a basis for a significant test of the model. The fuel is a mixture of 22 percent argon in hydrogen; this mixture retains the simplicity of the hydrogen chemical kinetics while avoiding the complication associated with the low gas density of pure hydrogen. The experiment applies simultaneously laser-Raman scattering, which measures the mixture fraction f, and laser-induced fluorescence, which measures the concentration of the hydroxyl radical, OH. This radical is an important intermediate species in the chain branching reactions that accelerate the fuel consumption and energy release. The mixture fraction is the mass of fuel elements per mass of mixture; it serves as a conserved scalar that measures the dilution of the mixture.

Using the conditions of Barlow et al.[20] we have computed the axial evolution of chemical species in the two reactors. For two jet velocities (75 and 150 m/s). Fig. 2 shows the predicted OH mole fractions and the fuel mixture fractions as a function of distance from the nozzle. The solid curves are for the homogeneous reactor and the dashed curves are for the flame-sheet reactor. As shown in the upper panel, the mixture fraction in the homogeneous reactor is inversely proportional to the axial coordinate ($f \sim d_o/x$), while the model maintains a stoichiometric mixture fraction in the flame reactor until near the flame tip. The flame tip occurs at about 50 diameters, where the mixture fraction in the homogeneous reactor reaches the stoichiometric point. The mixture fraction is independent of velocity, because the jet is momentum-dominated throughout this flame. Accordingly, the turbulent flame length is independent of Reynolds number.

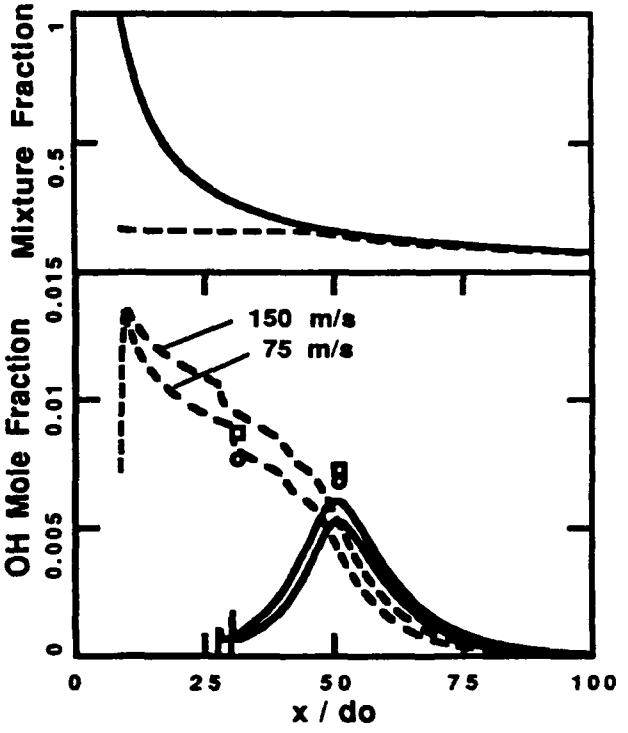

Figure 2. Predicted mixture fraction and OH mole fraction profiles for the H_2/Ar flame of Barlow et al.[20] at two jet velocities. Also shown are measured OH mole fractions at 30 and 50 diameters; circles represent u_o=75 m/s; squares represent u_o=150 m/s. Solid curves represent the homogeneous reactor and dashed curves represent the flame-sheet reactor. The mixture fraction solution (upper panel) is independent of velocity.

The laser-based measurements are reported for two axial locations: 30 and 50 diameters. At any location, an ensemble of simultaneous f-OH measurements span a range of values. For comparison to the flame reactor, we select only f-OH pairs where f is within 5 percent of stoichiometric value, $f = 0.16$. The average of these conditioned pairs, shown as a single point in Fig. 2, is in good agreement with the model. At 30 diameters, the homogeneous reactor is fuel rich ($f \approx 0.3$), so there is very little OH present. However, the flame-sheet reactor is nearly stoichiometric, and its OH concentration is very close to the observed values. Further downstream at 50 diameters, dilution of the homogeneous reactor has brought it close to the stoichiometric condition, and the OH concentration has risen to about the same value as that in the flame-sheet reactor. We emphasize that both the prediction and measurement are substantially above the stoichiometric equilibrium mole fraction of 0.005. Accordingly, the model captures these essential features of chemical reaction with simultaneous mixing. In comparing the results at two different jet velocities, we see that the OH concentration is smaller in the slower jet, because the residence time increases and the reactions advance closer to equilibrium.

NO_x Production in Hydrogen Flames

Since as noted above we do not have an adequate treatment of buoyancy influences on hydrogen flames, we have not yet made an extensive study of NO_x production in this fuel. Instead, only the data and corresponding model runs for the study of Chen and Driscoll[17] are discussed. A comparison of model results and data appear in Fig. 3, which plots the emission index, EI (the mass of NO_x per mass of fuel), versus the inverse of the nominal residence time, τ_o. Although the absolute NO_x emission index values differ significantly, the data and model results agree in the nature of the dependence of the emission on the nominal residence time. Note that this definition of residence time scales with the actual residence time (integrated for a particle with the average velocity) only for a jet that is momentum-dominated for its entire length. Nevertheless, except for the slowest velocities considered here, these hydrogen jet flames are momentum dominated.

In this range, the data and model results for the three different nozzle diameters each collapse to a single curve. Our simplification of the energy equation in Eq. (10) suggests that if the flame is adiabatic, the solutions will collapse at the velocities where the flame is momentum dominated. The fact that there is a collapse of the data suggests that the radiation loss in these flames is relatively small. The radiation model for hydrogen flames uses a correlation for the emissivity of a gas mixture as a function of the partial pressure of H_2O.[21] Based upon this correlation, the model predicts that about 5 to 10 percent of the total heat release from the flame is lost to radiation. As mentioned in the discussion of Eq. (10), the radiation loss varies with the inverse of the jet velocity, $1/u_o$. Using a similar model - without buoyant effects - Tyson et al.[22] pointed out the importance of radiation loss in predicting NO_x emissions.

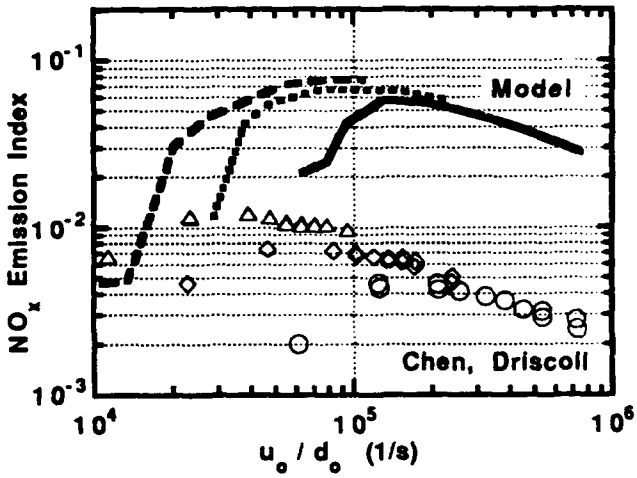

Figure 3. Comparison of predicted and measured emission index for hydrogen-air jet flames, plotted against the inverse of the nominal residence time ($1/\tau_o = u_o/d_o$). Data is from Chen and Driscoll.[17] Data and solutions are given for three diameters: circles and solid curve, 0.159 cm; diamonds and dotted curve, 0.26 cm; triangles and dashed curve, 0.37 cm.

These observations are in aggreement with Chen and Driscoll,[17] who achieved a further collapse of the data by dividing the emission index by $L^3/d_o^2 u_o$; this scaling was originally suggested by Peters and Donnerhack.[23] However, we find the scaling in Fig. 3 interesting, in that it shows that for each nozzle diameter, the lowest velocities drop off the line. In other words, the trend of emission versus residence time is reversed when buoyancy becomes important; the slope is positive. As expected, the emission decreases with velocity when the flame is momentum dominated. We note that for the momentum-dominated flames, the predicted slope is roughly the same as can be inferred from the data, $EI \sim \tau_o^{1/2}$; in aggreemnt with earlier findings of Bilger and Beck,[24] who made measurements at constant Froude number. However, it is apparent that the variation in the radiation loss with jet velocity also plays some role in the way the predictions begin to fall off the line in the momentum-dominated regime.

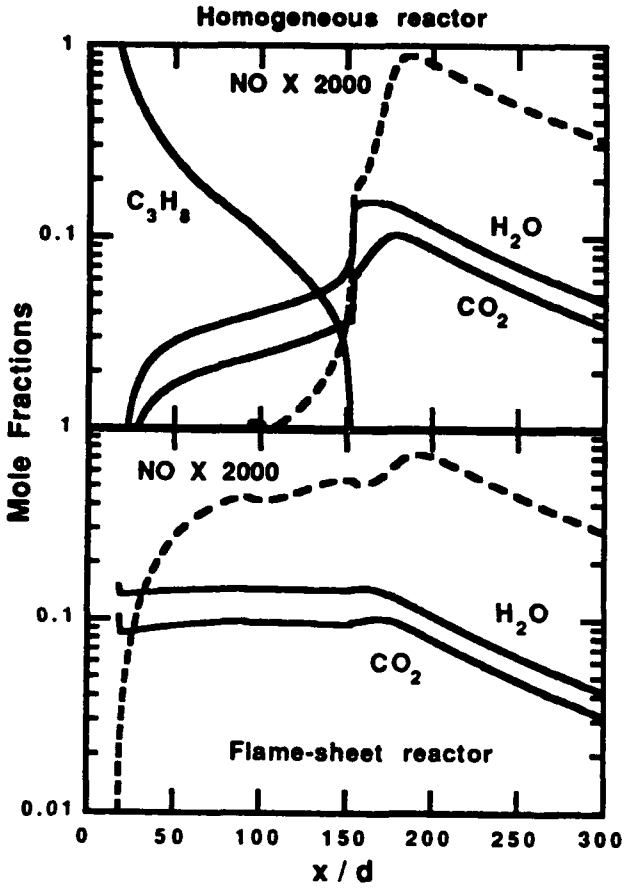

Figure 4. Computed species mole fractions in the two reactors for a propane jet (u_o=69 m/s, d_o=0.386 cm). Beyond the flame tip ($\approx$ 200 diameters), the concentration of the product species decreases due to entrainment and dilution. The NO is first produced in the flame-sheet reactor, but the final emission is dominated by the reactions in the homogeneous reactor.

NO_x Production in Propane Flames

Turns and Lovett[25] recently measured the NO_x in the combustion products from a propane flame attached to a 3.8 mm diameter nozzle with jet velocities ranging from 11 to 69 m/s. We model this flame using a propane-air oxidation mechanism (259 reactions and 55 species) derived from Westbrook and Pitz[26] and incorporating the nitrogen chemistry from Miller and Bowman.[27] Figure 4 shows axial development of composition of the flame-sheet and homogeneous reactors. For the first 50 diameters, NO rapidly increases in the flame-sheet reactor, due to production by the thermal-NO mechanism at high temperature. Surprisingly, a slight *decrease* in NO occurs at about 100 diameters; this is caused by fuel-rich reactions in the homogeneous reactor that remove NO. (The removal of NO in fuel-rich combustion is the basis of the staging and reburning for NO control in power plants.) As the homogeneous reactor evolves from fuel-rich chemistry to fuel-lean chemistry at the flame tip (170 diameters at this velocity), the NO in the homogeneous reactor rapidly increases. The rapid chain-branching reactions in the homogeneous reactor produce NO and control the total emission that the model predicts. Consequently, modifications to the model near the nozzle have little impact on the total NO_x unless they change the residence time in the flame tip region. This may be physically consistent with the concept that there is a "final reactive eddy" at the flame tip that dominates the emissions. This conclusion is supported by the recent measurements of Lovett and Turns[28] who sinusoidally pulsed the flow of fuel from the nozzle at a wide variety of frequencies and amplitudes. Although they observed significant change in the visible structure of the flame near the nozzle, there was no change in the amount of NO_x produced. Beyond the flame tip, the NO concentration decreases primarily due to dilution by entrained air (see Fig. 4).

While the present work supports the idea that radiation is important in propane flames, we find that the primary factor influencing the nature of the dependence of the emission index on velocity is buoyancy. Figure 5 compares the data of Turns and Lovett[25] to the model prediction with various assumptions regarding the radiation loss and buoyancy. The dashed curve shows the model prediction when only the correlations for momentum-dominated flow are used for an adiabatic flame. Not only is the magnitude of the emission index too large, but the dependence on velocity is incorrect. However, when the buoyant-flow correlations are included in the model, the velocity dependence is as observed, and the magnitude is much closer to the data. Further improvement in model prediction occurs when radiation loss from the reactors is included. In a propane flame, the radiation model is complicated by the presence of soot. Using empirical data for CO_2 and H_2O in the gas mixture, we estimated an emissivity of $\epsilon = 0.05$. The model prediction using this value in the radiation model is shown by the solid curve in Fig 5. However, the estimated radiation loss in these calculations is probably too low, becuase we have not attempted to include the radiation from soot. If we simply adjust the radiation loss until the model matches the data at a given velocity, we find that an emissivity of $\epsilon = 0.17$ brings the model into agreement with the data of Turns and Lovett.[25]

A detailed examination of the species production rates of the individual reactions, integrated over the length of the flame, shows that the prompt and thermal NO_x mechanisms contribute approximately equally to the emission index. However, a discrepancy, as yet unresolved, between the present results and those of Lovett and Turns, is in the percentage of NO_2 in the NO_x; they find fractions as large as 50 percent, whereas the model predicts only a few percent.

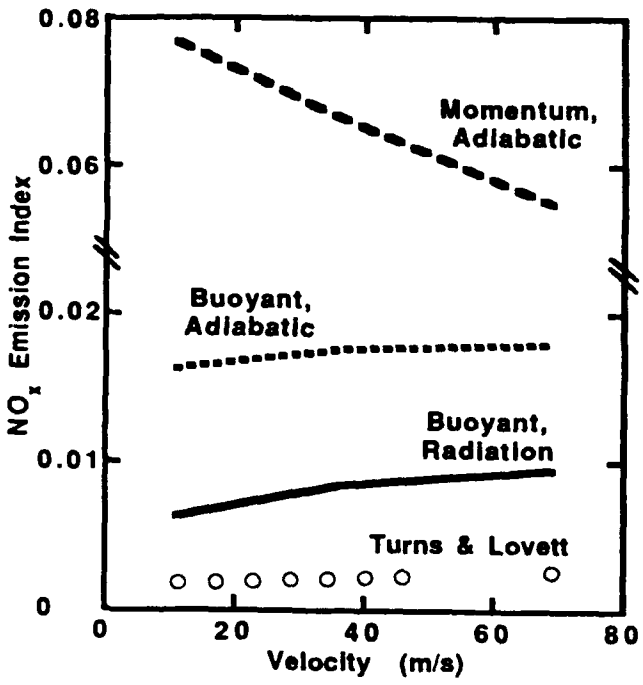

Figure 5. Comparison of the predicted and measured emission index for a propane jet as a function of jet velocity (d_o=0.386 cm). Data is from Turns and Lovett.[21] Dashed curve is solution for an adiabatic case using only the correlations for momentum-dominated flow. Solution in dotted curve includes the buoyancy correlations. Solid curve solution includes radiation loss using $\epsilon = 0.05$, estimated for the gas mixture (neglecting radiation from soot).

Conclusion

We have developed a computationally efficient model that is an effective tool to examine kinetically controlled phenomena in turbulent jet flames. The combination of simple turbulent-mixing correlations and detailed chemical kinetics allows us to examine the interaction of the kinetics with the physical mechanisms of mixing, residence time, buoyancy, and radiation. As test cases we have used the model to predict the super-equilibrium OH in hydrogen flames. We have also applied the model to predict NO_x formation in turbulent hydrogen and propane flames. After accounting for buoyancy and thermal radiation effects, the computed emissions are in qualitative agreement with the experimental measurements. Our model shows that the slope of emission versus jet velocity is negative for a momentum-dominated jet, but positive when buoyancy influences a portion of the jet. The velocity range for the hydrogen flames we examined contains both regimes, so we see the emission trend change as the velocity increases. The propane flames are influenced by buoyancy, but by running the model with and without the buoyant correlations, we see that the observed trend of increasing NO_x with velocity is explained by buoyancy. In both hydrogen and propane flames, a significant radiation energy loss is necessary to bring the predicted emission index down to the magnitude of the data.

Future work on this model includes more accurate treatment of radiation and buoyancy, extensive comparisons of the predictions to the available experimental data, and replacing the flame-sheet reactor with a diffusion flame (such as studied by Drake and Blint[29]).

Acknowledgments

We are grateful to Dr. Charles Westbrook and James Miller for their help in implementing the reaction mechanism. Our discussions with Dr. William Houf has provided important input to the radiation model. Ongoing discussions with Prof. Godfrey Mungal have significantly influenced the development of this model. We thank Profs. Steven Turns and James Driscoll for many useful discussions of their data. This work was sponsored by the Gas Research Institute with Drs. Thomas Roose and Robert Gemmer as contract monitors.

Appendix

As discussed in the main text, the flame-sheet reactor represents only the hot, reactive portion of the diffusion layers. The mass flux into this reactor is dynamically adjusted to maintain a stoichiometric inflow from the combination of the streams from the homogeneous reactor and the surroundings. The procedure is accomplished in three stages. Starting at the initial condition near the nozzle, the first stage returns excess fuel to the homogeneous reactor without entering the flame-sheet reactor. We set an initial value of α_o in this region, and calculate β as a function of the homogeneous mixture fraction using $\beta = (F_h + F_s(1-\alpha_o) + \alpha_o - 2)/(F_h - 1)$ where $F_h = f_h/f_{\phi=1}$ and $F_s = f_s/f_{\phi=1}$. The fuel mixture fraction f is computed by the sum

$$f = \sum_{k=1}^{K} \frac{Y_k}{W_k} \sum_{j=\mathrm{C,H}} a_{kj} M_j$$

where a_{kj} is the number of atoms of element j in species k, M_j is the atomic mass of element j and the inner summation runs only over elements in the fuel (carbon and hydrogen). We set $\alpha_o = 0.7$ for all computations presented, which means that 70 percent of the fluid that enters the diffusion layer from the surroundings does not enter the flame-sheet reactor, but enters the homogeneous reactor instead.

In the second stage, $\beta = 0$, and we use all the fuel mixture from the homogeneous reactor. The fraction

of the excess oxidizer from the surroundings that enters the homogeneous reactor is $\alpha = (F_h + F_s - 2)/(F_s - 1)$. This continues until the homogeneous reactor approaches the stoichiometric mixture fraction, and α approaches a value of $\alpha_{max} = 0.8$. Beyond this point, the parameters are fixed and both reactors are diluted by the surrounding fluid at approximately the same rate.

References

1. Whitelaw, J. H. and Jones, W. P.: *Twentieth Symposium (International) on Combustion*, p. 233, The Combustion Institute (1985).
2. Chen, J. Y., Kollmann, W., and Dibble, R. W.: *Combust. Sci. and Tech.* to appear (1989).
3. Pope, S. B.: Twentythird Symposium (International) on Combustion, to appear (1991).
4. Broadwell, J. E.: "A Model for Reactions in Turbulent Jets: Effects of Reynolds, Schmidt, and Damköler Numbers," *Turbulent Reacting Flows: USA-France Workshop on Turbulent Reactive Flows*, Ed. by R. Borghi and S. N. B. Murthy, Springer-Verlag Lectures Notes in Engineering **40**, pp 257-277, (1988).
5. Broadwell,J. E., and Breidenthal, R. E.: *J. Fluid. Mech.* **125** 397 (1982).
6. Broadwell, J. E., and Mungal, G. M.: *Twenty-Second Symposium (International) on Combustion*, p. 579 The Combustion Institute, (1988).
7. Broadwell, J. E., and Mungal, G. M.: "Large Scale Structures and Molecular Mixing," general lecture at the IUTAM Symposium on Fluid Mechanics of Stirring and Mixing, U.C.S.D., La Jolla, August 1990, to appear in *Physics of Fluids* (1991).
8. Oppenheim, A. K.: *Dynamics of Reactive Systems* (J. R. Bowen, J.-C. Leyer, R. I. Soloukhin, Eds.) Vol. 105, Progress in Astronautics and Aeronautics, (1985).
9. Effelsberg, E. and Peters, N.: *Combust. and Flame* **50** 351 (1983).
10. Dixon-Lewis, G., David, T., Gaskell, P. H., Fukutani, S, Jinno, H., Miller, J. A., Kee, R. J., Smooke, M. D., Peters, N., Effelsberg, E., Warnatz, J., and Behrendt, F.: *Twentieth Symposium (International) on Combustion*, p. 1983, The Combustion Institute (1984).
11. Bar-Eli, K. and Noyes, R. M.: *J. Chem. Phys.* **85** (1986).
12. Dibble, R. W., Broadwell, J. E., Lutz, A. E., and Kee, R. J.: *A Model for the Simulation of Complex Chemical Kinetics in a Turbulent Jet, with Application to the removal of NO_X*, Central States Section Combustion Institute Meeting, (1989).
13. Ricou, F. P. and Spalding, D. B.: *J. Fluid Mech.* **11**, 21 (1963).
14. Avery, J. F. and Faeth, G. M.: *Fifteenth Symposium (International) on Combustion*, p. 501, The Combustion Institute (1974).
15. Dahm, W. J. A. and Dimotakis, P. E.: *AIAA J.* **25** 1216 (1985).
16. Becker, H. A. and Yamazaki, S.: *Combust. and Flame* **33** 123 (1978).
17. Chen, R-H. and Driscoll, J. F.: Twenty-Third Symposium (International) on Combustion, to appear (1990).
18. Johari, H.: "Flame Length Measurements of the Turbulent Plume," *Physics of Fluids A*, **2** (7), July (1990).
19. Petzold, L. R.:"A description of DASSL: a differential/algebraic system solver," Sandia National Laboratories report SAND82-8637, (1982).
20. Barlow, R. S., Dibble, R. W., Lucht, R. P., and Chen, J. Y.: *Combust. and Flame* in press (1990).
21. Siegal, R. and Howell, J. R.: *Thermal Radiation Heat Transfer*, McGraw-Hill, p. 624 (1981).
22. Tyson, T. J., Kau, C. J., and Broadwell, J. E.: "A Model of Turbulent Diffusion Flames and Nitric Oxide Generation. Part II," to appear as an EPA Report (1990).
23. Peters, N. and Donnerhack, S.: *Eighteenth Symposium (International) on Combustion*, p. 33, (1981).
24. Bilger, R. W. and Beck, R. E.: *Fifteenth Symposium (International) on Combustion*, p. 541, The Combustion Institute (1975).
25. Turns, S. R. and Lovett, J. A.: *Combust. Sci. and Tech.* in press (1989).
26. Westbrook, C. K. and Pitz, W. J.: *Combust. Sci. and Tech.* **37** 117 (1984).
27. Miller, J. A., and Bowman, C. T.: *Prog. in Energy and Combust. Sci.*, in press (1990).
28. Lovett, J. A. and Turns, S. R.: *AIAA Journal* in press (1989).
29. Drake M. C. and Blint, R. J.: General Motors Report GMR0206, submitted to *Combust. and Flame* (1989).

Appendix J

LAPPAS, T., LEONARD, A. AND DIMOTAKIS, P. E. [1991] "An Adaptive Lagrangian Method for Computing 1-D Reacting and Non-Reacting Compressible Flows," *AIAA* 29th *Aerospace Sciences Meeting*.

AIAA 91-0249

An Adaptive Lagrangian Method for Computing 1-D Reacting and Non-Reacting Flows

T. Lappas, A. Leonard and P.E. Dimotakis
Graduate Aeronautical Laboratories
California Institute of Technology
Pasadena, CA

29th Aerospace Sciences Meeting
January 7-10, 1991/Reno, Nevada

An Adaptive Lagrangian Method for Computing 1-D Reacting and Non-Reacting Flows

Tasso Lappas**, Anthony Leonard†, and Paul E. Dimotakis‡

Graduate Aeronautical Laboratories
California Institute of Technology
Pasadena, Ca 91125

Abstract

A method for computing one-dimensional unsteady compressible flows, with and without chemical reactions is presented. This work has focused on the accurate computation of the discontinuous waves that arise in such flows. The main feature of the method is the use of an adaptive Lagrangian grid. This allows the computation of discontinuous waves and their interactions with the accuracy of front-tracking algorithms. This is done without the use of additional grid points representing shocks, in contrast to conventional front-tracking schemes. The Lagrangian character of the present scheme also allows contact discontinuities to be captured easily. The algorithm avoids interpolation across discontinuities in a natural and efficient way. The method has been used on a variety of reacting and non-reacting flows in order to test its ability to compute accurately and in a robust way complicated wave interactions.

1. Introduction

Several methods for computing unsteady inviscid compressible flows have appeared in the literature in recent years. The emphasis has been on the ability of these numerical schemes to compute accurately discontinuous waves which develop and their interactions.

High-resolution shock-capturing methods for hyperbolic conservation laws is one category of such methods which have been used successfully in recent years. A basic feature of these methods is that the conservative formulation is used which allows for shocks and their interactions to be captured automatically without special effort. This is characteristic of all older shock-capturing methods such as the Lax-Wendroff scheme[7], the MacCormack scheme[9], the original Godunov scheme[4], etc. In all such methods, discontinuous waves of the solution are represented as steep fronts, i.e. smeared over a finite number of computational cells. A second and more important feature of recent high-resolution schemes is the special effort which is made to achieve higher order spatial and temporal accuracy so as to represent discontinuous waves of the solution as accurately as possible, i.e. to reduce the smearing effect which is typical of all shock-capturing methods. Such schemes are the TVD schemes[5,6], the various MUSCL-type schemes[14], the PPM scheme[2] (Piecewise Parabolic Method), etc. A comparative study of some of these schemes for real gases is given in a review article by Montagné, *et al*[10]. The basic high-resolution shock-capturing methods have been developed for nonlinear scalar hyperbolic conservation laws. It is for this case that there exists a sound mathematical theory. For nonlinear hyperbolic systems of equations in one space variable the theory is not as clear and the numerical methods used for these systems apply formally the same techniques as in the scalar case, but with the additional use of exact or approximate Riemann solvers. A classical

** Graduate Student, Aeronautics.

† Professor of Aeronautics.

‡ Professor of Aeronautics and Applied Physics, member AIAA.

Riemann problem is solved locally at each computational cell boundary in order to compute the various flux terms required. This is the essential ingredient of the original Godunov scheme and it is present in most successful high-resolution schemes. The various flux-vector splitting techniques[13,15] have essentially incorporated in them an approximate Riemann solver. Finally, their extension to more than one space dimension is done without sound mathematical foundation.

Another category of numerical schemes that have been used is that of the shock-fitting or front-tracking methods. Although they have not been used as extensively as the shock-capturing methods, they have been quite successful in one-dimensional problems. A good review of these methods, as well as of many shock capturing methods, is given by Moretti[11]. These schemes are typically based on a non-conservative formulation and an effort is made to detect and identify the various discontinuous waves and compute their interactions explicitly. This is usually accomplished by introducing additional computational elements representing such waves and using the Rankine-Hugoniot jump conditions. This technique leads to complex programming logic. Identifying the waves and computing their interactions accurately is crucial for obtaining a meaningful and stable solution. For flows with complicated wave interactions such schemes may not be as robust as the shock-capturing schemes, even in one space dimension.

The research which is presented in this paper is part of a greater effort which aims to combine the characteristics of the above two categories of numerical schemes and to develop a method which will share the advantages and eliminate most of the disadvantages of both. This has been accomplished in the case of one-dimensional flow by the scheme presented in this paper. The increased accuracy which is provided in the computation of complicated wave interactions and its robustness have made this scheme especially valuable for the computation of reacting gas flows where detonation waves are present.

The scheme is based on a conservative shock-capturing Godunov-type scheme, very much like van Leer's MUSCL scheme[14]. The new feature, introduced here, is an adaptive Lagrangian grid which increases the accuracy with which discontinuous waves and their interactions are computed. Without introducing additional computational elements, i.e. refining the grid, or special computational elements to represent these waves, the shocks and contact discontinuities are computed as true discontinuites, without the smearing effect typical of shock-capturing methods. The basic conservative shock-capturing capabilities of the scheme are not diminished. The one-dimensional Lagrangian grid is endowed with the capability to track various fronts and, thus, the shock-capturing and the front-tracking ideas are combined properly.

It was deemed interesting to try this scheme on 1-D flows of reacting gases in light of the increased accuracy and robustness with which detonation waves and their interactions could be computed. The interest in such flows is evident by the number of papers appearing in the literature. For example, numerical calculations, with increased accuracy, of the one-dimensional instability of plane detonation waves may be of great interest in confirming existing theories which are based on linear stability analysis (e.g. see Lee and Stewart[8]).

The computer code developed is also able to compute one-dimensional cylindrically and spherically symmetric flows, as well as plane flows with area change. It is thus possible to compute explosions and implosions and study the effect of curvature on detonation wave speed and stability. Most of the results presented are basically validation runs and calculations demonstrating the abilities of the method and the potential use for specific 1-D problems of interest. All results shown are for a perfect gas, although a general equation of state can be incorporated in this scheme in a straightforward way.

2. Formulation and Numerical Method

The basis for the method is a conservative Godunov-type scheme similar to the MUSCL scheme introduced by van Leer[14]. The different feature in the present scheme is that the Lagrangian formulation is used instead of the Eulerian and that an adaptive grid is used. The inviscid flow of a reacting perfect gas mixture is considered. The assumption of a simplified reacting mixture is made, according to which there are two species present at any time, the reactant and the product. The reactant is converted to the product by a one-step irreversible exothermic chemical reaction. This assumption is

made in order to compare with the many theoretical and numerical results which are available in the literature for this case. The chemical reaction rate is given by the standard Arrhenius law

$$\dot{z} = -K z\, T^{\alpha} \exp\left(-E/R_g T\right) , \qquad (1a)$$

where z is the mass fraction of unburnt gas, K is a positive constant, which essentially gives a time scale, E is the activation energy of the chemical reaction, R_g is the gas constant, T is the absolute temperature and α is also a constant. The simplified Arrhenius model, where the reaction rate is a step function depending on the temperature, has also been used. For the simplified model the rate is given by

$$\dot{z} = -K z H\left(T - T_c\right) , \qquad (1b)$$

where

$$H(x) = \begin{cases} 1, & x > 0 , \\ 0, & x \leq 0 , \end{cases}$$

and T_c is a given critical temperature.

The problem under consideration is a special case of the general problem of solving numerically the nonlinear hyperbolic system of the form

$$\frac{\partial U}{\partial t} + \frac{\partial F(U)}{\partial x} = G(U) , \qquad (2)$$

where U is the appropriate solution vector. As usual, x denotes the Eulerian space variable. If the Lagrangian formulation is used, a system of exactly the same form is obtained. For non-reacting flow $G(U) = 0$. Most numerical methods use Eq. (2) as their starting point and, using a finite volume discretization, obtain the scheme of the following general form

$$U_j^{n+1} = U_j^n - \frac{\Delta t}{\Delta x}\left(\tilde{F}_{j+1/2} - \tilde{F}_{j-1/2}\right) + \Delta t\, \tilde{G}_j \qquad (3)$$

giving the solution, in an average sense, in the j^{th} cell at the time level $n+1$. The numerical flux terms $\tilde{F}$ are computed at the boundaries of each cell. An important feature of every numerical method is the calculation of these flux terms in a way that guarantees stability and accuracy.

For the present scheme, a different approach will be taken. It is informative to formulate the problem by writing the conservation laws in integral form for an arbitrary control volume $V(t)$, whose bounding surface $S(t)$ moves with a velocity $\mathbf{u}_b$ (Reynolds' Transport Theorem). These equations will be applied to each computational volume of the discrete numerical scheme. This is done so that the conservation equations and their discrete counterparts are written in a way which is independent of the Eulerian or Lagrangian formulation that will be adopted eventually. Moreover, it is easier to see from these equations how the idea for the adaptive nature of the grid was motivated. The conservation equations in integral form are

$$\frac{d}{dt}\int_{V(t)} \rho\, dV + \int_{S(t)} \rho\, (\mathbf{u} - \mathbf{u}_b)\cdot d\mathbf{S} = 0 \qquad (4)$$

$$\frac{d}{dt}\int_{V(t)} \rho\mathbf{u}\, dV + \int_{S(t)} \rho\mathbf{u}\, (\mathbf{u} - \mathbf{u}_b)\cdot d\mathbf{S} + \int_{S(t)} p\, d\mathbf{S} = 0 \qquad (5)$$

$$\frac{d}{dt}\int_{V(t)} \rho e_t\, dV + \int_{S(t)} \rho e_t\, (\mathbf{u} - \mathbf{u}_b)\cdot d\mathbf{S} + \int_{S(t)} p\mathbf{u}\cdot d\mathbf{S} = 0 \qquad (6)$$

$$\frac{d}{dt}\int_{V(t)} \rho z\, dV + \int_{S(t)} \rho z\, (\mathbf{u} - \mathbf{u}_b)\cdot d\mathbf{S} - \int_{V(t)} \dot{z}\, \rho\, dV = 0 . \qquad (7)$$

These are written for an arbitrary control volume $V(t)$, whose bounding surface $S(t)$ has a velocity $\mathbf{u}_b$. In the above equations, e_t is the total specific energy, which includes the chemical energy, i.e.

$$e_t = e + \frac{1}{2}u^2 + q_0 z , \qquad (8)$$

where e is the specific internal energy, q_0 is the heat release of the chemical reaction, and $u = |\mathbf{u}|$ is the magnitude of the fluid velocity. The perfect gas assumption is also made, i.e.

$$p = (\gamma - 1)\rho e . \qquad (9)$$

Since the boundaries of the computational cells will be moving, it is useful to consider the flow map

$$\mathbf{x} = \mathbf{X}(\xi, t) , \qquad (10)$$

which gives the position of the fluid particle that was initially ($t = 0$) at the position ξ. Thus, ξ is a convenient Lagrangian marker for the fluid particles in the flow.

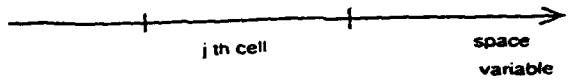

FIG. 1 Finite volume discretization in one space dimension. The space variable can be the Eulerian x or the Lagrangian ξ. The boundaries of the j^{th} cell are denoted by the subscripts $j \pm 1/2$.

Consider now the case of one dimensonal flow. A finite volume formulation is used, i.e. space is discretized by a set of computational cells as shown in Fig. 1.

The conservation equations are now written for the j^{th} cell of the computational grid

$$\frac{dm_j}{dt} + (\rho \Delta u_b)_{j+1/2} - (\rho \Delta u_b)_{j-1/2} = 0 \tag{11}$$

$$\frac{d}{dt}(m_j u_j) + (\rho u \Delta u_b)_{j+1/2} - (\rho u \Delta u_b)_{j-1/2} + p_{j+1/2} - p_{j-1/2} = 0 \tag{12}$$

$$\frac{d}{dt}(m_j e_{tj}) + (\rho e_t \Delta u_b)_{j+1/2} - (\rho e_t \Delta u_b)_{j-1/2} + (up)_{j+1/2} - (up)_{j-1/2} = 0 \tag{13}$$

$$\frac{d}{dt}(m_j z_j) + (\rho z \Delta u_b)_{j+1/2} - (\rho z \Delta u_b)_{j-1/2} - \dot{z}_j m_j = 0 , \tag{14}$$

where

$$\begin{aligned} \Delta u_b &\equiv u - u_b \\ m_j &\equiv \int_{x_{j-1/2}}^{x_{j+1/2}} \rho dx \\ m_j u_j &\equiv \int_{x_{j-1/2}}^{x_{j+1/2}} \rho u dx \\ m_j e_{tj} &\equiv \int_{x_{j-1/2}}^{x_{j+1/2}} \rho \left(e + \frac{1}{2}u^2 + q_0 z \right) dx \\ m_j z_j &\equiv \int_{x_{j-1/2}}^{x_{j+1/2}} \rho z dx . \end{aligned}$$

Average values of all quantities in the j^{th} cell are denoted by the subscript j and values of various quantities at the two boundaries of the cell are denoted by the subscripts $j \pm 1/2$. Note that average values are mass-averaged values. By defining

$$\begin{aligned} F_m &\equiv \rho \Delta u_b \\ F_u &\equiv \rho u \Delta u_b + p \\ F_e &\equiv \rho e_t \Delta u_b + pu \\ F_z &\equiv \rho z \Delta u_b , \end{aligned} \tag{15}$$

the equations of motion can be written in the more familiar form

$$\begin{aligned} \frac{dm_j}{dt} + (F_m)_{j+1/2} - (F_m)_{j-1/2} &= 0 \\ \frac{d}{dt}(m_j u_j) + (F_u)_{j+1/2} - (F_u)_{j-1/2} &= 0 \\ \frac{d}{dt}(m_j e_{tj}) + (F_e)_{j+1/2} - (F_e)_{j-1/2} &= 0 \\ \frac{d}{dt}(m_j z_j) + (F_z)_{j+1/2} - (F_z)_{j-1/2} &= m_j \dot{z}_j . \end{aligned} \tag{16}$$

Note the extra degree of freedom provided in the flux terms by the, as of yet unspecified, term Δu_b. The motion of the cell boundaries is determined by

$$\frac{dx_{j\pm1/2}}{dt} = (u_b)_{j\pm1/2} \tag{17}$$

and the average density in each cell is given by

$$\rho_j = \frac{m_j}{x_{j+1/2} - x_{j-1/2}} . \tag{18}$$

The equation of state (9) provides the means for computing the average pressure in the j^{th} cell,

$$p_j = (\gamma_j - 1)\rho_j \left(e_{tj} - q_0 z_j - \frac{1}{2}u_j^2 \right) . \tag{19}$$

Eqs. (16) are integrated in time explicitly. The procedure followed in solving these equations is similar to that used in most methods, which are higher-order extensions of the original Godunov scheme, e.g. the MUSCL scheme. At every time instant, average values of the solution are known in each computational cell. Linear variations of the primitive variables, i.e. density ρ, pressure p and velocity u, are assumed in each cell. A Riemann problem is then set up locally at each cell interface. The solution to this problem gives the velocity, pressure and density needed to compute the flux terms (15). So far, the fact that the Lagrangian formulation is being used, has not appeared explicitly in the description of the method. It is now that this choice is made and all quantities are considered as functions of time t and the Lagrangian space coordinate ξ. The interpolation procedure is carried out in ξ-space and, assuming linear variation, the generic quantity q varies as

$$q(\xi) = q_j + (q_\xi)_j (\xi - \xi_j) , \tag{20}$$

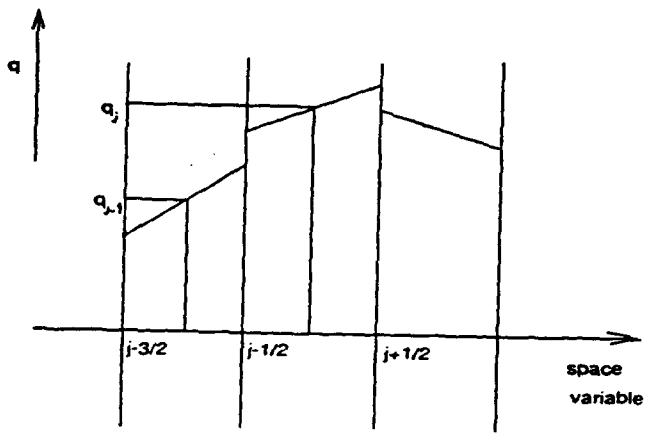

FIG. 2 Linear variation of the generic quantity q in the j^{th} cell. In general, q is discontinuous at the cell interfaces.

in the j^{th} cell, where q_j is the mass-averaged value in the cell, ξ_j is the center of the cell (in Lagrangian space) and $(q_\xi)_j$ is the slope of q in this cell, which is assumed to be constant. Note that discontinuities of these quantities are allowed at the cell interfaces, as shown in Fig. 2.

The slopes are chosen using the van Leer[16] slope limiter, but the adaptive nature of the grid, which will be described next, makes the choice of limiter less important than in the typical higher-order Godunov-type schemes. In fact, the adaptive grid allows more freedom in choosing the interpolation scheme, because additional information on the location of the various waves is always available at each time instant. The slope $(q_\xi)_j$ is computed, following van Leer[16], by

$$(q_\xi)_j = \text{ave}\left(q_\xi^- , q_\xi^+\right) , \tag{21}$$

where

$$q_\xi^- = \frac{q_j - q_{j-1}}{\xi_j - \xi_{j-1}} , \quad q_\xi^+ = \frac{q_{j+1} - q_j}{\xi_{j+1} - \xi_j} ,$$

$$\text{ave}(x,y) \equiv \frac{x+y}{2}\left[1 - \frac{(x-y)^2}{x^2+y^2+c^2}\right] ,$$

and c^2 is a small constant ($c^2 \ll 1$).

At each cell interface, two constant states q^- and q^+ are required to be used as the initial condition for the Riemann problem. There are many ways of doing this. One way is to specify for the $j+1/2$ interface

$$\begin{aligned} q^-_{j+1/2} &= q_j + (q_\xi)_j\,(\xi_{j+1/2} - \xi_j) \\ q^+_{j+1/2} &= q_{j+1} + (q_\xi)_{j+1}\,(\xi_{j+1/2} - \xi_{j+1}) , \end{aligned} \tag{22}$$

i.e. the values of q on either side of the interface, as given by Eq. (20). The method used in the present scheme is shown in Fig. 3. The domain of dependence of $\xi = \xi_{j+1/2}$ over the time interval Δt is estimated by the characteristics at the time level t. In the Lagrangian formulation of the problem the characteristic speeds are given by

$$c_\pm = \pm\frac{\rho}{\rho_0}a , \tag{23}$$

where ρ_0 is the initial density ($t = 0$) and a is the speed of sound. The constant states $q^\pm$ are then determined as the averages of Eq. (20) over the domains $\Delta\xi^\pm$. See Fig. 3.

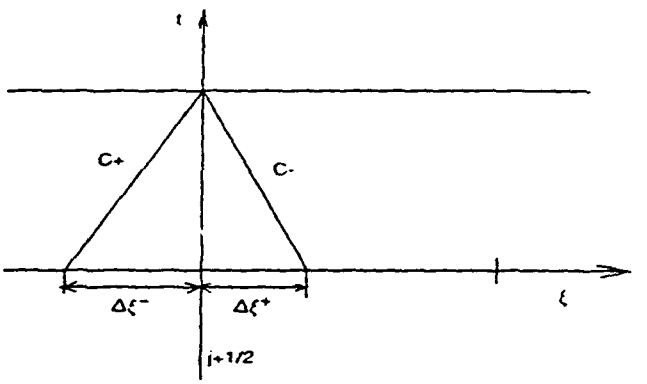

FIG. 3 The constant states $q^\pm$, which are to be used as the initial condition for the Riemann problem at the interface $j+1/2$, are obtained by averaging the linear interpolant over the domains of dependence $\Delta\xi^\pm$.

The ratio $\Delta\xi^-/\Delta\xi^+$ has proven useful in detecting developing shocks in the flow. Where the flow is smooth, without steep gradients, the above ratio is

$$\frac{\Delta\xi^-}{\Delta\xi^+} \simeq 1 .$$

The regions, where this ratio deviates from unity by more than 10%, are considered critical regions. The full nonlinear Riemann solver is used only in these regions. Everywhere else the simple acoustic approximation to the Riemann problem solution is used. It was found in all the numerical experiments performed, that in addition to the above criterion, finding local extrema of the slopes in pressure, density and velocity was very useful in determining these regions. Other criteria may also be

used. It is important that the criteria be conservative enough, so that no critical regions are missed, but they are not crucial in detecting discontinuous waves. The detection of important discontinuous waves is ultimately done by examining the solutions to the local Riemann problems.

The motivation for the adaptive grid comes from the definition of the flux terms, as given by Eqs. (15). The term Δu_b, essentially the motion of the cell boundary, is unspecified. The idea is to specify it at each cell interface, so that all important discontinuous waves coincide with cell boundaries, at every discrete time level. The solution of the Riemann problem at a given interface provides all the information needed to identify all the important waves emanating from this interface, as well as their strengths and speeds. This information is enough to specify Δu_b. Since all important waves coincide with cell boundaries, it is guaranteed that, at subsequent time instants, the evolution of these waves will be determined properly by the solution of the local Riemann problems. In the numerical experiments carried out, shock waves computed by the local Riemann solvers were considered important enough to track if the shock Mach number was greater than 1.01 and contact discontinuities were considered important if the ratio of the densities on either side was greater than 1.05.

The grid is, basically, Lagrangian, i.e. most cell boundaries move with the local fluid velocity and, hence $\Delta u_b = 0$. It is easy to see that the same ideas on the adaptivity of the grid can be used on a grid that is primarily Eulerian. The same equations can be applied directly.

An example of this adaptive procedure is shown in Fig. 4. A strong shock wave moving to the right is computed by the Riemann solver at the interface $i-1/2$ at time $t \simeq t_0$. The decision is made to assign a velocity to the adjacent cell boundary $i+1/2$, so that at time $t = t_0 + \Delta t$ the shock coincides with the interface $i+1/2$. Another possibility would be to have the interface $i-1/2$ move with the shock. The decision is made depending on which interface would be required to move a shorter distance in Lagrangian space.

It is evident from this example that a relation between the velocities in real space and the velocities in Lagrangian space is needed to update the Lagrangian grid. Consider the motion of a cell boundary given by the trajectory $x = x_b(t)$. This boundary is moving with a velocity $u_b = \dot{x}_b(t)$, which,

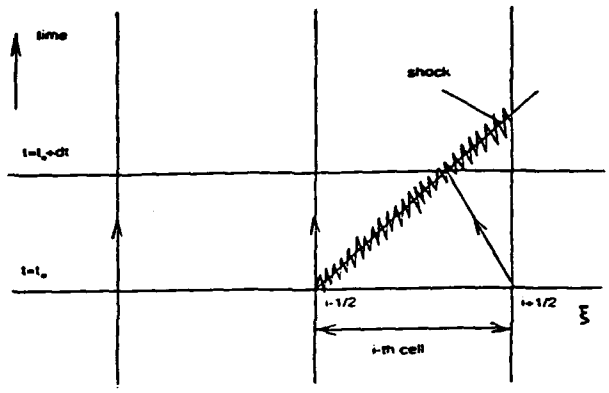

FIG. 4 The appropriate velocity is assigned to the cell interface $i+1/2$ in order to intercept the shock at the subsequent discrete time level.

in general, is different from that of the fluid u. This motion corresponds to a motion in ξ-space given by the trajectory $\xi = \xi_b(t)$ with velocity $v_b = \dot{\xi}_b(t)$. The relation between the two velocities is found with the use of the flow map

$$x = X(\xi, t) ,$$

which is essentially Eq. (10) written here for one-dimensional flow. The cell boundary motion is given by

$$x_b(t) = X(\xi_b(t), t) , \tag{24}$$

and, hence,

$$u_b = \left(\frac{\partial X}{\partial t}\right)_\xi + \dot{\xi}_b(t) \left(\frac{\partial X}{\partial \xi}\right)_t , \tag{25a}$$

or

$$u_b = u + v_b \left(\frac{\partial X}{\partial \xi}\right)_t . \tag{25b}$$

The derivative of the flow map is numerically approximated and assumed constant in each cell, i.e.

$$\left(\frac{\partial X}{\partial \xi}\right)_j \simeq \frac{x_{j+1/2} - x_{j-1/2}}{\xi_{j+1/2} - \xi_{j-1/2}} . \tag{26}$$

The velocities of the various waves, which are computed by the Riemann problems, can be translated into velocities in ξ-space by using Eq. (25b).

Collisions and reflections from walls can be treated in a straightforward way using this adaptive grid. A typical collision case is shown in Fig. 5. At time $t = t_0$, two strong shock waves are computed at the interfaces $i - 1/2$ and $i + 1/2$, moving at each other with speeds that allow for a collision before time $t = t_0 + \Delta t$. The time step is adjusted locally, i.e. only for the three cells $i - 1$, i and $i + 1$, so that at the intermediate time instant the collision point coincides with the cell boundary $i + 1/2$. The Riemann solver at this interface, at the intermediate time instant, will compute the two shock waves emerging from the collision and the adjacent cell boundaries will be able to track them in the same way at subsequent times. This leads to a robust way of handling wave interactions, without loss of accuracy.

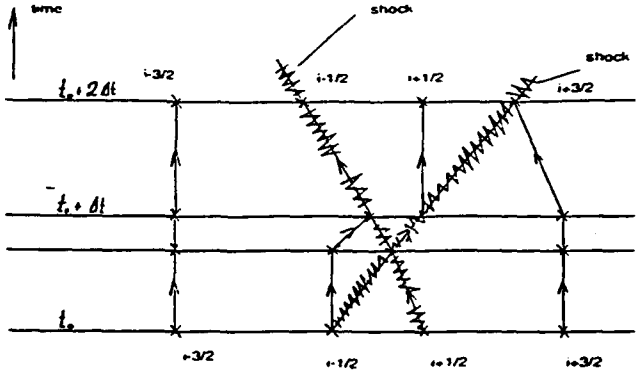

FIG. 5 The typical collision of two shocks is shown. The time step is adjusted locally so that the collision point coincides with the cell interface $i + 1/2$ at the intermediate time step.

3. Riemann Solver

The Riemann solver is an important ingredient of the numerical scheme. It provides the means for computing the velocity and the pressure at the cell interfaces and, thus, the various flux terms required. It also gives valuable information about the local waves emanating from each cell interface. As explained in the previous section, the Lagrangian grid adapts in such a way that important discontinuous waves and collision points coincide with cell boundaries at each time instant. It is, therefore, necessary to be able to identify the waves emanating from these critical cell boundaries at subsequent times. This is what the Riemann solver accomplishes. A variety of exact and approximate Riemann solvers have appeared in the literature in recent years. In all these solvers the focus is on computing the velocity and pressure of the contact discontinuity, which appears after the breakup of the initial discontinuity of the Riemann problem. In the present scheme it is crucial to identify the exact wave pattern as well. This information is used to assign the appropriate velocities to adjacent cell boundaries so that all important waves are tracked and to adjust the time step locally so that collisions are computed accurately.

3.1 Non-reacting perfect gas

Consider the case of the Riemann problem for inviscid flow of a perfect gas without chemical reactions. The initial condition at time $t = 0$ consists of two constant states denoted by the subscripts r and l. Note that it is possible to have two different perfect gases on either side of the $\xi = 0$ location, as indicated by the different specific heat ratios, i.e. γ_r and γ_l. See Fig. 6. The space variable ξ is the Lagrangian space coordinate. At time $t = 0^+$ the general wave pattern shown in Fig. 7 will develop.

There is a wave moving to the right (positive ξ) denoted by R, a wave moving to the left (negative ξ) denoted by L and a contact discontinuity C which remains at $\xi = 0$ for all time, i.e. moves with the local fluid velocity. The waves R and L are either shocks or expansion waves, depending on the initial condition. Across the contact discontinuity C the pressure p_f and velocity u_f are continuous, but the density has a jump discontinuity at $\xi = 0$ for all time. The density is ρ_{fl} for $\xi < 0$ and ρ_{fr} for $\xi > 0$. It is known that the solution to this

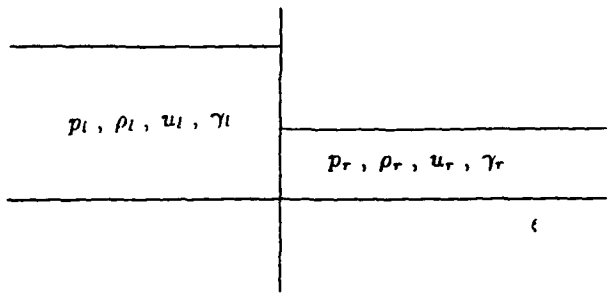

FIG. 6 Initial condition for the Riemann problem. The variable ξ is the Lagrangian space coordinate.

initial value problem exists and is unique for arbitrary initial conditions. Moreover, the solution is self-similar and the shock waves propagate with a constant velocity and strength. That is why they are represented by straight lines in the (ξ,t) diagram.

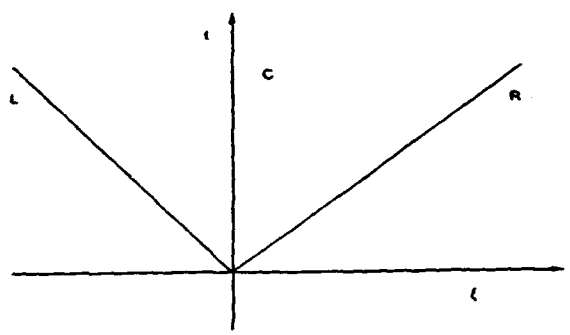

FIG. 7 General wave pattern resulting from the breakup of the original discontinuity of the Riemann problem. C is a contact discontinuity. L and R can be either shocks or expansion waves.

There are four wave patterns possible for this problem. The solution will be found for each of these wave patterns for the special case of a perfect gas.

(i) L-shock, R-shock

Across the shock R the following relationship holds

$$r \equiv \frac{u_f - u_r}{a_r} = \frac{2}{\gamma_r + 1}\left(M_r - \frac{1}{M_r}\right) . \quad (27)$$

M_r is the shock Mach number defined by

$$M_r \equiv \frac{U_r - u_r}{a_r} , \quad (28)$$

where U_r is the shock velocity and $a_r = \sqrt{\gamma_r p_r/\rho_r}$ is the speed of sound in the undisturbed region r. Similarly for the shock L,

$$\frac{u_l - u_f}{a_l} = \frac{2}{\gamma_l + 1}\left(M_l - \frac{1}{M_l}\right) . \quad (29)$$

where M_l is the shock Mach number for L. Equations (27) and (29) can be solved for the shock Mach numbers to give

$$M_r = \frac{\gamma_r + 1}{4} r + \sqrt{\left(\frac{\gamma_r + 1}{4}\right)^2 r^2 + 1} \quad (30)$$

$$M_l = \frac{\gamma_l + 1}{4}\frac{u_l - u_f}{a_l} + \sqrt{\left(\frac{\gamma_l + 1}{4}\right)^2 \left(\frac{u_l - u_f}{a_l}\right)^2 + 1} . \quad (31)$$

The pressure ratios across the two shocks are given by the following equations

$$\frac{p_f}{p_r} = 1 + \frac{2\gamma_r}{\gamma_r + 1}(M_r^2 - 1) \quad (32)$$

$$\frac{p_f}{p_l} = 1 + \frac{2\gamma_l}{\gamma_l + 1}(M_l^2 - 1) . \quad (33)$$

From Eqs. (30)–(33) one obtains a single equation for the unknown r,

$$G(r) \equiv 1 - \frac{p_l}{p_r} + \gamma_r \frac{\gamma_r + 1}{4} r^2 + \gamma_r r \sqrt{\left(\frac{\gamma_r + 1}{4}\right)^2 r^2 + 1} - \frac{p_l}{p_r}\gamma_l \frac{\gamma_l + 1}{4}\left(\frac{u_l - u_r}{a_l} - \frac{a_r}{a_l} r\right)^2 - \frac{p_l}{p_r}\gamma_l \left(\frac{u_l - u_r}{a_l} - \frac{a_r}{a_l} r\right) \sqrt{\left(\frac{\gamma_l + 1}{4}\right)^2 \left(\frac{u_l - u_r}{a_l} - \frac{a_r}{a_l} r\right)^2 + 1} = 0 . \quad (34)$$

This equation is solved numerically using a Newton-Raphson method. Once r is obtained, all other quantities of interest follow from Eqs. (27)-(33). The densities are determined by

$$\frac{\rho_{fi}}{\rho_i} = \frac{(\gamma_i+1)\,M_i^2}{2+(\gamma_i-1)\,M_i^2}\,, \qquad i = r,l\,. \tag{35}$$

It is important to be able to determine if this wave pattern will develop for a given initial condition. For this solution to be possible, certain compatibility conditions must hold. These are easily found by noticing that in Eqs. (27) and (29) the shock mach numbers M_r and M_l must be greater than 1. It then follows that the following compatibility condition must hold

$$u_r \le u_f \le u_l\,, \tag{36}$$

or, equivalently,

$$\begin{aligned} u_r - u_l &\le 0 \\ 0 \le r &\le \frac{u_l - u_r}{a_r}\,. \end{aligned} \tag{37}$$

(ii) L-expansion wave, R-shock

In this case, Eqs. (27),(28),(30) and (32), derived previously, still hold for the shock wave R. In addition to these equations, the following equation gives the pressure ratio across the isentropic expansion wave,

$$\begin{aligned} \frac{p_f}{p_l} &= \left(1+\frac{\gamma_l-1}{2}\frac{u_l-u_f}{a_l}\right)^{2\gamma_l/(\gamma_l-1)} \\ &= \left(1+\frac{\gamma_l-1}{2}\frac{u_l-u_r}{a_l}-\frac{\gamma_l-1}{2}\frac{a_r}{a_l}r\right)^{2\gamma_l/(\gamma_l-1)}\,, \end{aligned} \tag{38}$$

where r is defined in Eq.(27). Combining Eqs. (30),(32) and (38) a single equation in r is obtained, as in the previous case,

$$\begin{aligned} F(r) \equiv\ & 1+\gamma_r\frac{\gamma_r+1}{4}r^2+\gamma_r r\sqrt{\left(\frac{\gamma_r+1}{4}\right)^2 r^2+1} \\ & -\frac{p_l}{p_r}\left(1+\frac{\gamma_l-1}{2}\frac{u_l-u_r}{a_l} \right. \\ & \left. -\frac{\gamma_l-1}{2}\frac{a_r}{a_l}r\right)^{2\gamma_l/(\gamma_l-1)} = 0\,, \end{aligned} \tag{39}$$

which is solved numerically. The densities are determined by Eq. (35) across the shock and by the isentropic relation

$$\frac{\rho_{fl}}{\rho_l} = \left(\frac{p_{fl}}{p_l}\right)^{1/\gamma}\,,$$

across the expansion wave.

The compatibility conditions are found by noticing that across the expansion wave L, $0 \le p_f/p_l \le 1$ and across the shock R, $p_f/p_r \ge 1$. Using Eqs. (32) and (38) the following relations are found, after some algebra,

$$\begin{aligned} p_r/p_l &\le 1 \\ u_r - u_l &< \left(\frac{2}{\gamma_l-1}\right)a_l\,, \end{aligned} \tag{40}$$

and

$$\begin{aligned} \frac{u_l-u_r}{a_r} \le r < \frac{u_l-u_r}{a_r}+\left(\frac{2}{\gamma_l-1}\right)\frac{a_l}{a_r} \\ 0 \le r\,. \end{aligned} \tag{41}$$

(iii) L-shock, R-expansion wave

This case is exactly the same as case (ii) with the transformation $\xi \longrightarrow -\xi$.

(iv) L-expansion wave, R-expansion wave

In this case, there are two expansion waves and the pressure ratios across them are given by

$$\begin{aligned} \frac{p_f}{p_l} &= \left(1+\frac{\gamma_l-1}{2}\frac{u_l-u_f}{a_l}\right)^{2\gamma_l/(\gamma_l-1)} \\ \frac{p_f}{p_r} &= \left(1+\frac{\gamma_r-1}{2}\frac{u_f-u_r}{a_r}\right)^{2\gamma_r/(\gamma_r-1)}\,. \end{aligned} \tag{42}$$

From Eqs. (42) the following single equation in r is obtained,

$$\begin{aligned} S(r) \equiv\ & \left(1+\frac{\gamma_r-1}{2}r\right)^{2\gamma_r/(\gamma_r-1)} \\ & -\frac{p_l}{p_r}\left(1+\frac{\gamma_l-1}{2}\frac{u_l-u_r}{a_l} \right. \\ & \left. -\frac{\gamma_l-1}{2}\frac{a_r}{a_l}r\right)^{2\gamma_l/(\gamma_l-1)} = 0\,, \end{aligned} \tag{43}$$

which is solved numerically with the Newton-Raphson method. The compatibility conditions are once again found by noticing that across the expansion waves $0 \leq p_f/p_l \leq 1$ and $0 \leq p_f/p_r \leq 1$, which, using Eqs. (42), give

$$0 \leq u_r - u_l < 2\left(\frac{a_r}{\gamma_r - 1} + \frac{a_l}{\gamma_l - 1}\right) \qquad (44)$$

and

$$\begin{aligned} -\frac{2}{\gamma_r - 1} &< r \leq 0 \\ \frac{u_l - u_r}{a_r} &\leq r < \frac{u_l - u_r}{a_r} + \left(\frac{2}{\gamma_l - 1}\right)\frac{a_l}{a_r} . \end{aligned} \qquad (45)$$

3.2 Acoustic approximation

The solution to the Riemann problem becomes easier to obtain when the initial conditions are such that the waves R and L shown in Fig. 7 are so weak that linear acoustic theory can be used. This happens when the distance, in some sense, between the two constant states r and l is small. The waves R and L can then be treated as acoustic waves with the pressure ratios across them given by the simple relations,

$$p_f = p_r + \sqrt{\gamma_r p_r \rho_r}\,(u_f - u_r) \qquad (46a)$$

$$p_f = p_l - \sqrt{\gamma_l p_l \rho_l}\,(u_f - u_l) . \qquad (46b)$$

Combining Eqs. (46a) and (46b), one finds

$$u_f = (p_l - p_r + \sqrt{\gamma_r p_r \rho_r}\,u_r + \sqrt{\gamma_l p_l \rho_l}\,u_l)\,/\,(\sqrt{\gamma_r p_r \rho_r} + \sqrt{\gamma_l p_l \rho_l}) . \qquad (47)$$

The densities behind these waves are given by

$$\rho_{fi} = \rho_i\,(p_f + \mu_i^2 p_i)\,/\,(p_i + \mu_i^2 p_i) , \qquad (48)$$

where

$$\mu_i^2 \equiv (\gamma_i - 1)/(\gamma_i + 1) , \qquad i = r, l .$$

3.3 Reacting perfect gas mixture

So far, the classical Riemann problem for non-reacting inviscid flow has been considered. The solution to this problem, as mentioned before, is a self-similar solution, i.e. depending on x/t only. For the case of a simple reacting mixture the nonlinear system of equations, that needs to be solved, is of the form

$$\frac{\partial U}{\partial t} + \frac{\partial F(U)}{\partial x} = G(U) , \qquad (49)$$

where

$$U = \begin{pmatrix} \rho \\ \rho u \\ \rho\,(e + \frac{1}{2}u^2) \\ \rho z \end{pmatrix} , \quad G(U) = \begin{pmatrix} 0 \\ 0 \\ 0 \\ -\rho \dot{z} \end{pmatrix} ,$$

$$F(U) = \begin{pmatrix} \rho u \\ \rho u^2 + p \\ \rho u\,(e + \frac{1}{2}u^2) + pu \\ \rho z u \end{pmatrix} .$$

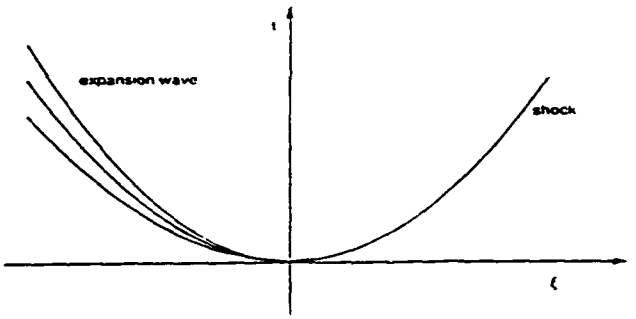

FIG. 8 This is a typical wave pattern resulting from the breakup of the initial discontinuity of the Riemann problem for the case of a simple reacting mixture. The solution is no longer self-similar.

This is written using the Eulerian formulation, but one obtains a system of exactly the same form, if the Lagrangian formulation is used. The Riemann problem solution, described so far, is for the non-reacting case, i.e. $G(U) = 0$. For the reacting case, jumps in the concentration of unburnt gas z are allowed only across contact discontinuities, but not across shocks. The solution to this problem is more complicated and no longer self-similar.

In Fig. 8, a typical wave pattern is shown. The shock and expansion waves are curved in the (ξ,t) plane, i.e. they are accelerating. The solution to this generalized Riemann problem has been worked out by Matania Ben-Artzi[1]. It is shown that the solution approaches the solution of the classical Riemann problem for the non-reacting case in the limit $\xi \rightarrow 0$ and $t \rightarrow 0$. The more complicated generalized Riemann solver given by Ben-Artzi provides higher order accuracy over the usual non-reacting solver. Numerical experiments were performed using the present adaptive Lagrangian scheme with both Riemann solvers. It was found that the simpler solver gave results which were just as good. The acceleration of the various waves was captured numerically quite accurately.

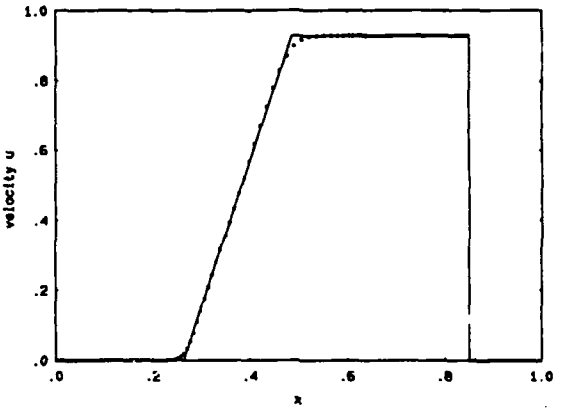

FIG. 9a Velocity profile at time $t = 0.20$ for Sod's shock tube problem with $N = 150$ computational cells. The solid line represents the exact solution and the boxes represent the numerical solution.

4. Numerical results

A number of test cases were run using this numerical scheme. The cases were chosen primarily to validate the code and to demonstrate its potential for solving 1-D problems with complicated wave interactions. The scheme is particularly useful for computing unsteady reacting flows involving detonation waves and their interactions.

The first case is the classical shock-tube problem. It is an important validation run for the code. The initial conditions used are those proposed by Sod[12]. At time $t = 0$ a diaphragm at the location $x = 0.5$ separates the two constant states

$$\begin{aligned} p_l &= 1.0 \quad \rho_l = 1.0 \quad u_l = 0.0 \,, x < 0.5 \\ p_r &= 0.1 \quad \rho_r = 0.125 \, u_r = 0.0 \,, x > 0.5 \,, \end{aligned} \tag{50}$$

for a perfect gas with $\gamma = 1.40$. $N = 150$ computational cells are used in this calculation. In all the results presented, the solutions are given as functions of the Eulerian space variable x , even though the calculation is done in Lagrangian space. The Lagrangian aspect of the scheme is evident by the increased density of computational points in compression regions. The comparison between the numerical solution and the exact solution shown in Fig. 9is excellent. Note that the expansion wave is computed with the accuracy of typical shock-capturing schemes, since no effort is made to track expansion waves. The shock wave and the contact discontinuity are computed with no smearing.

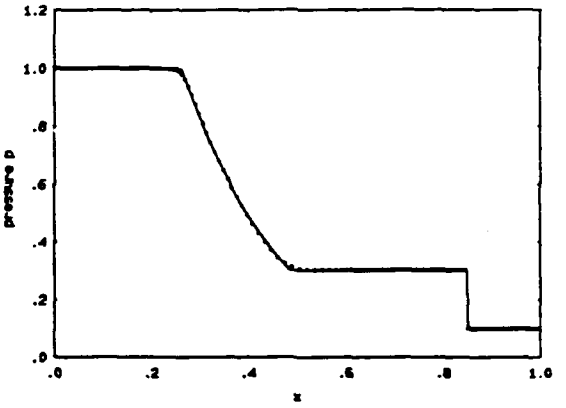

FIG. 9b Pressure profile at time $t = 0.20$ for Sod's shock tube problem with $N = 150$ computational cells. The solid line represents the exact solution and the boxes represent the numerical solution.

In order to demonstrate the ability of the scheme to compute complicated wave interactions accurately, the shock tube problem is carried a step further. Reflecting walls are assumed present at the locations $x = 0$ and $x = 1$. The computation is continued to see how the multiple reflections of the shock from the walls and its collisions with the contact discontinuity are calculated. In Fig. 10, the solution is shown after the first reflection of the shock wave from the wall at $x = 1$, which occurs at $t = 0.285$. In Fig. 11, the reflected shock has collided with the contact discontinuity and a new shock wave has been generated. The solution at

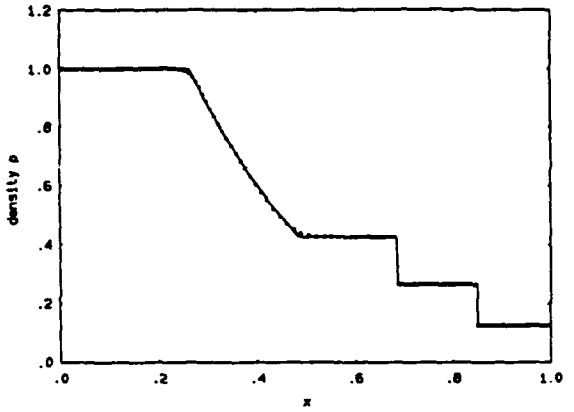

FIG. 9c Density profile at time $t = 0.20$ for Sod's shock tube problem with $N = 150$ computational cells. The solid line represents the exact solution and the boxes represent the numerical solution.

subsequent times is shown in Figs. 12 and 13. The computation was carried out until time $t = 7.88$. That corresponds to many reflections of the original shock. In a real experiment viscous effects would have made the process die down much sooner. In Fig. 14, the entropy of the system is shown as a function of time. As $t \rightarrow \infty$, the system approaches the state predicted by thermodynamics, since the scheme is fully conservative. Any scheme which conserves total mass and energy will give the correct final entropy. In this case it is $s = 0.1168$ in the appropriate dimensionless units. This is an important point worth repeating here. The conservative character of the scheme is not compromised by the use of the adaptive grid technique.

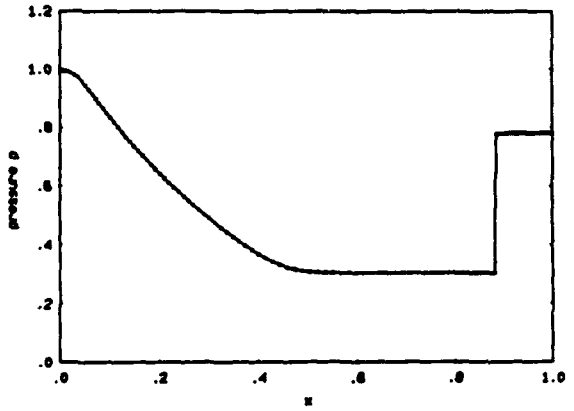

FIG. 10a Pressure profile at time $t = 0.40$. The shock has reflected from the wall at $x = 1$.

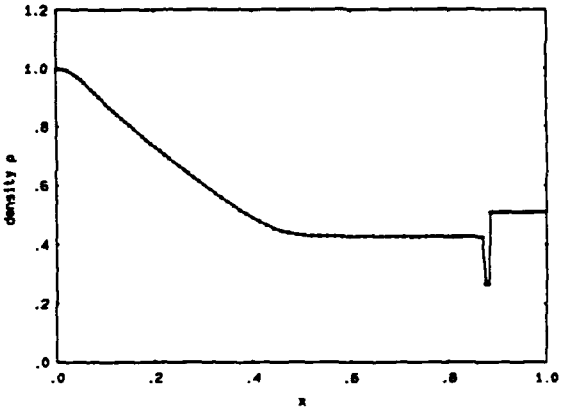

FIG. 10b Density profile at time $t = 0.40$. The shock has reflected from the wall at $x = 1$.

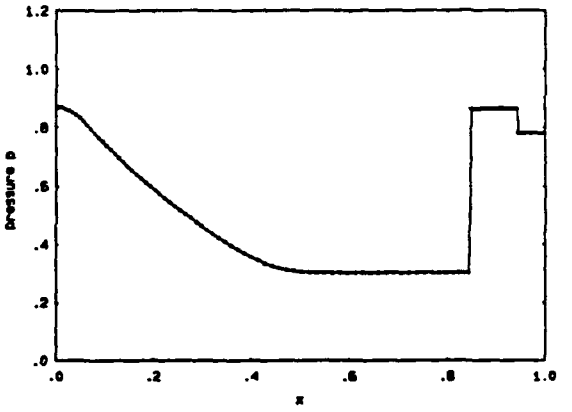

FIG. 11a Pressure profile at time $t = 0.45$. The reflected shock has collided with the contact discontinuity. A secondary shock has been generated.

Another test case is that of a steady detonation wave. The well known ZND theory (Zel'dovich-VonNeumann-Doering) for a steady detonation is used to compare with the numerical solution obtained using this scheme. As a first check, the profile of a steady detonation wave, computed using the ZND theory, is given as the initial condition to the unsteady code. The solution after time $t = 10$ (10,000 time steps) is then superimposed on the ZND solution and compared. The comparison, shown in Fig. 15, is excellent. The standard Arrhenius law, given by Eq. (1a), is used for the chemical reaction rate with $\alpha = 0$, i.e.

$$\dot{z} = -K z T^{\alpha} \exp(-E/R_g T) .$$

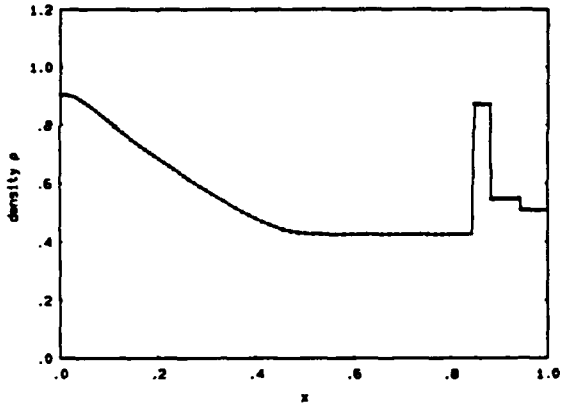

FIG. 11b Density profile at time $t = 0.45$. The reflected shock has collided with the contact discontinuity. A secondary shock has been generated.

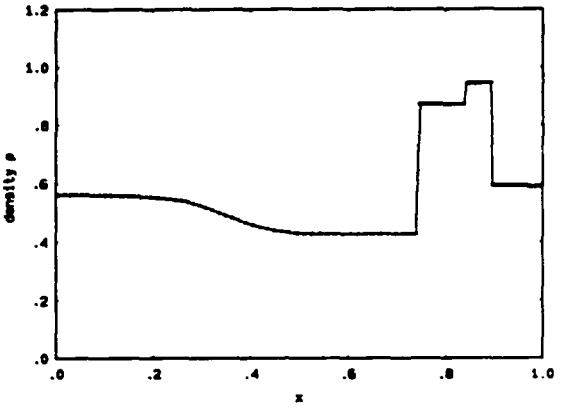

FIG. 12b Density profile at time $t = 0.61$. An acoustic wave has been generated from the collision of the secondary shock with the contact discontinuity.

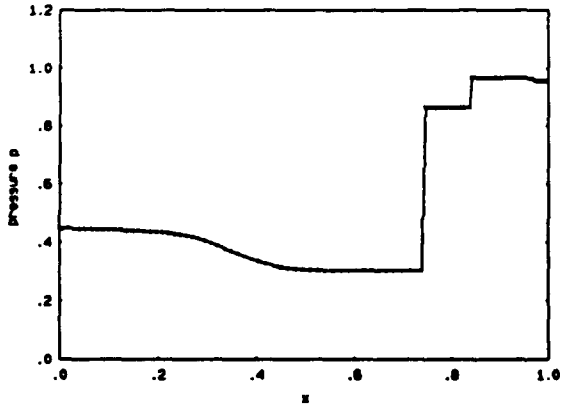

FIG. 12a Pressure profile at time $t = 0.61$. An acoustic wave has been generated from the collision of the secondary shock with the contact discontinuity.

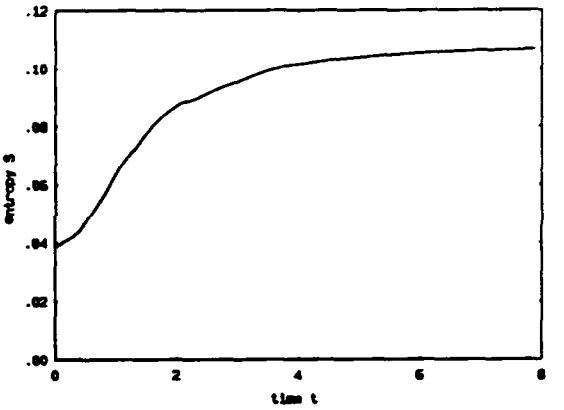

FIG. 14 Entropy of the system as a function of time for the shock tube problem with multiple reflections.

The parameters used for this test run are

$$\gamma = 1.2 \, , \; q_0/R_g T_0 = 50 \, , \; E/R_g T_0 = 40 \, ,$$

where the subscript 0 denotes the undisturbed region into which the detonation propagates. This steady detonation wave corresponds to an overdrive factor of $f = 1.6$. The overdrive factor is defined by

$$f = D^2/D_{CJ}^2 \, ,$$

where D is the detonation wave speed and D_{CJ} is the detonation speed corresponding to the Chapman-Jouguet point. For details on the ZND theory see the book by Fickett and Davis[3].

The case of unsteady detonation waves will now be considered. For the following cases the simplified Arrhenius chemical rate law is used (Eq. (1b)), i.e.

$$\dot{z} = -K z H(T - T_c) \, ,$$

where T_c is a critical temperature above which the chemical reaction begins. Fig. 16 shows the evolution of an unsteady detonation propagating in an undisturbed region. It is the well known piston problem. The motion of the piston, starting at $x = 0$, generates a shock which raises the temperature of the gas above the critical value T_c. The chemical reaction begins and the detonation wave accelerates into the undisturbed region. The nu-

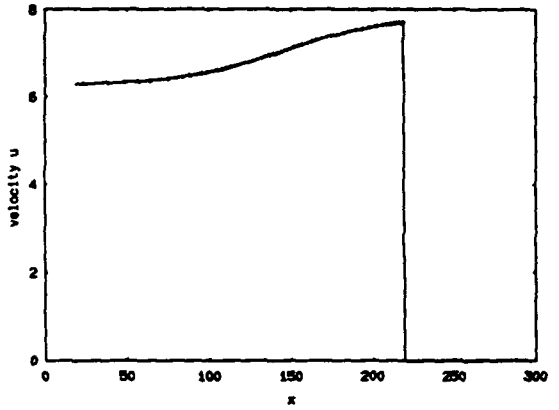

FIG. 15a Velocity profile at $t = 10$. The solid line is the solution given by the ZND theory. The boxes are the numerical solution.

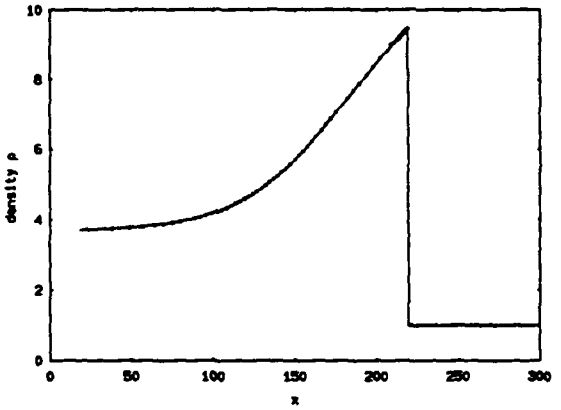

FIG. 15c Density profile at $t = 10$. The solid line is the solution given by the ZND theory. The boxes are the numerical solution.

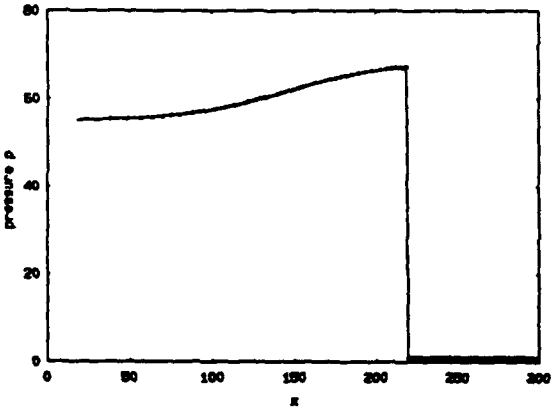

FIG. 15b Pressure profile at $t = 10$. The solid line is the solution given by the ZND theory. The boxes are the numerical solution.

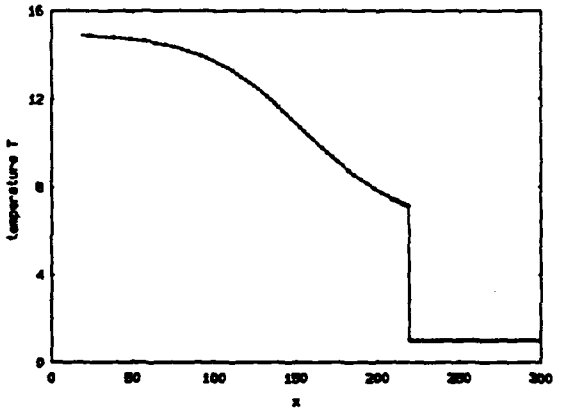

FIG. 15d Temperature profile at $t = 10$. The solid line is the solution given by the ZND theory. The boxes are the numerical solution.

merical values used in this run are

$$\gamma = 1.4\,, \qquad q_0 = 20\,, \qquad T_c = 1.3\,,$$

where all quantities are normalized with the corresponding values in the undisturbed region. The *piston velocity* is taken to be $u_p = 1$.

A more interesting case is shown in Fig. 17. The initial condition is a smooth pressure distribution with zero initial velocity, which leads to isentropic compression and eventually shock formation. If in this compression the temperature of the gas becomes larger than T_c, then the chemical reaction starts and a detonation wave is generated. The formation of the shock from a smooth flow is captured very well by this scheme. The numerical values used in this run are

$$\gamma = 1.4\,, \qquad q_0 = 20\,, \qquad T_c = 1.2\,,$$

where all quantities are normalized appropriately. The normalization is such that the initial temperature of the gas at rest is $T_0 = 1$. The initial pressure distribution is given by

$$p_0(x) = 0.1 + 3.0\exp(25x^2)\,.$$

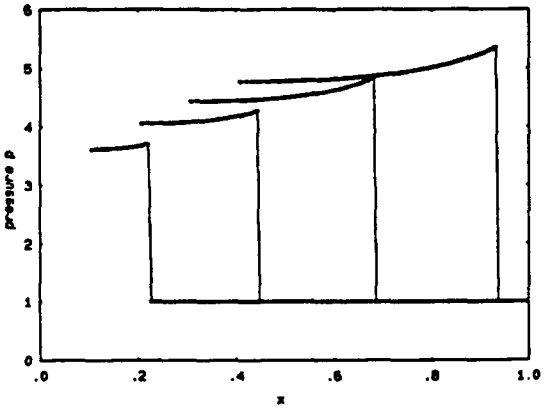

FIG. 16a Pressure profiles for the piston problem. The detonation wave generated accelerates into the undisturbed region. In this case the critical temperature is $T_c = 1.3$. Times $t = 0.1, 0.2, 0.3, 0.4$.

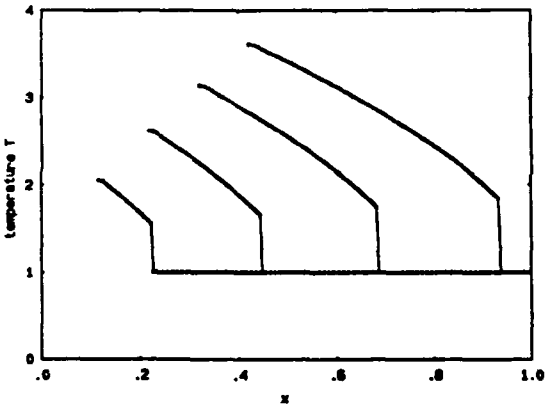

FIG. 16b Temperature profiles for the piston problem. The detonation wave generated accelerates into the undisturbed region. In this case the critical temperature is $T_c = 1.3$. Times $t = 0.1, 0.2, 0.3, 0.4$.

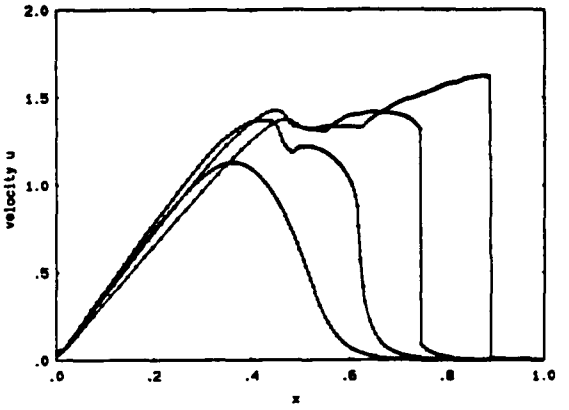

FIG. 17a Velocity profiles for a smooth compression. When the compression raises the temperature above the critical value $T_c = 1.2$ the reaction begins and a detonation wave is formed. Times $t = 0.075, 0.150, 0.225, 0.300$.

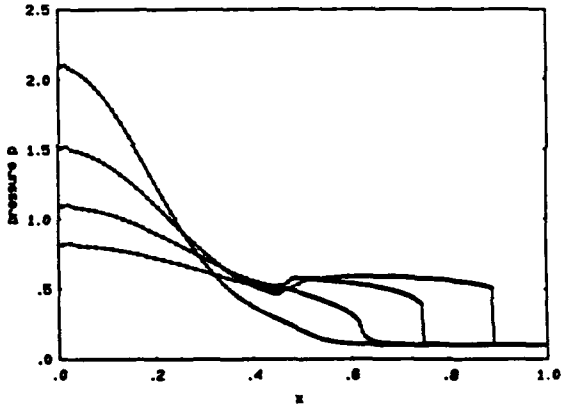

FIG. 17b Pressure profiles for a smooth compression. When the compression raises the temperature above the critical value $T_c = 1.2$ the reaction begins and a detonation wave is formed. Times $t = 0.075, 0.150, 0.225, 0.300$.

5. Conclusions

An adaptive numerical scheme has been presented for the computation of flows with complicated interactions of discontinuous waves. Its accuracy and robustness, as demonstrated by numerical experiments make it a valuable tool, especially for the study of unsteady reacting flows with detonation waves. The conservative formulation gives the method all the advantages of higher-order shock-capturing schemes and its adaptive characteristic allows for good accuracy near shocks with no smearing effect. The advantages of the conservative shock-capturing schemes are combined with the advantages of the front-tracking methods very well to give a useful computational scheme.

Acknowledgements

This work is part of a larger effort to investigate mixing and combustion, sponsored by the Air Force Office of Scientific Research Grant No. 88-0155, whose support is gratefully acknowledged.

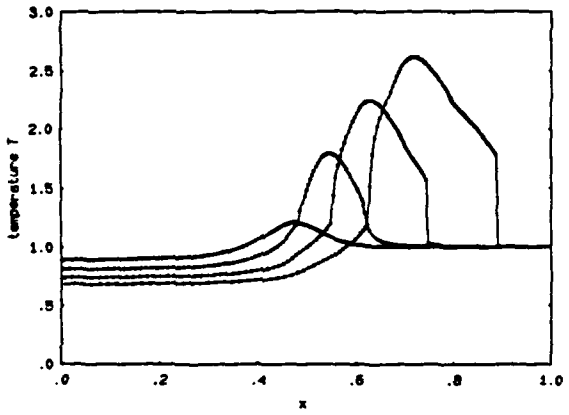

FIG. 17c Temperature profiles for a smooth compression. When the compression raises the temperature above the critical value $T_c = 1.2$ the reaction begins and a detonation wave is formed. Times $t = 0.075, 0.150, 0.225, 0.300$.

References

1. BEN-ARTZI, M. [1989] "The Generalized Riemann Problem for Reactive Flows", *J. Comput. Phys.* **81**, 70–101.

2. COLELLA, P. and WOODWARD, P.R. [1984] "The Piecewise Parabolic Method (PPM) for Gas Dynamical Simulations", *J. Comput. Phys.* **54**, 174–201.

3. FICKETT, W. and DAVIS, W.C. [1979] *Detonation* (University of California Press).

4. GODUNOV, S.K. [1959] "A Finite Difference Method for the Numerical Computation of Discontinuous Solutions of the Equations of Fluid Dynamics", *Mat. Sb.* **47**, 271–306.

5. HARTEN, A. [1983] "High Resolution Schemes for Hyperbolic Conservation Laws", *J. Comput. Phys.* **49**, 357–393.

6. HARTEN, A. [1984] "On a Class of High Resolution Total-Variation-Stable Finite-Difference Schemes", *SIAM Journal of Numerical Analysis* **21**, 1–23.

7. LAX, P.D. and WENDROFF, B. [1960] "Systems of Conservation Laws", *Commun. Pure Appl. Math.* **13**, 217–237.

8. LEE, H.I. and STEWART, D.S. [1990] "Calculation of linear detonation instability: one-dimensional instability of plane detonation", *J. Fluid Mech.* **216**, 103–132.

9. MACCORMACK, R.W. [1969] "The Effect of Viscosity in Hypervelocity Impact Cratering", AIAA Paper No. 69-354.

10. MONTAGNÉ, J.-L.,YEE, H.C. and VINOKUR, M. [1989] "Comparative Study of High-Resolution Shock-Capturing Schemes for a Real Gas", *AIAA J.* **27**(10), 1332–1346.

11. MORETTI, G. [1987] "Computation of Flows with Shocks", *Ann. Rev. Fluid Mech.* **19**, 313–337.

12. SOD, G.A. [1978] "A Survey of Several Finite Difference Methods for Systems of Nonlinear Hyperbolic Conservation Laws", *J. Comput. Phys.* **27**, 1–31.

13. STEGER, J.L. and WARMING, R.F. [1981] "Splitting of the Inviscid Gasdynamic Equations with Application to Finite-Difference Methods", *J. Comput. Phys.* **40**, 263–293.

14. VAN LEER, B. [1979] "Towards the Ultimate Conservative Difference Scheme. V. A Second-Order Sequel to Godunov's Method", *J. Comput. Phys.* **32**, 101–136.

15. VAN LEER, B. [1982] "Flux-Vector Splitting for the Euler Equations", *Lect. Notes Phys.* **170**, 507–512.

16. VAN LEER, B. [1984] "On the Relation Between the Upwind-Differencing Schemes of Godunov, Engquist-Osher and Roe", *SIAM J. Sci. Stat. Comput.* **5**(1), 1–20.